ENHANCED ASSESSMENT OF PROJECTED LANDSLIDE ACTIVITY UNDER PRECIPITATION AND SEISMICITY

FINAL REPORT

PROJECT SPR 808

Oregon Department of Transportation

ENHANCED ASSESSMENT OF PROJECTED LANDSLIDE ACTIVITY UNDER PRECIPITATION AND SEISMICITY

Final Report

PROJECT SPR 808

by

Ben A. Leshchinsky
Adam M. Booth
Michael J. Olsen
Nicolas Mathews
Kara Kingen

for

Oregon Department of Transportation
Research Section
555 13th Street NE, Suite 1
Salem OR 97301

and

Federal Highway Administration
1200 New Jersey Avenue SE
Washington, DC 20590

July 2021

Technical Report Documentation Page

1. Report No. FHWA-OR-RD-22-02	2. Government Accession No.	3. Recipient's Catalog No.
4. Title and Subtitle Enhanced Assessment of Projected Landslide Activity Under Precipitation and Seismicity		5. Report Date July 2021 6. Performing Organization Code
7. Author(s) Ben Leshchinsky: 0000-0003-3890-1368 Adam Booth: 0000-0002-7339-0594 Mike Olsen: 0000-0002-2989-5309 Nick Matthews: 0000-0002-4647-4039 Kara Kingen: 0000-0001-5130-5064		8. Performing Organization Report No. SPR 808
9. Performing Organization Name and Address Oregon Department of Transportation (ODOT) Research Section 555 13th Street NE, Suite 1 Salem, OR 97301		10. Work Unit No. (TRAIS) 11. Contract or Grant No.
12. Sponsoring Agency Name and Address Oregon Dept. of Transportation Research Section 555 13th Street NE, Suite 1 Salem, OR 97301 Federal Highway Admin. 1200 New Jersey Avenue SE Washington, DC 20590		13. Type of Report and Period Covered Final Report 14. Sponsoring Agency Code
15. Supplementary Notes		

16. Abstract: Regional assessments of potential landsliding are useful means of mitigating loss of life, property, and infrastructure, especially when exacerbated by rainfall and seismic events. Susceptibility maps are useful tools for characterizing hazard and risk tied to potential landslides. The method presented herein enables characterization of the area, volume, and distribution of discrete landslide shapes, informing enhanced susceptibility analyses. The method also enables consideration of destabilizing forces from seismic and rainfall events. A new age-roughness curve for the Pacific Northwest constrains physical drivers linked to individual landslides from a landslide inventory, enabling more refined consideration of landslide driving forces during 3D forensic analyses. This further enhances susceptibility analyses by providing refined distributions of soil shear strength. The methodologies herein are validated by comparing rainfall-induced susceptibility to known landslides from a landslide inventory and by comparing empirical relationships between area and volume, developed using the proposed methodology, to empirical relationships found in literature. Finally, susceptibility maps are used to produce hazard maps, linking susceptibility and the probability of driving events, and a suite of coarse risk metrics. These risk metrics include maps and profiles showing closure times, repair costs, commodity losses, and rerouting costs associated with ODOT right-of-way (ROW). The analyses herein also provide useful tools for resilience planning.

17. Key Words Landslides, precipitation, seismicity, lidar	18. Distribution Statement Copies available from NTIS, and online at https://www.oregon.gov/ODOT/Programs/Pages/Research-Publications.aspx		
19. Security Classification (of this report) Unclassified	20. Security Classification (of this page) Unclassified	21. No. of Pages 280	22. Price

SI* (MODERN METRIC) CONVERSION FACTORS

APPROXIMATE CONVERSIONS TO SI UNITS

Symbol	When You Know	Multiply By	To Find	Symbol
		LENGTH		
in	inches	25.4	millimeters	mm
ft	feet	0.305	meters	m
yd	yards	0.914	meters	m
mi	miles	1.61	kilometers	km
		AREA		
in^2	square inches	645.2	millimeters squared	mm^2
ft^2	square feet	0.093	meters squared	m^2
yd^2	square yards	0.836	meters squared	m^2
ac	acres	0.405	hectares	ha
mi^2	square miles	2.59	kilometers squared	km^2
		VOLUME		
fl oz	fluid ounces	29.57	milliliters	ml
gal	gallons	3.785	liters	L
ft^3	cubic feet	0.028	meters cubed	m^3
yd^3	cubic yards	0.765	meters cubed	m^3
NOTE: Volumes greater than 1000 L shall be shown in m^3.				
		MASS		
oz	ounces	28.35	grams	g
lb	pounds	0.454	kilograms	kg
T	short tons (2000 lb)	0.907	megagrams	Mg
		TEMPERATURE (exact)		
°F	Fahrenheit	(F-32)/1.8	Celsius	°C

APPROXIMATE CONVERSIONS FROM SI UNITS

Symbol	When You Know	Multiply By	To Find	Symbol
		LENGTH		
mm	millimeters	0.039	inches	in
m	meters	3.28	feet	ft
m	meters	1.09	yards	yd
km	kilometers	0.621	miles	mi
		AREA		
mm^2	millimeters squared	0.0016	square inches	in^2
m^2	meters squared	10.764	square feet	ft^2
m^2	meters squared	1.196	square yards	yd^2
ha	hectares	2.47	acres	ac
km^2	kilometers squared	0.386	square miles	mi^2
		VOLUME		
ml	milliliters	0.034	fluid ounces	fl oz
L	liters	0.264	gallons	gal
m^3	meters cubed	35.315	cubic feet	ft^3
m^3	meters cubed	1.308	cubic yards	yd^3
		MASS		
g	grams	0.035	ounces	oz
kg	kilograms	2.205	pounds	lb
Mg	megagrams	1.102	short tons (2000 lb)	T
		TEMPERATURE (exact)		
°C	Celsius	1.8C+32	Fahrenheit	°F

*SI is the symbol for the International System of Measurement

ACKNOWLEDGEMENTS

The authors would like to thank the members of the ODOT Research Section, ODOT project champions Curran Mohney and Geoff Crook, ODOT research coordinator Kira Glover-Cutter and the Technical Advisory Committee - Susan Ortiz, Pete Castro, Tom Braibish, Phil Wurst, Nick Testa, and Emily Cline - for their sage advice and assistance in the preparation of this report. They also appreciate the assistance of Becky Knudson and Dejan Dudich in performing the traffic delay modeling. They appreciate the assistance of Sophie Brown who contributed retaining wall cost data. They also thank Dr. Joshua Roering of University of Oregon for his invaluable help in providing insight and scripts for characterizing distributed regolith depths for the study sites. They also thank the Oregon Lidar Consortium for providing the lidar data utilized in this study. Finally we thank the drill crew from HazTech for their excellent help during site investigation of the Hooskanaden landslide.

DISCLAIMER

TABLE OF CONTENTS

LIST OF TABLES

LIST OF FIGURES

1.0 INTRODUCTION

1.1 PROBLEM STATEMENT

With thousands of active landslides saturating lifeline routes and overwhelming ODOT's mitigation capacity, the development of a new tool to prioritize landslides is imperative for maintaining the safest and most efficient transportation system possible. Landslides are frequent hazards that affect the operation, maintenance, and construction of Oregon highways, resulting in negative economic, environmental, and social impacts for Oregon communities. To fully support optimized resiliency efforts, focused mapping that integrally considers landslide susceptibility in context of geotechnical properties, potential seismic events, and projections of extreme precipitation events is critical for informed selection of priority areas.

1.2 BACKGROUND AND SIGNIFICANCE OF WORK

Predictive factors such as landslide activity, precipitation projections, and geotechnical properties can be integrated together with seismic models to specifically filter and select for seismic landslide "hot spots" localized along lifeline corridors for targeted mitigation. In general, large, young landslides are most likely to move during an earthquake or climatic event. Until recently, comprehensive corridor assessment of landslide age has been field intensive, subjective, and cost prohibitive. This research applies a new, lidar-based technique to remotely estimate landslide ages over large swaths of terrain by calibrating a relationship between landslide age and the "roughness" of the landslide deposit. Because the technique enables dating large numbers of landslides over timescales of hundreds to thousands of years, it can be used to calculate landslide recurrence intervals, as well as to identify the youngest, most active slides. This data is then coupled with observed geometric properties, seismic modeling inputs representative of possible earthquake scenarios, and site-specific, back-calculated geotechnical and hydrological properties to optimize landslide susceptibility models for "hot spot" risk mapping along emergency routes.

When considering long-term resiliency planning, seismic landslide projections must also be weighed in context with risks associated with extreme precipitation and seismic events. Over the next few decades, precipitation events are projected to increase in both magnitude and frequency across western Oregon. As water is a major driver of slope failures, increased precipitation will not only drive yearly winter landslides along critical routes, but also increase the potential impacts of a seismic event. The Pacific Northwest has historically been subject to the effects of long-duration, high amplitude shaking from the offshore Cascadia Subduction Zone. The rupture of this fault is expected to generate peak ground accelerations (Figure 3.10) of approximately 1g over broad areas of the coast, decreasing to 0.1g by ~ 100 km inland, which would be sufficient to trigger numerous landslides in the western part the state, particularly in the Oregon Coast Range. The resilience of these lifeline highways is critical as they accommodate much of the commercial and emergency access to the Coastal communities, which are expected to be most severely affected. Therefore, it is critical to pursue integration of precipitation projections that

incorporate the increasingly extreme precipitation events, coupled with refined susceptibility mapping focused along lifeline corridors for targeted selection of “hot spots” for mitigation and planning for both climatic and seismic events.

2.0 LITERATURE REVIEW

2.1 INTRODUCTION TO LANDSLIDES

Landslides are a natural hazard that have major societal, economical, and environmental impacts, realizing over four billion dollars of damage every year and up to 7,000 worldwide casualties per year (Schuster and Highland, 2001; Petley, 2012) (Figure 2.1). These numbers are likely an underestimate due to the incorporation of landslide casualties into larger causative events, such as earthquakes, wildfire, and heavy rainfall – the latter increasing with global climate change (Petley, 2012). These deleterious effects are exaggerated due to a lack of social or engineering awareness of surrounding landslide activity (Burns, 2014). These impacts are not limited to the tragedy of lost lives or financial hardship; infrastructure, including roads, rail, and utilities are frequently impacted at major economic costs and a reduced quality of life, and in the worst cases, prevent aid and access to victims of natural disasters (Aruperes, 2016; Spitzer, 2016). These landslide occurrences also taint drinking water and harm ecosystems from deposition of large quantities of debris and sediment (Schuster and Highland, 2001).

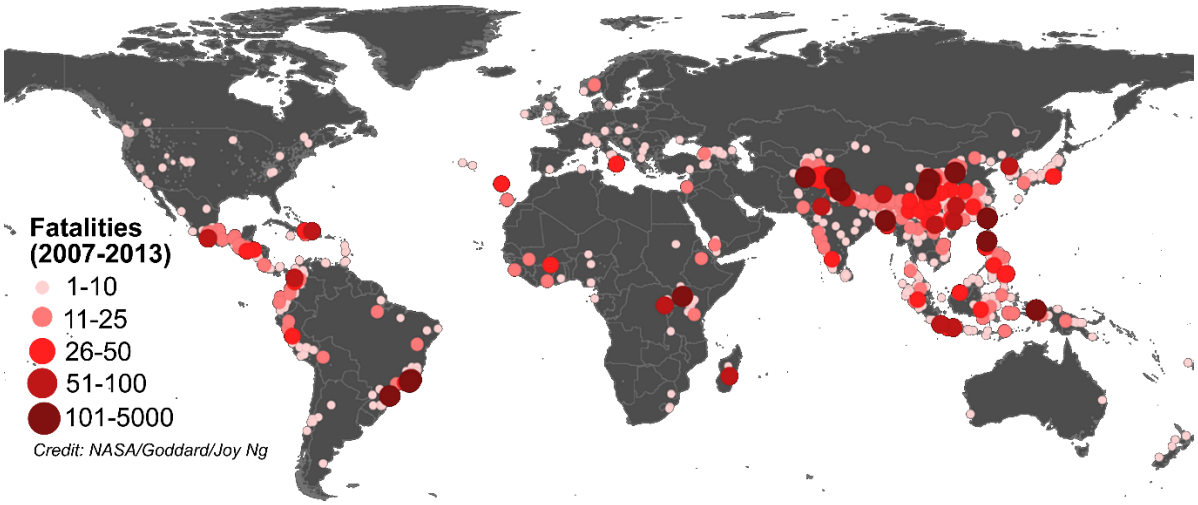

Figure 2.1: Landslides are a worldwide issue, causing billions of dollars of damage and realizing thousands of fatalities every year. (Credit: Joy Ng, NASA Goddard).

Landslides occur because of various destabilizing processes and may occur in various forms. They are typically characterized by the rate at which a slide moves, the type of movement that occurs, and the materials that comprise the slope failure (Cruden, 1991). Cruden and Varnes (1996) classify landslides into five types: falls, topples, slides, spreads, and flows. Slides occur when masses of earth displace upon the surface, exhibiting movements that are broadly categorized as rotational or translational. These observed movements range from very rapid, resulting in catastrophic mobility of landslide deposits, to very slow, exhibiting movements that may be imperceptible but devastating structurally (Gill and Malamud, 2017). This landslide

activity, described as the rate and frequency of failure, is prompted by destabilizing conditions that stem from natural and/or anthropogenic processes (Cruden and Varnes, 1996).

Common external destabilizing processes that affect landslide activity are well-understood qualitatively but are poorly-constrained quantitatively. Anthropogenic influences include excavation of stabilizing terrain, placement of fills on unstable terrain, and adverse alteration of site hydrology (Olmacher and Davis, 2003; Dai et al., 2002; Gokceoglu et al., 2005). Natural destabilizing processes include heavy rainfall, seismic loading, and toe undercutting from the erosive power of water (Chigira and Yagi, 2006; Bonzanigo et al., 2007). These failures are further driven by adverse geologic conditions, such as bedding planes, weak seams, and weathering that often govern the types of movement realized (Anbalagan, 1992). Significant research characterizes the destabilizing effects of earthquakes (Newmark, 1965; Bray and Rathje, 1998; Khazai and Sitar, 2000; Saygili and Rathje, 2008; Jibson, 2011; Hess et al., 2017), adverse geology (Fredlund and Krahn, 1977; Khazai and Sitar, 2004; Eberhadt et al., 2005), construction (Alonso et al., 1993; Wang et al., 2014), and recently rainfall (Rahardjo et al., 2001; Baum et al., 2008; Cai and Ugai, 2004; Lu and Godt, 2008). However, other destabilizing factors, such as weathering, erosion, and hydrologic changes are not well-quantified as they are difficult to measure. Quantifying the interaction of these long-term influences on stability is fundamental to assessing landslide activity.

2.1.1 Landslides Drivers: Seismic, Climatic and Geological Drivers

A landslide occurs when the driving shear stress acting on the incipient failure plane exceeds the shear strength of that failure plane, as commonly expressed in most generic form as a factor of safety, *FS*:

$$\boldsymbol{FS = \frac{c + \sigma' \tan \phi'}{\tau_{dr}}} \qquad \textbf{(2-1)}$$

Where:

c is cohesion,

σ' is the effective normal stress,

ϕ' is the angle of internal friction of the failure plane material, and

τ_{dr} is the mobilized shear stress.

Instability occurs when $FS < 1$, which can be accomplished by **seismic**, **climatic**, and **geological** drivers acting on a wide range of time scales. Changes in these three triggering mechanisms over time can influence the frequency of landsliding.

Seismic shaking can trigger landsliding by temporarily increasing the driving stress or decreasing the normal stress and reducing strength, either of which causes a reduction in the factor of safety. It can also induce compaction of unconsolidated sediments, which temporarily

increases pore pressure and promotes instability or in some cases liquefaction. Review of the current global seismic-landslide inventory (Keefer, 1984) shows that moderate-to-large magnitude earthquakes trigger thousands to tens of thousands of landslides over regions often exceeding 10,000 km^2, and that the volume of sediment mobilized by landslides generally scales with the earthquake magnitude (Malamud et al., 2004).

Seismically triggered landslides may cause mass destruction and great loss of human life in populated areas (e.g. Yin et al., 2009; Collins and Jibson, 2015), and those landslides are often the primary cause of fatalities that are not a direct result of shaking (Marano et al., 2010). Owing to their potentially large volumes, high travel velocities, and long runout distances, co-seismic landslides, such as those documented during the 1994 M_W 6.7 Northridge earthquake (e.g., Harp and Jibson, 1996), the 2008 M_W 7.9 Wenchuan earthquake (e.g., Yin et al., 2009; Ouimet, 2010; Dai et al., 2011), and the 2015 M_W 7.8 Gorkha Nepal earthquake (e.g., Collins and Jibson, 2015; Kargel et al., 2016), significantly impact the natural and built environments. They obstruct transportation networks, damage structures, produce large amounts of sediment, and deposit landslide dams (e.g., Korup and Clague, 2009; Ouimet, 2010), often leading to significant economic impacts, in some cases exceeding the combined financial losses from all other seismic effects.

Ages of pre-historic landslides can cluster around seismically active periods (Hermanns and Strecker, 1999), and with precise dating, some specific landslides have been tied to specific earthquakes, such as the ~1,100 ybp Seattle Fault rupture. That event likely triggered rock avalanches in the Olympic Mountains (Schuster et al., 1992), as well as large slumps in the glacial sediments underlying the Puget Lowlands (Jacoby et al., 1992).

Climatically triggered landslides can also cause significant loss of life in populated areas (Petley, 2012) and affect transportation networks. Precipitation is the main cause of climatically triggered landslides, where short and intense storms or longer and less intense storms can both trigger widespread landsliding (Caine, 1980). Precipitation infiltrates into the soil and increases pore pressures in the saturated subsurface, thereby causing a decrease in the effective normal stress and a decrease in landslide strength (Figure 2.2) (Terzaghi, 1950). In addition to responding to individual storms, pore water pressure can change over longer timescales in response to changing climatic conditions and groundwater flow conditions to influence the frequency of landsliding (Bilderback et al., 2014). For example, records of dated landslides from a variety of mountain ranges suggest that relatively cool and/or humid periods (Hermanns and Strecker, 1999; Soldati et al., 2004; Borgatti and Soldati, 2010; Booth et al., 2017), or periods with high climatic variability (Trauth et al., 2003) correlate with temporal clustering of landslide ages. Relatively cool and humid conditions would tend to increase infiltration of water to the depths of potential landslide failure planes, while increased climatic variability would increase the likelihood of extreme precipitation events triggering landslides.

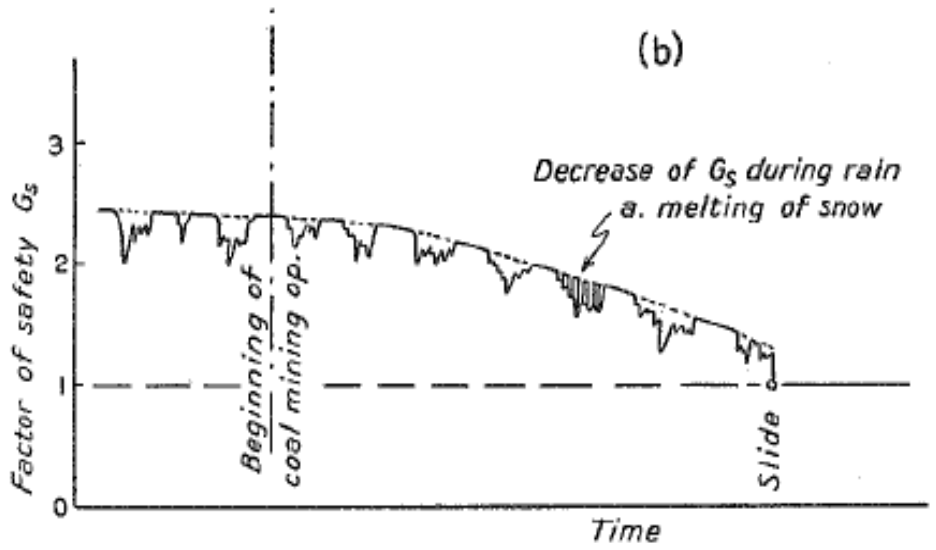

Figure 2.2: From Terzaghi (1950). Illustration of how a hillslope's factor of safety, G_s, can change over time in response to short term fluctuations in precipitation as well as long term strength degradation and loss of cohesion.

Geologic drivers of slope instability include the composition and structure of the soil and underlying bedrock and how those parameters relate to the shape of the topography. For deep-seated landslides that occur in bedrock, an especially common geologic condition that promotes landsliding is the presence of dip slopes, where a weak layer of sedimentary or volcanic rock dips in the same direction as the topography. Such conditions are common throughout the Oregon Coast Range where layers of weak siltstone serve as landslide failure planes and are often interbedded with stronger sandstones or volcanic rocks (Trimble, 1963; Roering et al., 2005; Madin and Niewendorp, 2009). In addition to weak bedding planes, faults and fractures are weaker than intact rock, and the orientation of those features can control where, when, and what types of landslides occur (Cruden, 1976; Hermanns and Strecker, 1999; Jaboyedoff et al., 2011; Booth et al., 2014). In general, those weak structures must dip steeply enough so that the factor of safety can drop below one, and there must be accommodation space for the failure plane to daylight from the hillslope (Norrish and Wyllie, 1996). For shallow landslides, a strong contrast in hydraulic conductivity across the soil-bedrock interface often facilitates high pore pressures along that structure, allowing a landslide failure plane to develop there (Dietrich et al., 1992; Montgomery and Dietrich, 1994; Iverson, 2000). Such contrasts in hydraulic conductivity also occur at other geologic boundaries in the subsurface and can influence the sizes and styles of landsliding (Perkins et al., 2017).

Like the previous drivers of landsliding, geologic drivers may change over time and influence the frequency of landsliding. Over relatively long time scales, on the order of millennia, strength degradation can occur, which often causes a decrease in cohesion, thereby reducing the shear strength of a potential failure plane (Figure 2.2). Additionally, fluvial or glacial erosion at the toes of hillslopes generates topographic relief, allowing for higher driving stresses and increased accommodation space for landslides (Schmidt and Montgomery, 1995).

2.2 LANDSLIDE ACTIVITY

Landslide activity refers to the relative movement rate of a landslide or the time since the landslide last moved (Cruden and Varnes 1996). An *active* landslide is currently moving, and if that landslide stops, it is initially considered *suspended*. If the landslide remains stable for at least one annual climatic cycle, it becomes *inactive*. Inactive landslides may be considered *dormant* if the conditions that promoted past movement are still present, *abandoned* if those conditions no longer persist, or *stabilized* if measures to prevent future movement have been taken by humans. Natural factors that affect landslide activity include river- or wave-induced undercutting of toe slopes, geologic weathering, or extreme events like heavy rainfall, wildfire, or earthquake (Highland and Bobrowsky, 2008). Anthropogenic processes (i.e. human-induced) may also contribute to landslide activity through poor construction practices, timber harvest, or alteration of hydrogeologic conditions (Larsen, 2008; Gill and Malamud, 2017). It is understood that anthropogenic influences have resulted in more frequent landslides (Glade, 2003; Meusburger and Alewell, 2008; Cevasco et al., 2014).

Assessing landslide activity conventionally requires continual updating of landslide inventories. Often, these updates include data regarding the volume, time, and cause of landslides. Activity may then be defined as landslide volume over time (Guzzeti et al., 2009), number of slope failures over time (Jakob, 2000), or observed movements for slow-moving slides (Coe et al., 2003). Landslide volume is an effective way of characterizing activity after extreme events (Begueria, 2006), but it may neglect the patterns and types of movements associated with conventional slide features. Quantifying the number of slides over time ignores the size and behavior of features. One of the most effective means of assessing activity is characterizing landslide movement (Crozier, 2010). Quantitative assessment of movements may stem from direct monitoring using instrumentation or remote sensing techniques. Instrumentation is often limited by expense and site access. One-time collection of remote sensing data, much like slope stability analyses, tend to provide information only about a single moment in time. When captured in sequence, however, remote sensing data may provide insight into movement of slides. The relative age of a landslide, a proxy for activity, is often assessed qualitatively in the field or from remote sensing data based on interpretation of its surface morphology (Figure 2.3). Prior to remote sensing techniques, these qualitative assessments of potential landslide activity typically rely on the subjective judgment of professionals who characterize geologic, hydrologic, climactic, geomorphic, and seismic influences in a given location. The boundaries of an active or historic landslide typically consist of a sharp, unvegetated head scarp, similarly sharp and unvegetated lateral flanks with small streams running along them, and a well-defined, bulbous toe that has not been modified by fluvial erosion (McCalpin, 1984; Keaton and DeGraff, 1996). The interior of the landslide generally has little vegetation, and the ground surface consists of hummocky topography, sharp internal scarps, and numerous closed depressions that may contain standing water. If the landslide remains dormant, these features gradually become less distinct as other non-landslide processes modify the topography. Vegetation establishes itself on previously unvegetated areas, the initially rugged landslide surface becomes smoother and more subdued, and a stable drainage network becomes established and incised into the landslide and its surroundings. Additionally, the landslide's toe is progressively eroded by the stream, and terraces may be cut into it. This transition typically takes place over hundreds of years to more than 10 kyrs, after which the landslide becomes difficult to distinguish from the surrounding topography.

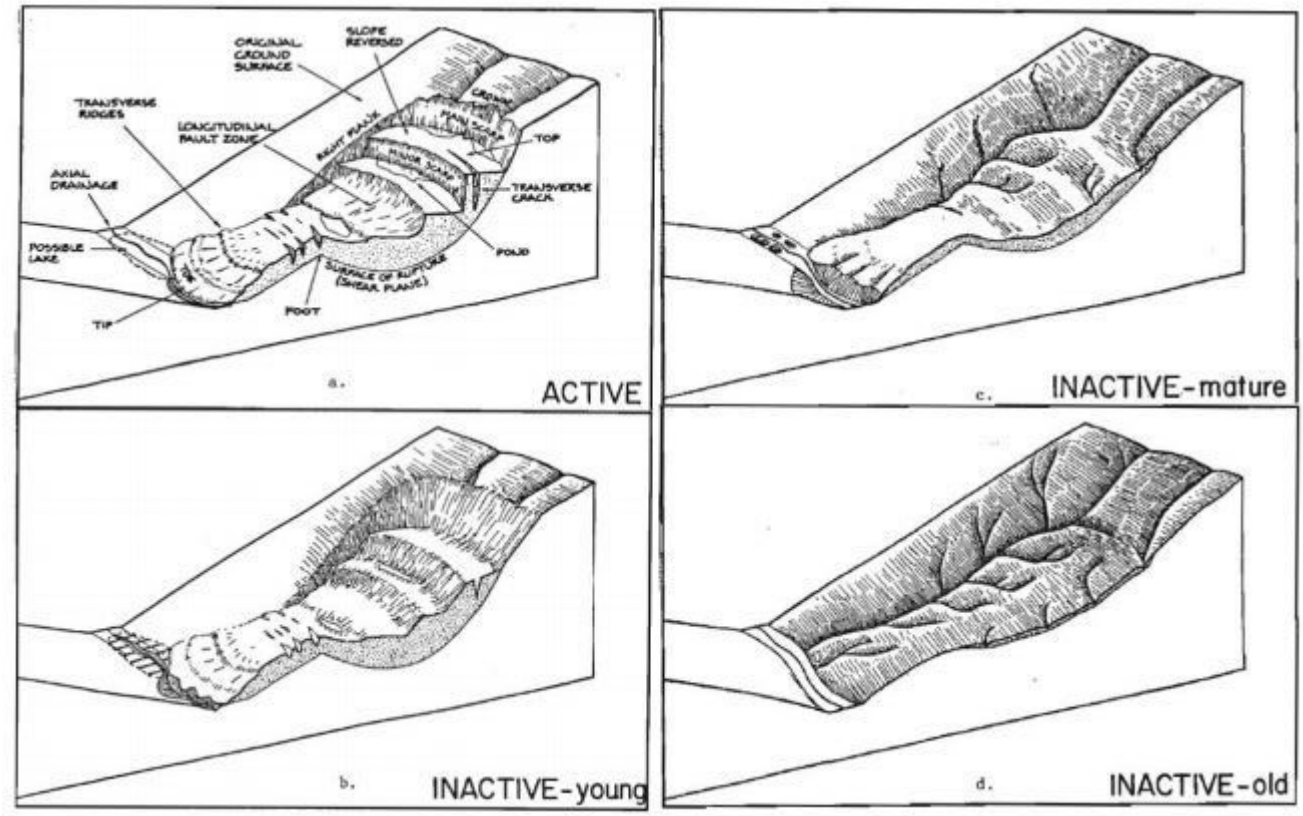

Figure 2.3: From McCalpin (1984). Schematic diagrams showing changes to landslide morphology with time since it was last active.

Recently, high resolution, bare earth lidar data has facilitated quantitative analysis of the qualitative processes described above. For example, various measures of surface roughness have proven capable of distinguishing the hummocky deposits of active or recent landslides from stable terrain, allowing the automated production of landslide maps with up to 90% accuracy (Booth et al., 2009; Jaboyedoff et al., 2012; Berti et al., 2013). Topographic data can also be used to automatically detect head scarps and map deposits downslope of them to produce accurate landslide maps (Leshchinsky et al., 2015). Although such maps may be influenced by the quality of the topographic data, especially when those data are collected using different equipment, at different times of year, or in areas with variable vegetation cover (Burns et al., 2010), in general, there are many different methods to quantify topographic data that produce similar quality landslide maps in a semi-automated fashion (Berti et al., 2013). Surface roughness can also objectively distinguish different parts of a larger landslide complex with different activity or failure styles (McKean and Roering, 2004; Glenn et al., 2006).

In addition to distinguishing landslides from stable terrain, quantitative analysis of surface roughness has recently been shown capable of distinguishing landslides of different age over the Holocene (the most recent geologic epoch beginning 11,700 years ago) (LaHusen et al., 2016; Booth et al., 2017). Roughness reflects landslide age because near surface soil transport systematically smooths topography over time. After a landslide has occurred, subsequent soil transport processes systematically erode high standing areas and deposit soil in low lying areas,

such that short length scale topographic features smooth more rapidly than long length scale features (Crank, 1975; Roering et al., 1999; Mudd and Furbish, 2007). Importantly, this process occurs on un-incised areas of the landslide deposit where overland flow of water is largely absent and focusing analysis on just those portions of the landslide deposit where soil transport is dominant has been essential to develop a relationship between a landslide's age and its surface roughness. Strong contrasts in lithology, small ranges in landslide ages, and not isolating the landslide deposit for surface roughness measurement have prevented clear relationships between age and roughness in some studies (Goetz et al., 2014).

Remote sensing based methods of assessing landslide activity have been an important extension of traditional dating techniques because they allow activity to be estimated for large numbers of landslides compared to traditional field-based dating methods. Direct landslide age determination often involves radiocarbon dating samples of organic material, such as trees, that were killed at the time of the landslide. However, this technique can be severely limited by a lack of dateable material, landslide reactivations, or time, access, and cost constraints (Panek, 2015). For these reasons, the most thorough previous work dating landslides with radiometric methods has dated at most a few tens of deep-seated landslides (Borgatti and Soldati, 2010), and radiometric dates are best suited to landslides that occurred as a single or short duration event.

2.2.1 Assessing Landslide Susceptibility

Landslide susceptibility and potential activity is typically determined by a geotechnical assessment of slope stability, which does not explicitly account for time-dependent factors. This commonly employs limit equilibrium approaches that simplify assumptions about failures (Duncan, 1996). Such underlying assumptions include (1) that the landslide is a rigid mass, (2) the kinematics of the failure surface are known, and (3) the hypothetical statics are appropriate (Duncan and Wright, 1980). Through a coupling of time-dependent geotechnical, hydrological and geometric functions, these analyses can be advanced to capture landslide activity in consideration of realistic hydrologic and geologic spatial variability and time dependent factors, such as seismic time histories or precipitation intensity. This demonstrates utility as a planning tool when applied to a regional scale, particularly when shown in map form.

Landslide susceptibility mapping identifies regions of slope instability based on probabilities of landslide occurrence. "Hazard map" is often confused as a synonym for "susceptibility map;" however, the two should be distinguished. In particular, hazard maps are developed by considering the temporal occurrence or recurrence and magnitude of failure, and susceptibility maps consider whether conditions would likely lead to failure (Hervás and Bobrowsky, 2009). Aside from qualitative susceptibility mapping (i.e., maps developed by allowing experience and judgement to dictate the spatial limits of a hazard), two primary types of methods for creating quantitative susceptibility maps exist in practice: (1) statistical methods (Ayalew and Yamagishi, 2005; Carrara et al., 1991; Dai and Lee, 2002; Ohlmacher and Davis, 2003; Xu et al., 2013), and (2) deterministic methods, often calibrated to statistical distributions of geotechnical inputs and landslide spatial properties (Bellugi et al., 2015; Dietrich et al., 1995; Milledge et al., 2014; Miller and Sias, 1998; Van Westen and Terlien, 1996). Statistical methods typically utilize the historical links between landslide distribution and the factors controlling a landslide (e.g., slope); whereas deterministic methods for creating susceptibility maps utilize mechanical properties of

the soil (e.g., density, friction angle) to express instability as a factor of safety, defined as the ratio of forces resisting failure to forces driving failure (Ayalew and Yamagishi, 2005).

An integral part of effective landslide susceptibility mapping is the use of Geographic Information Systems (GIS). Modern remote sensing techniques, such as Light Detection and Ranging (lidar), have significantly improved the ability to capture topographic information for generating Digital Elevation Models (DEM) at high resolution, particularly in locales covered with vegetation (Sithole and Vosselman, 2004; Hopkinson et al., 2004). Derivative products, such as slope and slope direction (i.e., aspect), can be calculated for each cell of a DEM. Accordingly, lidar-derived DEMs enable the extraction of relevant topographic and geomorphic information at high resolution, which can be used to improve landslide susceptibility maps (Burns and Madin, 2009; Jabodeyeff et al., 2012; Jebur et al., 2014; Jebur et al., 2015; Mahalingam and Olsen, 2015; Mahalingam et al., 2016). A common approach in GIS raster analysis is to compute slope values by finding the maximum rate of change in elevation among neighboring cells in the DEM, which is highly dependent on resolution. Slope estimates will vary based on the spatial scale of interest. Hence, slope estimates will vary with different DEM resolutions, which will ultimately yield differing estimates of landslide susceptibility (Mahalingam and Olsen, 2016).

Deterministic methods for assessing shallow landsliding are usually performed using two-dimensional (2D) limit equilibrium analyses, such as the infinite slope analysis, which can employ the raster structure of DEMs (Dietrich et al., 1995; Iida, 2004; Tsai and Yang, 2006; Van Westen and Terlien, 1996; Wu and Sidle, 1995). A fundamental assumption of the infinite slope analysis is that an infinitely-long planar slope surface fails along a single failure plane. Thus, lateral boundary forces are neglected during the analysis, which is realistic for shallow landsliding on slopes characterized by consistent soil depths over broad regions. Although the infinite slope analysis is a relatively simple analysis method, comparison of results for infinite slope and finite element methods show that the infinite slope analysis is suitable for modeling shallow landsliding on slopes with length to height ratios of 25 or larger (Milledge et al., 2012). In contrast, three-dimensional (3D) slope stability methods account for edge effects and yield higher factors of safety than 2D methods (Duncan, 1996). An example of an edge effect considered in 3D methods is the lateral shear resistance generated by lateral earth pressure acting against the slope failure's boundary (Arellano and Stark, 2000). Three-dimensional stability methods for shallow soils resemble a sliding block analysis and have more recently been used to calculate factors of safety for a given digital elevation model (Bellugi et al., 2015; Dietrich et al., 2007; Milledge et al., 2014).

2.3 GIS AND REMOTE SENSING METHODS TO ASSESS LANDSLIDE HAZARDS AND IMPACTS

New remote sensing techniques and geographic information systems (GIS) have become critical technologies (Cao et al., 2016; Guzzetti et al., 2012) to identify, investigate, and map landslides to produce landslide inventories as well as provide critical data layers to support susceptibility and hazard mapping (a more complete summary of different mapping techniques and associated purposes is provided in the ODOT SPR-786 final report (Leshchinsky et al., 2018)). Several techniques utilized in practice include, but are not limited to:

1. Differential interferometric synthetic aperture radar (DInSAR) measures displacements (Belardinelli et al., 2005) at high (mm-level) accuracies.

2. Panchromatic QuickBird satellite imagery – useful for topographic change analyses (Niebergall et al., 2007).

3. Airborne, mobile, terrestrial, and unmanned aircraft systems (UAS)-based geodetic lidar-scans, which can create detailed, 3D point clouds used for monitoring changes in the terrain (Jaboyedoff et al., 2012; Olsen et al., 2012; Olsen, 2013; Conner and Olsen, 2014) at high resolutions. Lidar has a key advantage of being able to penetrate the canopy to capture important morphological features to define the landslide. As a result, lidar technology will be discussed in more detail in the following section.

4. Photogrammetry – very useful to quickly capture data over a large area of freshly occurred landslides. It can be difficult to capture old landslides where vegetation masks key morphological features needed to detect the landslide. (e.g., Borghuis et al., 2007).

5. UAS-based Structure from Motion (SfM) – digital cameras mounted to a UAS map and record spatial and temporal measurements (Niethammer et al., 2012).

Use of remote sensing methods and GIS platforms facilitate landscape-scale hazard inventories without the practical challenges of physically verifying landslide features (Van Westen et al., 2008; Burns and Madin, 2009). These platforms can also incorporate models of hazards such as earthquakes (Luzi et al., 2000) or precipitation. Not only does the use of some new remote sensing technologies enable landscape-scale collection of topography; some techniques such as lidar remove artifacts from vegetation or forest canopies from the models, clearly exposing the bare-earth beneath. However, when data obtained from remote sensing is used to develop models to predict and forecast landslides, the models become very complex. A reliable inventory of existing landslides is a critical input to evaluate potential hazards across a landscape. The process of creating the inventories was the subject of SPR-786 (Leshchinsky et al., 2018).

2.3.1 Lidar Technology

Light detection and ranging (lidar) technology emits laser pulses at defined, horizontal and vertical angular increments and utilizes the travel time of the pulse to produce a detailed, 3D point cloud. Because lidar is an active sensor, it has the ability to penetrate through opening in the canopy to capture detailed information on the ground surface below. A variety of processing techniques exist to filter ground points and create a Digital Terrain Model (DTM). These approaches depend on the type of terrain and vegetation characteristics. Common approaches including lowest elevations, ground surface steepness, ground surface elevation difference, and ground surface homogeneity are reviewed in Meng et al. (2010). Repeat surveys through time enable damage and deterioration analyses at unprecedented detail across multiple scales.

Currently, an initiative, the 3D elevation plan (3DEP), headed by the USGS, is underway to obtain airborne lidar data across the entire U.S. at meter level resolution (Snyder, 2012; Sugarbaker et al., 2014). Oregon has formed an Oregon Lidar Consortium (OLC) to pool lidar

acquisitions efforts, of which ODOT is a contributing member. DOGAMI, who leads the OLC, utilizes this lidar data to generate new landslide inventories, which they integrate into the Statewide Landslide Inventory Database of Oregon (SLIDO).

In the last decade, lidar has become the go-to tool for landslide inventorying and mapping. Jaboyedoff et al. (2012) reviews lidar usage for landslide mapping and monitoring in great detail. Lidar has been used to undertake detailed geological assessments of several landslides, enabling improved understanding of the processes and mechanisms contributing to landslide movement. Considerable work has also been undertaken in recent years to document the patterns of landslides and mechanisms for failure, particularly in forested environments where lidar provides detailed surface topography to delineate landslides that were previously undetectable.

2.3.1.1 ***Lidar inventory methods***

Landslide inventorying approaches are reviewed in detail in the final report for SPR-786 and are only summarized herein (Leshchinsky et al., 2018). These approaches include: (1) *Manual digitization* from lidar hillshades and other base layers (e.g., Burns and Madin, 2009; Schultz, 2004; Schultz, 2007); (2) *Statistical\Machine Learning* approaches (Booth et al. 2009; Mora et al., 2014) in which the user manually maps a section of the region of interest and then utilizes statistical or machine learning techniques (e.g., Li et al., 2015) to correlate the presence and absence of landslide with other variables (called training or calibration) to map landslides across the remainder of the terrain. Often, a portion of the samples are used for testing (i.e., validation) of the model; (3) Physics-based modeling such as the Contour Connection Method (Leshchinsky et al., 2015 and further expanded in ODOT SPR786 (Leshchinsky et al., 2018)); and (4) *Combination with another sensor* such as InSAR or terrestrial lidar (Wang et al., 2013).

2.3.1.2 ***Susceptibility mapping***

A variety of GIS approaches are employed in landslide susceptibility mapping using lidar (summarized in the SPR740 Final Report (Olsen et al., 2015; Mahalingam et al., 2016); Hess et al., 2017). At their core, most approaches input relevant data layers and combine them into a model through a weighting strategy. The variables considered in these approaches vary widely (summarized in Mahalingam et al., 2016); hence, it is critical to statistically test each variable to ensure it has a meaningful contribution. In particular, data quality can vary drastically between individual data layers; hence, although physically a variable may be important for the mechanism of landsliding, it may actually adversely affect the model due to poor or unavailable data. Unfortunately, often in practice, the ability of the variable to appropriately capture the physical processes is often overlooked in the development of these models, where one can quickly be lost in the numerical computations. Care should be taken to ensure that the model and the associated variables/data layers are consistent with current knowledge of physical mechanisms. Finally, models are often highly calibrated to a specific locale and may not be suitable elsewhere with different geologic and climatic conditions.

Examples of the many approaches include: (1) Weighted overlay analysis – where a series of independent variables contributing the landslide hazard are reclassified to a

common scale, multiplied by a specific weight (often determined by judgement) for each independent variable, and then summed to produce the overall score, (2) Discriminant Analysis such as multilinear least squares regression approaches, (3) logistic regression, where a logit function considers multiple variables with weights calibrated using the training dataset indicating locales with and without landslides in the training data (e.g., Lee et al., 2006; Pradhan et al., 2010), (4) Artificial Neural Networks, where an automated machine learning approach is used to determines the appropriate weights, and (5) Support Vector Machines, which use supervised binary classifiers based on statistical learning theory to analyze the contributions of each variable (e.g., Pawluszek and Borkowski, 2016).

In fact, Mahalingam et al. (2016) found that using solely lidar derived data layers (e.g., slope, aspect, compound topographic index, stream power index, etc.) produced landslide susceptibility maps with similar accuracy results to a wide range of approaches in the literature that require several data layers.

Recently, Burns et al. (2016) produced a detailed, statewide landslide susceptibility map for the state of Oregon, however, this map does not explicitly consider a suite of specific destabilizing events. Further, this map does not consider the size, shape, runout, volume, or likelihood of failure considering localized lithologies, topography or localized moisture conditions. The technique presented herein captures all of these factors.

2.3.1.3 ***Hazard mapping***

Similar techniques used in susceptibility mapping can be utilized in hazard mapping as well (e.g., Pradhan et al., 2009). For example, Pradhan and Lee (2010) used a logistic regression analysis to produce rainfall-induced landslide hazard maps. Their approach lacks a physical model and directly incorporates the occurrence/non-occurrence to develop a weighted equation for probability. Studies such as ODOT SPR-740 (Olsen et al., 2015) or the Oregon Resilience Plan (Madin and Burns, 2013) utilized lidar data (wherever available) as a key input to perform landslide hazard analyses for the state of Oregon. Note that recent refinements to the SPR-740 methodology are documented in Sharifi-Mood et al. (2017).

2.3.1.4 ***Risk Mapping***

Risk mapping considers the consequences of the potential hazards. Recently ODOT SPR-786 (Leshchinsky et al., 2018) utilized landslide inventories derived from lidar-DEMs using CCM (countour connection method) to develop a risk mapping framework to estimate potential economic impacts of road closures due to reactivation of inventoried landslides.

2.4 OREGON'S CHANGING CLIMATE

A recent report from the National Academies of Science (2016) has conclusively demonstrated that climate change has led to an increase in the frequency and intensity of daily temperature extremes and has contributed to a widespread intensification of daily precipitation extremes

(Stott, 2016). This behavior poses an immense challenge for infrastructure asset management in the Pacific Northwest and elsewhere (Federal Highway Administration, 2016). For example, the impacts of landslides have cost upwards of $10 million per year in Oregon (Burns and Madin, 2009), sometimes resulting in hundreds of millions of dollars during extreme events (winter of 1996/1997). These geohazards result in not only direct economic impacts, but also a range of indirect effects including the closure of critical right-of-way and in some instances, loss of life. Such impacts are likely to increase with more extreme weather events, placing the challenge of planning for improved infrastructure resilience in the face of climate change directly on state and federal transportation agencies. In other Northwest regions such as Oregon and Washington, coastal bluffs—home to hundreds of miles of right-of-way—are more quickly eroding from higher sea levels and storm surge occurrences, requiring more resources to maintain. This impending challenge for state transportation agencies is not in the distant future and the FHWA is urging state agencies to implement climate change adaptation programs to assess vulnerability and risk of geohazards towards infrastructure (FHWA, 2016). The primary means of implementation are through developing geohazard monitoring, assessment and forecasting datasets, tools, and maps so the interaction of risk and vulnerability with climate change may be assessed.

Typically, climate projections are based on projected emissions pathways, the most common being RCP4.5 and RCP8.5, representative of lowered or increased carbon outputs in the future. Considering a RCP8.5 pathway, the annual precipitation in Oregon is expected to increase by approximately 3% and 6% by 2050 and 2080, respectively (Dalton, M, et al, 2017). Although there is significant uncertainty with these projections, there is confidence that wetter winters and springs are likely to occur (Rupp et al., 2017). This is troublesome as both the winter and spring are the primary timeframe where landslides are expected to occur in Oregon. There are a variety of climate models that provide insight into increasingly extreme precipitation, however, there is little information on how these changes may influence current, stationary intensity-duration-frequency (IDF) curves that describe potential extreme precipitation, likely owing to the significant uncertainty associated with precipitation projections. However, current climate models may enable an idea of how much the intensity of extreme precipitation events may change – for example 11-18% for winter storms (Warner et al., 2012). Any relative increase in precipitation may increase the frequency, magnitude, and location of landsliding in Oregon.

2.5 OREGON'S SEISMIC SETTING AND FUTURE

Oregon has a high seismic hazard. Most recently, the Scott Mills (M 5.6) earthquake, a shallow, crustal earthquake, resulted in $30 million in damages. However, the most severe earthquakes in Oregon are derived from the Cascadia subduction zone (CSZ, James et al., 2000), which is a convergent plate boundary extending from Vancouver Island to northern California. The most recent, large CSZ earthquake occurred on January 26, 1700, with an estimated moment magnitude of 9.0. Nevertheless, in western Oregon, earthquakes on the Cascadia Subduction Zone (CSZ) have been a frequent source of seismic shaking over the geologic past, with large earthquakes occurring every 300-500 years on average. Based on the record of offshore turbidites, the CSZ has produced 19 full or partial margin ruptures over the past 10 ky (Goldfinger et al., 2012), many of which probably caused severe shaking in the study area that was sufficient to trigger landslides (*USGS Earthquake Hazards Program* (https://earthquake.usgs.gov/scenarios/)). Those turbidite records as well as tsunami deposits in

coastal areas suggest that the most recent of the full margin rupture earthquakes occurred at A.D. 1700, ~480 ybp, ~800 ybp, ~1,200 ybp, ~1,500 ybp, and ~2,500 ybp (Figure 2.4) (Atwater et al., 2003; Nelson et al., 2006; Goldfinger et al., 2012).

From this turbidite study, geologists estimate that the probability that a CSZ earthquake will occur in the next 50 years ranges from about 7 – 15% for a magnitude 8.7 to 9.3 earthquake affecting the entire Pacific Northwest to about 37% for a magnitude 8.3 to 8.6 earthquake affecting southern Oregon (OSSPAC, 2013; Goldfinger et al., 2012).

The Oregon Seismic Safety Policy Advisory Commission (OSSPAC) released the Oregon Resilience Plan to provide policy recommendations to prepare for a major CSZ Earthquake and Tsunami (OSSPAC, 2013). Oregon DOT was charged with classifying critical highways as lifeline routes. Through this ground-breaking effort, several ground failure maps, including landslide probability and displacement maps were generated using a HAZUS-based framework (Madin and Burns, 2013). Sharifi-Mood (2017) extended these mapping efforts to consider other scenarios and develop an automated process. An open file report summarizing these products is forthcoming, but the resulting maps are available at http://ohelp.oregonstate.edu.

A current subject of investigation is the potential of the CSZ to initiate new landslides or reactivate existing landslides throughout the Oregon Coast Range. Oregon DOT SPR-740 (Olsen et al., 2015) evaluated potential impacts of seismically induced landslides on lifeline corridors. Unfortunately, insufficient information exists to isolate the triggering mechanisms of the landslides scattered throughout Oregon's coast range, so it is often unclear as to how the landslides originated.

Currently, no landslides in western Oregon have been precisely dated to the most recent CSZ earthquake, although at least some appear to have been activated at that time based on extrapolating current movement rates (Schulz et al., 2012). Furthermore, the best documented subduction zone earthquake, the 2011 Tohoku earthquake in Japan, triggered thousands of landslides up to several hundred kilometers from the fault (Wartman et al., 2013), suggesting that a CSZ earthquake would have similar effects in western Oregon.

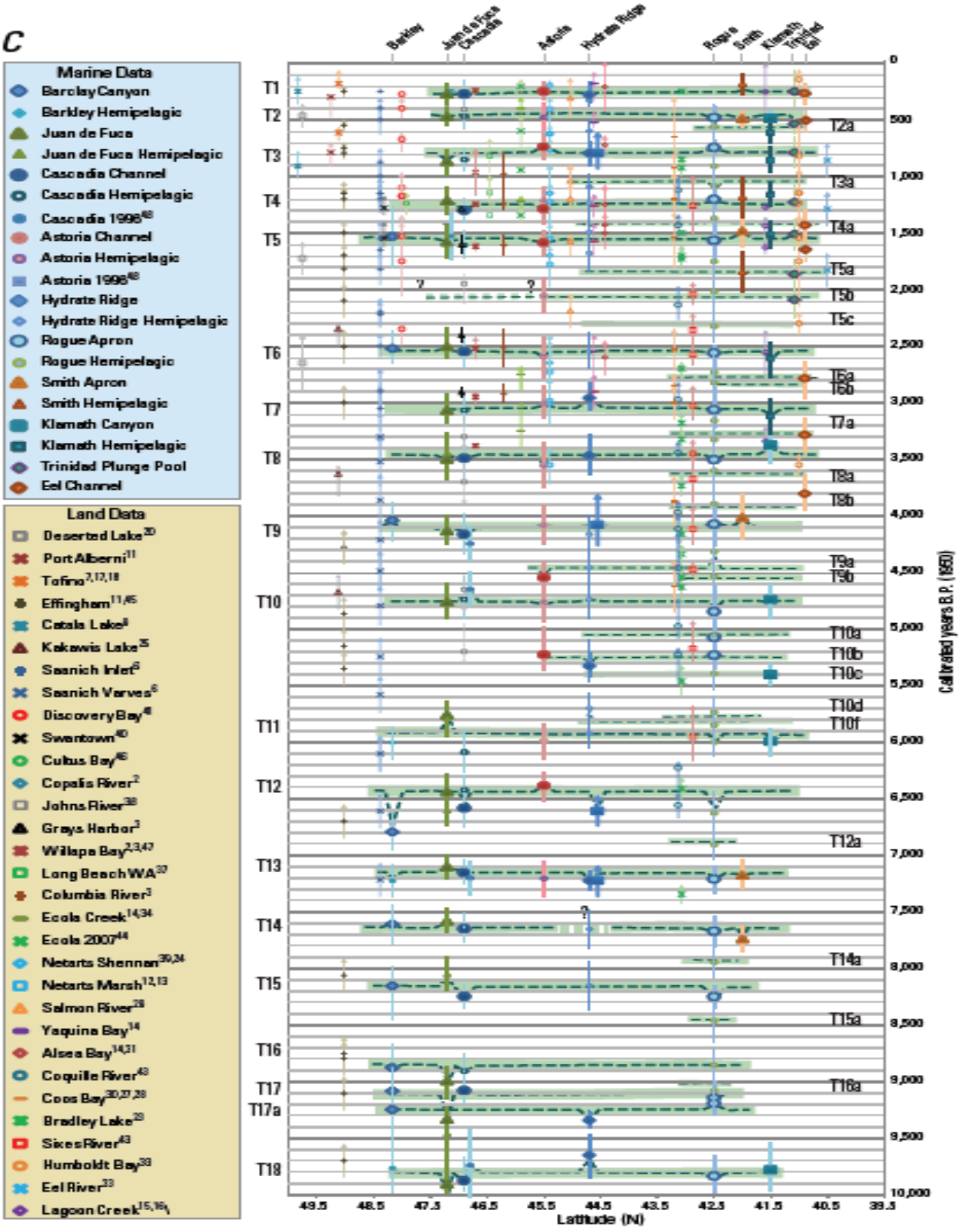

Figure 2.4: From Goldfinger et al. (2012). Space-time diagram showing the date and extent of CSZ ruptures from both marine turbidite and land data.

2.6 OPPORTUNITIES AND CURRENT LIMITATIONS

It is understood that changing climate may result in increased landslide activity, however, regional assessments of these impacts are limited in terms of (1) integrating possible rainfall intensity scenarios and (2) incorporating site-specific conditions determined from landslide inventories. There are limited models to assess rainfall-induced landsliding, particularly at a regional scale, primarily limited to simplistic infinite slope analyses. This research will provide a more rigorous, mechanics-based assessment of potential rainfall events on landslide susceptibility. Furthermore, there is limited research that has forensically analyzed large databases of landslides using a deterministic, physics-based framework as a baseline for assessing potential future slope failures. The advent of lidar bare earth digital elevation models have not only enabled improved inventorying, but improved forensics and assessment of susceptibility. The use of lidar-derived components of landslide susceptibility mapping also direct integration within a GIS framework, enabling improved planning and asset management considering current climate conditions and possible extreme storm events.

Following strong seismic shaking, significant landsliding is expected – however, regional assessments of potential coseismic slope failures are limited to coarse, probabilistic models that are not based in mechanics or tailored to site specific conditions. Knowing which inventoried landslides are the result of past earthquakes enables a back-analysis that considers seismicity, enhancing the appropriateness of back-calculated parameters used in seismic susceptibility analyses. As mentioned above, the availability of bare earth lidar establishes improved inventorying, assessment of the nature of "coseismic" landslide geometry, and assessment of regional susceptibility. As discussed in the previous paragraph, research that has tied in large-scale back-analyses of landslides considering seismic- or precipitation forcing are limited.

Finally, there is limited research that has performed large-scale geotechnical forensic analyses based on age-surface roughness relationships determined from carbon-dated material. This provides new insight into the frequency and magnitude of landslide drivers. The proposed integrated framework will leverage insight into landslide activity derived from age-roughness relationships to enhance back analysis of past slope failures, providing more rigorous and site-specific evaluation of geotechnical parameters and the past seismic- or precipitation-forcing events that cause landslides. Coupling with projections of possible precipitation or seismic events provides a powerful means of assessing the frequency and magnitude of landslides.

3.0 METHODOLOGY

3.1 OVERVIEW

The goal of SPR-808 was to develop an enhanced framework to assess landslide susceptibility under precipitation- and seismic-forcing through forensic investigation of existing landslides in Oregon. This framework was applied to representative highway corridors in Oregon: US Highway 30 (US30), OR Route 6 (OR06), US Highway 20 (US20), and OR Route 42 (OR42) that traverse the Oregon Coast Range (See Section 3.2 for further details). The specific objectives of this project were to:

1. Modify existing landslide age-roughness relationships and apply to the selected corridors through field investigation and carbon dating.

2. Use age-roughness relationships, forensic slope stability analyses, and existing landslide inventories to determine the distributions of geotechnical shear strength parameters.

3. Develop methods to determine landslide susceptibility in the selected corridors using a suite of slope stability analyses and back-analyzed geotechnical properties.

4. Use landslide susceptibility and storm and seismic event probabilities to determine hazard in the selected corridors.

5. Develop a method to assess infrastructure risk from landslide susceptibility.

6. Perform various susceptibility and risk assessments for a suite of climatic and seismic projections.

This document describes the methodology used to achieve the research goals listed above. Primary research products include:

1. Development of a simplified forensic framework that uses landslide inventories to enhance susceptibility and hazard outputs through use of (1) age-roughness relationships for landslide deposits, and (2) rupture surface mapping and forensic analysis of landslide deposits.

2. Creation of a framework that uses outputs of forensic analyses to provide regional estimates of landslide susceptibility and hazard under a combination of seismic- and climate-forcing conditions.

3. Maps of landslide susceptibility, hazard, and risk for US30, OR06, US20, and US42 considering (1) precipitation forcing, (2) seismic forcing, and (3) multi-hazard scenarios.

4. Risk metrics, such as: 1) durations of landslide-induced highway closure; 2) costs related to highway repair, commodity loss, and traffic rerouting.

3.2 CORRIDORS AND SITES USED IN ANALYSIS

For this study, four corridors were selected for assessment of susceptibility, hazard, and risk. The corridors are all representative of lifelines used to connect the Willamette Valley with the Oregon Coast. Understanding the impacts of landslides on these corridors is relevant for planning and recovery efforts, both in context of extreme precipitation and earthquake events. The four corridors include right-of-way (ROW) of US Highway 30, OR Route 6, US Highway 20, and US Route 42 that traverses the Oregon Coast Range (Figure 3.1). Throughout this document, these corridors are referenced to as US30, OR06, US20, and OR42, respectively. Additionally, a small portion of US Highway 101 containing the recently activated Hooskanaden landslide was investigated. Hooskanaden was investigated to determine whether it was coseismic and could be used as a benchmark for the forensic analyses herein. However, C14 dating techniques reflected that the landslide may not be coseismic in origin. Nonetheless, it was still valuable for (1) further calibrating surface roughness-landslide age relationships *and* (2) as a well-documented landslide case study (Alberti et al., 2020). Each of these corridors (1) is landslide-prone, (2) has associated landslide inventories mapped with lidar, (3) has different geological conditions, and (4) is critical to commerce and well-being of Oregon communities, making these highways priorities for resilience planning efforts.

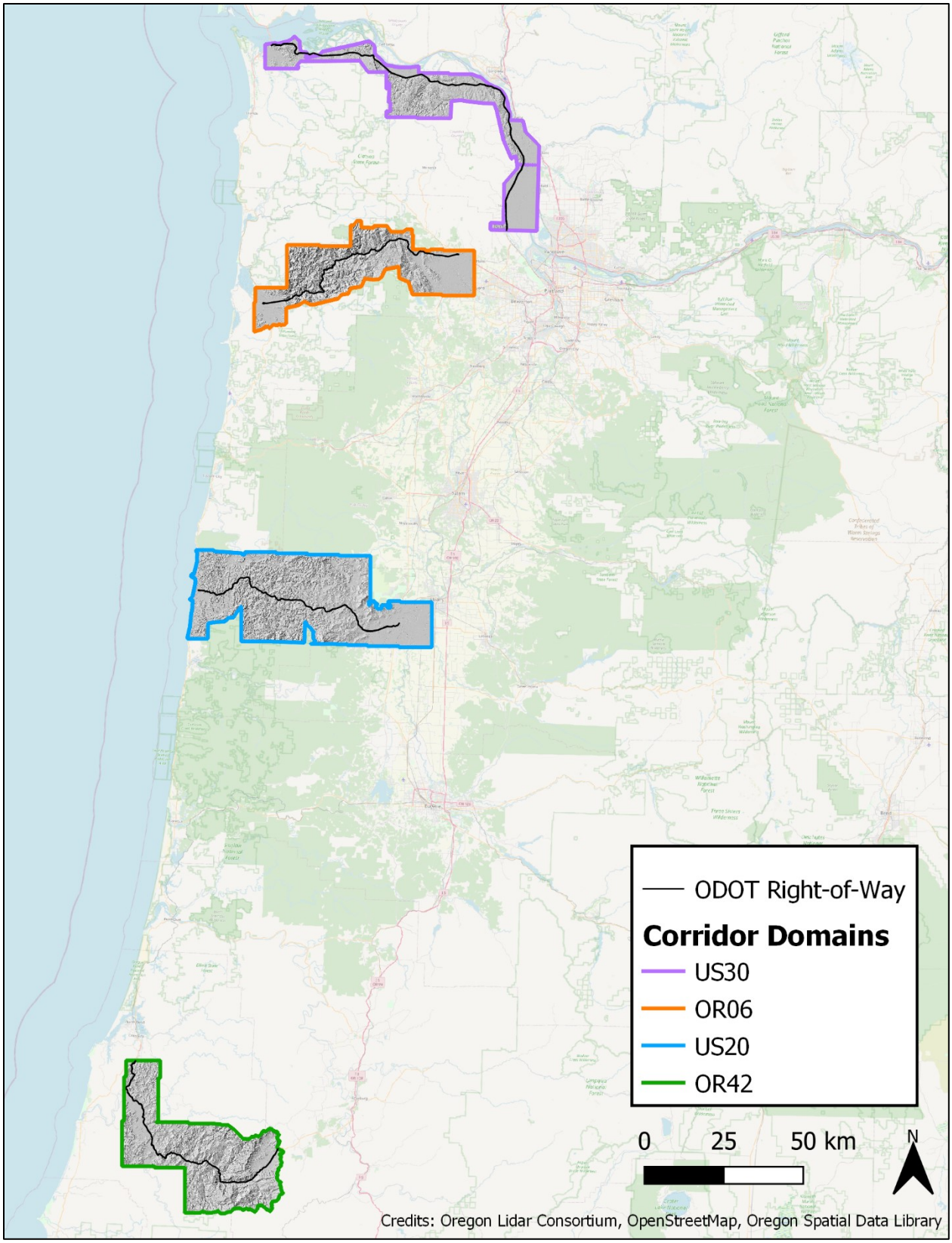

Figure 3.1: Overview map of corridors used in this study.

3.2.1 US Highway 30 (US30)

US30 follows the western stretch of the Columbia River, and is subject to slope failures every year. Serving as a major route for commerce and access to the Oregon Coast, US30 is considered a Tier 1 Seismic Lifeline. This highway traverses Troutdale Formation and Columbia River Basalts just west of Portland, eventually transitioning to sedimentary Astoria formation further west. Four landslide inventories mapped with lidar (SLIDO) are available for the proposed corridor. The study area spans from milepost 21 to milepost 96 (Figure 3.2). Full lidar coverage is available for this area.

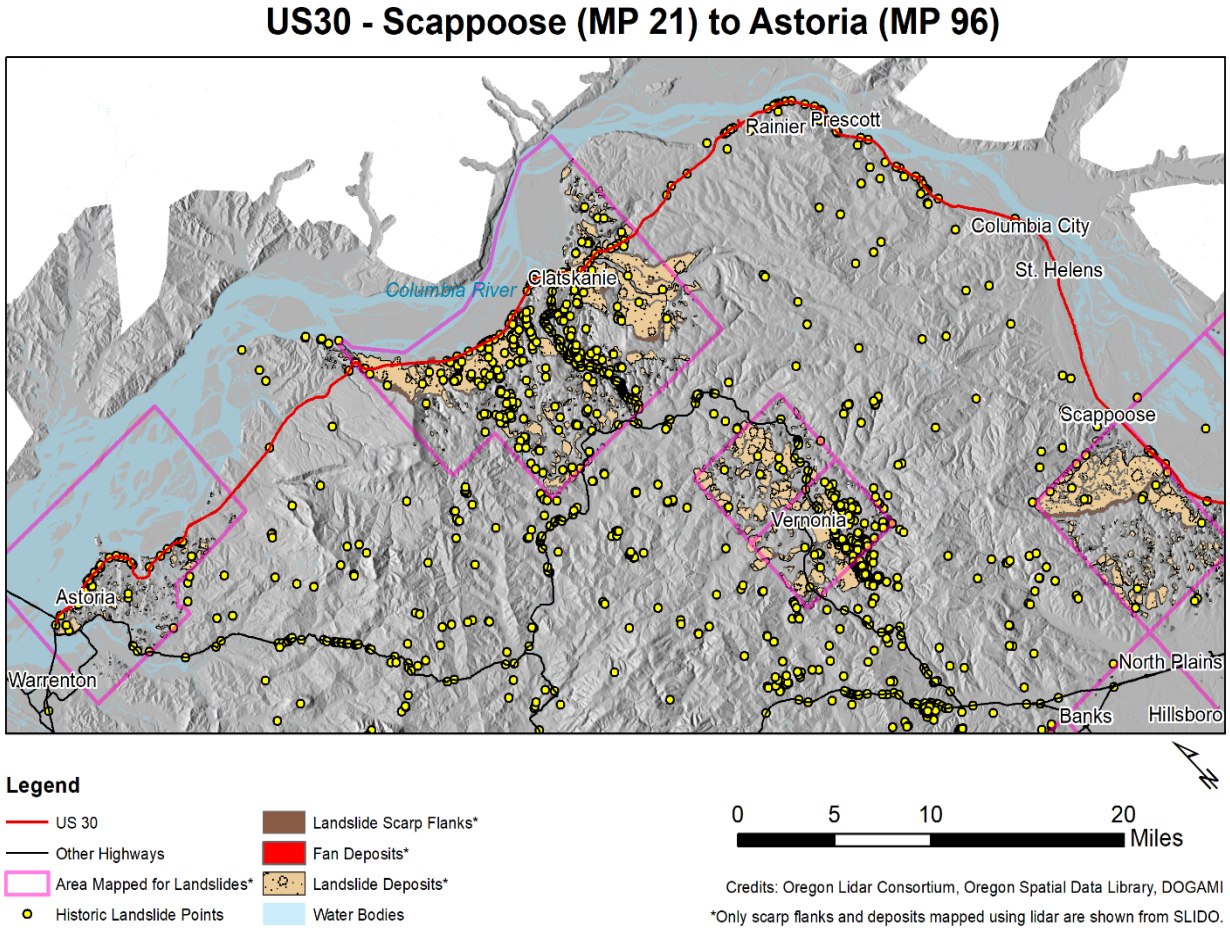

Figure 3.2: Lidar bare earth hillshade, SLIDO landslide inventory and right-of-way for US Highway 30, traversing between Scappoose (MP 21) and Astoria (MP 96).

3.2.2 OR Highway 6 (OR06)

OR06 spans the Coast Range between the Washington County and Tillamook. While not a seismic lifeline, this highway is subject to some of the most frequent landslide activity of any of Oregon's coastal connection routes. This highway traverses Yamhill formation in the east along with a mélange of Tillamook Volcanics for much of its western reaches. The study area spans from milepost 0 to milepost 49 (Figure 3.3). One landslide inventory mapped with lidar (SLIDO)

is available for the proposed corridor, existing in the eastern portion of the highway. Full lidar coverage is available for the given area.

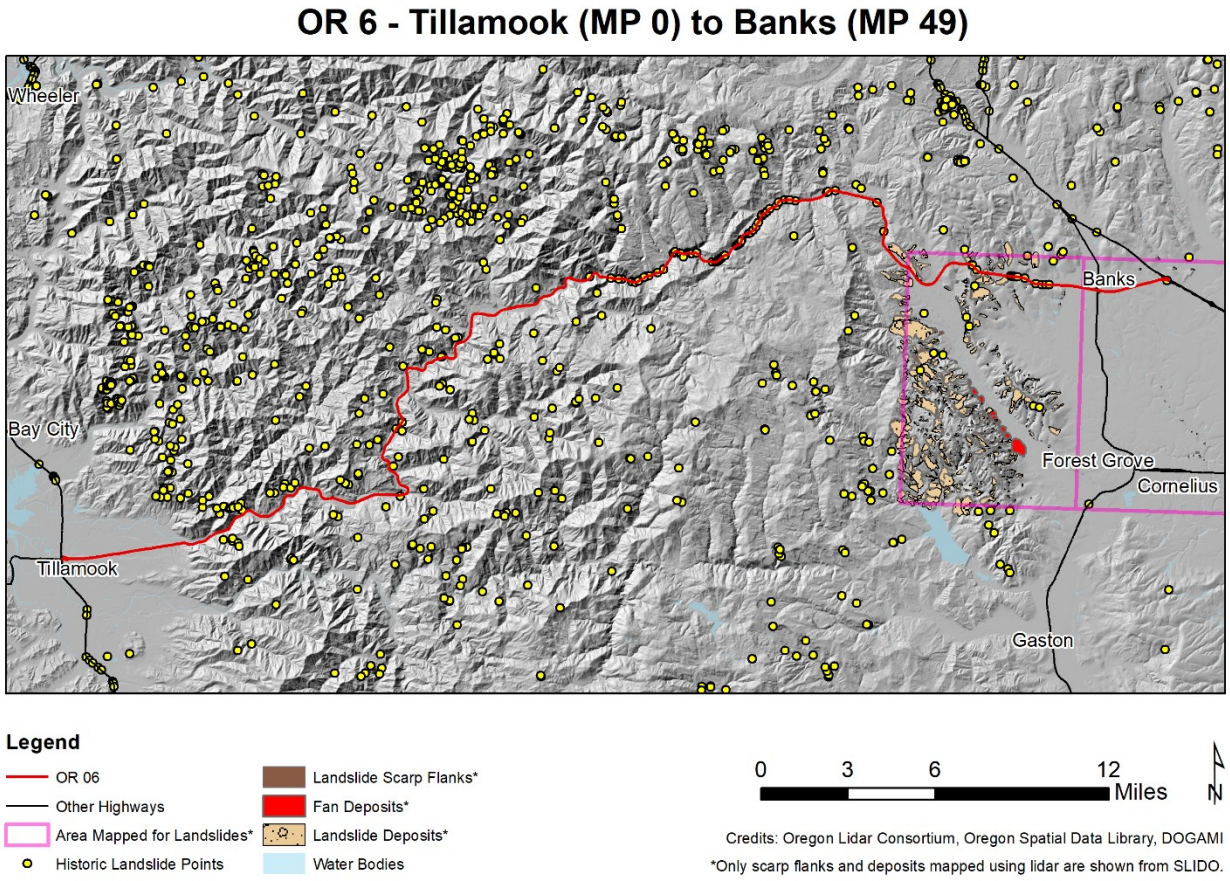

Figure 3.3: Lidar bare earth hillshade, SLIDO landslide inventory and right-of-way for OR Highway 6, traversing between Tillamook (MP 0) and Banks (MP 49).

3.2.3 US Highway 20 (US20)

US20 is the longest road in the United States, spanning between Newport, Oregon and Boston, Massachusetts. For this study, a problematic stretch between milepost 0 (Newport) and milepost 50 (Philomath) is analyzed (Figure 3.4). This stretch of US20 is a Tier 3 Seismic Lifeline. Besides the landslides encountered in the PME realignment, the highway is subject to frequent landslide activity, often owing to the notoriously unstable geologic conditions that characterize the region. This span primarily traverses Tyee formation, which is characterized by rhythmically-bedded layers of sandstone and siltstone that is highly susceptible to weathering and failure. One very large landslide inventory mapped with lidar (SLIDO) is available for the proposed corridor, existing near the central portion of the highway. Full lidar coverage is available for the given area.

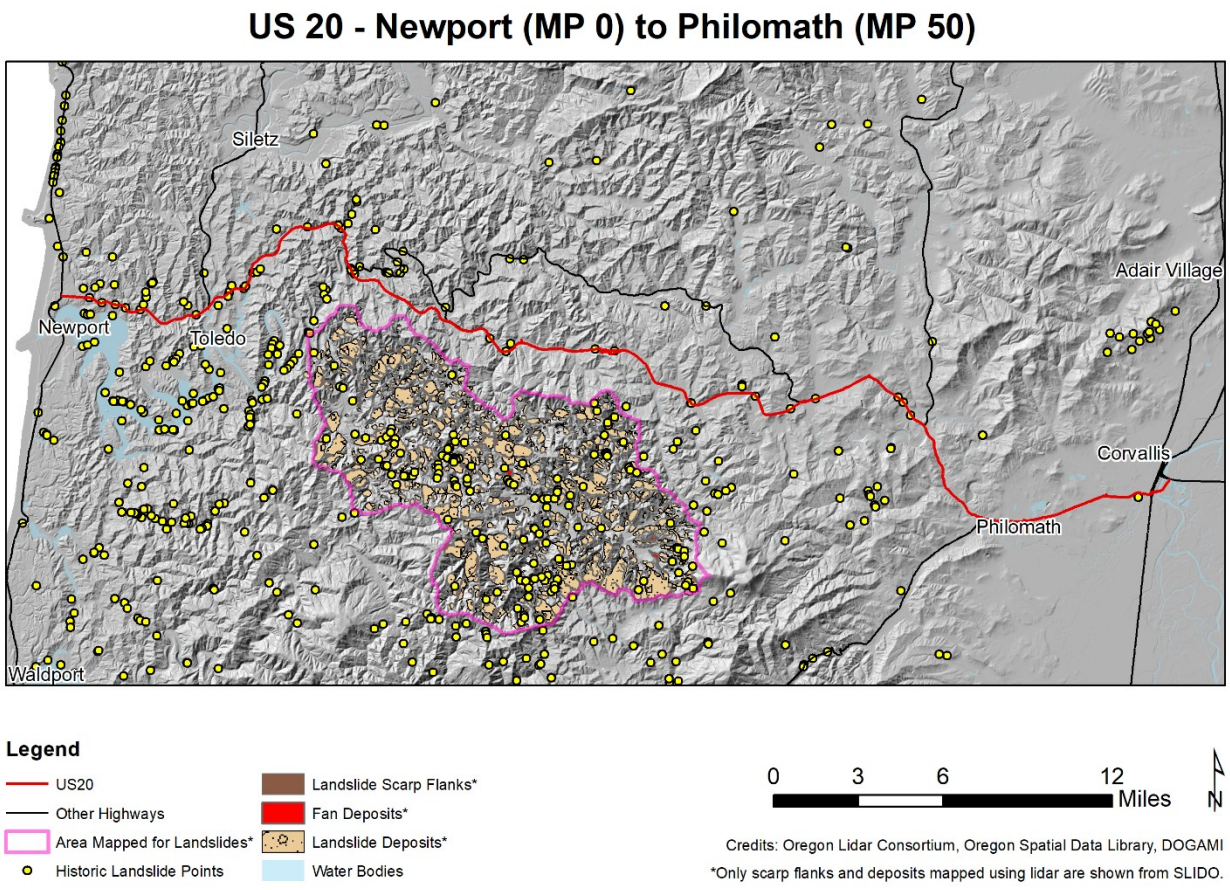

Figure 3.4: Lidar bare earth hillshade, SLIDO landslide inventory and right-of-way for US Highway 20, traversing between Newport (MP 0) and Philomath (MP 50).

3.2.4 OR Highway 42 (OR42)

OR42 connects the southern portion of the Willamette Valley with the Oregon Coast. This highway is classified as a Tier 3 Seismic Lifeline. For this study, right-of-way between milepost 10 (Coquille) and milepost 74 (Winston) is analyzed (Figure 3.5). This highway is subject to frequent landslide activity and was, in fact, closed for several weeks due to a large landslide at the boundary between Coos and Douglas counties. Highway 42 spans the complex mélange of geologic conditions that characterize the southern, coastal portion of Oregon. For this stretch of right-of-way, this includes Six Rivers, Western Klamath, and Umpqua terranes. Much of the western stretch of the highway has been mapped using SICCM, completed as part of the scope of ODOT SPR-786 (Leshchinsky et al., 2018). There is a large landslide inventory (SLIDO) available just north of this study site. Full lidar coverage is available for the given area.

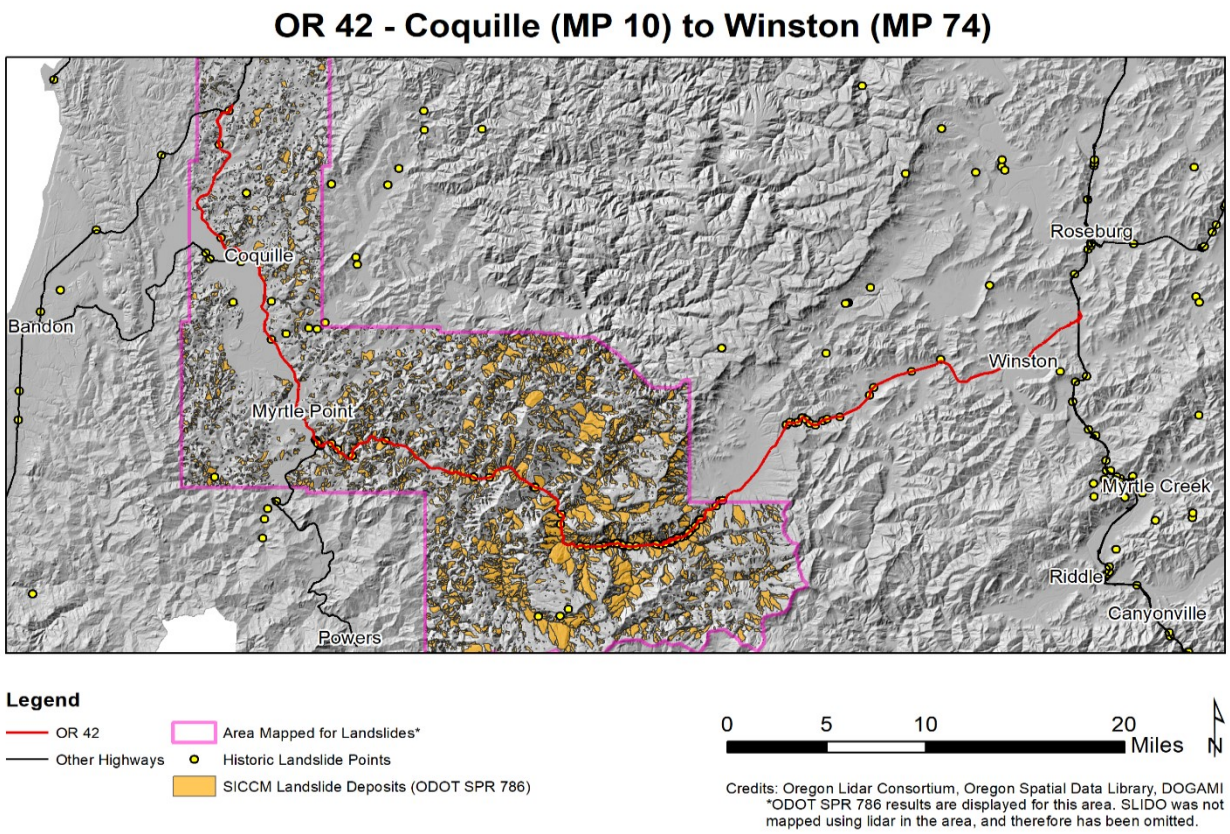

Figure 3.5: Lidar bare earth hillshade, SLIDO landslide inventory and right-of-way for OR Highway 42, traversing between Coquille (MP 10) and Winston (MP 74).

3.3 MODIFICATION OF AGE-ROUGHNESS RELATIONSHIPS FOR LANDSLIDES IN SELECT OREGON CORRIDORS

Age-roughness relationships (e.g., Figure 3.6) for landslides describe the climatic and seismic setting of each inventoried landslide at failure. This information helps constrain relevant parameters for forensic analyses performed later in the project. The methodology used to establish these relationships is as follows (Booth et al., 2017):

In general, we use the geomorphological landslide inventory approach to document patterns of landsliding in space and time along several Oregon highway corridors. A "geomorphological" landslide inventory includes landslides that resulted from multiple and possibly unknown past triggers, as opposed to an "event" inventory that includes all landslides from a specific, known trigger (Malamud et al., 2004). While large numbers of landslides can be included in geomorphological inventories, the ages of the landslides are typically not well known, making it challenging to disentangle the spatial patterns of landslides resulting from different triggering events or more gradual changes in slope stability conditions in the past. A major limitation in expanding the utility of those inventories has been the challenge of dating large numbers of landslides, which we overcome in this work by developing novel proxies for landslide age that can be measured remotely from high-resolution topographic information and calibrated with limited traditional dates (LaHusen et al., 2016; Booth et al., 2017). This approach enables us to

date, by proxy, hundreds to thousands of landslides in the highway corridors that have occurred over the past 10 ky or more and discern how the landscape has responded to past climatic and seismic events. This aspect of the work is possible in western Oregon because of the near complete availability of high-resolution (~ 1-meter point spacing) bare earth lidar data.

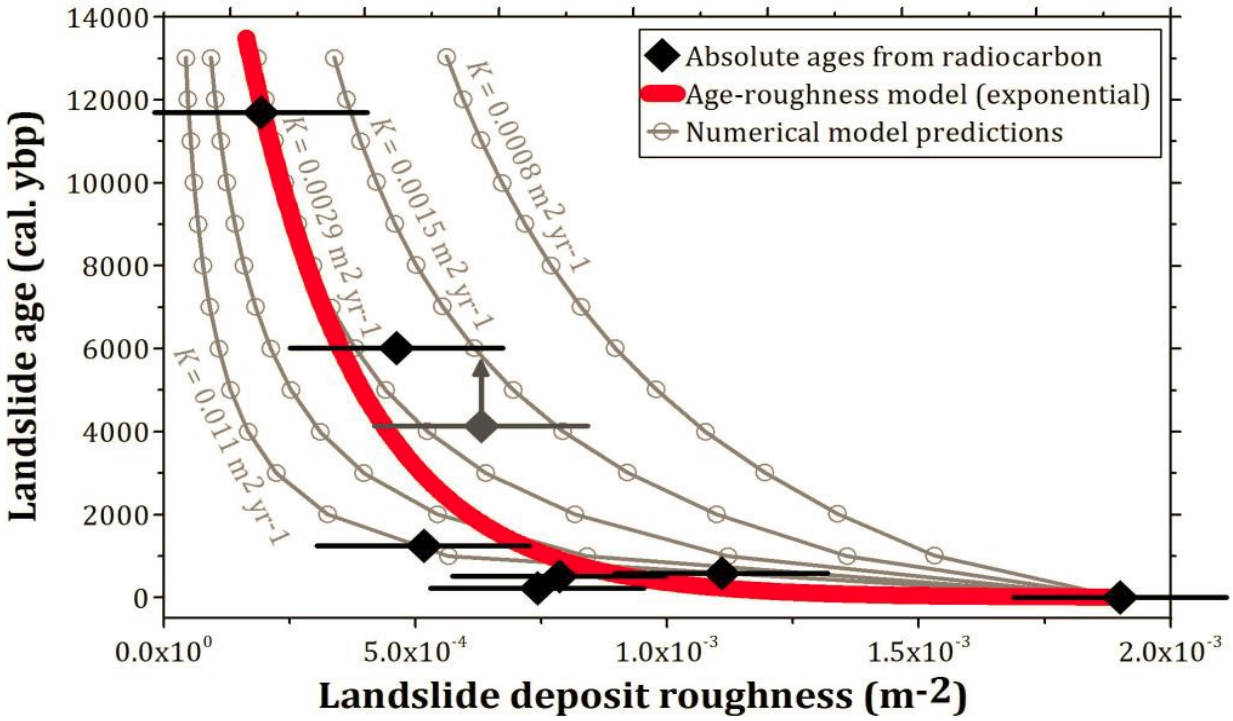

Figure 3.6: Example of an age-roughness model developed for landslides in the North Fork Stillaguamish River valley, Washington from Booth et al. (2017).

3.3.1 Radiocarbon Dating and Fieldwork

Confident, absolute age dating of multiple landslides is the fundamental data needed to develop surface roughness-based proxies for landslide age. Those dates form the backbone of an age-roughness model, which quantifies how soil transport and other geomorphic processes modify a landslide surface over time once the landslide becomes inactive. Radiocarbon dating of organics found in landslide deposits is the most widely applied landslide dating technique (Panek, 2014) and is well suited to forested regions such as western Oregon. The region has been forested throughout the Holocene, so that there is a high likelihood of woody organic material being entrained in prehistoric landslide deposits. Radiocarbon dating is effective for ages up to about 40,000 years before present, and has analytical uncertainties that are typically just hundreds of years. The most extensive dating of landslides in other regions has also relied primarily on radiocarbon dating of organics (Soldati et al., 2004; Borgatti and Soldati, 2010).

Although radiocarbon-based dating of landslides is well-suited to the study area, this dating technique can involve complications in interpreting ages given the complexities of landslide movements. For example, deep-seated landslides often exist as large complexes where different movement styles may occur on different parts of the complex at different times. Reactivations

may remobilize older landslide deposits, thereby incorporating organic material that is older than the most recent landslide. Because of this possibility, radiocarbon ages from organics in a landslide deposit are often interpreted to be a maximum age for the landslide. However, part of a landslide complex that reactivates may also incorporate fresh organic material, which would yield a radiocarbon age that is younger than the surrounding landslide complex (Dufresne et al., 2010). It follows that uncertainties associated with the interpretation of landslide movement history may considerably expand the analytical uncertainties of radiocarbon dating. We address this issue in this work in three ways:

1. First, we located multiple samples from each of several "benchmark" landslides that we use to define the age-roughness model (as described in 3.3.2 below). If multiple dates from a single landslide are consistent with one another, this would indicate that the landslide being dated likely failed as a single main event, or possibly multiple events spaced close enough in time to allow overlapping radiocarbon ages. To target this type of landslide, we focus on those with similar morphology including relatively high, arcuate head scarps and relatively low-sloping, hummocky deposits, which suggest that may have failed as rapid, short-duration events. On the other hand, if multiple dates from the same landslide are inconsistent, this has the potential to reveal the details of the timing of the landslide's past movement episodes (Bovis and Jones, 1992; Soldati et al., 2004).

2. Second, large scale, lidar-based landslide mapping with targeted field verification allows us to distinguish individual, discrete landslides within larger landslide complexes. We therefore are able to confidently tie radiocarbon ages to specific landslides rather than more generally to larger landslide complexes.

3. Third, many landslides along western Oregon highway corridors overlap one another so that cross-cutting relationships clearly indicate relative ages, which we capitalize on to reduce the uncertainty on individual landslide ages with Bayesian statistics. For example, consider two overlapping landslides. Radiocarbon dating of multiple samples of organics from each landslide would produce two groups of absolute ages that are likely to have uncertainties of several hundred years or more (LaHusen et al., 2016; Booth et al., 2017). If these two groups of ages overlap, the chronological information of relative age can be used to truncate the probability density functions of absolute age associated with each landslide, thereby improving precision. This chronological information has the greatest effect on overlapping landslides with similar absolute ages, and we target such landslide pairs in our field dating campaign.

We undertook several rounds of fieldwork to locate samples for radiocarbon dating from landslides spanning a wide range of ages and failure styles, focusing on thorough dating of several benchmark landslides and overlapping landslide pairs as described above. This work targeted accessible locations where samples are likely to be exposed by gully or river incision into landslide deposits.

3.3.2 Surface Roughness Analysis

Another way to discern useful age information from potentially large uncertainties associated with radiocarbon dating of individual landslides is to dramatically increase the number of dated landslides. This requires a widely applicable proxy for age that can be measured remotely. By increasing the sample size of dated landslides in this way, we are able to discern broad spatiotemporal patterns of landsliding to compare to independent climatic and seismic records, even where individual landslides may not be precisely or directly dated. Capitalizing on existing airborne lidar is essential to the proposed work because lidar can penetrate the thick vegetation of the Pacific Northwest, which ordinarily obscures landslide features in aerial photos or other remote sensing techniques (Haugerud et al., 2003). Lidar data with a bare earth raster resolution point spacing of ~1 m has been collected for much of western Oregon and is publicly available through the Oregon Lidar Consortium. We also capitalized on ongoing efforts by DOGAMI to collect additional lidar data in the region. We tested different metrics for quantifying surface roughness of landslide deposits and head scarps using lidar data to develop this age proxy.

Surface roughness of landslides may generally reflect a combination of the failure style, relative activity, material properties, or time since the landslide last moved (McKean and Roering, 2004; Glenn et al., 2006; Goetz et al., 2014; Booth et al., 2009, 2017). Furthermore, the quality of the bare earth lidar data may influence measurements of surface roughness, especially when those data are collected using different equipment, at different times of year, or in areas with variable vegetation cover (Burns et al., 2010; Berti et al., 2013). To isolate the roughness signature of landslide age, it is therefore essential to control for as many of these variables as possible and to correct for systematic biases due to differences in lidar data. We therefore focused on landslides that have failed in a similar style in similar geotechnical materials, and use the numerous overlapping lidar data sets to identify and correct for any systematic differences in topographic data.

Roughness should reflect landslide age because near surface soil transport systematically smooths topography over time. A recent landslide can be identified in the field or in topographic data by locating arcuate head scarps, displaced blocks bounded by internal scarps, hummocky topography, and ponded water or springs in the middle of a slope (Keaton and DeGraff, 1996). These diagnostic features are initially sharply defined, but become more subdued with time, and tend to become indistinguishable from the surrounding stable terrain over slightly longer than Holocene timescales in the western United States (McCalpin, 1984). Since soil transport is a non-linear, diffusive process (Roering et al., 1999), shorter length scale topographic features smooth more rapidly than longer length scale features (Crank, 1975; Mudd and Furbish, 2007). We quantified this smoothing process as a function of length scale by focusing on hummocky landslide deposits.

We quantified roughness of landslide deposits using the 2D Fourier and wavelet transforms of the topographic data, which measure topographic variability as a function of length scale (Kumar and Foufoula-Georgiou, 1997; Perron et al., 2008; Booth et al., 2009). To isolate the smoothing effects of soil transport, we systematically excluded parts of the deposits affected by gully incision, as well as human-made features, from the roughness analysis. To ensure that we objectively define gullies, we applied uniform criteria based on topographic metrics such as drainage area, slope, and curvature (Lashermes et al., 2007; Passalacqua et al., 2010a, 2010b,

2014; Pelletier, 2013). To avoid bias, we completed all landslide and gully mapping prior to computing roughness values. Roughness is quantified for every pixel in the lidar digital elevation models (DEMs) in a moving window framework, then averaged for each landslide polygon to assign a single representative roughness value to each deposit. The performance of each roughness metric is evaluated in two ways. First, we determined the percentage of relative ages that the roughness metric correctly classifies for all landslide pairs with clear cross-cutting relationships. Second, we correlated the deposit roughness with absolute age determined from radiocarbon dating for the benchmark landslides (3.3.1) and identify the smallest misfit.

This concept of morphologic dating has been successfully applied to fault scarps and other scarp-like landforms such as terrace risers for the purpose of relative dating (Hanks et al., 1984, Avouac, 1993; Rosenbloom and Anderson, 1994; Hanks, 2000; Hilley et al., 2010). We extend these scarp diffusion techniques by simulating soil transport on landslide deposits with a landscape evolution model if dateable organics cannot be found (Booth et al., 2013, 2017). The model specifically simulates non-linear soil diffusion, which has well established, independently determined values for its two key parameters -- a hillslope transport coefficient and a critical slope -- for the Oregon Coast Range (Roering et al., 1999, 2007). Using a known, constant value for the hillslope transport coefficient will force landslide morphology to reflect age alone, and not variation in the efficacy of soil transport processes, which we expect to be similar throughout western Oregon. The initial condition for each model run will be a large landslide with a well-known recent age. We applied the soil diffusion model to simulate changes in the deposit with time and quantify its predicted surface roughness, and determine the best-fit match to the observed topography, averaged over the entire head scarp. The main product of this task is therefore one or more rigorous, statistically defined relationships between landslide age and roughness that will allow us to estimate the ages of hundreds to thousands of landslides.

3.4 DATA ACQUISTION AND PROCESSING

The proposed methodology utilizes several datasets to assess the influence of seismic and climatic drivers on both forensically obtained soil shear strengths and landslide susceptibility. Landscape geometry is derived from a digital elevation model (DEM), hydrological conditions are derived from antecedent soil moisture coupled with applied rainfall events, and seismic conditions are derived from spatial distributions of peak ground acceleration (PGA).

3.4.1 Digital Elevation Models

Digital elevation models (DEMs) are sourced from the DOGAMI Lidar Viewer. Tiles containing elevation data are imported into a GIS software (both ArcMap 10.7 and QGIS 3.14 are used for different aspects of this study), where they are resampled to a resolution of 6 meters and compiled into a mosaic surrounding the corridors used in this study. The DEM extents for each corridor are shown throughout this study in susceptibility, hazard, and risk maps (see Appendices A-D).

3.4.2 SLIDO Inventoried Landslides

Inventoried landslides are available from the Statewide Landslide Information Database for Oregon (SLIDO current version 3.4), compiled by the Oregon Department of Geology and

Mineral Industries (DOGAMI; Figure 3.7). SLIDO is a geographic information systems (GIS) compilation of Oregon landslides derived from geologic reports and hazard studies from the U.S. Geologic Survey (USGS), DOGAMI, and the U.S. Forest Service (USFS), primarily. The database contains two primary datasets: 1) Historical landslides mapped as point features, primarily resulting from aerial photograph interpretation following rainfall events from the Pineapple Express in 1997 and 1998, and 2) polygons from more detailed mapping efforts for specific regions. The methodology of Special Paper 42 is utilized to expand this compilation via detailed mapping from high resolution lidar DEMs (Burns and Madin, 2009). Note that the landslide maps in SLIDO come from a wide range of sources and most have not been developed yet from high resolution lidar DEMs, resulting in many landslide features missing from the database. Fortunately, the source of each landslide in the inventory is carefully identified in the database. Landslides features have also been identified using the Scarp Identification + Contour Connection Method (SICCM), a DEM-based, automated landslide detection tool developed at Oregon State University with support from the Oregon Department of Transportation and the US Forest Service (Bunn et al., 2019; Leshchinsky et al., 2018). While these features were investigated for use in this project, they were not utilized due to their lack of a defined head scarp, which is required for the forensics methodology described in Section 3.7.2. However, with further development, SICCM may be a useful asset in future landslide forensic analyses. Future work will seek to refine the forensic technique to either create headscarps using SICCM or simply use SICCM polygons in inversion techniques. Landslide inventories from SLIDO exist for the four Coastal Range lifeline corridors described in the scope of this study – US30, OR06, US20 and OR42. An example of SLIDO inventoried landslides (deposits and head scarps) is shown in Figure 3.7.

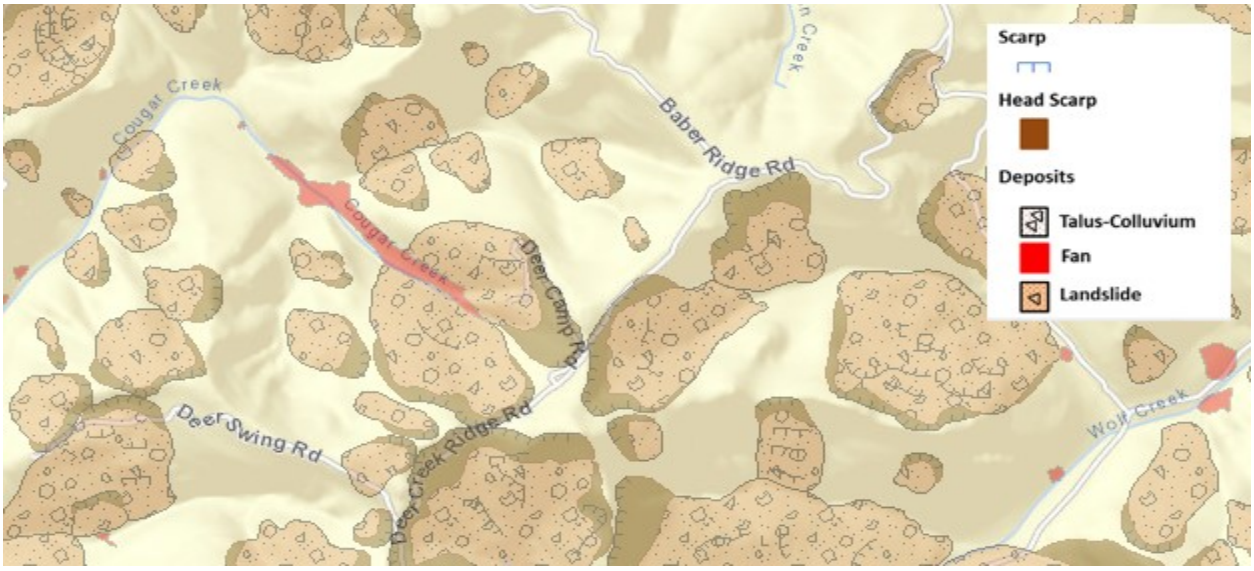

Figure 3.7: Example of SLIDO inventoried landslide deposits and head scarps (after Burns and Madin, 2016).

3.4.3 Hydrological Data

Hydrological conditions for each simulation are obtained through the analysis of several datasets: soil moisture in the rootzone, soil textural classification and corresponding hydrological

parameters, and storm recurrence interval rainfall data (see Section 3.5.2 for detailed methodology).

Soil moisture is acquired from the National Snow and Ice Data Center (NSIDC) in the form of 9 km resolution rasters of volumetric water content in the rootzone (0-1 meter deep). The rasters are created using the Soil Moisture Active Passive (SMAP), a satellite that measures soil moisture using an orbiting radiometer. The data used in this study are Level 4 (L4) products, which are geophysical model outputs created using SMAP data (Reichle et al., 2018). For this study, soil moisture rasters representative of summer conditions are created by computing the mean of August 15th rootzone soil moisture rasters for the years 2015-2019. Soil moisture rasters representative of winter conditions are created by computing the mean of February 15th rootzone soil moisture rasters for the years 2016-2019. Finally, mean rootzone soil moisture rasters are resampled to match the resolution of the DEMs.

Rasters of soil textural classification are used to define a spatial distribution of soil properties for each corridor. This is an important aspect of both computing antecedent hydrological conditions and the hydrological response to precipitation. Before classifying soils by textural classes, rasters of soil composition are obtained from the SoilGrids project, made available by the International Soil Reference and Information Centre (ISRIC). Rasters of clay percentage and sand percentage are resampled to match the resolution of the processed DEMs and run through a textural classification algorithm (Hoffman, 2021). For a given cell, this algorithm assigns a textural class based on the distribution of sand, clay, and silt within each raster soil. Figure 3.8 shows the textural classification triangle that the classification algorithm is based on, as defined by the United States Department of Agriculture (USDA) Natural Resources Conservation Service (NRCS). Figure 3.9 shows a map of soil textural classification and the spatial context of each corridor.

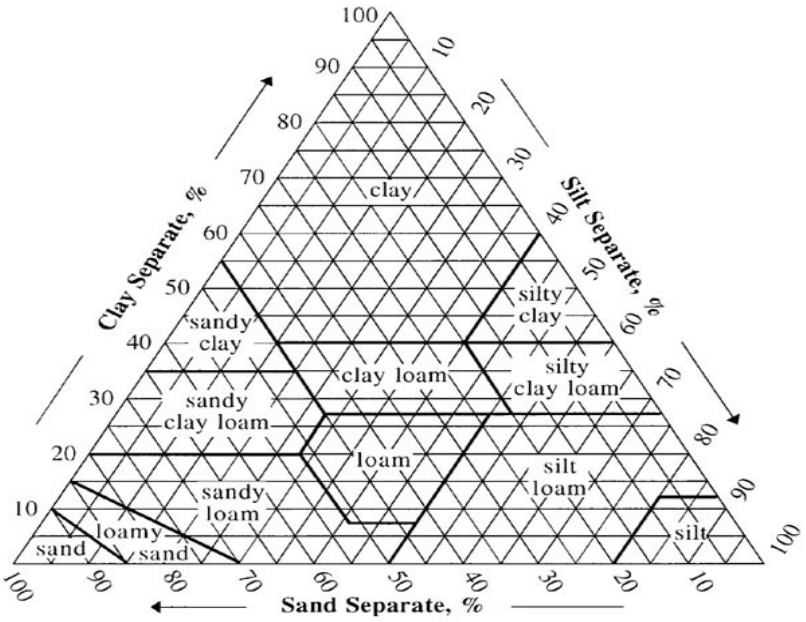

Figure 3.8: Textural classification of soils, based on sand, clay, and silt composition (USDA Natural Resources Conservation Service Soils).

Average hydraulic parameters are then assigned to each textural soil class according to the ROSETTA Model (Schaap et al., 2001). These properties, shown in Table 3.1, help determine how stresses within the soil are affected by both antecedent moisture and rainfall infiltration. Note that in Table 3.1, θ_s is saturated volumetric water content, θ_r is residual volumetric water content, α and n are van Genuchten (1980) fitting parameters, and k_s is saturated hydraulic conductivity. Rainfall data are digitized ODOT 24-hour precipitation maps, as seen in Appendix H of the ODOT Hydraulics Manual (Oregon Department of Transportation, 2014). Rasters of 24-hour rainfall are resampled to match the resolution of the aforementioned corridor DEMs before application in the analyses herein.

Table 3.1: Hydrological Parameters of Soil by USDA Textural Class, as Defined by the ROSETTA Model.

USDA Textural Class	θ_r (cm^3/cm^3)	θ_s (cm^3/cm^3)	α	n	k_s (cm/day)
Sand	0.053	0.375	0.035	3.18	2.81
Loamy Sand	0.049	0.39	0.035	1.75	2.02
Sandy Loam	0.039	0.387	0.027	1.45	1.58
Loam	0.061	0.399	0.011	1.47	1.08
Silt Loam	0.065	0.439	0.005	1.66	1.26
Silt	0.05	0.489	0.007	1.68	1.64
Sandy Clay Loam	0.063	0.384	0.021	1.33	1.12
Clay Loam	0.079	0.442	0.016	1.42	0.91
Silty Clay Loam	0.09	0.482	0.008	1.52	1.05
Sandy Clay	0.117	0.385	0.033	1.21	1.06
Silty Clay	0.111	0.481	0.016	1.32	0.98
Clay	0.098	0.459	0.015	1.25	1.17

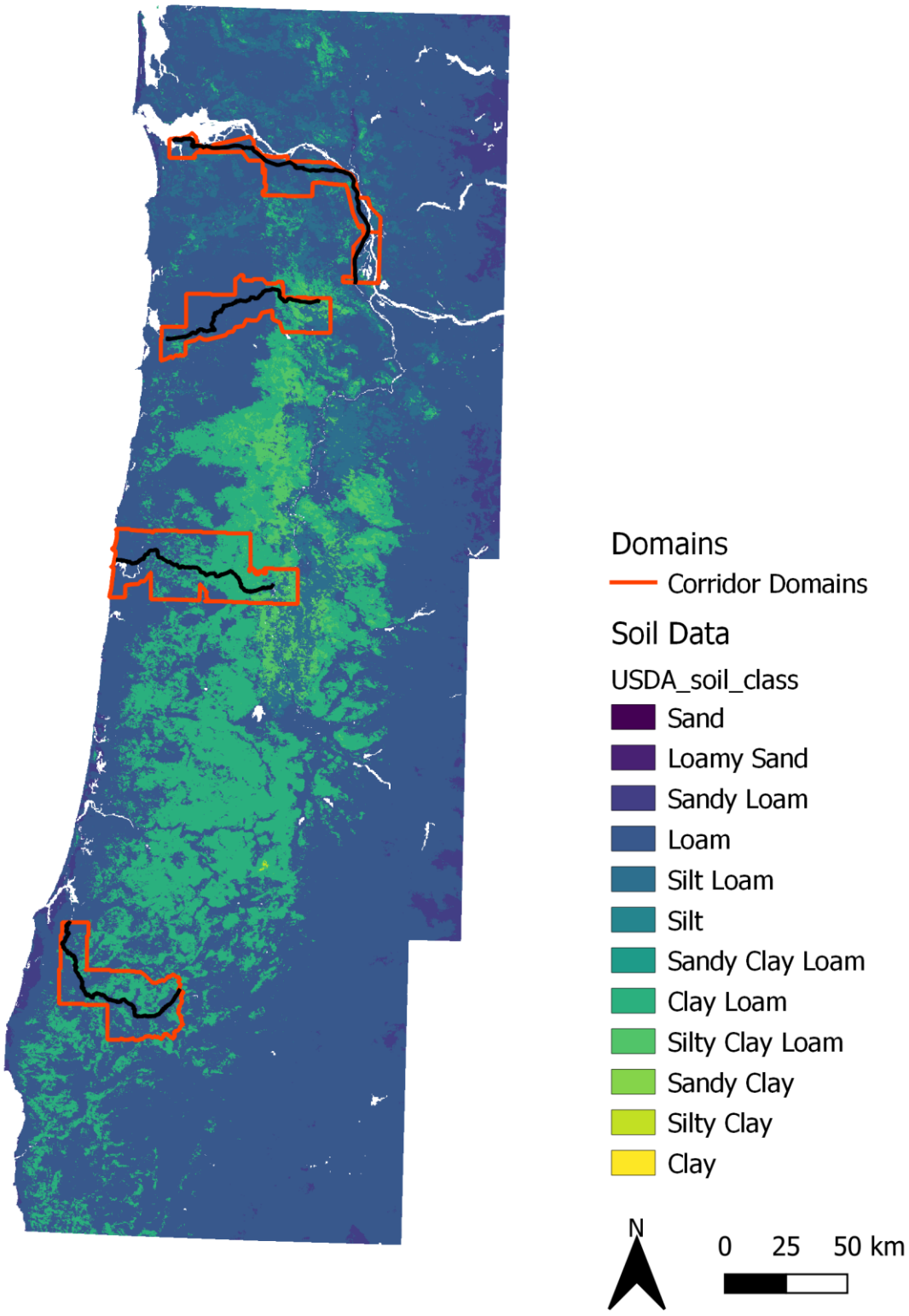

Figure 3.9: Map of soil textural class with superimposed corridor domains.

3.4.4 Seismic Data

Earthquakes produce accelerations capable of mechanically destabilizing hillslopes, making their consideration an important component of slope stability in seismically active areas. In this study, spatial distributions of peak ground acceleration (PGA) in Oregon, USA are used to estimate seismic forcing on hillslopes. Rasters containing predictive geospatial distributions of peak ground acceleration (PGA) for several rupture scenarios (M8.1, M8.4, M8.7, M9.0) are currently available in the webGIS platform, O-Help (http://ohelp.oregonstate.edu) developed for the Cascadia Lifelines Program (CLiP). Specifics of how these scenarios are generated are discussed in Sharifi-Mood (2017), which is based on the methodology created by Madin and Burns (2013) for the Oregon Resilience Plan. The scenarios are designed for potential ruptures ranging from a partial rupture along the California and Southern Oregon segments to a full rupture from California to British Columbia. For each rupture, rock PGA values on a coarse grid were provided by the USGS through their shakemap algorithms applying attenuation relationships. These values were then adjusted based on NHERP site classification (based on geology and sparse VS data) to account for site amplification effects. PGA rasters for all four rupture scenarios considered are shown in Figure 3.10.

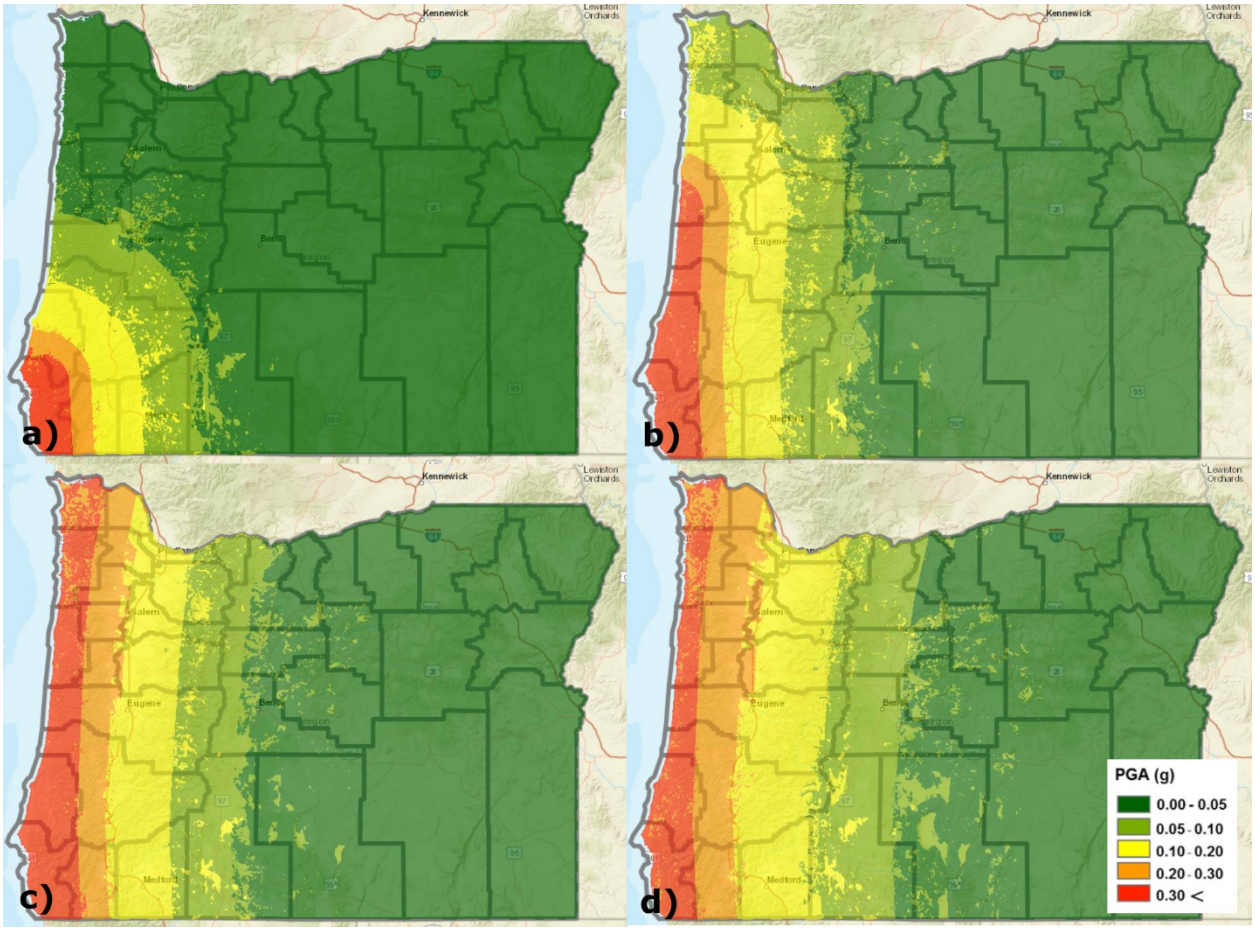

Figure 3.10: Rasters of peak ground acceleration (PGA) used in this study (from O-HELP database; based on Sharifi-Mood, 2017): a) M8.1; b) M8.4; c) M8.7; d) M9.0.

3.5 INITIAL CONDITIONS

Prior to forensic analysis or susceptibility assessment, numerous spatially variant parameters must be computed using the data discussed in Section 3.4. These parameters are used to constrain the environmental conditions that determine the strength and stresses within the soil, and ultimately, the stability of slopes within a given DEM.

3.5.1 Depth of Soil

The proposed methodology assumes that the potential slip surface, for a given cell, exists in the depth of regolith, d. However, this depth exhibits significant spatial variability and cannot be precisely determined on a regional scale without employing extensive instrumentation. Thus, a non-linear hillslope evolution model, which simulates simultaneous tectonic uplift, soil production, and soil transport over a given time interval, is used to estimate soil depths for a given DEM (Roering, 2008). This model assumes that the rate of soil production declines exponentially with depth, and that soil transport is nonlinearly-related to both slope angle and soil depth. Further, this model has been shown to produce topography more representative of the Oregon Coast Range than previous hillslope evolution models (Roering, 2008). A complete methodology for this model may be found in Roering (2008). Figure 3.11 shows an example of soil depth distribution for a region of OR42, near Gales Creek, OR. Note that the modeled mantle tends to be deeper in valleys (areas of high deposition) and shallower upon ridgelines or escarpments (areas of relatively high erosion rates).

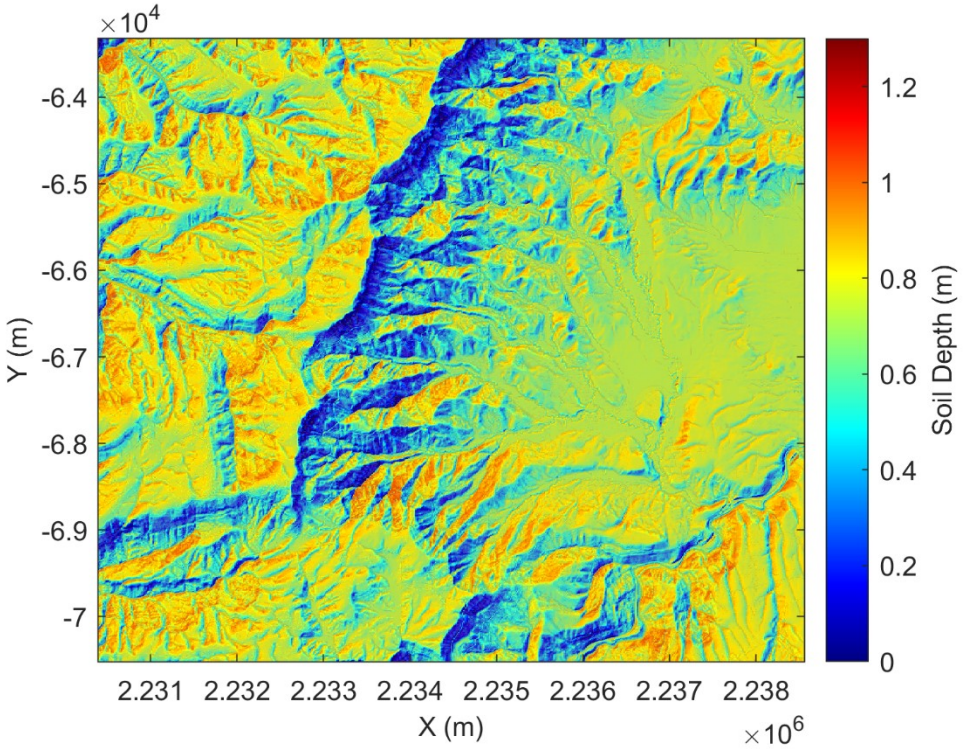

Figure 3.11: Distribution of modeled soil depth for a region of OR42, near Gales Creek, OR.

3.5.2 Antecedent Hydrology, Rainfall, and Hydrological Stress

Hydrological conditions play a significant role in soil strength, and consequently, landslide susceptibility. The proposed methodology combines soil moisture data, soil classification data, and unsaturated soil mechanics to constrain the relationship between hydrology and soil strength. Soil type is determined using an algorithm that classifies soils based on sand and clay content. Corresponding hydraulic parameters from the ROSETTA pedotransfer function lookup table – synonymous with van Genuchten parameters – are then assigned to each cell. These parameters determine how stresses will evolve in the soil when subject to antecedent moisture and rainfall.

Antecedent hydrological conditions for a given distribution of soil moisture are defined by determining an estimate of groundwater depth and capillary water based on remotely-sensed volumetric water content from the surface and root zone (1 meter in depth). This data is determined for summer (August 15th mean moisture for 2015-2019) and winter (February 15th mean for 2016-2019) conditions from Soil Moisture Active-Passive (SMAP; Reichle et al., 2018) for each cell. The groundwater position corresponding to each cell is defined using an inversion method based on van Genuchten (1980) fitting parameters that describe the profile of volumetric water content with depth.

Each column in the soil mantle has an initial profile of volumetric water content (θ_o) corresponding to an iterative fit that meets the defined volumetric water content from SMAP at the root zone (1m) depth (θ_{rz}). The described fit adheres to:

$$\boldsymbol{\theta = \frac{\int_0^H \theta_{res} + (\theta_{sat} - \theta_{res})[1 + (\alpha h)^n]^{\left(-\left(1-\frac{1}{n}\right)\right)} dz}{H}} \quad \textbf{(3-1)}$$

Where:

θ_{sat} is saturated volumetric water content,

θ_{res} is residual volumetric water content,

α and n are van Genuchten fitting parameters, all of which are determined from ROSETTA pedotransfer functions.

Further, dz is depth increment, integrated from the surface to a depth H, and h is head. From this, we may determine what boundary conditions meet the prescribed volumetric water content at any arbitrary depth. For root zone volumetric water content, this is defined as:

$$\boldsymbol{\theta_{rz} = \frac{\int_0^1 \theta_{res} + (\theta_{sat} - \theta_{res})[1 + (\alpha h)^n]^{\left(-\left(1-\frac{1}{n}\right)\right)} dz}{1}} \quad \textbf{(3-2)}$$

Through this, the volumetric water content at any depth may be determined. A given volumetric water content profile also enables determination of the saturated depth of soil, which is H when $\theta = \theta_{sat}$. The determination of a volumetric water content profile also enables determination of pore pressure (suction or positive) at any depth, defined as:

$$\boldsymbol{u(z) = -\gamma_w(-h_{sat} - z)[1 + \alpha((-h_{sat} - z)^n)]^{-(1-1/n)}}$$

(3-3)

Where:

γ_w is the unit weight of water and z is depth.

Infiltration is introduced through considering an average volumetric water content for a given depth during antecedent conditions ($\overline{\theta_o}$) and applying a rainfall intensity flux (i) for a timestep dt, whereas a new average water content ($\bar{\theta}$) is determined as:

$$\boldsymbol{\overline{\theta}(t,z) = \overline{\theta}(t - dt, z) + d\theta = \overline{\theta}(t - dt, z) + \frac{idt}{H}}$$

(3-4)

Thereafter, a new profile of θ and u is determined using Equations 3-1 and 3-3. This simple bucket model accounts for changing positive and negative pore pressure, while also accounting for rise in the groundwater table. Each profile is converted into a lookup table (Figure 3.12) used to determine u at the slip surface for a given cell. Note that in Figure 3.12, $\theta_{rz,0}$ is the initial volumetric water content at the root zone depth.

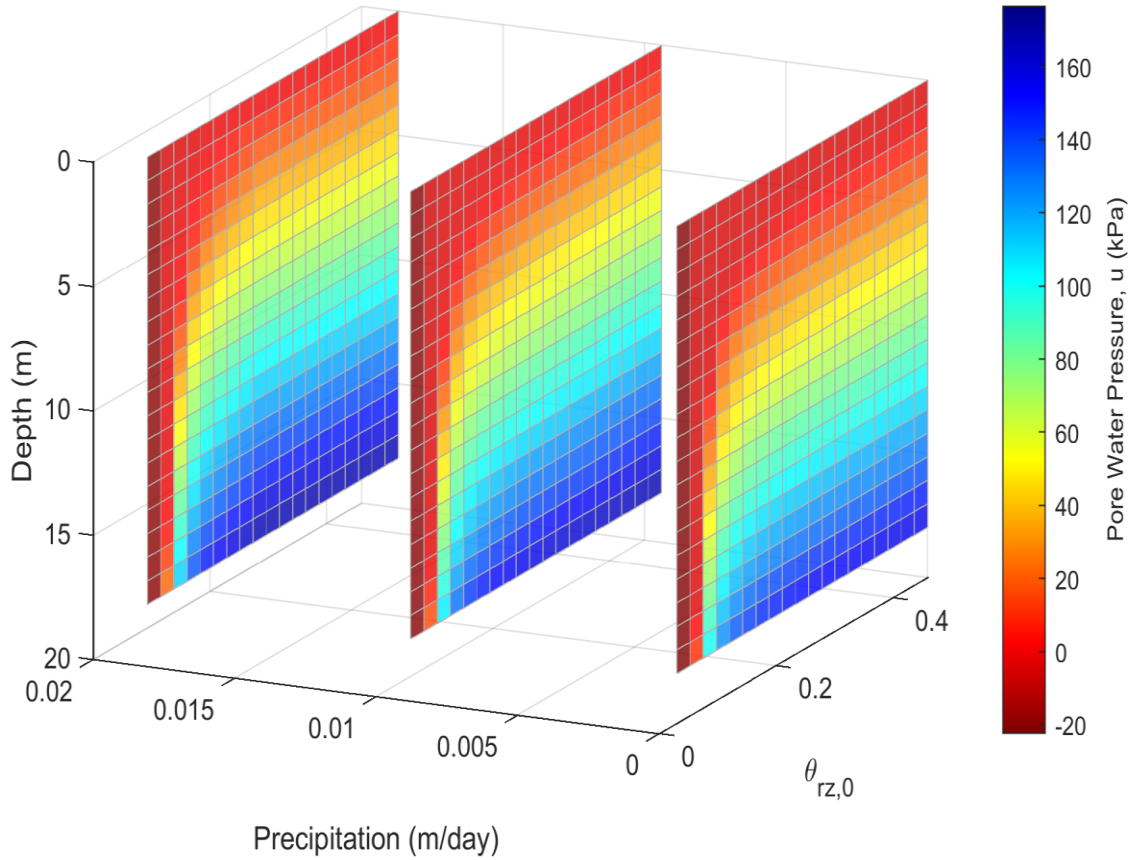

Figure 3.12: Cross sections of example of lookup table showing final values of pore water pressure at depth, given various rates of rainfall, for Loamy Sand.

3.5.3 Changes in Climatic Conditions

Several climate projections, based on numerous models, exist with the purpose of predicting long-term, future variations in climate. These projections use varying methodologies and assume varying emissions trends to compute outputs. In this study, raster data of precipitation anomaly is used to scale precipitation values tied to extreme rainfall events. The precipitation anomaly used is a multi-model mean derived from 20 downscaled CMIP5 models for the period 2040-2069, in the winter (Dec-Jan-Feb), assuming the Representative Concentration Pathways (RCP) 8.5 emissions scenario (total radiative forcing from all forces equal to 8.5 watts/m^2; Riahi et al., 2011). Anomaly data used in this study is acquired from The Climate Toolbox (https://climatetoolbox.org/) and is shown in Figure 4-149a.

In this study, future values of 24-hour rainfall are computed by multiplying ODOT 24-hour rainfall rasters by precipitation anomaly. Note that this approach carries limitations, as the presented rainfall anomaly is a percent change of the 30-year base-period climatological average and extreme rainfall events may not scale directly with changes in mean rainfall over a given period of time (Ragno et al., 2018). Once 24-hour rainfall rasters are scaled by precipitation

anomaly rasters, the same methodology described in Section 3.5.2 is employed to determine hydrologically-derived stresses within the soil.

3.6 SLOPE STABILITY ANALYSIS

Slope stability analyses based on digital elevation models (DEMs) require different spatial considerations than conventional, two-dimensional slope stability methods as it requires consideration of (1) three-dimensional characteristics such as topography, (2) spatial characteristics, (3) geospatial variability of geotechnical properties, and (4) computational efficiency to handle large regions. Upon development of an appropriate slope stability approach that can handle raster-based data, such as DEMs, both (1) forensic assessment of landslides and (2) projections of future instability can occur. The preliminary principles of this approach will be advanced to be able to account for clustering of pixels, to be spatially analyzed for the equilibrium of forces, and to enable discrete potential landslide geometry to be captured. This will require specific, raster-based logic that integrates principles of geomechanics, in this project termed the *Region Grow 3D Method* (RG3DM).

3.6.1 Three-Dimensional Limit Equilibrium

Slope stability is assessed using a 3D adaptation of the Janbu (1973) limit equilibrium procedure (Hungr, 1987). This method is used to determine the force balance for each raster cell, or the ratio of resisting forces to driving forces among an assumed slip surface. Resisting force, F_{re}, for each raster cell is computed as follows:

$$\boldsymbol{F_{re} = c'A + (N - uA) \tan \phi'} \tag{3-5}$$

Where:

c' is cohesion,

A is area of the slip surface,

N is normal force on the slip surface,

u is hydrological stress (may be negative for suction or positive for positive pore water pressure), and

ϕ' is the angle of internal friction.

N is computed as follows:

$$\boldsymbol{N = W \cos \alpha} \tag{3-6}$$

Where:

α is slope angle and W is soil weight, computed as follows:

$$\boldsymbol{W = DA} \tag{3-7}$$

Where:

D is soil depth.

F_{re} is resolved into X and Y components, $F_{re,x}$ and $F_{re,y}$, respectively by multiplying F_{re} by the X and Y slope gradients.

$$\boldsymbol{F_{re,x} = \frac{dz}{dx} F_{re}} \tag{3-8}$$

$$\boldsymbol{F_{re,y} = \frac{dz}{dy} F_{re}} \tag{3-9}$$

Driving force, F_{dr}, for each raster cell and resulting X and Y components are computed as follows:

$$\boldsymbol{F_{dr} = W\,(\sin\alpha + k\cos\alpha)} \tag{3-10}$$

$$\boldsymbol{F_{dr,x} = \frac{dz}{dx} F_{dr}} \tag{3-11}$$

$$\boldsymbol{F_{dr,y} = \frac{dz}{dy} F_{dr}} \tag{3-12}$$

Where:

k is the pseudostatic coefficient describing seismic acceleration.

Note that, using this approach, equilibrium in the Z-direction is implicitly satisfied. The force balance, FB, or ratio of resisting to driving forces, is then computed for each cell:

$$\boldsymbol{FB = \frac{F_{re}}{F_{dr}}}$$

(3-13)

The proposed approach is useful in that it may capture seismicity, the influence of hydrology and rainfall, and characterize the influence of topography on stability. However, it lacks the ability to characterize landslides with irregular geometry or nonplanar failure geometry. For this reason, a method, such as the RG3D may better capture realistic landslide geometry that deviates from shallow, translational failures. However, many of the mechanics and principles associated with this approach are foundational to this proposed RG3D approach.

3.6.2 Region Grow 3D Method (RG3D)

In order to characterize the stability of discretely sized, irregularly shaped, variable-thickness potential slope failures within a raster-based framework, it is important to balance both appropriate mechanics with computational efficiency. Through such an approach, it is possible provide reasonable, raster-based, map outputs of landslide susceptibility at a regional scale. The *Region Grow 3D Method* (RG3D) does this through use of DEM derivatives and principles of force equilibrium, providing an opportunity to determine object-based identification of possible landslides with geometry that deviates from a grid cell. Thus, with estimates of geotechnical properties (shear strength), hydrological properties (water levels), and topographic indices (slope, aspect, soil depth to bedrock), one may account for discrete slope failures. Note that RG3D produces a distribution of potential landslide shapes throughout a landscape. However, when paired with a means of quantifying uncertainty in input parameters, RG3D may be used to produce maps of landslide susceptibility portraying the likelihood of landslide occurrence. The methods used to create susceptibility maps are explained further in Section 3.8.

3.6.2.1 ***Classification of Unstable Landslide Clusters***

Following the creation of a raster containing FB for each cell, cells are then classified as either stable or unstable, based on its respective value of FB. A value of 1 indicates an unstable cell and a value of 0 indicates a stable cell. These values are stored in a binary *stability matrix* (SM):

$$\boldsymbol{SM_i = \begin{cases} 1, & FB_i \leq 1 \\ 0, & FB_i > 1 \end{cases}}$$

(3-14)

Unstable cells within the SM coinciding with any *no-grow zones*, discussed in the following section, are made stable, and the remaining unstable cells are grouped into landslide *clusters*. Prior to clustering, however, a suite of image processing tools is used to eliminate artifacts that may not agree with typical realistic landslide geometry. During this process, lone cells of instability are assumed to be negligible and are made stable, unstable spurs that are one cell wide are made stable, and small gaps surrounded by unstable cells are made unstable. An image processing technique called *connected*

components, within MATLAB, then identifies groups of unstable cells in proximity. Each group is identified as an individual landslide clusters eligible for potential cluster dilation.

3.6.2.2 ***No-Grow Zones***

Without appropriate boundary conditions, clusters of unstable cells within the SM may wrap around ridgelines or grow across valleys, creating unstable shapes contrary to the geometry of typical landslides. To limit this behavior, *no-grow zones* are implemented as regions that remain stable, regardless of their respective classifications within the SM. They are also used as boundaries during cluster dilation, disabling cluster growth into no-grow regions while implementing the RG3DM. They are defined as a combined network of ridgelines and valleys. Ridgeline boundaries constrain landslide growth to single hillslopes, while valley boundaries prevent landslides from crossing drainages. Ridgelines are identified by, first, inverting the given DEM as follows:

$$\boldsymbol{Z_{inv} = -(Z - Z_{max}) + Z_{min}} \tag{3-15}$$

Where:

Z_{inv} is the inverted elevation of the raster cell,

Z is the raster cell elevation, Z_{max} is the maximum raster elevation, and

Z_{min} is the minimum raster elevation.

Next, flow accumulation within drainages is computed using the *flowacc* function from TopoToolbox 2 (Schwanghart and Scherler, 2014). If flow accumulation meets a user defined threshold, then the drainage is identified as a valley. When the DEM is inverted back to its original configuration, previously identified valleys are then identified as ridgelines. Similarly, valleys are identified by performing the same flow accumulation assessment on the non-inverted DEM. Cells identified as ridgelines and valleys are then combined into a single raster, and processed using various image-processing techniques to produce a final raster of *no-grow zones*.

3.6.2.3 ***Cluster Boundary Forces***

To improve force estimates stemming from realistic landslide geometry, a 3D prism of boundary soil surrounding each cluster is computed. A series of wedges informed by passive and active earth pressure angles are built around the perimeter of each landslide cluster. Once these wedges are combined, the resulting prism provides an estimate of forces stemming from an uphill "active" zone and a downslope "passive" zone, where the active zone contributes additional driving forces to the cluster and the passive zone provides the cluster with a stabilizing buttress. The angles defining these wedges range from the passive earth pressure angle, α_P, in line with the direction of sliding, and the active earth pressure angle, α_A, in line with the direction opposite of sliding (Figure 3.13a):

$$\alpha_P = 45° - \frac{\phi'}{2}$$

(3-16)

$$\alpha_A = 45° + \frac{\phi'}{2}$$

(3-17)

The wedge angles for each boundary cell, α, are then interpolated linearly around the boundary of the cluster (Figure 3.13b). Triangles are then projected from the perimeter (Figure 3.13c), which are used to create the cluster boundary structure (Figure 3.13d). Each wedge forming the boundary structure (Figure 3.13e) may then assessed using the methodology described in Section 3.6.1 to determine the contribution of boundary forces to the landslide cluster. Note that unlike cells within the main landslide body, these wedges do not necessarily adhere to the geometry of the DEM grid; their geometry is solely defined by the depth of soil on the landslide boundary and the wedge angle, where the wedge angle defines the slope of the failure interface. Once geometry is defined, the driving and resisting forces in the x- and y-direction are computed and added to the summation of forces for the main landslide body. In short, while wedges may differ in geometry from cells within the main landslide body, they are individually evaluated for stability using the exact same physics.

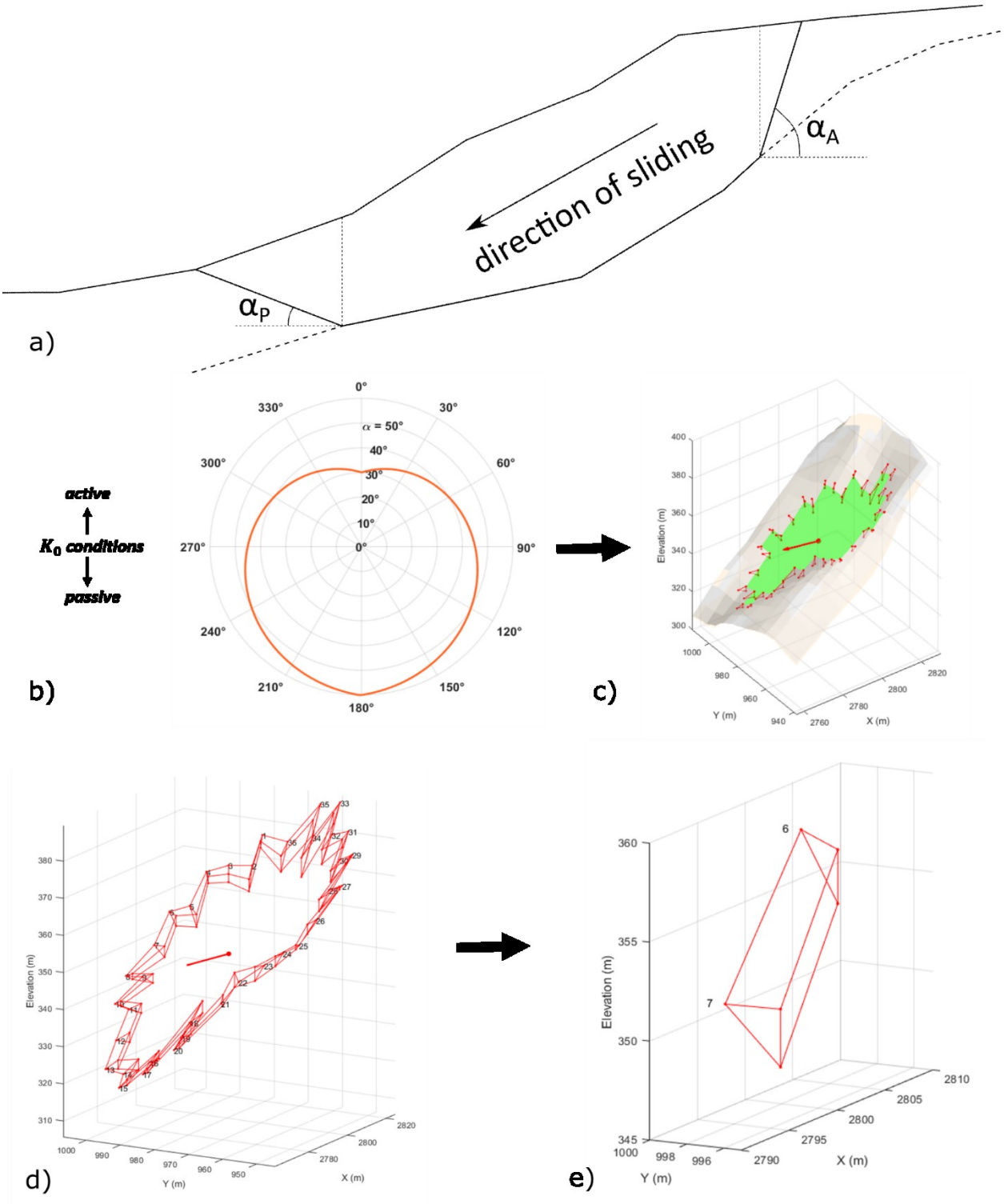

Figure 3.13: Landslide cluster boundary structure: a) definition of active and passive earth pressure angles; b) interpolation of earth pressure angles around perimeter of cluster; c) creation of earth pressure triangles around cluster; d) assembled boundary structure; e) single wedge from boundary structure to be assessed using 3D slope stability method.

3.6.2.4 ***Initial Assessment of Cluster Stability***

Each landslide cluster is initially assessed for stability. First, driving forces and resisting forces, including boundary forces, are summed and the deficit of resisting forces in the X and Y direction, are computed:

$$\boldsymbol{D_x = \sum_{i=1}^{n} (F_{dr,x_i} - F_{re,x_i})}$$

(3-18)

$$\boldsymbol{D_y = \sum_{i=1}^{n} (F_{dr,y_i} - F_{re,y_i})}$$

(3-19)

Where:

D_x and D_y are the force deficits in the X and Y direction, respectively,

i is the cell number within the given cluster, and n is the number of cells within the given cluster.

The magnitude deficit, D, is then compared to a value of allowable error, $E_{allowable}$, for each cluster and the cluster is defined as either *stable* or *unstable*:

$$\boldsymbol{D = \sqrt{{D_x}^2 + {D_y}^2}}$$

(3-20)

$$\begin{cases} \boldsymbol{stable}, & \boldsymbol{D \leq E_{allowable}} \\ \boldsymbol{unstable}, & \boldsymbol{D > E_{allowable}} \end{cases}$$

(3-21)

Where:

$E_{allowble}$ is a user-defined value of allowable magnitude force deficit.

In this study, $E_{allowble}$ is equal to 1% of the cluster's total weight.

Note that this value of error is arbitrary, but was determined, through trial and error, to be an acceptable tolerance with respect to convergence. A user-defined, acceptable margin of error is a necessary component of most limit equilibrium approaches; this value is usually selected as a compromise between model accuracy and computational expedience.

Unstable clusters are then grown using *cluster dilation*, which allows them to be made stable by adding cells and their respective forces to the cluster. Typically, as steep, unstable clusters grow into gentler terrain, stabilization eventually occurs due to an increase in net friction within gently sloped shear interfaces. Incremental growth continues until a stable condition is achieved or there are no remaining eligible cells to be added.

3.6.2.5 ***Cluster Dilation***

Cluster dilation begins by identifying cells on the edge of the cluster, or *boundary cells*. Note that these are simply grid cells on the boundary of the main landslide body and are unrelated to the boundary wedge structure discussed in Section 3.6.2.3. This is achieved by using the *imdilate* function, from the MATLAB image processing toolbox, to dilate the cluster by one cell in all directions. However, not all identified boundary cells are eligible for addition to the cluster. In order to be considered eligible for addition, a boundary cell must meet the following conditions: 1) The cell must be downhill of all adjacent cells within the landslide cluster; 2) The cell must not intersect with a defined no-grow zone or the DEM boundary.

Once boundary cells are filtered for eligibility, they are then classified in order of their capability to satisfy force equilibrium. First, the available deficit force of each eligible cell is determined as follows:

$$\boldsymbol{D_{elig,x_i} = F_{elig,dr,x_i} - F_{elig,re,x_i}} \tag{3-22}$$

$$\boldsymbol{D_{elig,y_i} = F_{elig,dr,y_i} - F_{elig,re,y_i}} \tag{3-23}$$

$$\boldsymbol{D_{elig_i} = \sqrt{D_{elig,x_i}{}^2 + D_{elig,y_i}{}^2}} \tag{3-24}$$

Where:

D_{elig,x_i} and D_{elig,y_i} are the force deficits of each eligible cell in the X and Y direction, respectively,

D_{elig_i} is the magnitude force deficit of each eligible cell,

F_{elig,dr,x_i} and F_{elig,re,x_i} are driving and resisting forces, respectively, for each cell, in the X direction, and

F_{elig,dr,y_i} and F_{elig,re,y_i} are driving and resisting forces, respectively, for each cell, in the Y direction.

Once available deficit forces are computed, a *growth cycle* begins. Each eligible force deficit is first subtracted from the cluster force deficit:

$$\boldsymbol{R_i = D - D_{elig_i}} \quad \textbf{(3-25)}$$

Where:

R_i is the remainder of the cluster force deficit.

The array R is then sorted, with the smallest and largest values corresponding to the boundary cells most and least likely to satisfy force equilibrium, respectively. The boundary cell producing the smallest remainder of cluster force deficit is then added to the cluster and removed from the list of eligible boundary cells. From there, D is reassessed using Equations (3-20 - 3-24), Equation (3-25) is used to reassess remainders, and the best cell is again selected. This process is repeated until there are no more eligible boundary cells remaining for the current growth cycle.

Due to force directionality, non-uniform soil depths (driving forces), and other potential forces, not all eligible boundary cells will contribute to overall cluster stability. Thus, once the array of eligible boundary cells is depleted, the cluster's state of stability is examined after each individual cell addition. Once the most stable configuration of added cells is determined, that configuration is applied to the landslide cluster and all other eligible cells are discarded. From there, force equilibrium is re-evaluated. If the cluster is still eligible for cluster dilation, another round of eligible boundary cells are identified and another growth cycle is initiated. Otherwise, the cluster is considered stable and cluster dilation ceases.

Through being able to account for changing depth throughout a landslide cluster, this model may implicitly capture either translational or deep-seated landslide geometry, a key advance when compared to prior susceptibility models. Furthermore, it enables direct assessment of geotechnical, hydrological, and seismic inputs through forensic analyses, described in the following sections.

3.7 FORENSICS FROM LANDSLIDE INVENTORIES AND AGE ROUGHNESS ANALYSIS

3.7.1 Inferring Landslide Forcing from Age-Roughness Analysis

A key step in landslide forensics is back-analyzing inventoried landslides using conditions that induced failure. In this study, the main drivers considered are those from precipitation or seismicity. While we often associate landsliding in Oregon with periods of heavy rainfall, many of the scars of past landslides may well have been driven by violent shaking from past Cascadia

Subduction Zone (CSZ) events. However, isolating which landslides occurred due to precipitation- or seismic-forcing is a non-trivial task and an important component in the forensics performed herein. In this study, modified age-roughness relationships (Section 3.3) are used to determine a period of time in which SLIDO inventoried landslides may have occurred. Through this approach, the physical conditions present at the time of insipient landslide failure may be inferred. If the age of a given landslide corresponds with an event in the paleoseismic record (Figure 2.4), it is assumed that failure was induced by a CSZ seismic event and appropriate seismic intensity measures are used during forensic analysis. Given the uncertainties in radiocarbon and surface roughness-based landslide dating, a fraction of landslides identified in this way may have been triggered by other, non-seismic events, so some overprediction of coseismic landslides is expected. Note that while the CSZ has produced 19 full or partial ruptures over the last 10,000 years (Figure 2.4; Atwater et al., 2003; Nelson et al., 2006; Goldfinger et al., 2012), confidence intervals related to carbon dating organics limit the identification of seismic landslides to those triggered by the most recent 1700 earthquake. Within the presented forensics framework, landslides coinciding with the 1700 event are assumed to be triggered by a M8.7 earthquake. Alternatively, aseismic landslides are assumed to by hydrologically-driven and triggered by a 100-year rainfall event. Figures 4.20-4.23 show SLIDO inventoried landslides classified by age-roughness classification, for each corridor in this study.

3.7.2 3D Forensics Framework

To compile a distribution of shear strength parameters that may be used in susceptibility analyses, SLIDO inventoried landslides are forensically assessed for each corridor. Each landslide is assessed using a two step methodology, in which: 1) a 3D rupture surface geometry is computed and 2) shear strength is back-calculated using the 3D slope stability framework described in Section 3.6.1. Note that the back-analysis of soil strengths herein consider the influence of both seismicity and forces induced from hydrological conditions.

3.7.2.1 ***Estimating 3D Rupture Surface Geometry***

In order to back-calculate soil shear strengths from landslides using the proposed 3D slope stability method, 3D geometry of the landslide must first be constrained. SLIDO inventoried landslides exist as 2D delineations of landslide extents, requiring further processing to constrain this geometry. Thus, the 3D rupture surface is calculated using a hybrid-spline method described in Bunn et al. (2020a). This method begins by projecting a thin-plate spline beneath the inventoried landslide. The projection of the spline into the subsurface is guided using angles inspired by Rankine earth pressure theory (Rankine, 1857). The spline creates a smooth failure surface constrained to a group of control points.

Inventoried landslides are classified into two distinct categories: compound or rotational. Compound landslides are those whose deposits have not displaced sufficiently to evacuate the extents of their respective failure surface. Rotational landslides are those whose deposits have displaced significantly and have mostly or entirely evacuated the extents of their respective failure surface. These landslides are categorized by fitting a two-term Fourier series (Santamarina and Cho, 2004) to their rupture extents. If the Fourier series approximation fits the planview rupture extents well, the landslide is

classified at rotational; if the Fourier series does not fit the planview rupture extents well, the landslide is classified as compound. For rotational landslides, the ground surface bounding the failure surface is fit using another thin-plate spline, in order to approximate pre-failure geometry. For compound landslides, original topography from a DEM is assumed to be the pre-failure ground surface. Parameters used to fit the thin-plate spline rupture surfaces are optimized using three well-characterized landslides in the Oregon Coast Range, USA. For this study, the regularization parameter, λ, angle enforcement parameter, ψ, and the friction angle, ϕ', are equal to 0.83, 0.26, and 25°, respectively. Note that this input friction angle is used to guide the entry angles of the spline, as defined using Rankine earth pressure theory. A more detailed description of this methodology and its respective assumptions may be found in Bunn et al. (2020a).

3.7.2.2 ***Back-Calculation of Shear Strength Parameters***

Once the rupture surface of each landslide is calculated and the 3D geometry of the landslide is constrained, the force balance of the landslide is assumed to be equal to one. From there, the friction angle of the soil, ϕ', may be iteratively solved using the 3D Simplified Janbu (1973) slope stability method in Section 3.6.1, where forces are summed and a single friction angle is computer per landslide. More information may be found in Bunn et al., (2020b). This method is based on the same physics used in RG3D and may consider a wide range of triggering factors (antecedent moisture, rainfall, seismicity). In this study, a modified age-roughness relationship for the Pacific Northwest (Section 4.2) is used to identify coseismic landslides, for which an additional seismic body force is considered during forensic evaluation. More details on assumptions tied to physical inputs, for this study, may be found in Section 4.3.1. This is repeated for all eligible SLIDO inventoried landslides within a corridor and a distribution of ϕ' is created. SLIDO inventoried landslides are only eligible for analysis if they have a mapped area of deposits and a mapped head scarp, as these features are required to calculate a 3D rupture surface. Distributions of ϕ' for each corridor are shown in Section 4.3.1. These distributions include probabilities tied to ranges of soil strength, ϕ'; when these probabilities, associated soil strength values, and RG3D are used in conjunction, susceptibility maps portraying the size, location, and likelihood of landsliding may be constrained (discussed further in Section 3.8).

3.7.3 Inferred Hydrological and Landslide Characteristics from the Highway 20 PME Realignment

The following describes the general process for the organization of instrumentation readings from the Pioneer Mountain to Eddyville U.S. 20 highway realignment project (PME). The purpose of PME instrumentation was to monitor the active landslides within the project site so that mitigation methods could be developed and their effectiveness carefully monitored. The results from these efforts were also used as validation for the forensic methods outlined in Bunn et al. (2020a-b), where the Big Slide and Box Slide served as validation for forensically-derived landslide failure surface geometries. This data was critical as it provided two of four landslides used in the validation approach owing to its extensive characterization. Additionally, PME hydrological data is currently being used to understand the relationship between rainfall and the groundwater response within a drained landslide (ODOT Project SPR 834 – in progress). Note

that while attempts were made to model groundwater depths for the US20 corridor using this data, an alternate approach to modeling groundwater was adopted for this SPR808 project. Instrumentation was active from 2007 up to 2016 with varying numbers of active instruments at any given time. These instruments were installed throughout this time period and are spread out over approximately 4 miles of the project with higher concentrations at the observed landslides and cuts added for the highway realignment. The instruments that are being used from the PME geotechnical monitoring are the 250 piezometers (PZ), 150 inclinometers (IC), 22 in-place-inclinometers (IPI), and 7 weirs at the drainage arrays. Rainfall data was also collected for the site and is included in the data set. Micro-Electro-Mechanical-System (MEMS) inclinometer strings, extensometers, and settlement sensors were part of the geotechnical monitoring at PME but are not part of this data processing. A script was created to import data in a consistent, time-stamped, georeferenced framework, presented in Appendix J, the output of which is shown in Figure 3.14. Details regarding data types are shown below.

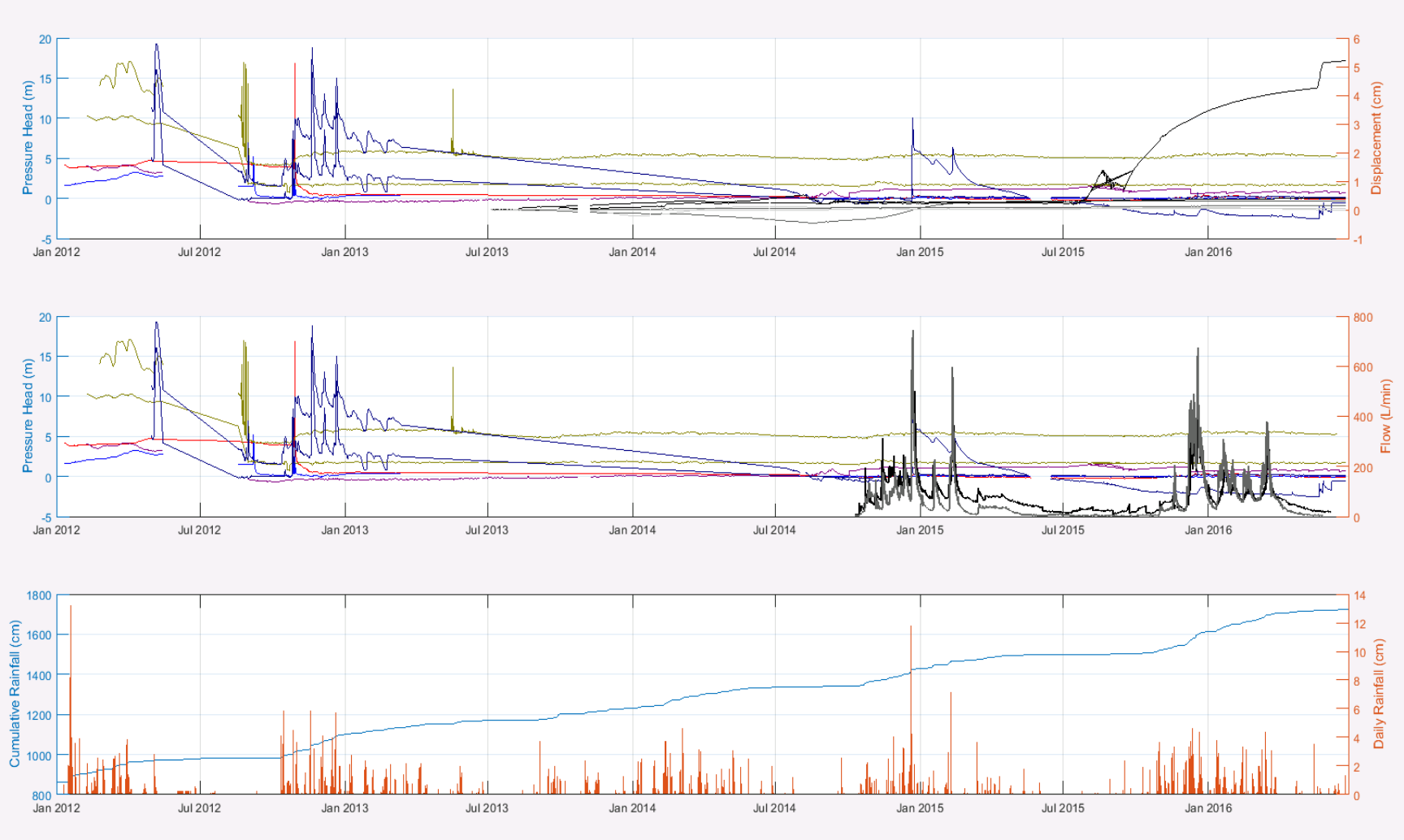

Figure 3.14: Example output from PME database structure.

3.7.3.1 ***Location of Instrumentation***

Each instrument except the weir and rainfall data is associated with a boring name. These borings have their location recorded in terms of northing and easting. The northing and easting are located based on the Oregon Coast Zone of the Oregon Coordinate Reference System (OCRS). The northing and eastings have been converted to latitude and longitude. With each boring being located with latitude and longitude a digital elevation model can also be added to the data set. The instrumentation that are associated with a boring name also have a depth to the device recorded within the data set. All the instrumentation except the weir and rainfall data can now be located within a digital elevation model with latitude, longitude, and depth.

3.7.3.2 ***Purpose of Data Formatting***

The instrumentation readings are primarily stored within excel spreadsheets. These existing excel files contain columns of readings associated with a date and time but are not organized in a way that data is easily accessed and plotted. Modified excel files are created by moving desired values and readings to consistent locations within the existing excel files. These modified excel files are then read by a MATLAB import script and transferred to MATLAB structures where the data is more easily accessed and figures can be created.

The MATLAB structures are the final format of the data. There is a structure for each of the following, IPI, PZ, IC, Weir, and Rainfall. Each structure contains the all the instrumentation for that category and the associated data for each individual instrument. The MATLAB format is preferred because of the processing and organizational abilities of the program. Instrumentation can be called based on boring name, latitude and longitude, and slide name. The instrumentation may be plotted with a digital elevation model to investigate both spatial and temporal relationships. Each instrument will have a date/time vector with associated readings. These readings will be different for each type of instrument, as outlined below.

3.7.3.3 ***Piezometer Data***

Vibrating wire piezometers and standpipe piezometers were used for the monitoring with the majority being vibrating wire piezometers. Many of these piezometers were connected to monitoring and control units (MCUs) in 2013 and the excel file format changed. This required multiple modified excel file formats for the data import scripts. Each piezometer in the PZ MATLAB structure has the below vectors and values associated with it.

Vectors: Date/time, Head pressure, Pressure head, Groundwater elevation

Scalars/Strings: Boring name, Landslide designator, Latitude, Longitude, Ground surface elevation, Tip depth, Stick up

3.7.3.4 ***Inclinometer Data***

In-place-inclinometers (IPIs) and periodic manual inclinometer readings are available from the PME and Hooskanaden monitoring. An example of outputs from Hooskanaden are shown in Figure 3.15. One MATLAB structure was used for the IPIs and one structure was used for the manual inclinometer readings. Each IPI in the IPI MATLAB structure has the below vectors and values associated with it.

Vectors: Date/time, A movement, B movement

Scalars/Strings: Boring name, Landslide designator, Latitude, Longitude, Ground surface elevation, Depth to top, Depth to bottom, Length, Previous displacement, A orientation, B orientation.

Each manual inclinometer has the below matrices, vectors, and values associated with it. The rows of A and B movement matrices relate to the depth vector and the columns relate to the date/time vector.

Matrices: A movement, B movement

Vectors: Date/time, depth

Scalars/Strings: Boring name, Landslide designator, Latitude, Longitude, Ground surface elevation, A orientation, B orientation

3.7.3.5 ***Weir Data***

One data structure was used for the all the available weirs. The drainage arrays that each weir encompasses can be located on the PME site plans. Each weir has the below vectors and values associated with it.

Vectors: Date/time, Flow

Scalars/Strings: Landslide designator.

Precipitation Data

One data structure was used for the rainfall data. The rainfall structure has the below vectors and values associated with it.

Vectors: Date/time, Day total, Cumulative total

Scalars/Strings: None.

Syntax used in Structure Creation

- Existing excel files
    - All the piezometer, IPI, weir, etc. data in existing excel format

- Modified excel files
    - The excel files that are organized and used to import the data to MATLAB structures
- IPI
    - Only the in-place-inclinometer data
- PZ
    - Only the vibrating wire piezometers
- Weir
    - Only the weir data
- Rainfall
    - Only the rainfall data
- IC
    - The inclinometer readings that are in the .dpw format
- MATLAB Structures
    - The IPI, VWP, Weir, etc. data in their final format
- Data import scripts
    - The scripts used to move data from modified excel file to the MATLAB structures

3.7.4 Inferred Hydrological and Landslide Characteristics from the Hooskanaden Landslide Instrumentation

Although the Hooskanaden Landslide is one of the most active earthflows on the Oregon Coast, surprisingly little information is available regarding its geotechnical and geological composition. During the month of November 2017, drilling and instrumentation installation at this site occurred. During this time, a state-of-the-art MEMS in-place inclinometer system was installed within the 240-foot deep hole in order to characterize the shear profile and landslide velocity. Along with the MEMS system, two piezometers were installed to monitor pore pressures at 120 feet (36.6 m) and 230 feet (70.1 m) in depth. Due to excessive movements (greater than 7 inches [0.18 m] of shear within a 1.5 foot [0.46 m] wide shear plane), both piezometers and inclinometer systems were compromised by February of 2018. Nonetheless, the drilling investigation provided insight into a landslide with a distinctively different strata than the progressive slope failures found within Tyee formation (e.g., PME) and provided near-real time

insight into landslide velocities of active earthflows found in the geologic mélange of the Southern Oregon Coast Range, relevant to analysis of Highway 42. Figure 3.15 presents the displacement results obtained while the MEMs sensors were functional.

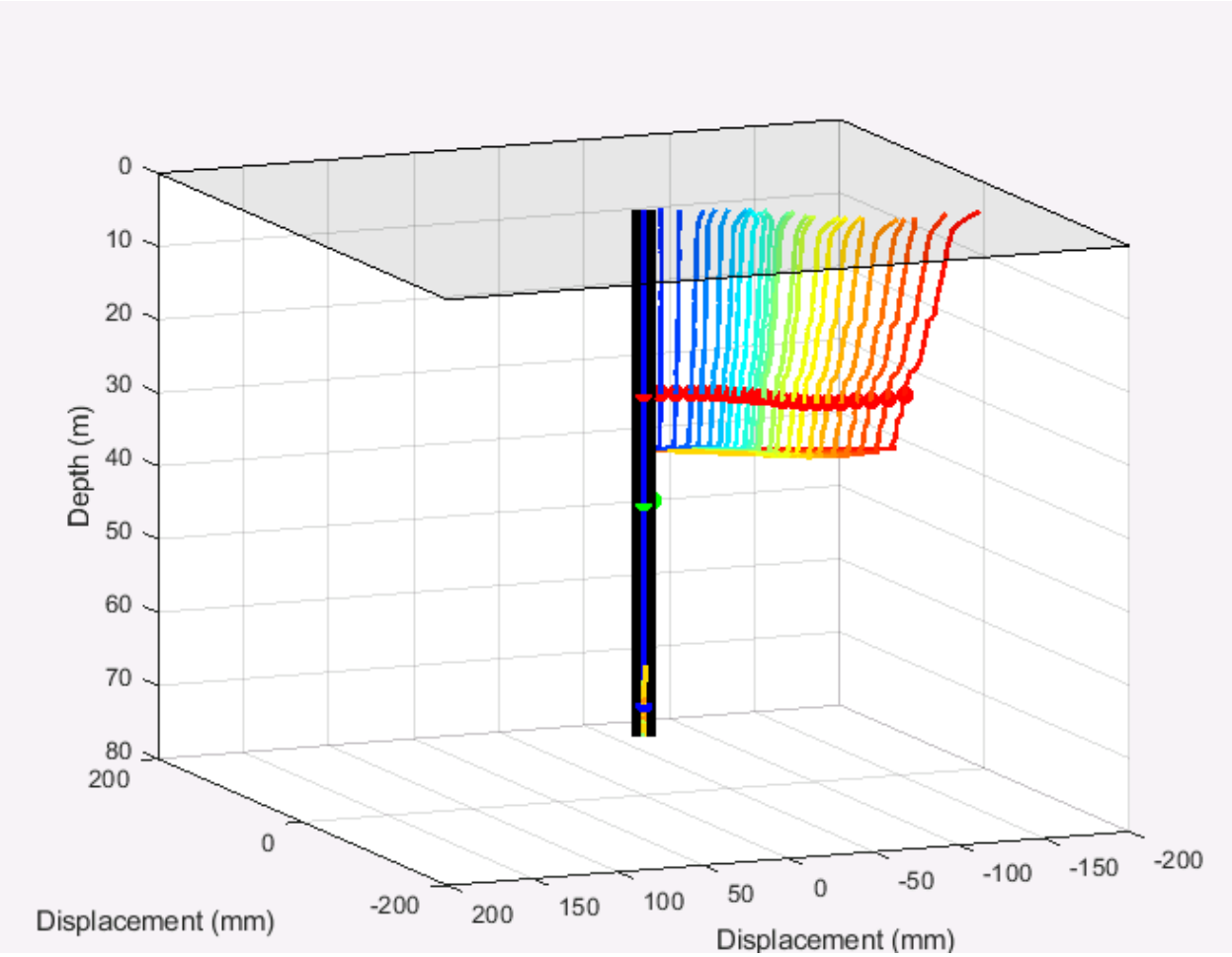

Figure 3.15: Time-dependent inclinometer profile from the Hooskanaden landslide.

3.8 LANDSLIDE SUSCEPTIBILITY ANALYSIS

Back-calculated shear strength parameters are coupled with the RG3D to create a landslide susceptibility framework. Susceptibility mapping extends beyond landslide inventory mapping by considering factors that cause landsliding and using these factors to predict where landslides may occur in the future (Highland and Bobrowsky, 2008). Susceptibility analyses herein are performed by applying RG3D once per each bin of a given shear strength distribution, where the distribution is developed using methods described in Section 3.7.2 (Figure 3.16a-c). The shear strength value for each bin (used in RG3D analysis) is the median value of ϕ' and c (if applicable). So, if a given shear strength distribution contains 10 bins, RG3D will be applied to a DEM 10 times, each producing a unique landslide distribution. Each landslide distribution is saved as a grid, where pixels superimposed by landslide shapes are assigned the probability tied to the shear strength bin; these grids are then summed to generate a map portraying the size, location, and likelihood of landslide activity for a given DEM and set of input conditions (e.g.,

antecedent moisture, rainfall, seismicity). This methodology is summarized in Figure 3.16 and details on the susceptibility methods used herein are as follows:

1. Friction angle, ϕ', supplemented by cohesion, c' (when applicable), is computed for each forensically-analyzed slide within a corridor. Computed shear strengths are then compiled to attain a statistical representation of soil shear strengths within a DEM (Figure 3.16a; further examples of distributions shown in Section 4.3.1).

2. A DEM for the area of interest is selected and processed in GIS software for slope stability analysis.

3. The RG3D (Section 3.6) is implemented for all shear strength bins in the forensically computed shear strength distribution. The shear strength value for each bin (used in RG3D analysis) is the median value of ϕ' and c (if applicable). Note that each shear strength bin will produce a unique distribution of discrete landslide shapes, corresponding with a unique set of Mohr-Coulomb shear strength parameters (c' and ϕ'; Figures 3.16a-c). These landslide distributions are a binary representation of landslide activity (will the slope fail or not?) for a single set of shear strength parameters, as opposed to a landslide susceptibility map, which is computed in step 5.

4. For a given soil strength bin, a grid is created and saved, in which each pixel of a DEM superimposed by a discrete landslide shape (from the distribution computed in step 3) is assigned that soil strength bin's probability. This is repeated for all shear strength values within a shear strength distribution.

5. The grids created in step 4, containing probabilities of landsliding, are then summed to create a map portraying the size, location, and likelihood of landsliding for a given DEM and set of physical inputs (e.g., antecedent moisture, rainfall, seismicity, shear strength distribution). Note that the size and location of potential landslide activity is a product of RG3D analyses, while likelihoods of landsliding stem from the distribution of potential shear strengths (Figure 3.16d).

Susceptibility maps are created to reflect potential conditions in Oregon's future. These data can be used to help planners predict the long-term effects and distributions of landslides caused by both seismicity and precipitation. Seismic landslide projections are presented in the form of a parametric study, with input parameters governing behavior being based on earthquake recurrence intervals derived from the CSZ paleoseismic record (Figure 2.4), rainfall recurrence intervals from the ODOT Hydraulics Manual, and climate projections derived from a suite of climate models (The Climate Toolbox).

Given the geologic timescale of fault activity on the CSZ, rhythmic paleoseismic behavior is considered an appropriate proxy for near-future behavior. The recurrence interval along the fault is 300-500 years, on average (Goldfinger et al., 2012); 318 years have passed since the last megathrust event, meaning that another event could occur anywhere from now to the distant future. Given the unpredictability of earthquake magnitude on the CSZ, a suite of seismic scenarios will be considered, ranging from an M8.1 event to an M9.0 event. PGA values from the rasters shown in Figure 3.10 will be used to inform forward-analyses using the RGM.

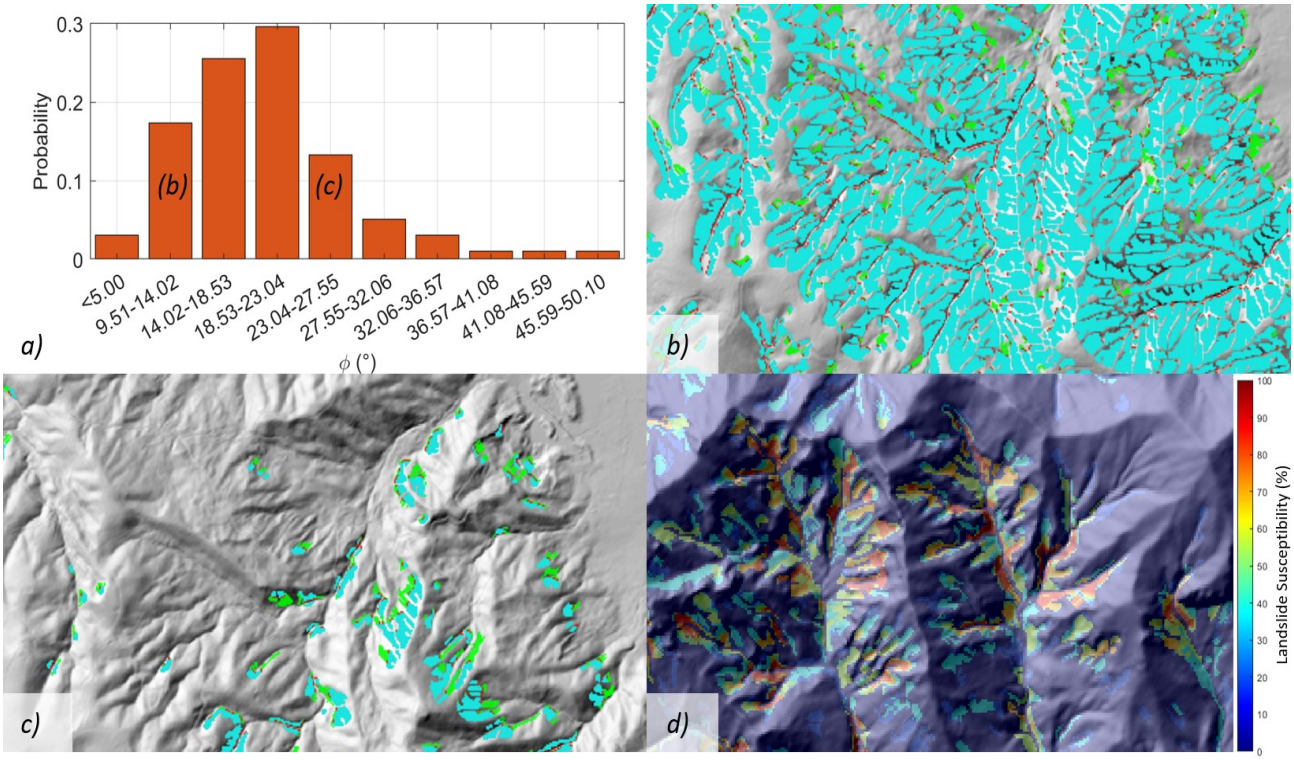

Figure 3.16: Conceptual description of susceptibility method: a) example of distribution of soil shear strength, using 3D forensics described in Section 3.7. Labels in bins correspond with parts b and c of this figure; b) RG3D-produced landslide shapes for bin (b); RG3D-produced landslide shapes for bin (c); d) Example of landslide susceptibility output.

3.9 HAZARD ANALYSIS

Hazard maps expand on susceptibility maps by not only showing where landslides may occur, but providing probabilities of occurrence *based on the likelihood of triggering events*. Deterministic approaches to hazard mapping focus on quantifying parameters such as factor of safety, displacement, or hazard index. These parameters may be expanded into a statistical, or probabilistic, framework to predict the probabilities of hazards occurring, based on determination of discrete landslide polygons and the associated likelihood of failure (uncertainty determined from distribution of shear strength properties *or* the likelihood of an event, e.g. 10-year storm or M8.4 rupture event in next 50 years).

Using susceptibility maps, in conjunction with event probabilities, hazard maps are produced to represent the likelihood of landsliding during specific rainfall, seismic, or multi-hazard events:

$$\boldsymbol{hazard = susceptibility * probability\ of\ event} \quad \textbf{(3-26)}$$

Probabilities of CSZ-induced earthquakes generating the PGA values shown in Section 3.4.4 (Figure 3.10), in the time period 2010-2060, are as follows: 40% for a M8.4 event, 14% for a

M8.7 event, and 9.5% for a M9.0 event (Goldfinger et al., 2012). While a spatial distribution of PGA's for a M8.1 CSZ earthquake is used in this study, there are currently no published probabilities corresponding to this event. In this study, hazard maps corresponding to seismic events only are generated by multiplying susceptibility maps by these values. Thus, seismic-only hazard maps represent the probability of an event occurring within a 50-year period from 2010-2060. Probabilities of rainfall events are based on recurrence intervals corresponding with each raster of 24-hour rainfall, obtained from the ODOT Hydraulics Manual. For example, in the case of a 10-year storm event, a given susceptibility map is multiplied by 1/10. The result is a distribution of rainfall-induced landsliding probability on any given year.

For multi-hazard scenarios, or scenarios in which a seismic event overlaps with a rainfall event, probabilities represent the likelihood of a specific multi-hazard event on a single day. In these cases, probabilities of both events are converted to a daily probability, multiplied together, and finally, multiplied by susceptibility. Probabilities tied to all seismic, rainfall, and multi-hazard events may be found in the file "closure_time_and_costs.xlsx" in the directory "SPR808_Repository\Results\closure_data" in the digital appendix.

3.10 RISK ANALYSIS

Risk maps show potential impacts or consequences of landslide occurrence (Highland and Bobrowsky, 2008). ODOT SPR-808 analyzes the impact of landslides on infrastructure, with focus on ODOT right-of-way (ROW). Using the aforementioned susceptibility mapping approach, landslide polygons computed using RG3D were superimposed upon several ODOT corridors to analyze risks posed by seismically-induced and rainfall-induced landslides. Building upon the approach from SPR-786 (Leshchinsky et al., 2018), a data-driven approach informed by ODOT's Transportation Planning Analysis Unit (TPAU) was used in conjunction with mechanical and geometric information from mapped landslides to assess risk. However, very different from SPR-786, this approach leverages the likelihood of landslides given specific events. In the context of landslides and the risks posed to infrastructure, risk is quantified through several quantitative metrics, including 1) the cost of infrastructure repair based on data from the *Unstable Slopes Database*, 2) the cost of economic loss due to closure based on TPAU projections, and 3) the duration of closure, based on landslide soil debris volumes and estimates of work rates for excavation. Figure 3.17 illustrates the relationship between these risk measures and details about these measures are further discussed in the following sections (based on SPR786; Leshchinsky et al., 2018).

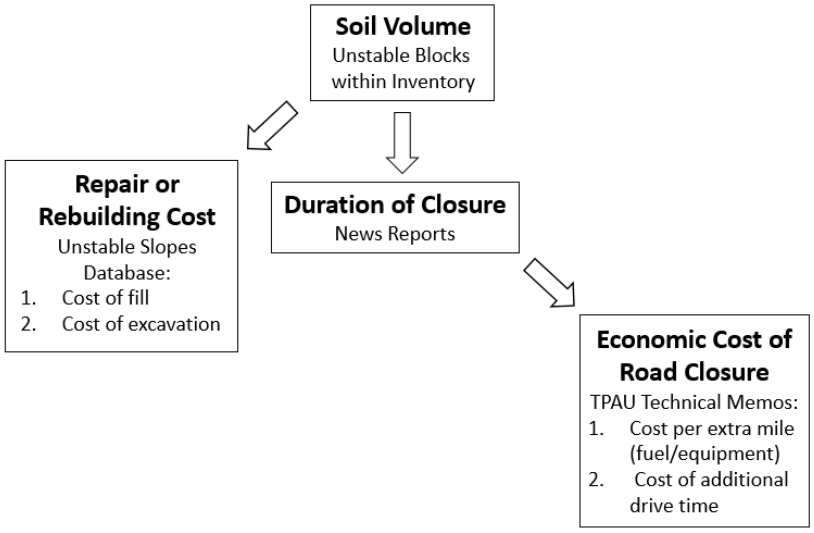

Figure 3.17: Relationships between various risk measures, after SPR-786 (Leshchinsky et al., 2018).

Risk is quantified by employing a DEM-based approach to first estimate the runout of susceptibility-derived landslide polygons and to analyze where landslide polygons overlap ODOT ROW. From there, the volume of material to be excavated and the type of repair required is determined.

3.10.1 Landslide Polygons from Susceptibility Maps

Susceptibility maps are converted into binary susceptibility maps, containing discrete landslide polygons, by applying a user-defined susceptibility threshold to previously generated susceptibility maps. In this study, a susceptibility threshold of 50% is assumed for all cases, meaning that pixels equal to 50% susceptibility or greater are assigned a one and the remaining cells are assigned a zero. The *connected components* image processing tool is implemented in MATLAB to regroup cells equal to 1 into discrete clusters of failed cells. These clusters compose a new suite of landslide polygons used in the following analyses.

3.10.2 Estimation of Landslide Runout

Landslide runout is estimated by assessing the potential energy dissipation of evacuated landslide deposits. The potential energy of a landslide polygon is defined as:

$$\boldsymbol{E_p = m_{total} g h = W_{total} h} \tag{3-27}$$

Where:

m_{total} is the total mass of the landslide polygon,

g is the acceleration of gravity, h is the fall height of the landslide polygon, and

W_{total} is the total weight of the landslide polygon.

Once the initial potential energy of the polygon is established, cells of soil mass downhill of the polygon are incrementally selected and added to the polygon. The frictional dissipation of potential energy induced by each added cell is defined as:

$$\boldsymbol{E_{diss} = W \cos \alpha - L \sin \alpha \tan \phi'} \quad \textbf{(3-28)}$$

Where:

W is the soil weight of the cell, α is the slope of the cell, and

L is the length of the cell.

The friction angle, ϕ', is derived from the strength distribution, considering the assumed susceptibility threshold.

For example, if the susceptibility threshold is 50%, as it is for the presented analyses, then the value of ϕ' corresponding with 50% in the cumulative distribution function (CDF) is selected for characterization of runout. An example strength distribution for OR06 and the associated CDF used to select ϕ' for runout estimation are shown in Figure 3.18. Table 3.2 shows values of ϕ' used for runout estimation for all corridors in this study, based on their respective forensically-analyzed strength distributions (shown in Section 4.3.1). The summation of E_{diss} for all cells eligible to be added to the polygon is then subtracted from E_p. If there is a remainder of potential energy, downslope cells are again added to the polygon and this process is repeated until E_p is equal to or less than zero. At this point, the landslide runout, or debris, is considered immobilized and the computed landslide runout is merged with the original polygon. An example of resulting landslide polygons and their runouts are shown in Figure 3.19. Finally, as a basis for additional risk analyses, a 60-foot (18.3 m) buffer is applied to each resulting landslide polygon. The following risk analysis is performed for both non-buffered and buffered landslide polygons, simply to provide additional, more conservative estimates of repair times, repair costs, and associated commodity flow and rerouting costs.

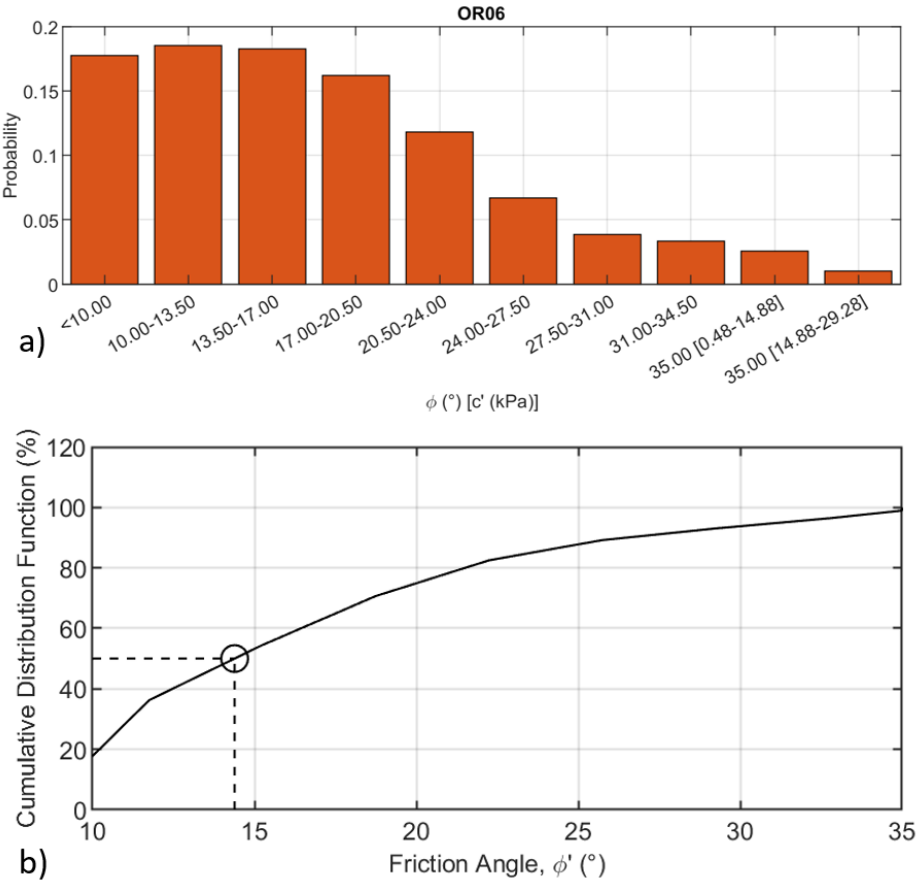

Figure 3.18: Example of selection of ϕ' for runout estimation for corridor OR06: a) strength distribution for corridor OR06; b) associated CDF showing selection of ϕ', corresponding with 50% susceptibility.

Table 3.2: Friction Angles used for Runout Estimation, Derived from Corridor's Respective Shear Strength Distribution.

Corridor	ϕ' used for Runout Estimation (°)
US30	11.5
OR06	14.4
US20	32.5
OR42	22.0

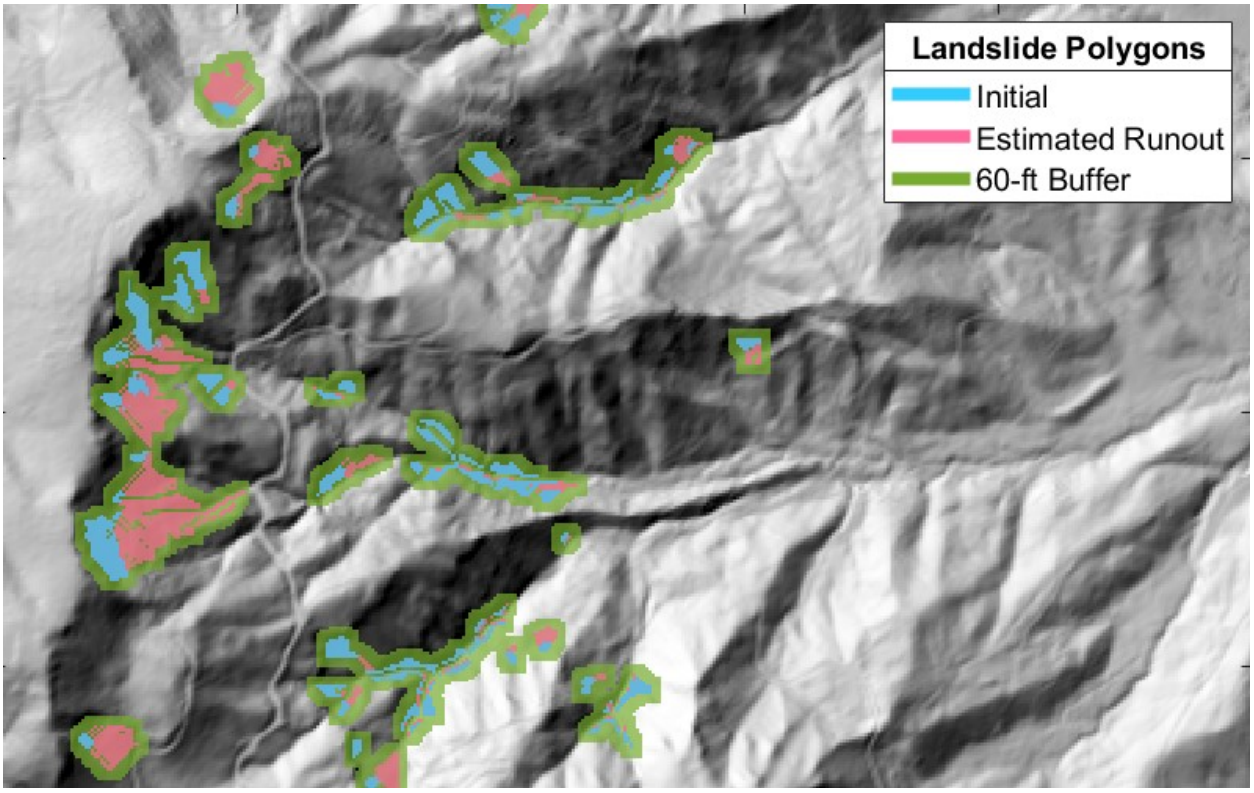

Figure 3.19: Example of landslide shapes, estimated landslide runout, and 60-foot (18.3 m) landslide buffer for a section of OR42 near Gales Creek, OR.

3.10.3 Landslide-Induced Repair Time and Costs on ODOT Right-of-Way

Landslide polygons and their corresponding runouts are superimposed on top of ODOT ROW to identify segments of highway that have been covered by landslide debris. Landslide debris is assigned the mean slope of the superimposed landslide cluster, the length of the covered highway segment is determined, and a prism of soil to be excavated is constructed. As a default repair method, debris is excavated to achieve a cut slope of 45°. Alternatively, a 70° retaining wall may be constructed if the slope of the failed slope exceeds 45°. A cross-sectional schematic of landslide debris is shown in Figure 3.2020. The volume of each debris prism is defined as follows:

$$\boldsymbol{V_{debris} = A_{debris} L_{hwy}} \tag{3-29}$$

Where:

A_{debris} is the cross-sectional area of the debris prism and

L_{hwy} is the length of the affected section of ROW.

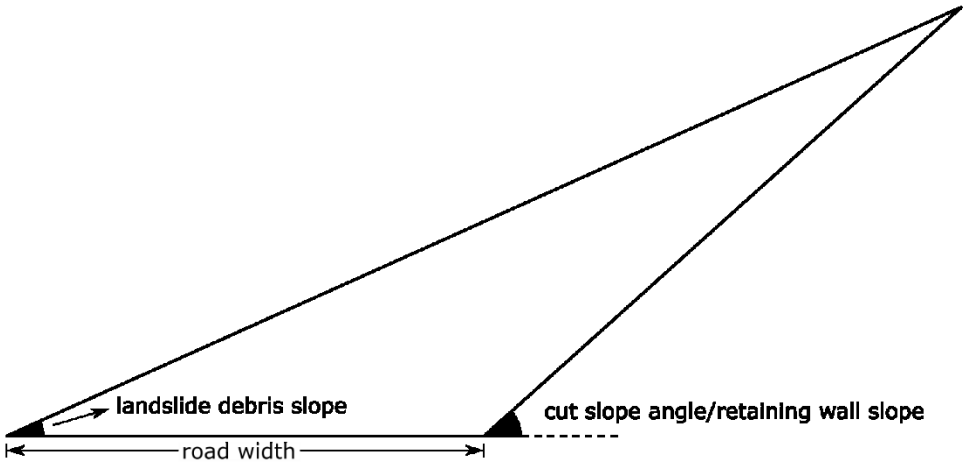

Figure 3.20: Cross-sectional schematic of landslide debris covering road.

Knowing these volumes, estimates of closure times and excavation costs are estimated for each affected segment of ROW. An excavation rate of $R_{ex} = 5000\,\frac{yd^3}{day}$, obtained through personal communication with Curran Mohney (ODOT), is assumed. Note that the rate of construction for a retaining wall is assumed to be included in the above rate of excavation. Closure time for affected segments of ROW is computed as:

$$\boldsymbol{T_{closure} = V_{debris}/R_{ex}} \tag{3-30}$$

Repair costs are obtained from the *Unstable Slopes Database* and construction rates are leveraged from SPR-786 (Table 3.3; Leshchinsky et al., 2018), as well as the 2018 ODOT Bridge Cost Data Sheet for Retaining Walls for 2016-2018 (courtesy of Sophie Brown, ODOT). For segments repaired using a cut slope, an average excavation cost of $C_{ex} = \$14.40/m^3$ is used. For segments requiring a retaining wall, the same cost of excavation is assumed and a retaining wall construction cost of $C_{wall} = \$59.20/ft^2$ is used. This value is the 2016-2018 average cost of a prefabricated modular retaining wall, as reported in the 2018 ODOT Bridge Cost Data Sheet for Retaining Walls. The cost of repair for each affected segment of ODOT ROW is:

$$\boldsymbol{C_{repair}} = \begin{cases} \boldsymbol{V_{debris}C_{ex}}, & \boldsymbol{\text{cut slope repair}} \\ \boldsymbol{V_{debris}C_{ex} + A_{wall}C_{wall}}, & \boldsymbol{\text{retaining wall repair}} \end{cases} \tag{3-31}$$

Where:

A_{wall} is the area of the retaining wall surface.

Table 3.3: Average Costs to Repair Infrastructure Following Landslide Debris Coverage (*Unstable Slopes Database*, SPR-786; Leshchinsky et al., 2018).

ODOT Region	General Excavation (Cost per m^3)	Stone Embankment (Cost per m^3)
1	$22.44	$34.61
2	$10.97	$20.66
3	$15.16	$30.69
4	$11.85	$16.65
5	$9.57	$17.50
Average	$14.40 (~$11.00 per cu. yd.)	$24.02 (~$18.50 per cu. yd.)

3.10.4 Closure Impact on Commodity Flow and Traffic Flow

In addition to the cost of repair, another means of assessing risk associated with landslide occurrence is through associated impacts on commerce and costs of rerouting traffic. Using established models from TPAU, the impact of closure or delay times on commodity flow and traffic flow may be established. For the four corridors assessed in this study, data outputs from TPAU inform daily losses for both eastern and western commodity flow between the Willamette Valley and Coastal Regions of Oregon. Values of daily cost tied to traffic re-routing, composed of additional operating costs and additional time costs, are also supplied. A summary of daily total commodity loss values and average daily costs of traffic rerouting are shown in Table 3.4. To compute the total costs associated with closure, all closure times along a given corridor are summed and that value is multiplied by the appropriate daily cost. Complete TPAU model outputs for SPR808, containing breakdowns of specific commodities and ranges of costs, can be found in the digital appendix.

Table 3.4: TPAU Generated Average Daily Costs of Commodity Flow Loss and Traffic Rerouting Expenses used in this Study.

Daily Total Commodity Flow Loss (USD)							
US30		**OR06**		**US20**		**OR42**	
Eastward	Westward	Eastward	Westward	Eastward	Westward	Eastward	Westward
$916,434	$1,374,117	$410,389	$558,468	$690,750	$693,986	$1,259,124	$1,592,548
Average Daily Cost of Traffic Rerouting (USD)							
$223,509		$109,658		$186,847		$125,582	

4.0 RESULTS

This section begins with an analysis of the 2019 displacement surge of the Hooskanaden landslide and a possible explanation for those movements. Then, the modified age-roughness curve for the Pacific Northwest and its related data is presented. From there, maps of SLIDO inventoried landslides identified to be seismically-driven are presented, along with forensically-produced strength distributions for the corridors analyzed herein. Using those strength distributions, a suite of susceptibility maps are generated, which are then used to produce hazard maps and a suite of course risk metrics, such as: maps of ODOT ROW closure, estimated closure times and repair costs for each corridor subjected to a variety of physical drivers, and estimates of commodity loss and rerouting costs as informed by TPAU data. Finally, the effects of climate change, and resulting increases in storm-induced precipitation are presented using maps of insipient failures and comparisons in susceptibility.

Susceptibility, hazard, and risk methodologies are applied to four corridors of ODOT ROW, with various climatic, hydrological, and seismic conditions applied. The following results demonstrate the varying spatial distributions and magnitudes of landslide failures associated with each unique combination of corridors and input parameters. Note that all maps in Sections 4.2-5.0 and Appendices A-D are in the NAD83/Oregon North projection (EPSG: 32126). A list of susceptibility scenarios analyzed in this study, without climate anomaly applied, is shown in Table 4.4. A list of additional scenarios considering climate change is shown in Table 4.7. Note that many of the data shown in this section are available for use and further examination in the digital appendix.

4.1 HOOSKANADEN LANDSLIDE ANALYSIS

To provide context for understanding the 2019 surge of the Hooskanaden landslide, we dated multiple samples of woody material exposed in the landslide's toe and constructed a time series of landslide displacements from manual feature tracking on 3 m resolution, orthorectified and georeferenced commercial satellite photos available from Planet Labs (planet.com) (2009-2019) and repeat terrestrial lidar scans (summer 2019). The displacement time series was compared to a precipitation time series covering the same time period and derived from weather station data near Brookings, approximately 20 km south of the landslide, archived on MesoWest (mesowest.utah.edu). We also provide an interpretation of subsurface stratigraphy and stability analysis of a field-developed cross section to better understand the landslide's surge behavior. Further description of the kinematics of the Hooskanaden surge event may be found in Alberti et al. (2020).

4.1.1 Stratigraphic Interpretation of Drill Log

To characterize subsurface properties of the Hooskanaden landslide, we developed a stratigraphic column from drill logs from the borehole used for the piezometer and inclinometer installation (Figure 4.1). The subsurface lithology here is predominately sandstone and mudstone

with highly sheared sections and slickenside surfaces beginning around 20 m depth. Based on the geologic background of this area it is reasonable to assume that this is representative of the source material for the Hooskanaden Landslide.

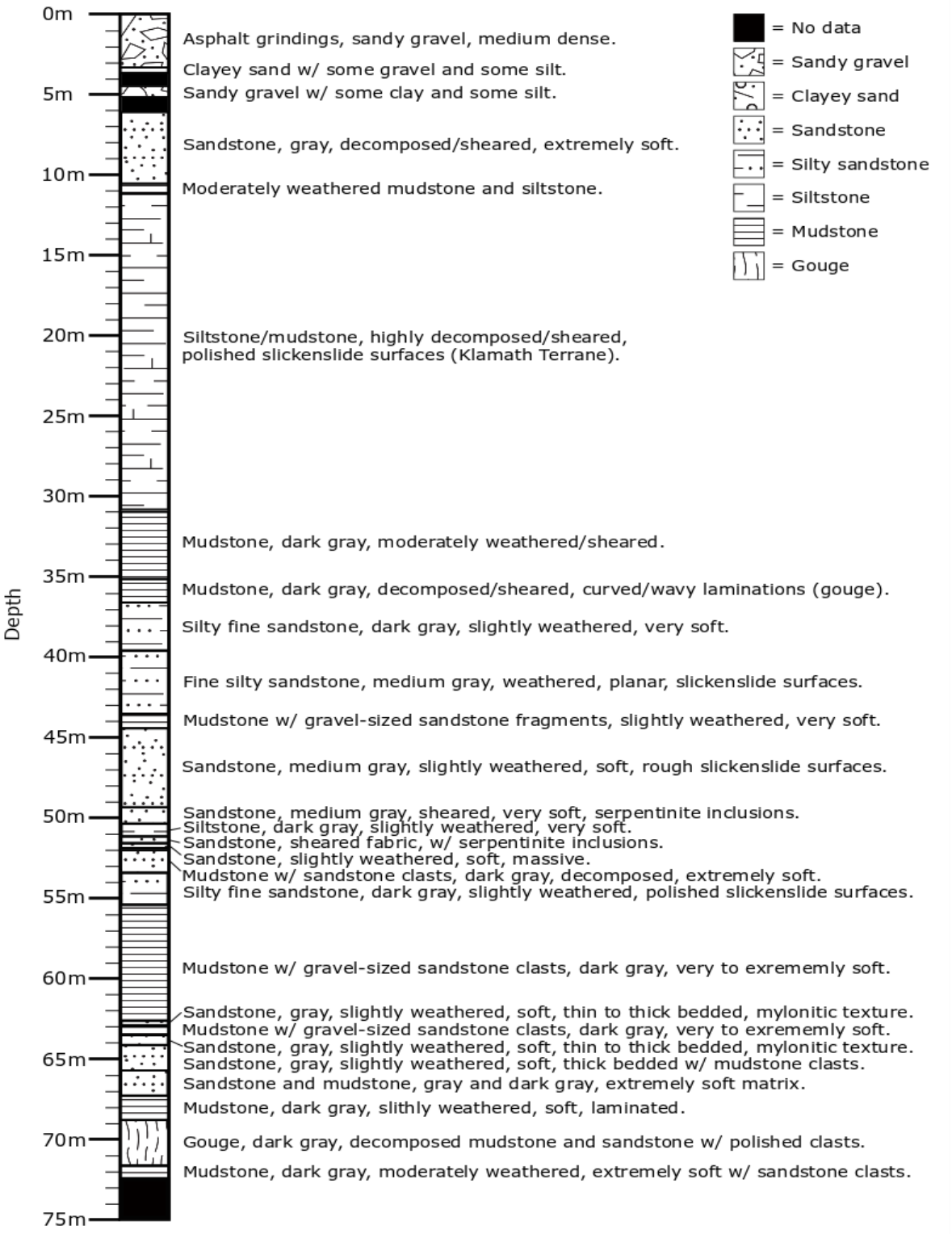

Figure 4.1: Stratigraphic column based on mud rotary drill log (after Alberti et al., 2020).

4.1.2 Field-Developed Cross-Section and Stability Analysis

Surface mapping efforts (Figure 4.2) were performed in late September of 2019, seven months following the most recent surge. Within the upper half of the slide (upslope from US101), the ground was still highly deformed and fractured in many sections, while other sections were still vegetated and showed little sign of ground disturbance (Figure 4.3). Additionally, there was a great deal of standing water found on the surface of the slide, despite being mapped at the end of the dry season. Figure 4.4 shows water continuously draining from a culvert that was installed beneath US101 when it was rebuilt following the last surge. While the presence of standing water was prevalent in both the upper and lower sections of the slide deposit, a particularly large sag pond (~100 by ~160 m) was observed just upslope of the uplifted slide toe (Figure 4.2). There is evidence of gullying along both lateral margins, although this was much more heavily observed along the southeastern margin.

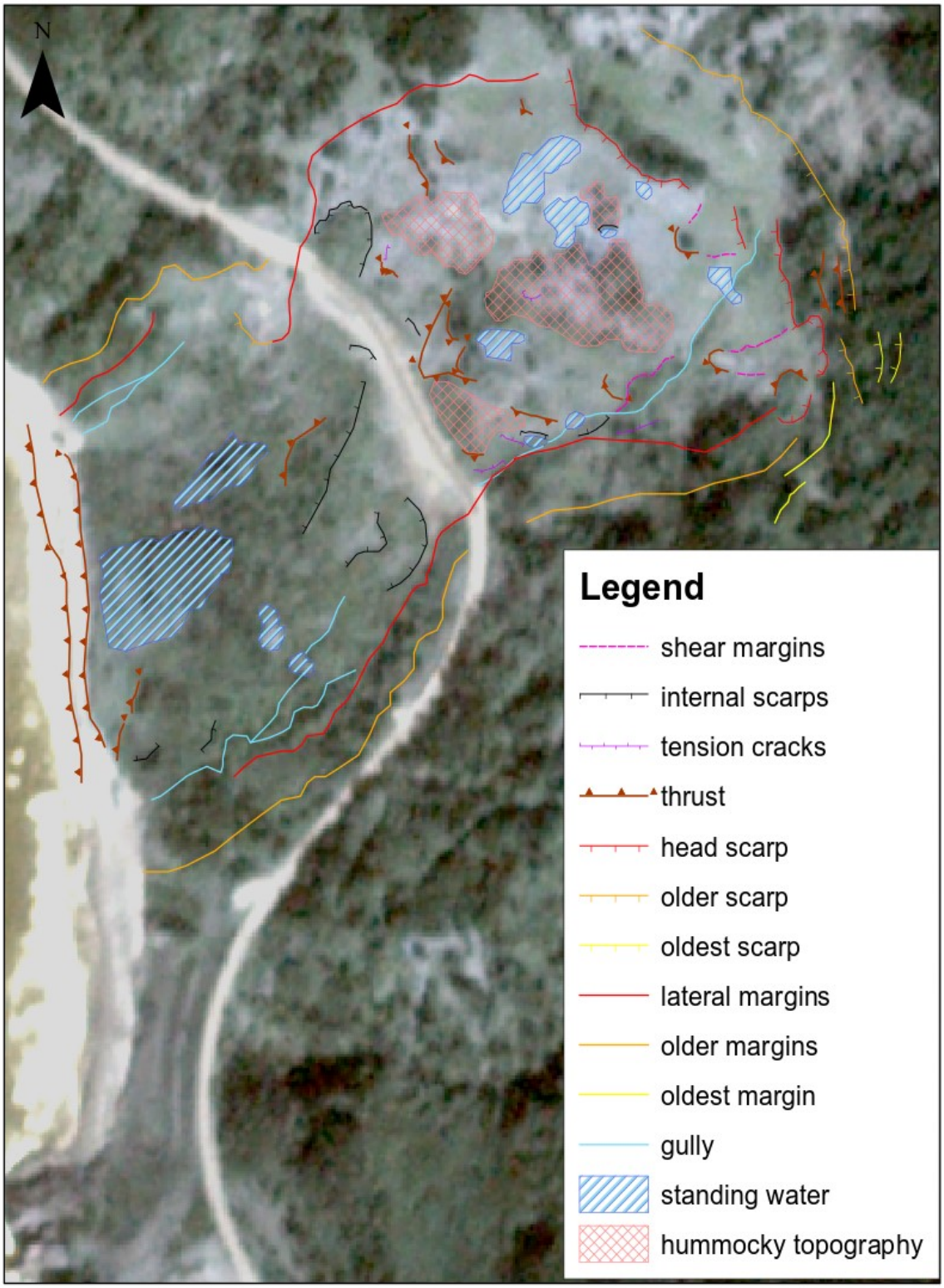

Figure 4.2: Map of surface features derived from field observations, overlying satellite image from Planet Labs taken September 21st, 2019 (after Alberti et al., 2020).

Hiking upslope revealed several discontinuous head scarps, likely related to the most recent surge event, as well as much more subdued scarp like features further upslope (Figure 4.2). Similarly, highly pronounced, angular shear margins were observed along the NW and SE flanks of the slide deposit, with more diffuse shear margins further out. The ground surface was heavily disturbed across the majority of the slide surface, with large, fractured, brittlely-deformed blocks, as well as deposits that suggested a softer composition with more internal deformation (mapped in Figure 4.2 as hummocky topography). Several internal scarps were also observed, bounding both brittle and soft-sedimentary failures, and predominately striking NNE in the lower half of the slide. Tension cracks were found only in the upper slide section along the southeast margin. Thrust features were found throughout the surface of the slide mass, most of which strike ~NW. The largest of these were observed at the toe of the landslide, which appeared to uplift and override a portion of the pre-existing beach on the wave-cut platform. This is consistent with observations made by Alberti et al. (2020), who site an apparent uplift as well as clockwise rotation of the toe during the most recent surge.

Figure 4.3: Image showing preserved evidence of ground deformation along the surface of the Hooskanaden Landslide (looking in downslope direction) in the late summer of 2019.

Figure 4.4: Image showing continuous drainage from a culvert installed beneath the newly reconstructed section of US Highway 101, taken in the late summer of 2019.

Field-developed cross-sections (locations shown in Figure 4.5), elevation data obtained from lidar, borehole data, mapped surface features, and locations where standing water was found were combined to generate a slope stability model using SLIDE (Figure 4.6). This model was calibrated to achieve a factor of safety (FOS) as close as possible to 1 (FOS = 1.006). The basal morphology of the slide mass (yellow) was constrained using the location and dip of the head scarp, the location of the failure surface observed at the toe, and the location of the borehole and depth to the failure surface. This does not appear to match the semi-circular failure plane morphology typically observed with larger landslides. Depth to the failure plane is greatest in the upper section and decreases in the mid-section (just above the highway), then it increases again before reaching the toe. The geometry of the water table (blue line) was constrained based on locations where standing water was observed on the landslide surface. Despite being mapped at the end of the summer, the water table still appears to be very close to the surface of the slide deposit and the surrounding topography.

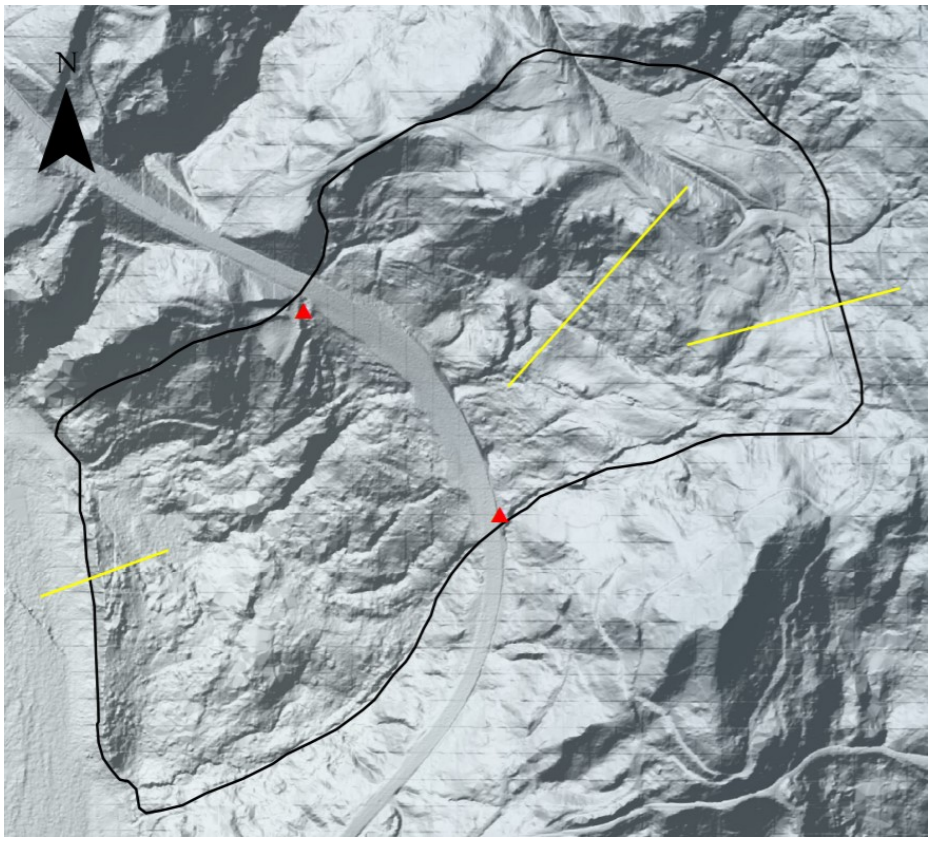

Figure 4.5: Locations of TLS data collection (red triangles), and field developed cross-sections (yellow lines), overlying 2015 lidar and hillshade derivative.

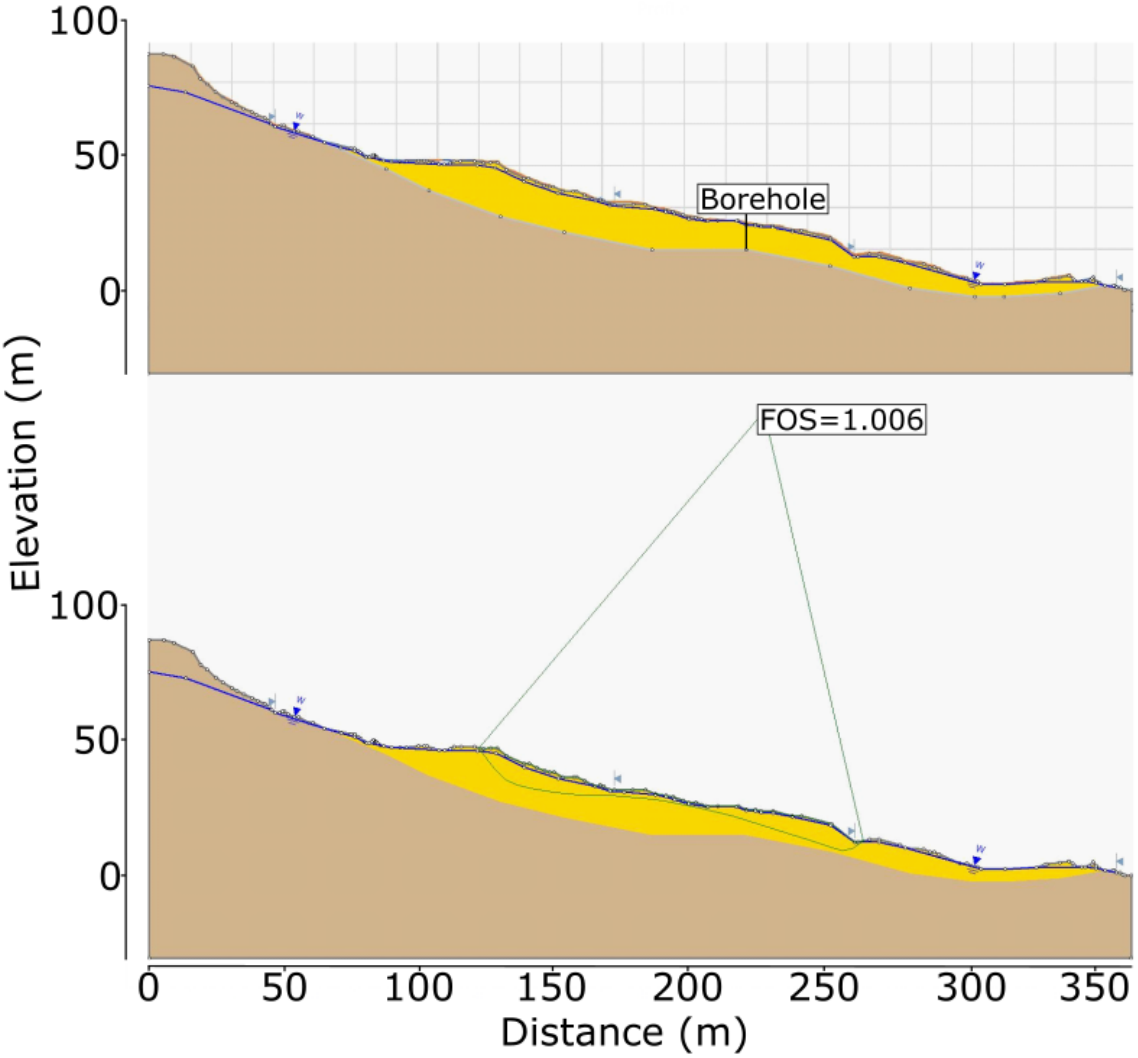

Figure 4.6: Profile of the Hooskanaden Landslide generated using SLIDE. The yellow area represents the slide material above the failure plane, the brown area represents the bedrock below the failure plane. The geometry of the water table is indicated by the blue line.

4.1.3 Landslide Kinematics at Seasonal to Annual Timescales

Feature tracking results from satellite photos covering the period 2009-2019 are displayed as both a displacement time series (Figure 4.7), and a velocity time series (Figure 4.7) to demonstrate the effects of normalizing displacements by the length of time between images. Maximum displacement or velocity refers to the single feature on the landslide's surface that moved the most in a given time period, and average displacement or velocity refers to the mean of all features that were tracked during a time period. There is an apparent baseline velocity of ~ 0.03 m/day within the average velocity data, though in many cases the minimum detectable distance (MDD) was higher than this (0.096 ± 0.063 m), suggesting that the apparent background rate may be due to noise in the images. Within the maximum velocity data, the baseline is closer to ~0.13 m/day, which exceeds the MDD. The highest maximum and average velocities occur in

December of 2016 (1.19 and 0.33 m/day respectively over a 17-day period), and February to March of 2019 (2.23 and 1.06 m/day respectively over an 18-day period).

Figure 4.7: Displacement (top), velocity (middle), and precipitation (bottom) time series. Displacement and velocity time series were derived by manual feature tracking on repeat satellite optical imagery collected by Planet Labs (planet.com), and the precipitation time series was derived from weather station data available on MesoWest (mesowest.utah.edu).

To independently check the satellite photo-derived velocities and document higher resolution displacement patterns, we acquired a series of terrestrial laser scans over summer 2019 (locations in Figure 4.5). The accuracy achieved in aligning TLS point clouds is shown in Table 4.1. Each

scan was assigned a TLS ID, with the first four numbers indicating the date of the scan, and the final number indicating the scan location (1 or 2). Rows and columns are labelled with TLS IDs, and the numbers at the intersections of rows and columns are the root-mean-square error (RMSE) resulting from the alignment of the stable portion of those two scans (reported in meters). In all cases, the accuracy achieved was within a few cm, 6.5 cm at most.

Table 4.1: Root-mean-square error (RMSE) reported during stable-ground alignment of terrestrial laser scans (TLS) in CloudCompare. Each TLS ID (Date_#) is shown as both a row and a column, the numbers at the intersections of each row and column show the RMSE (in m) for the alignment of those two clouds.

	06.08_1	**06.08_2**	**08.17_1**	**08.17_2**	**09.21_1**	**09.21_2**
06.08_1			0.02036		0.042253	
06.08_2				0.065649		0.02143
08.17_1	0.02036				0.016134	
08.17_2		0.065649				0.048953
09.21_1	0.042253		0.016134			
09.21_2		0.02143		0.048953		

Figure 4.8 shows the results of calculating distances between point clouds from scan locations TLS 1 (left column) and TLS 2 (right column). All distances are shown as absolute values, with a maximum distance of 10 m, and warmer colors representing greater distances. For all three time periods (June to August, August to September, and June to September, from top to bottom), there appears to be very little visible movement over the majority of the landslide surface. Average displacements are 0.001, 0.004, and 0.001 m respectively, which is less than the RMSE. From TLS 1 however, while the period from June to August still appears to be relatively inactive (average displacement of 0.009 m), from both August to September, and June to September, we can clearly see that movement has occurred (average displacements of 0.022 and 0.13 m respectively). This movement includes approximately 1 m of displacement near the northern margin of the landslide (Figure 4.8b-c).

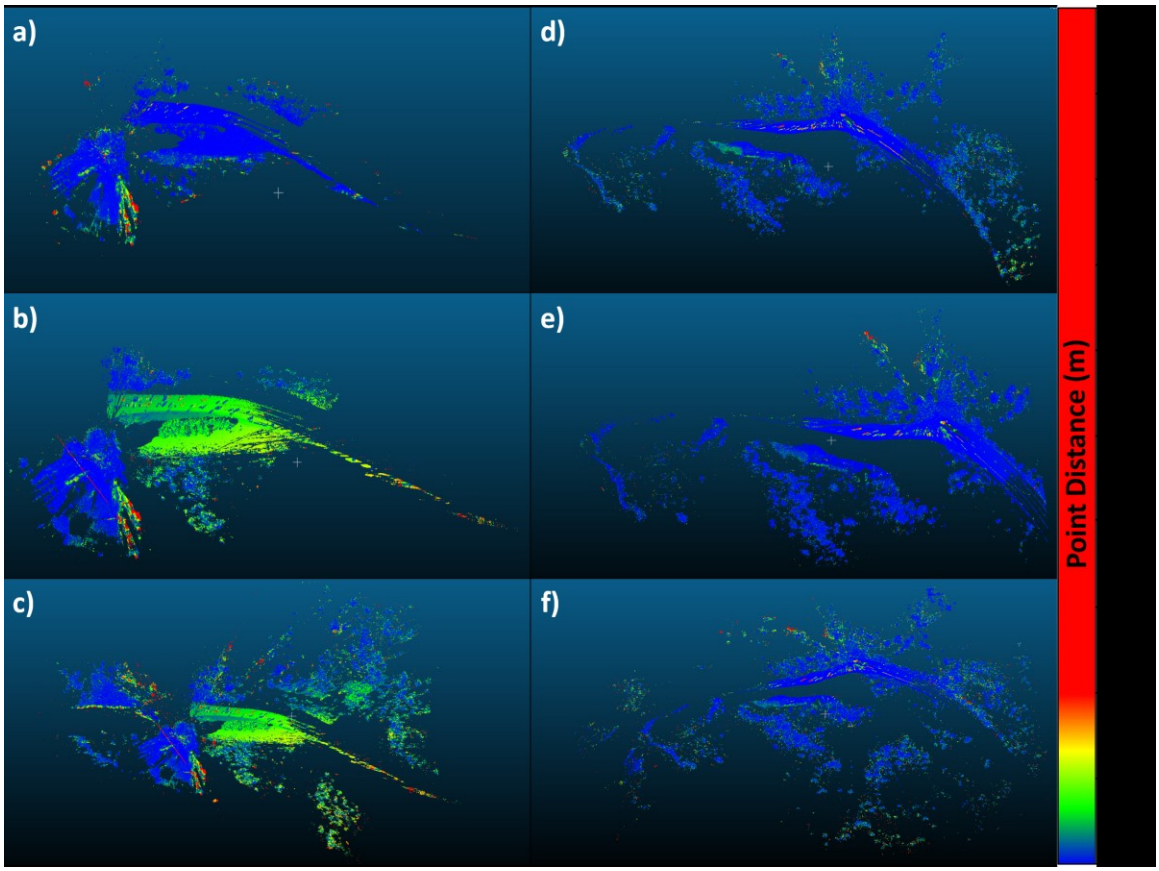

Figure 4.8: Distances between point clouds computed in CloudCompare using a least squares plane local model. Showing results for 06.08_1 to 08.17_1 (a), 08.17_1 to 09.21_1 (b), and 06.08_1 to 09.21_1 (c); as well as 06.08_3 to 08.17_3 (d), 08.17_3 to 09.21_3 (e), and 06.08_3 to 09.21_3 (f).

There does appear to be a correlation between increased precipitation recorded at Brookings (archived on MesoWest) and increased surface movement on the Hooskanaden Landslide, although the specific metric used to quantify precipitation is important (Figure 4.9). Both significant precipitation and increased displacement were recorded during January, and November of 2012, December of 2015, December of 2016, and February of 2019, which are known surge dates. Increased velocity was also shown during December of 2016 and February of 2019. However, there were other significant precipitation events (April of 2011, February, October, and December of 2014, October of 2016, February of 2017, and April of 2019) that did not appear to coincide with or directly precede an increase in either displacement or velocity.

During the most recent surge, higher velocities are observed in the mid-section of the slide nearest the highway, but particularly along the southeast margin in that section. If gullying activity is any indication, this appears to match the direction of groundwater flow (which appears to flow more north to south than the overall northeast to southwest motion of the earthflow).

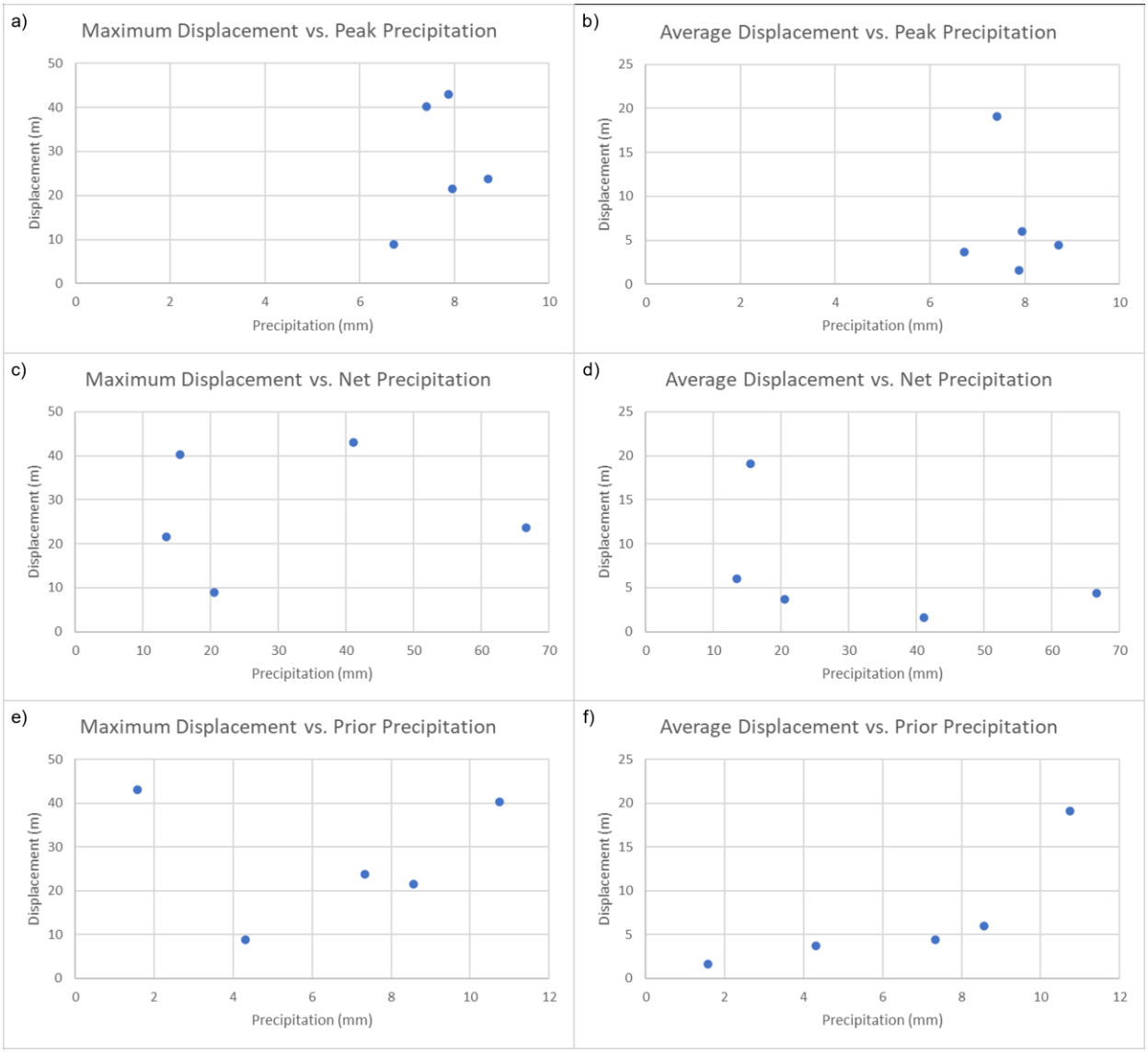

Figure 4.9: Displacement vs. precipitation for 6 different precipitation metrics. Displacement does not significantly correlate with most of the precipitation metrics (a-e), but does increase significantly and nonlinearly with prior precipitation, suggesting that long periods of above average precipitation prime the landslide for surges with greater displacements.

4.1.4 Century Timescales – 14C Analyses

In order to obtain an understanding of the earlier part of the Hooskanaden Landslide's life cycle, several samples were collected for radiocarbon (^{14}C) dating. These were taken from logs found preserved within the stratigraphy of the eroding toe, along the beach just below the earthflow (to the west). Using a chainsaw, rounds were cut from these logs, perpendicular to growth, in order to preserve the growth rings. From six total samples, three were initially selected for dating – HEF-0609-3 (43º13'03"N 124º22'36"W), HEF-0609-5 (43º13'08"N 124º22'37"W), and HEF-0609-6 (43º12'57"N 124º22'36"W) – based on their relative stratigraphy. Material from the

outermost growth ring, beneath the bark was submitted for each of the three selected samples to DirectAMS for ^{14}C analysis, in order to obtain the age closest to the time of tree death (Panek, 2015).

Initial results provided by DirectAMS for these samples were calibrated using OxCal (version 4.3) and the IntCal 13 atmospheric curve, to obtain an approximate calendar age for each of the samples. Within this calibration, the relative stratigraphy of the samples was also taken into account (assuming that older samples would be lower in the stratigraphy). By using the relative ages of these samples in the calibration model, we were able to better constrain the resulting possible calendar ages.

Based on the results of the stratigraphic calibration model, one of the initial three tree rounds was selected for further ^{14}C analysis (HEF-0609-6), using the preserved growth rings. By submitting multiple samples from the same tree, from specific growth rings that are a known number of years apart, it is possible to further constrain which part of the carbon calibration curve samples plot within; thereby eliminating some of the possible ages obtained during calibration.

This sample was highly weathered, and badly eroded on one side, making it difficult to determine the number of growth rings preserved. To prepare the sample, after sanding one side smooth, two transects were taken from the center of growth to the outermost edge. The locations of these transects were chosen to avoid fungal growth (and possible contamination), and to include the highest possible number of growth rings (furthest distance from the center of growth). Then each growth ring was counted and marked along the full length of each transect (Figure 4.10). Transect A had a total of 53 growth rings, while transect B had a total of 62 growth rings.

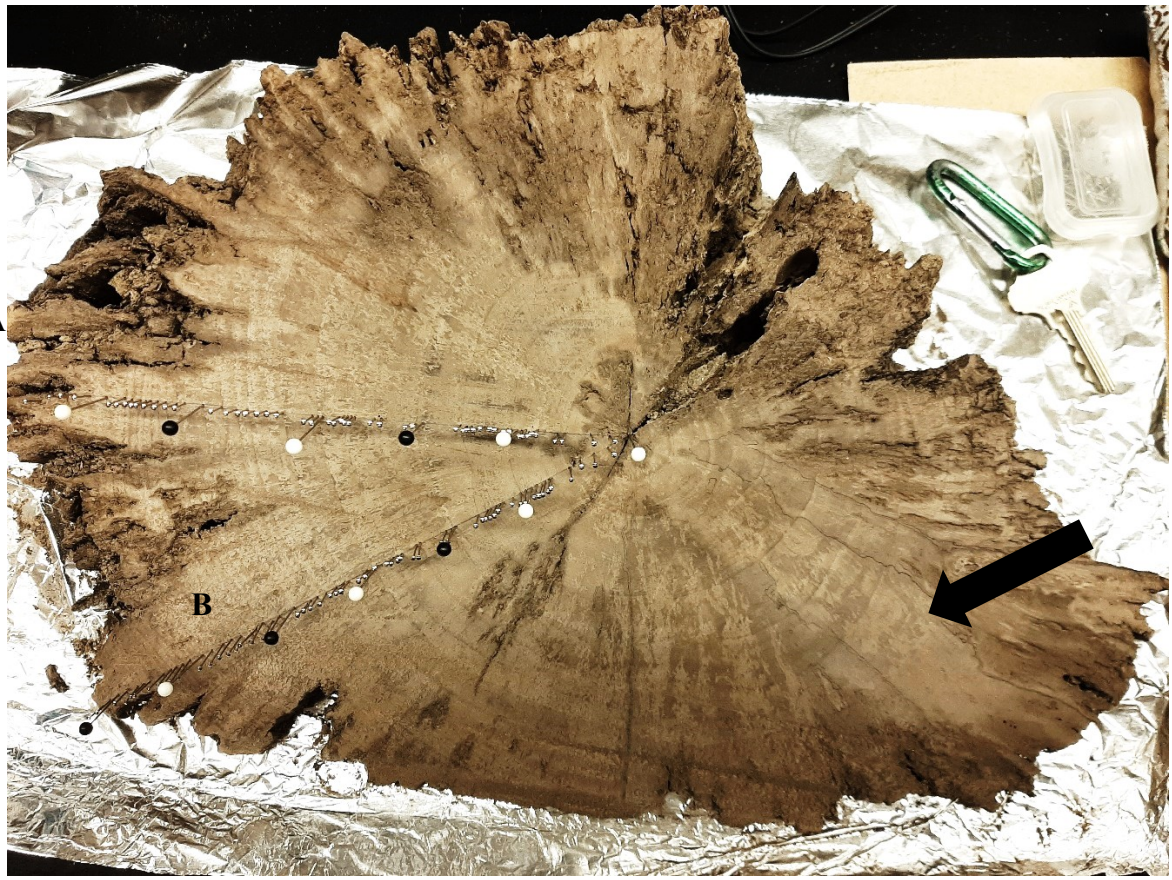

Figure 4.10: Tree round HEF-0609-6. Transects A and B are labelled, and growth rings counted along transects are marked with pins. Silver pins represent one ring, white pins represent 10 rings, and black pins represent 20 rings. The black arrow shows the location of a black fungal growth, which extends from the center of tree growth radially outward.

Prior to collecting any further sample material, sample HEF-0609-6 was examined by a biologist (Dr. Daniel Ballhorn, of the Ballhorn Chemical Ecology Lab at Portland State University) to determine more about the particular tree species. Dr. Ballhorn was able to identify this as a species of poplar (more specifically, *Populus trichocarpa*). This species has radially symmetrical growth rings under normal growth conditions, and can live up to around 200 years (DeBell, 1990). Additionally, Dr. Ballhorn identified some black fungal growth, growing perpendicular to the growth rings (indicated by the black arrow in Figure 4.10). This type of fungal growth is common in poplars, and typically persists only within the woody portion of the tree – not extending into the bark. Because this fungal growth, where present, extends all the way to the outer edge of the sample, it is unlikely that this sample has any bark left on it (and what was initially interpreted as bark, is likely just highly desiccated wood). Therefore, we cannot be certain that the outermost growth ring on this sample is the original outermost growth ring that was present at the time of tree death. Because this tree species can live up to 200 years, and there were 62 growth rings counted along transect B, it is possible that the outermost growth ring of the sample is younger than the original outermost growth ring of the tree. Therefore, the date of

the outermost growth ring submitted from the sample will be assumed to represent the minimum calendar date (or maximum geologic age) of tree death within 138 years.

For analysis, material was collected along transects A and B, from the outermost growth ring (HEF-0609-6-0), innermost growth ring (HEF-0609-6-62), and two additional intermittent growth rings (HEF-0609-6-15, and HEF-0609-6-38 respectively). The locations of the additional two samples were selected based on their assumed location on the carbon calibration curve (to reduce the number of possible calendar age results – referred to as "wiggle matching"), and growth ring thickness (thicker growth rings reduce the possibility of contaminating the sample by accidentally including material from adjacent growth rings). These four samples were then submitted to the National Ocean Sciences Accelerator Mass Spectrometry (NOSAMS) lab, at the Woods Hole Oceanographic Institution. This lab was selected to process our second set of samples, because they allow for processing with ^{13}C splits, which allows for less uncertainty. Initial results provided by NOSAMS were then calibrated using both a dendrochronological model (D_Seq) and a varve model (V_Seq) within OxCal, thus providing both a preferred and alternate model to best estimate the time of tree death.

It should be noted that there is some uncertainty regarding the meaning of these ^{14}C ages relative to the age of the earthflow. When dating landslides in general, the age of the outermost growth ring of an entrained wood sample is commonly accepted to be a close maximum age for landslide initiation (Panek, 2015). However, we are attempting to date a feature that has been consistently active (rather than an instantaneous failure) since at least the 1950s, which adds more uncertainty. Assuming that these samples were entrained upon initiation, and that they were still living immediately prior to being entrained, then their age represents the true age of the earthflow. However, if they were entrained during a subsequent period of movement sometime after initiation, they will still provide us with a minimum age. In contrast, if samples were collected from trees which were already dead upon initiation and entrainment, they will give an artificially old estimated age for Hooskanaden Landslide initiation. All of these possibilities will need to be considered when analyzing the calibrated ages.

The results from all radiocarbon calibration models are reported in Alberti et al. (2020). Overall, reported radiocarbon ages for all samples are between 43 and 170 yr BP. Age errors (σ) were all within 15 and 32 years. Samples HEF-0609-3, HEF-0609-5, and HEF-0609-6 were calibrated using a stratigraphic model. The oldest of these (HEF-0609-6) has the broadest range of possible calibrated ages, with calendar dates extending from about 1665 to 1875 AD. The middle sample (HEF-0609-5) has a range of possible calendar dates from about 1695 to 1920 AD. The final and youngest sample has the tightest range, and representing a likely date of approximately 1900 AD.

The second set of samples (HEF-0609-6-0, HEF-0609-6-15, HEF-0609-6-38, and HEF-0609-6-62) were calibrated using both the D_Seq and V_Seq models. These were all taken from the original sample HEF-0609-6, which was the oldest of the original sample set. Additionally, given the range of possible ages, it seemed likely to calibrate near ~1700 AD – the time of the most recent Cascadia earthquake. This suggested the need for more precise dating, using dendrochronology and 13C splits. Sample HEF-0609-6-0 was taken from the outermost growth ring, and HEF-0609-6-62 was taken from the innermost growth ring (62 rings in from the outermost ring).

In the D_Seq model, the model failed to include sample HEF-0609-6-15, as its predicted age was outside the range of possible ages given the dendrological constraints used. This model predicts roughly three possible age ranges for the outermost growth ring – one (with the highest probability of accuracy) from ~1730-1775 AD, another from ~1855-1875 AD, and a final from ~1925-1955 AD. The V_Seq model also predicts three possible age ranges for the outermost growth ring of my oldest sample – one from ~1740-1780 AD, another from ~1855-1880 AD, and the most probable one from ~1925-1955 AD.

Based on the results of both the D_Seq and the V_Seq models, the Hooskanaden Landslide appears to have initiated sometime between ~1750 and ~1940 AD – with the earlier end preferred by the D_Seq model, and the latter end preferred by the V_Seq model. Both models place the initiation of the Hooskanaden Landslide after the most recent Cascadia earthquake. However, the implications of these findings and their associated assumptions are worthy of further exploration.

The latter two models provided quite different most probable ages – one slightly younger than the most recent Cascadia earthquake (~1750 AD), and one much more modern (~1940 AD). The first of these was the D_Seq model, which did not allow for error to be included in the number of years between samples. As mentioned in Results, this model failed to include sample HEF-0609-6-15 based on the dendrological constraints, suggesting that there is likely error in the number of years between HEF-0609-6-0 and HEF-0609-6-15 (counted as 15 rings from the outermost growth ring), or HEF-0609-6-15 and HEF-0609-6-38 (counted as 23 growth rings). This could mean either that these growth rings were miscounted, or that extraneous material from adjacent rings was accidentally included in sample HEF-0609-6-15 prior to submission for analysis by NOSAMS. This seems to imply that the preferred model – which both allows for the possibility of error and successfully models all samples with the given constraints – but an age of ~1940 AD for the initiation of a landslide of this size seems unlikely.

First, because there would almost certainly be record of an event of that size from that time. ODOT has records on the Hooskanaden Landslide going back to 1958, when US101 was relocated to its current position, but they do not indicate how recently the slide deposit was active. Second, even if the most recent Cascadia earthquake did not cause immediate failure, it is possible that coseismic dynamic stress could have permanently damaged the basal surface (Carey et al., 2019), leaving it more susceptible to future failure. For these reasons, it seems more likely that a susceptible landmass would fail a few decades following a major seismic episode, rather than failing seemingly spontaneously two and a half centuries later. Since a modeled, calibrated age of ~1750 AD (270 years before 2020 AD) for the landslide is the only age consistent with the stratigraphic interpretation, the dedrochronologic model, and the varve model, we interpret that age as the most likely minimum age of the landslide.

It is also necessary to address what this possible age actually represents. Assuming that the oldest sample was entrained upon initiation (suggesting that no older representative samples exist), and that it was still living when entrained, the age of this sample represents the true age of the earthflow. The presence of an older representative sample seems unlikely, given that HEF-0609-6 was taken from the lowest visible stratigraphic unit identified as a failure plane. However, if this landslide failed below present sea-level, this possible lower stratigraphic failure plane would not be visible. It is possible however, that this sample was entrained after initiation, suggesting

that the modelled age provided in this study is artificially young for the age of the Hooskanaden Landslide. Another possibility is that sample HEF-0609-6 was collected from a tree which was already dead upon initiation and entrainment, which would also give an artificially old estimated age for Hooskanaden Landslide initiation.

In addition to providing specific age information about the Hooskanaden landslide itself, this radiocarbon dating campaign informed our interpretations of radiocarbon dates of wood samples from landslides in northwest Oregon, which were used to define the Pacific Northwest age-roughness model described in Section 4.2 below. Specifically, the Hooskanaden dating campaign highlighted the need to locate samples from the lowest stratigraphic levels of a landslide deposit possible to best constrain its minimum age and the need to use ancillary information about landslide age, if available, to interpret young radiocarbon ages, where the calibration of radiocarbon years to calendar years is ambiguous.

4.2 MODIFICATION OF AGE-ROUGHNESS RELATIONSHIP FOR THE PACIFIC NORTHWEST

4.2.1 Pacific Northwest Landslide Age-Roughness Model

To define the age-roughness model used to predict ages of paleo deep-seated landslides along highway corridors in the Oregon Coast Range (OCR), we combined a literature search for existing landslide dates in the region with acquisition of new dates in northwestern Oregon. Although analysis of the Hooskanaden landslide informed our interpretation of radiocarbon ages for these landslides, we did not include the Hooskanaden landslide in the age-roughness model because its long history of repeated surging obscured a direct relationship between its age and its surface roughness expression. Instead, we focused our dating campaign on identifying landslides that filled age gaps in previous work carried out in the Puget Lowlands of Washington (LaHusen et al., 2016; Booth et al., 2017). Unlike the OCR, that region was previously glaciated, such that the geomorphic record of landslides there is no older than ~16,000 kyr B.P., while the geomorphic record of landslides in the OCR is much longer. Another age gap in the previous age-roughness studies is landslides from roughly 1-5 kyr B.P. We analyzed landslides along the US 20 corridor, several of which have been previously radiocarbon dated by ODOT, to address the older age gap, and we conducted fieldwork in the northwestern OCR to date landslides that we deemed likely, based on their topographic expression, to fill in the younger age gap. In addition, we incorporated landslide dates from complementary work in the central OCR (LaHusen et al., 2020) that was in progress while this research (SPR808) was being carried out. Below, we detail results of the US 20 landslide analysis, then present our new dates from the northwestern OCR, and report the final Pacific Northwest age-roughness model. We then use the age-roughness model to identify bounds on the surface roughness of landslides that are consistent with the last Cascadia Subduction Zone (CSZ) earthquake in A.D. 1700 (250 cal. B.P.) and landslides that are likely to be younger and therefore triggered by climatic events.

In this report, ages are given in units of cal. B.P., which is defined as calibrated years before present, or in units of radiocarbon yrs B.P. Radiocarbon years before present were converted to cal. B.P. using the OxCal program and the IntCal 13 calibration curve (Ramsey, 2009). In this system, present is assumed to be A.D. 1950, so any landslides that occurred more recently were

assigned an age of 1 cal. B.P., which did not significantly affect the age-roughness model results, but allowed analysis of log-transformed ages.

4.2.1.1 ***US20 Landslides***

Radiocarbon dates for large, bedrock landslides were previously acquired by ODOT during construction of the US 20 realignment west of Eddyville, Oregon. Those dates were produced from samples of the outer growth rings of logs that were previously buried by landslides and subsequently unearthed by excavation or drilling. We relied on age data from internal ODOT documents provided by Nicholas R. Testa as well as a publicly available Geological Society of America field guide (Hammond et al., 2009). Several dates exceeded the range of the radiocarbon dating technique and provided only minimum ages for landslides, which was not sufficient information to use those ages to define the age-roughness model, although those ages were consistent with the model. However, five dates from four landslides were within the range of radiocarbon dating: the Cougar Creek landslide and three landslides near Eddyville named Eddy Creek B, C, and D (Figure 4.11). The only date from the Crystal Creek landslide provided a minimum age.

The Cougar Creek landslide complex consists of two main deep-seated landslides, and one sample excavated from the western margin of the easternmost landslide's toe (Figure 4.11) provided an age of 38.83 ± 0.86 radiocarbon kyr B.P. We assigned this age to the eastern landslide of the complex and analyzed just that part of the complex for surface roughness (described subsequently).

For Eddy Creek B, one sample from a borehole near the eastern shear margin of the landslide provided an age of 36.85 ± 0.38 radiocarbon kyr B.P. As this was the only date acquired for this landslide, we used it for that landslide in the age-roughness model.

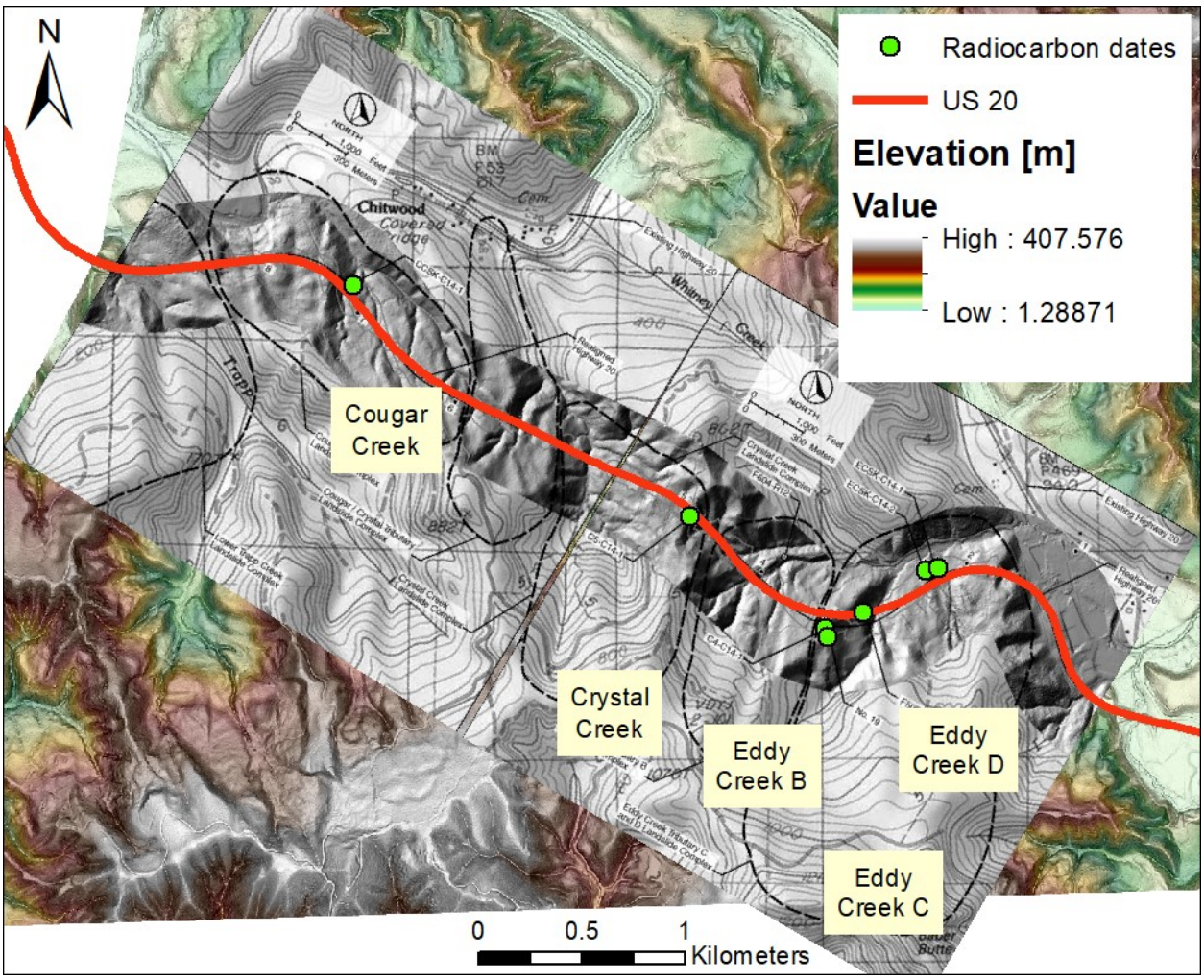

Figure 4.11: Context map for the US 20 Landslides used to define the age-roughness model. Background is a lidar-derived slope map colored by elevation, and overlain maps with paleo landslide outlines are from Hammond et al. (2009).

Eddy Creek C and D occur next to one another in a landslide complex, with the relatively older Eddy Creek C to the southwest of the relatively younger Eddy Creek D (Figure 4.11). Five dates came from samples collected from a road cut and borehole on the western margin of Eddy Creek C: >64.9, >63.9, >46.4, >40, and 40.92 ± 0.57 radiocarbon kyr B.P. Since these ages span at least 25 kyr, we interpret that the landslide has experienced multiple episodes of past movement, perhaps on failure planes at different depths, in order to bury trees with such a wide range of ages. We further interpret that the surface morphology of the landslide likely represents its most recent period of movement that was sufficient to generate topographic features such as hummocks and internal scarps or depressions, and therefore assign the only one of the five ages that is not a minimum age to this landslide for the age-roughness model. Two samples came from excavation of the toe of Eddy Creek D with ages of 17.85 ± 0.1 and 29.82 ± 0.1 radiocarbon kyr B.P. We used both these ages to define the age-roughness model. While assigning the radiocarbon ages to specific parts of the larger landslide complexes, as in the case of Eddy Creek C and D, requires some interpretation, our choices are supported by relative age

relationships. Eddy Creek D clearly cross-cuts Eddy Creek C and is therefore younger, which is consistent with all available radiocarbon dates.

In this study, we defined surface roughness as the standard deviation of slope in a 15 m moving window. There are many alternative definitions of surface roughness, but we chose this definition because it provided as good a fit to the age data as other more complex methods and is straightforward to calculate in standard GIS software. To ensure that the signal of smoothing of the landslide deposit with time is isolated from other natural and human processes, such as gully incision and road building, respectively, landslide deposits must be mapped with buffers around such features. Our procedure for quantifying the roughness of each landslide deposit, using the US 20 landslides as an example, was as follows:

1. Calculate slope from a 3 ft (0.9 m) lidar-derived bare earth digital elevation model (DEM). Slope is defined as the inverse tangent of the magnitude of the topographic gradient and is in units of degrees. In ArcGIS, this is computed with the *Slope* tool in the *Spatial Analyst* toolbox.

2. At each point in the DEM, calculate the standard deviation of the slope values within a 15 m diameter window centered on that point. We refer to the output as the roughness of each pixel in the DEM, and it also has units of degrees. In ArcGIS, this is computed with the *Focal Statistics* tool in the *Spatial Analyst* toolbox. Figure 4.12 is an example of a roughness map for the US 20 landslide area.

3. Determine the average roughness value within each landslide polygon. Polygons need to outline only the landslide deposit, excluding the head scarp, gullies, oversteepened face of an eroded toe if present, and roads or other human-modifications to the landscape (Figure 4.12). This can be accomplished by careful manual mapping for specific landslides or automated with feature extraction techniques and buffers for larger areas (described subsequently). Average roughness is determined in ArcGIS using the *Zonal Statistics* tool in the *Spatial Analyst* toolbox. Figure 4.13 is an example of landslide polygons colored according to their average roughness values for the US 20 landslides.

The known ages are then plotted against average deposit roughness as determined above and fitted to define an age-roughness model.

For the four US 20 landslides analyzed, deposit roughness varied from 2.83° to 3.84° (Table 4.2). As expected, these values are considerably lower than those of younger landslides in the Puget Lowlands, which ranged from about 4° to 8° (LaHusen et al., 2016). Where cross-cutting relationships occur (Eddy Creek C and D landslides), the younger landslide is also rougher than the older landslide, as expected.

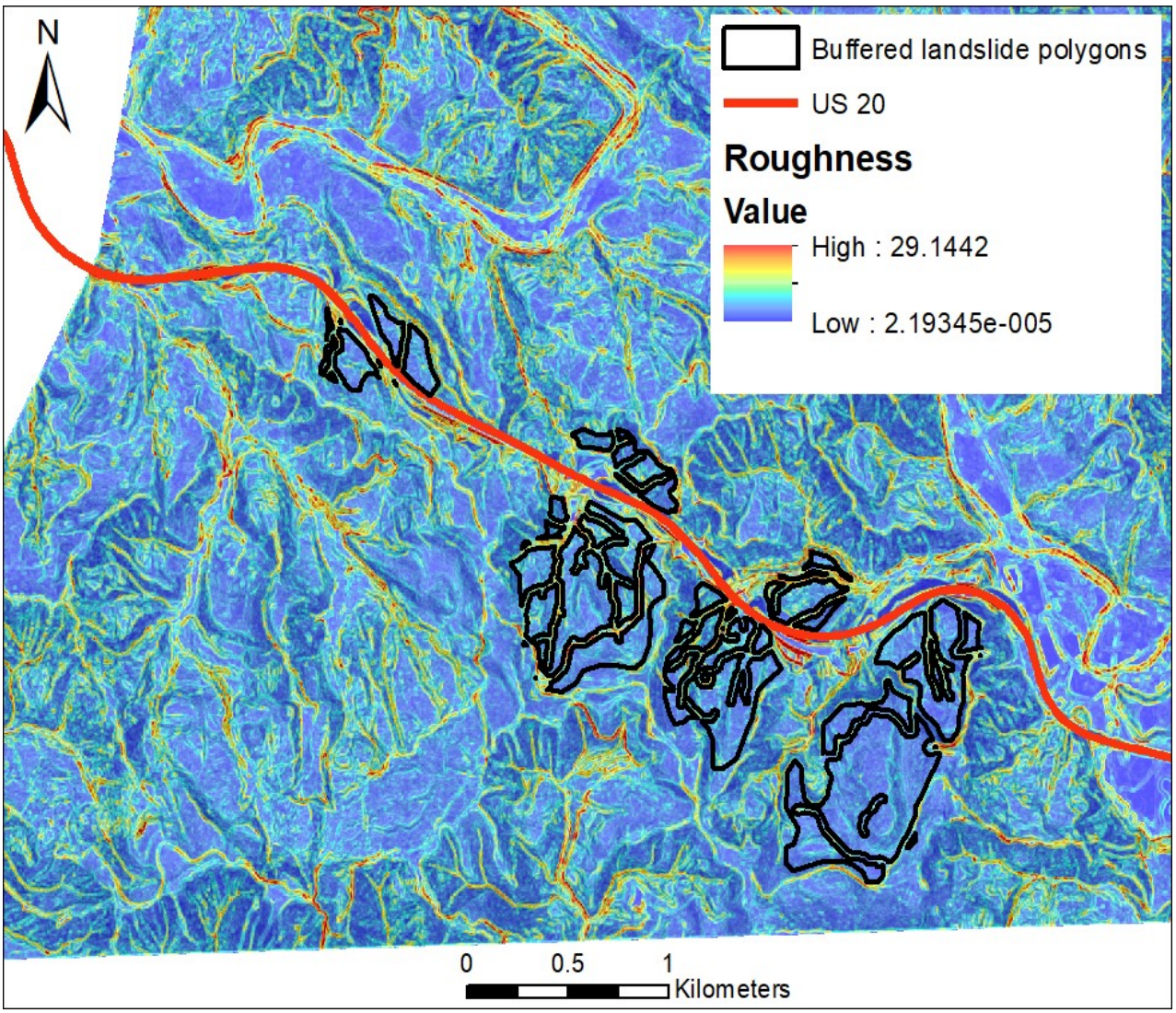

Figure 4.12: Roughness map for analyzed US 20 landslides, where roughness at each pixel in the lidar DEM is quantified as the standard deviation of slope in the surrounding 15 m diameter window. High roughness areas (yellow to red colors) correspond to road edges and incised channels, which have been buffered and removed from the landslide polygons outlined in black.

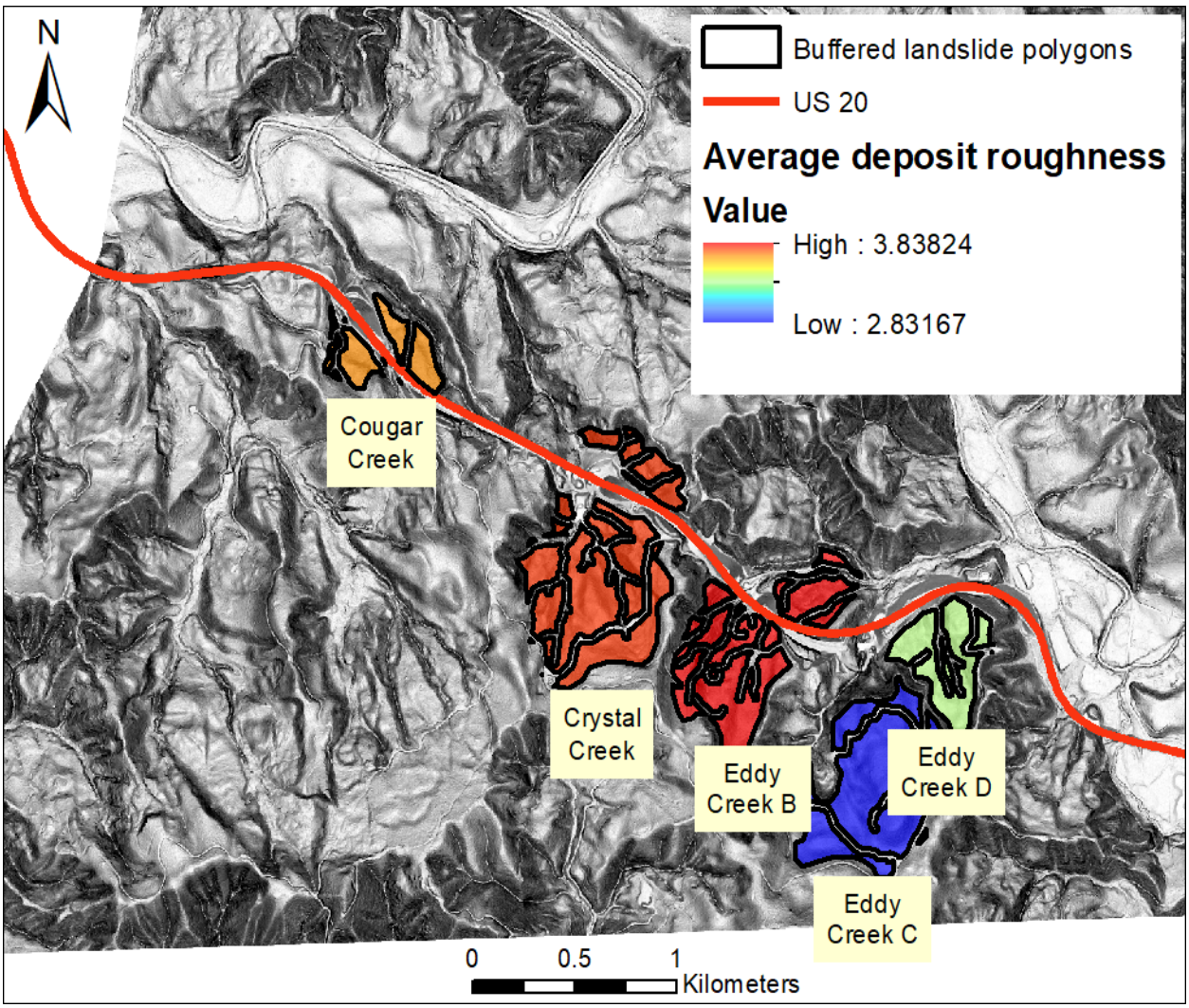

Figure 4.13: Map of average landslide deposit roughness for the five main landslide complexes along the US 20 realignment. Note that color scale for roughness is different than in Fig. 4.12 to highlight relative differences among the landslides.

Table 4.2: Landslide Ages from ODOT-based Work and Roughness Values used to Define Age-roughness Model.

Landslide name	Estimated age (cal. BP)	Deposit roughness (°)	Source
Diamond Mill	250	5.95	This project
Kenusky Crek	739	6.43	This project
Kings Mountain	719	5.00	This project
Marshland	10	7.57	This project
Cougar Creek	41 127	3.68	ODOT/Hammond et al. [2009]
Eddy Creek B	39 437	3.84	ODOT/Hammond et al. [2009]
Eddy Creek C	42 510	2.83	ODOT/Hammond et al. [2009]
Eddy Creek D	31 918	3.35	ODOT/Hammond et al. [2009]
Eddy Creek D	19 663	3.35	ODOT/Hammond et al. [2009]

4.2.1.2 ***Northwestern Oregon Coast Range landslides***

To fill out the younger portion of the age-roughness model, we undertook a field campaign to locate samples of organic material for radiocarbon dating of landslides that were likely younger than the US 20 landslides. Prior to fieldwork, we assessed possible landslide ages based on interpretation of their surface morphology following McCalpin (1984). While we visited many landslides in the field, three yielded organic material and reliable dates: the Diamond Mill and Kings Mountain landslides along the OR 6 highway corridor, and the Kenusky Creek landslide between US 30 and OR 47 (Figure 4.14). Additionally, we identified one historic landslide near US 30, the Marshland landslide, that was large enough for its surface roughness to be reliably measured.

Figure 4.14: Location map of dated landslides in the northwest OCR.

The Diamond Mill landslide is located just north of OR 6 near milepost 23 (Figure 4.15). It has a 370 m wide and ~30 m high toe that protrudes into the North Fork Wilson River, which is actively eroding its face. That fluvial erosion has exposed several wood fragments and larger logs near river level, which were sampled for radiocarbon dating. Three samples returned ages of 59 ± 29, 68 ± 28, and 137 ± 24 radiocarbon yrs B.P. The radiocarbon calibration curve is ambiguous at those ages, and all three ages calibrate to a relatively wide range of calendar ages broadly ranging from 277 cal. BP to 7 cal. B.P. However, we note that there are standing old growth trees and snags that were burned in the Tillamook Burns of the early-mid 20th century on the landslide deposit's surface, suggesting that it has not moved sufficiently to disrupt those trees since then. We therefore assign the oldest probable calibrated age of 250 cal. B.P. to this landslide for the age-roughness model. Athough this age overlaps the last CSZ earthquake, uncertainties in radiocarbon dating and calibration are not sufficient to definitively tie it to that event.

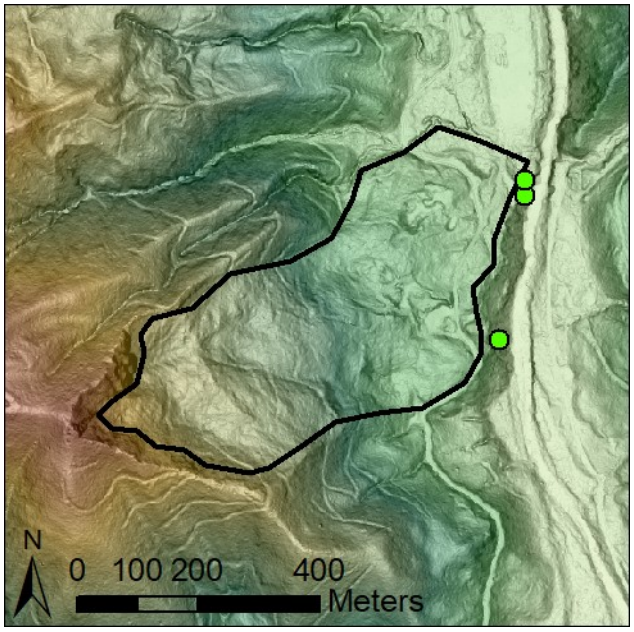

Figure 4.15: Site map for the Diamond Mill landslide, dated to 250 cal. BP based on three radiocarbon dates (sample locations shown as green circles).

The Kings Mountain landslide is located to the north of the Wilson River, immediately north of OR 6 between mileposts 25 and 26 (Figure 4.16). A deeply incised gully cuts through the deposit on the east side of its toe, and a wood fragment was located in an exposed gully wall there. The fragment's age was 706 ± 21 radiocarbon yrs B.P., which calibrated to a most likely calendar age of 719 cal. B.P, which we used for the age-roughness model.

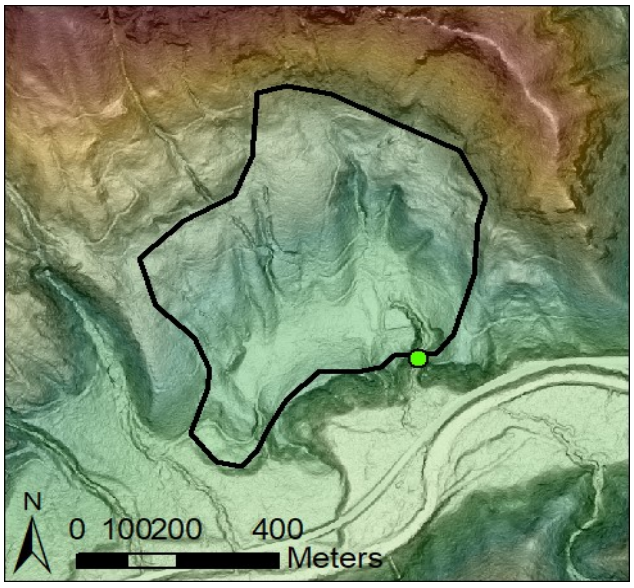

Figure 4.16: Site map for the Kings Mountain landslide, dated to 719 cal. BP based on a radiocarbon date from a stump buried in the landslide's toe (locations shown as green circles).

The Kenusky Creek landslide is located 8 km east of OR 47 at milepost 57 (Figure 4.17). The landslide's toe intersects Kenusky Creek, and there is a shallow pond upstream of the deposit. We located standing dead trees in the pond and a stump that was buried in place by the toe of the landslide and subsequently exposed by erosion of Kenusky Creek. A sample from a standing tree in the pond had an age of 188 ± 31 radiocarbon yrs B.P., while the stump sample had an age of 783 ± 27 radiocarbon yrs B.P. These ages are statistically inconsistent and likely reflect two different events. The younger age from the stump in the pond likely reflects dam building by beavers that happened after the landslide, as evidenced by an existing beaver dam and numerous lake level indicators recording fluctuations in lake level. In contrast, the date from the buried stump more directly dates the landslide event, and we adopt its calibrated calendar age of 739 cal. B.P. for the age-roughness model.

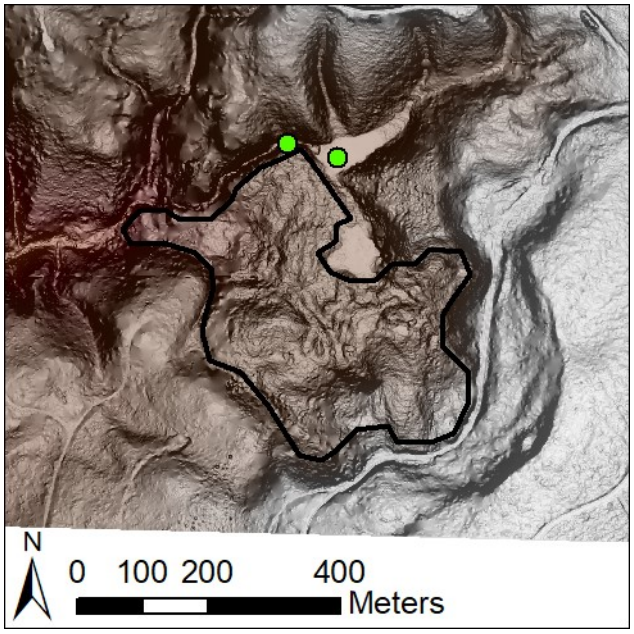

Figure 4.17: Site map for the Kenusky Creek landslide, dated to 739 cal. BP. Green dots are radiocarbon sample locations.

4.2.1.3 ***Final Pacific Northwest Age-Roughness Model***

We defined a Pacific Northwest age-roughness model using the ages and roughness values of all landslides described above in addition to those from four other studies, which documented landslide ages in the Puget Lowlands (LaHusen et al., 2016; Booth et al., 2017; Garriss, 2019) and the Tyee and Elkton formations of the central OCR (LaHusen et al., 2020). Note that the age-roughness models presented in two of those studies (Booth et al, 2017; LaHusen et al., 2020) used topographic curvature to define roughness, so they are not directly comparable to the age-roughness model reported here. We re-calculated roughness of those landslides using the standard deviation of slope definition for this report. To define the model and estimate its 95% confidence interval, we fit an exponential decay function to the age vs. roughness data by applying linear regression after log-transforming the ages. Regression parameters for any of the

individual data sets did not significantly differ from each other, so the final age-roughness model we report here is the fit to all data from all sites (Figure 4.18). That model is:

$$\boldsymbol{A = 3782700e^{-1.47R}} \qquad \textbf{(4-1)}$$

Where:

A is landslide age (cal. B.P.) and

R is average deposit roughness (°), which explained 81% of the variance in the log-transformed age data ($r^2 = 0.81$).

Due to the considerable scatter in the data, the 95% confidence intervals on this fit (Figure 4.18), which we take as measure of the uncertainty on any landslide age predicted from its measured roughness value, are relatively large, especially near the extreme values of the data. Relative uncertainty is lowest for an average deposit roughness of about 6° (predicted age of 538 cal. B.P.) and is +58%/–37%. The + and – signs indicate the upper and lower confidence intervals, respectively, and the upper interval is greater because the age data are log-transformed for determining the fit. Relative uncertainty increases smoothly toward both younger and older ages, and reaches +148%/–60% for the smoothest landslide in the data set with a roughness of 2.83°, and +232%/–70% for the youngest landslide in the data set. On the other hand, absolute uncertainties increase systematically with landslide age, and we provide a reference table for predicted ages and their 95% confidence intervals for integer values of roughness that span the range of the data shown in Figure 4.18 (Table 4.3). In summary, the age-roughness model derived here is useful for roughly estimating the ages of landslide that are unknown from more direct methods such as radiocarbon dating, but should not be used to precisely date a specific landslide of interest where better accuracy is required.

To apply the age-roughness model to existing landslide inventories for OCR highway corridors we first modified DOGAMI landslide deposit polygons from the SLIDO database. Since manually delineating gullies for these larger data sets was not feasible, we developed a feature extraction technique to objectively remove gullies as follows:

1. Create a flow accumulation raster from the lidar-derived DEM. In ArcGIS, this is accomplished by using the *Fill*, *Flow Direction*, and then *Flow Accumulation* tools in the *Spatial Analyst* toolbox.

2. Manually inspect the DEM and flow accumulation raster to identify a typical threshold accumulation value that corresponds to the locations of channel heads. For the OCR, a threshold of 10,000 m^2 (1 ha) was applied.

3. Reclassify the flow accumulation raster so that pixels above the threshold are given the value 1, and those below the threshold are given the value 0. In ArcGIS, use the *Reclassify* tool in the *Spatial Analyst* toolbox.

4. Convert the raster data to vector data using the *Raster to Polyline* tool in the *Conversion Tools* toolbox in ArcGIS. This approximates the channel network.

5. Apply a 15 m buffer on both sides of the channel network vectors using the *Buffer* tool in the *Analysis Tools* toolbox in ArcGIS. Since roughness is defined in a 15 m diameter window, this buffer width ensures that pixels with roughness values that may have been influenced by gullies, rather than only the landslide deposit surface, will be excluded.

6. Remove the buffered channel network from the DOGAMI landslide polygons. In ArcGIS, this is done with the *Merge* tool in the *Data Management Tools* toolbox, followed by the *Erase* tool in the *Analysis Tools* toolbox.

7. Repeat steps 5 and 6 for a vector map of the road network if available. In this study, we used ODOT's GIS layer of the public transportation network.

8. Use the resulting buffered landslide polygons to calculate average roughness using the *Zonal Statistics* tool in the *Spatial Analyst* toolbox in ArcGIS.

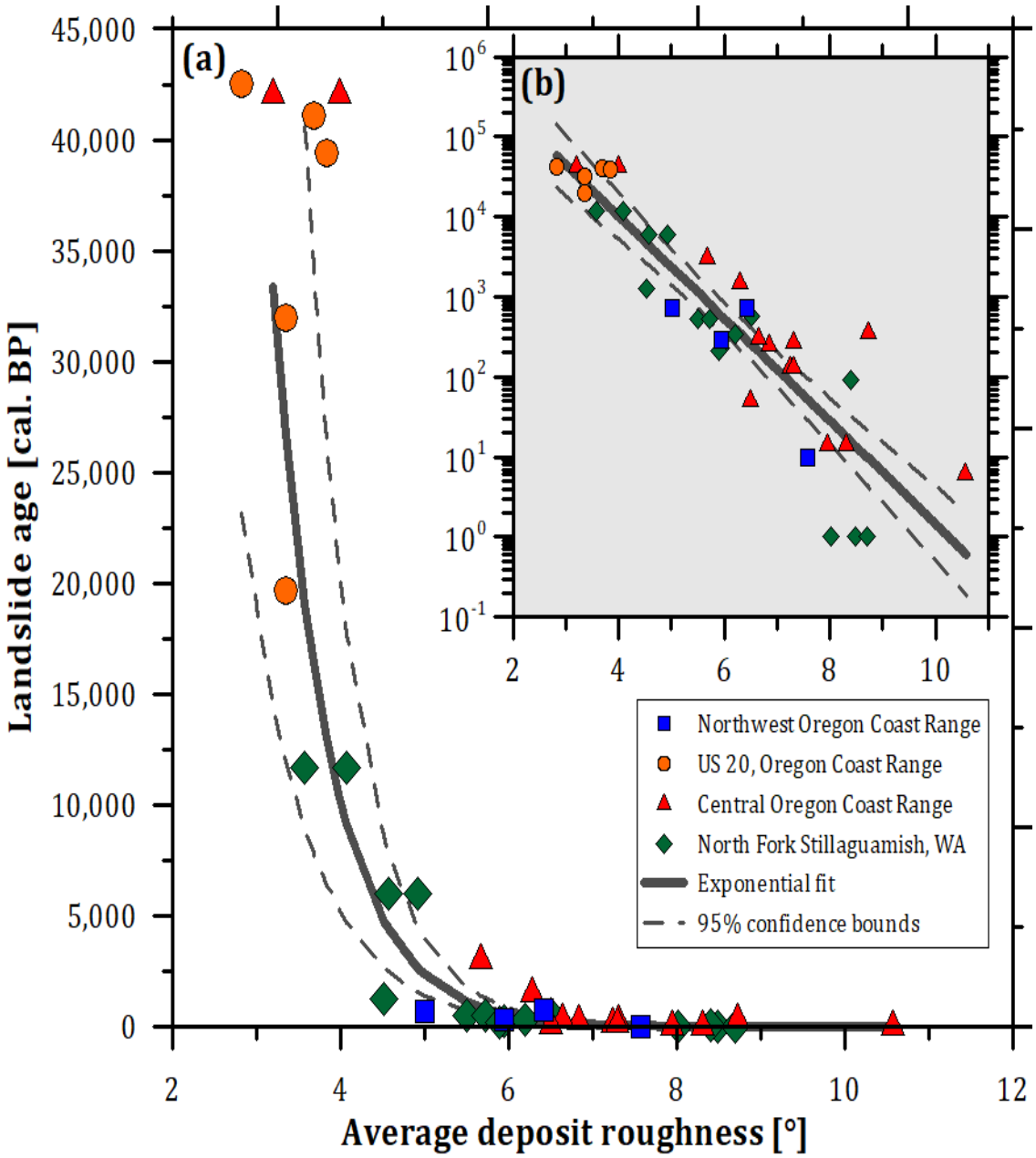

Figure 4.18: Landslide age from radiocarbon dating or historic records vs. average landslide deposit roughness, quantified as the standard deviation of slope in a 15 m moving window plotted with a linear (a) or logarithmic (b) y-axis. Radiocarbon dates from the Northwest Oregon Coast Range were newly acquired as part of SPR808, radiocarbon dates from US 20 in the Oregon Coast Range were compiled from ODOT records and Hammond et al. (2009), Central Oregon Coast Range landslide ages are from LaHusen et al. (2020), and North Fork Stillaguamish ages are from LaHusen et al. (2016), Booth et al. (2017), and Garriss (2019). Exponential fit and 95% confidence interval were determined by linear regression of the log-transformed ages against roughness.

Table 4.3: Reference Chart of ages and Uncertainties for Integer Values of Roughness.

Roughness (°)	Predicted age (cal. B.P.)	Lower 95% C.I. (cal. B.P.)	Upper 95% C.I. (cal. B.P.)
2	195 508	57 741	430 308
3	44 768	18 758	108 300
4	10 251	5 205	20 187
5	2 347	1 390	3 963
6	538	341	852
7	123	74	207
8	28	15	55
9	6.5	3.3	17
10	1.5	0.6	4.4

Within the uncertainties of the age-roughness model, it is possible to separate landslides into groups with predicted ages that are consistent or inconsistent with different potential triggers, such as earthquakes or climatic events. For each of the OCR highway corridors studied, we identified landslides with ages that overlap, within uncertainty, A.D. 1700 (250 cal. B.P.) to isolate landslides that were plausibly triggered by the last Cascadia Subduction Zone earthquake (Figure 4.19). While the dates of previous CSZ earthquakes are well known from offshore turbidites and tidal flat stratigraphy (e.g. Goldfinger et al., 2012), the large uncertainties on our age-roughness model do not allow identification of landslides that were plausibly triggered by those older earthquakes. Average roughness values that are consistent with 250 cal. B.P. range from 6.2° to 6.9°. Since there have been no major CSZ earthquakes since 250 cal. B.P., all landslides with a roughness value greater that 6.9° were likely climatically induced.

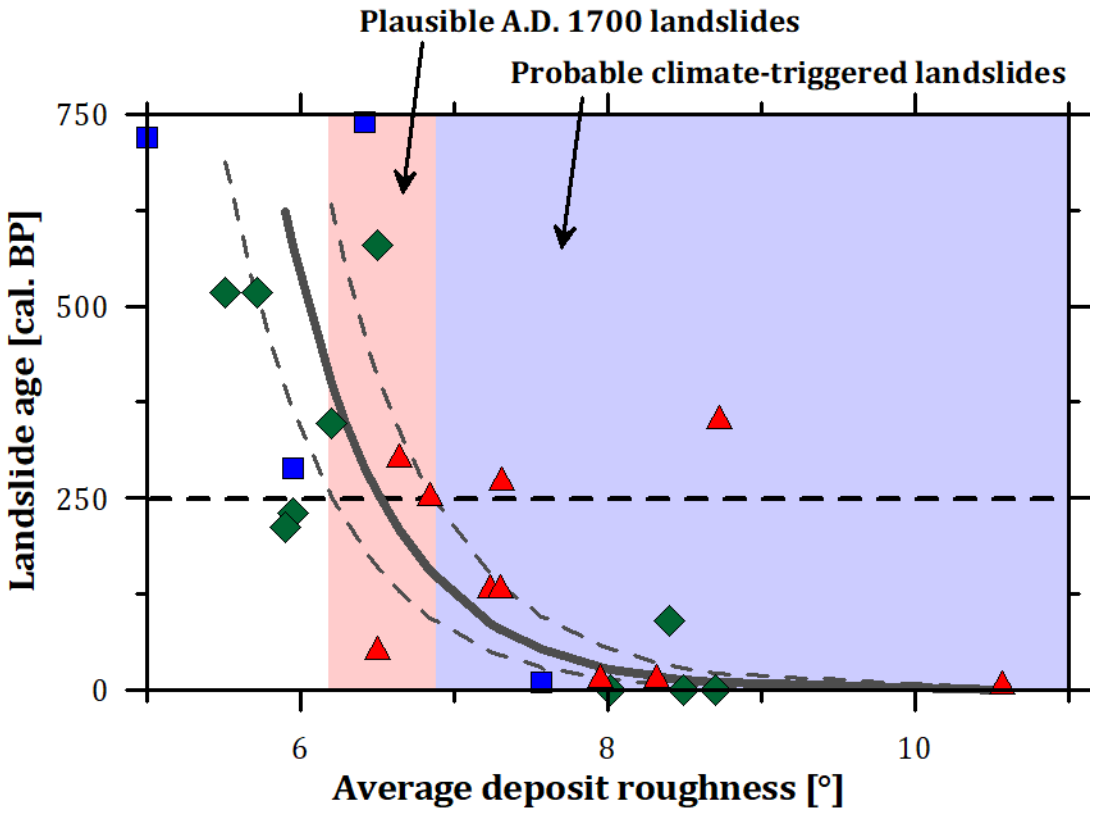

Figure 4.19: Zoom-in on age-roughness model for landslides younger than 750 cal. B.P. Dashed line at an age of 250 cal. B.P. (A.D. 1700) marks the date of the last CSZ earthquake. Pink shading indicates range of roughness values that are consistent with that age within uncertainty, and therefore plausibly earthquake-triggered, while blue shading indicates landslides that are likely younger and therefore likely climate-triggered.

4.3 FORENSIC LANDSLIDE ANALYSES AND RESULTING SHEAR STRENGTH DISTRIBUTIONS

3D forensic analyses, informed by the age-roughness curve presented in the previous section, are applied to each corridor's respective DEM to produce strength distributions that will inform susceptibility analyses. SLIDO inventoried landslides used in forensic analyses for each corridor are shown in Figures 4.20-4.23. Figures 4.20-4.23 also show the age-roughness classification of SLIDO inventories landslides. Note that OR42 uses a DEM and landslide inventory roughly 13 miles north of the OR42 corridor DEM. The 3D forensic analysis herein requires mapped deposits accompanied by a mapped scarp flank. There are no mapped landslides within the SLIDO database within the OR42 corridor DEM meeting these requirements, so an alternative DEM to the north is used in its place. The alternative forensics region is chosen for its similar lithology and climatic setting. The alternative forensic DEM used for OR42 is shown in Figure 4.23.

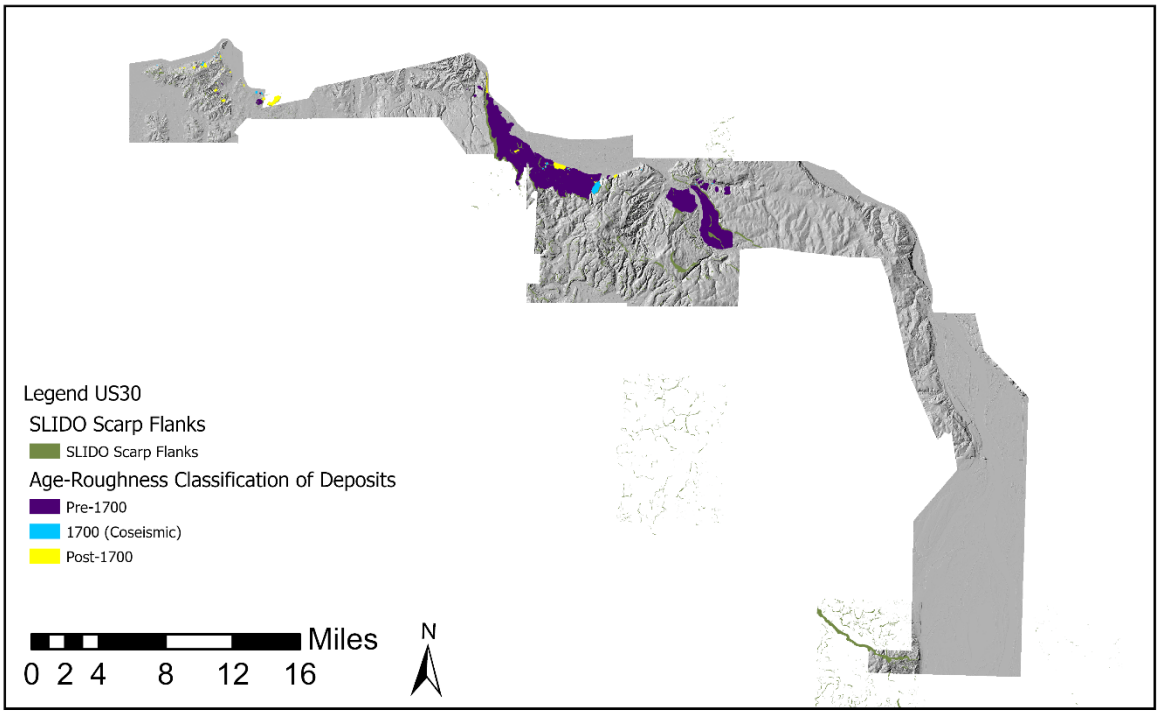

Figure 4.20: DEM and age-roughness classification of SLIDO inventoried landslides for corridor US30.

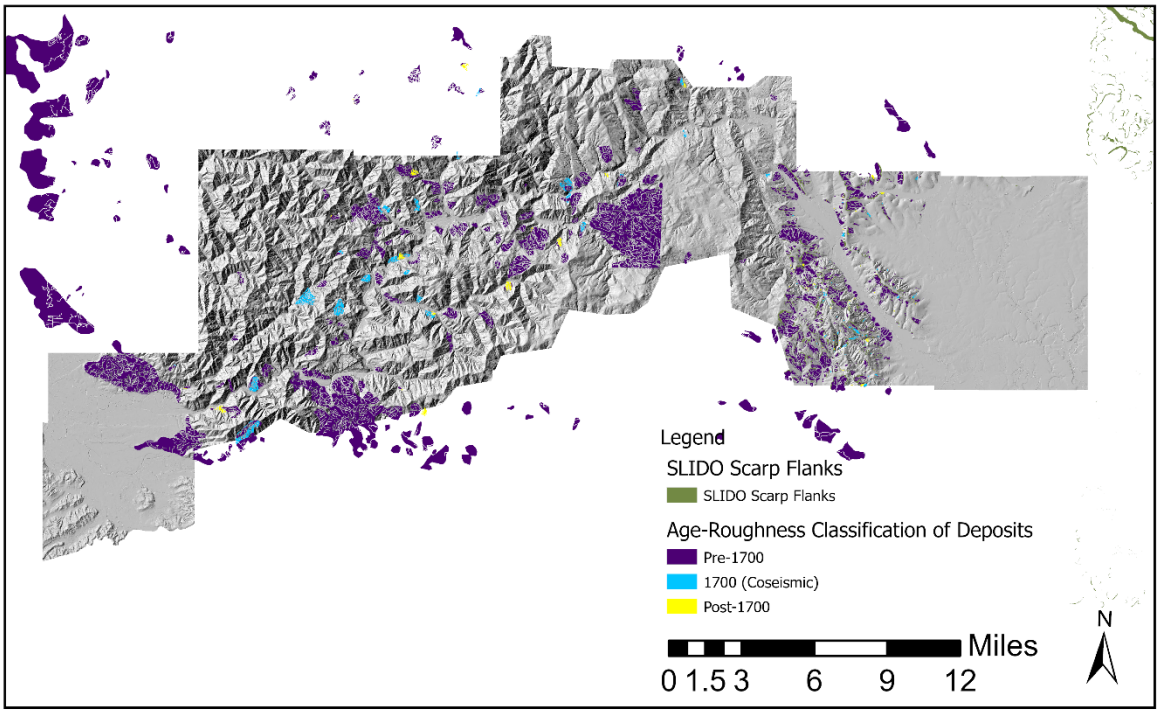

Figure 4.21: DEM and age-roughness classification of SLIDO inventoried landslides for corridor OR06.

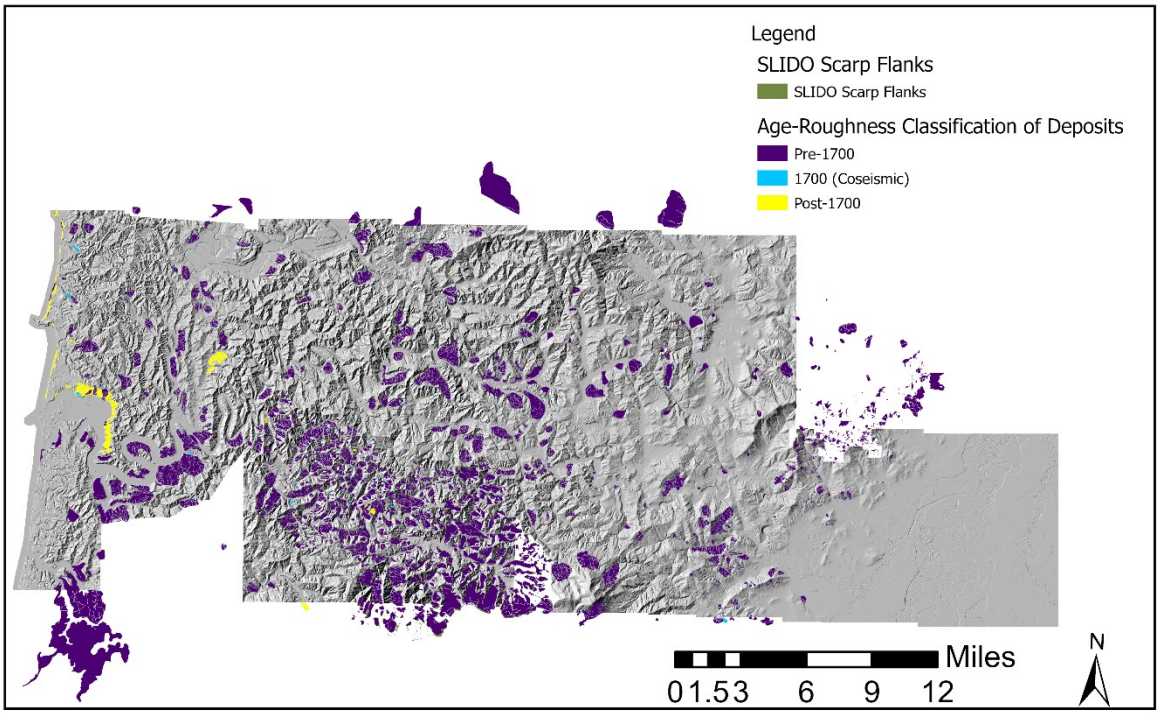

Figure 4.22: DEM and age-roughness classification of SLIDO inventoried landslides for corridor US20.

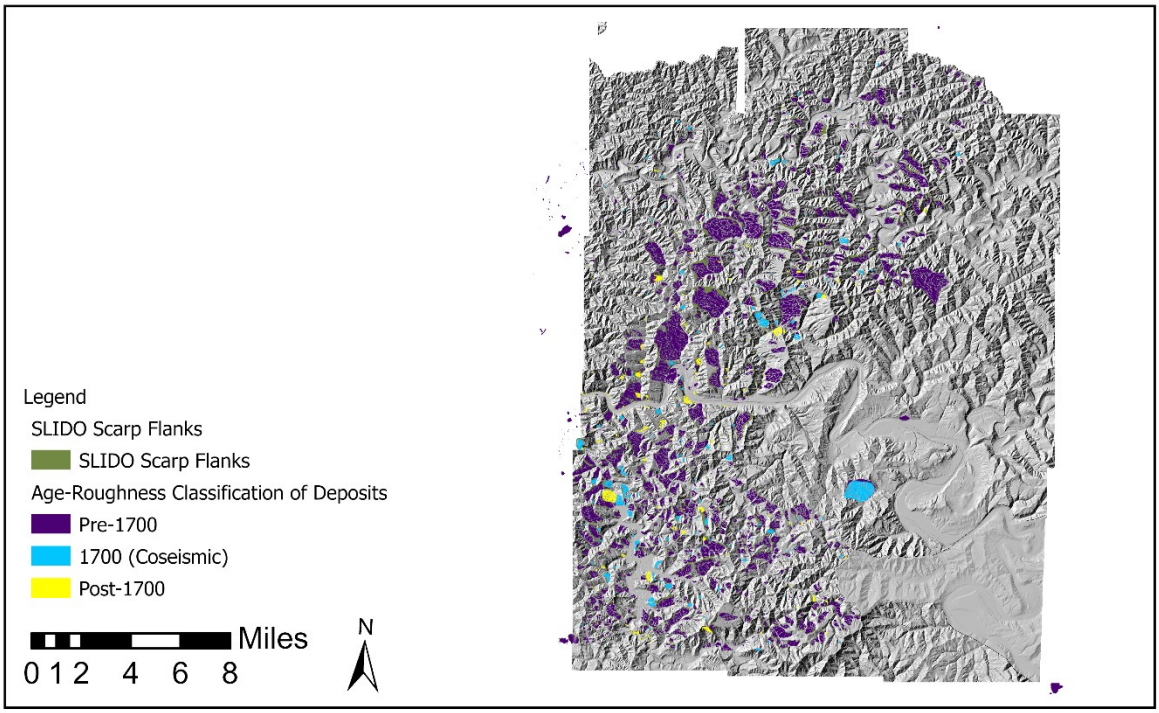

Figure 4.23: Alternative DEM and age-roughness classification of SLIDO inventoried landslides for corridor OR42.

4.3.1 Shear Strength Distributions Generated using 3D Landslide Forensics

Using the methods discussed in Section 3.7, distributions of soil shear strength are generated for each corridor analyzed in this study. Strength distributions are shown in Figures 4.24-4.27. Based on limitations on typically observed friction angles in natural soils (e.g. not quarried or unnaturally angular material), an upper bound of 35° is assumed for friction angles; additional soil strength beyond $\phi' = 35°$ is attributed to apparent cohesion. This is reflected in the strength distributions shown in Figures 4.24-4.27. Under the assumption that most landslides failed under drained conditions, and the continued activity in many of the documented failures, forensic analysis for friction-only conditions is reasonable. Note that for these distributions, coseismic landslide polygons (see Figures 4.20-4.23) identified using the Pacific Northwest age-roughness relationship are subjected to the M8.7 raster of PGA (Figure 3.10). Remaining landslides are assumed to be rainfall-induced and are subject to a 1000-year recurrence interval 24-hour rainfall event.

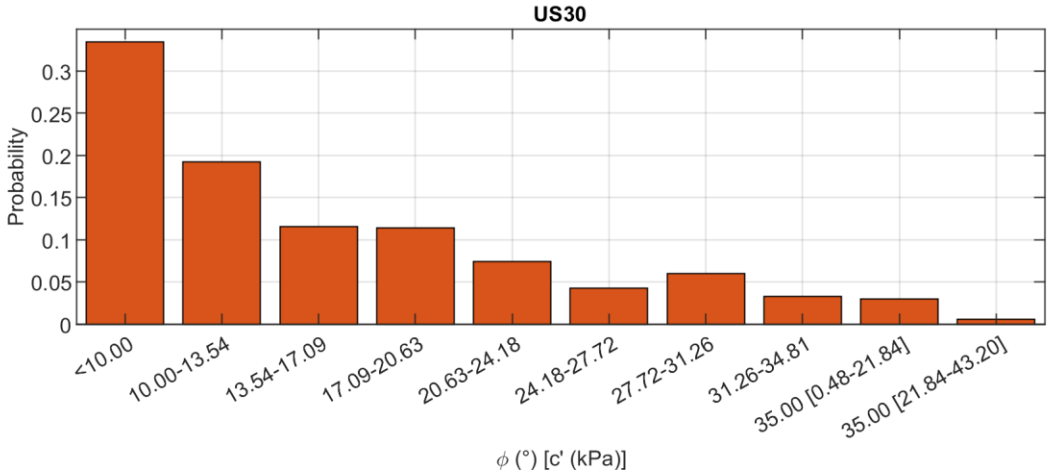

Figure 4.24: Soil shear strength distribution from back-analyzed SLIDO inventoried landslides for US30.

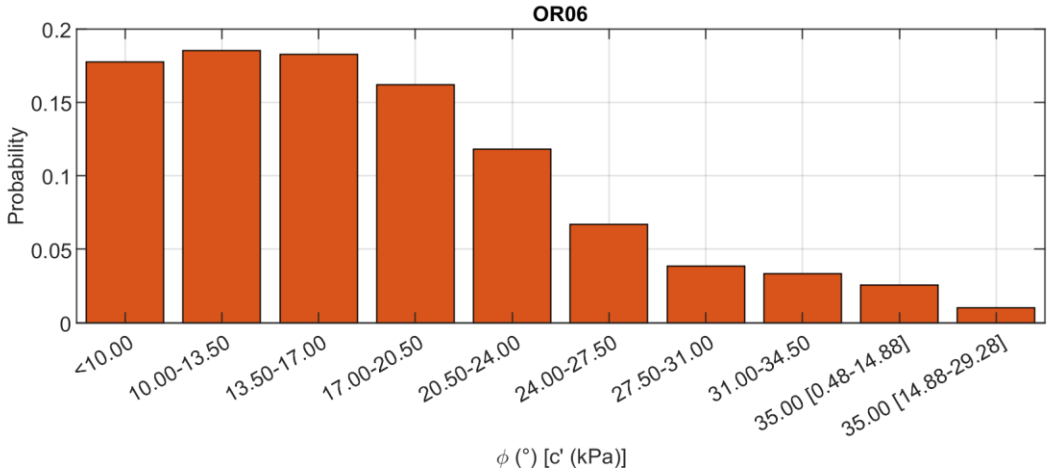

Figure 4.25: Soil shear strength distribution from back-analyzed SLIDO inventoried landslides for OR06.

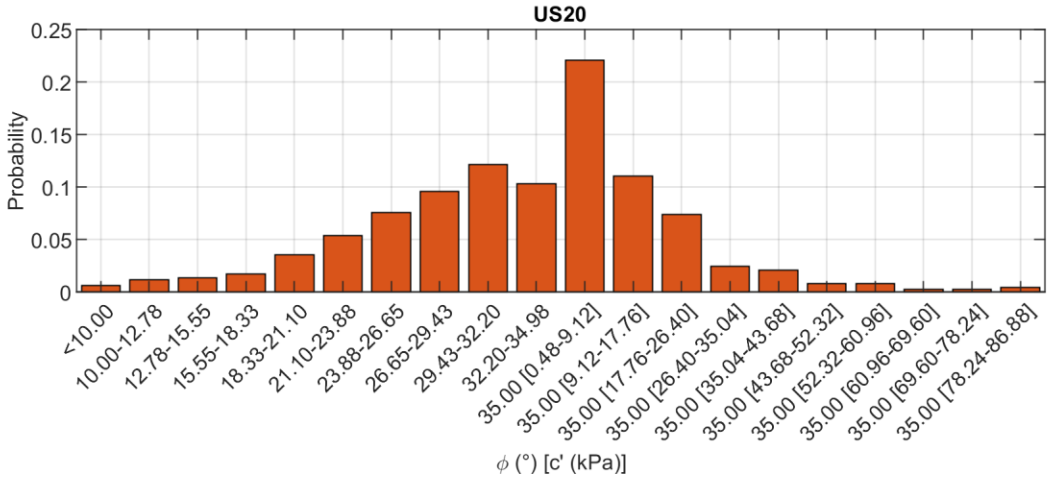

Figure 4.26: Soil shear strength distribution from back-analyzed SLIDO inventoried landslides for US20.

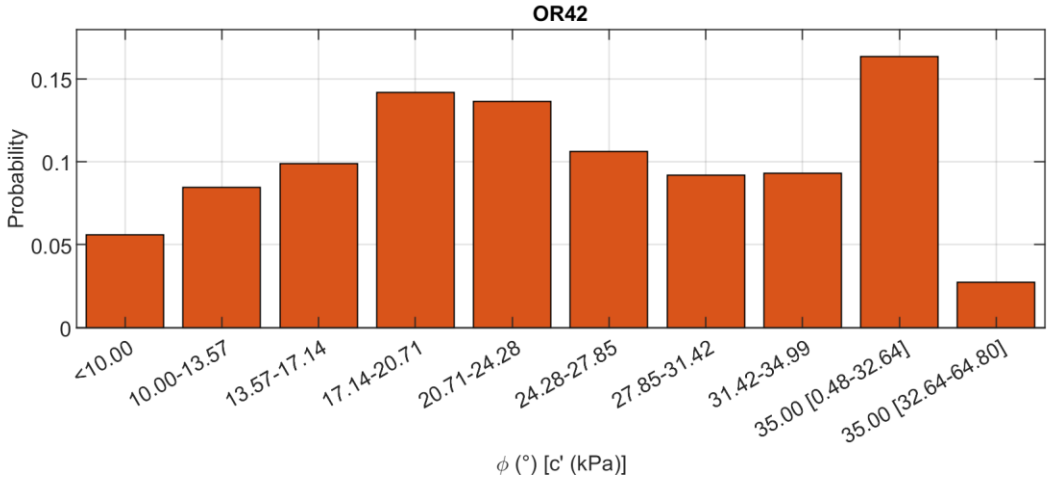

Figure 4.27: Soil shear strength distribution from back-analyzed SLIDO inventoried landslides for OR42 (alternative DEM shown in Figure 4.24).

4.4 SUSCEPTIBILITY

Susceptibility maps for all four corridors and various physical inputs are shown to highlight the effects of seismicity and rainfall on stability and to help with resilience planning in the event of a single- or multi-hazard event. The susceptibility maps herein are also used as inputs for results shown in Sections 4.5 and 4.6. To highlight changes in susceptibility stemming from physical inputs (moisture, rainfall, and seismicity), 24 unique scenarios are presented in this Section, as well as Sections 4.5 and 4.6. These selected 24 scenarios are highlighted in Table 4.4, which contains a full directory for all the scenarios considered in this study. Susceptibility maps for the 24 scenarios highlighted in Table 4.4 are shown in Figures 4.28-4.51. Note that a full suite of susceptibility maps for this study may be found in Appendix A.

Table 4.4: Directory of Scenarios used in this Study.

US30				OR06			
Season	**Storm Recurrence Interval**	**Seismic**	**Test #**	**Season**	**Storm Recurrence Interval**	**Seismic**	**Test #**
Summer	off	off	1	Summer	off	off	26
		8.1	2			8.1	27
		8.4	3			8.4	28
		8.7	4			8.7	29
		9.0	5			9.0	30
Winter	off	off	6	Winter	off	off	31
		8.1	7			8.1	32
		8.4	8			8.4	33
		8.7	9			8.7	34
		9.0	10			9.0	35
	10-year	off	11		10-year	off	36
		8.1	12			8.1	37
		8.4	13			8.4	38
		8.7	14			8.7	39
		9.0	15			9.0	40
	100-year	off	16		100-year	off	41
		8.1	17			8.1	42
		8.4	18			8.4	43
		8.7	19			8.7	44
		9.0	20			9.0	45
	1000-year	off	21		1000-year	off	46
		8.1	22			8.1	47
		8.4	23			8.4	48
		8.7	24			8.7	49
		9.0	25			9.0	50

Table 4.4 Cont.

US20				OR42			
Season	**Storm Recurrence Interval**	**Seismic**	**Test #**	**Season**	**Storm Recurrence Interval**	**Seismic**	**Test #**
Summer	off	off	51	Summer	off	off	76
		8.1	52			8.1	77
		8.4	53			8.4	78
		8.7	54			8.7	79
		9.0	55			9.0	80
Winter	off	off	56	Winter	off	off	81
		8.1	57			8.1	82
		8.4	58			8.4	83
		8.7	59			8.7	84
		9.0	60			9.0	85
	10-year	off	61		10-year	off	86
		8.1	62			8.1	87
		8.4	63			8.4	88
		8.7	64			8.7	89
		9.0	65			9.0	90
	100-year	off	66		100-year	off	91
		8.1	67			8.1	92
		8.4	68			8.4	93
		8.7	69			8.7	94
		9.0	70			9.0	95
	1000-year	off	71		1000-year	off	96
		8.1	72			8.1	97
		8.4	73			8.4	98
		8.7	74			8.7	99
		9.0	75			9.0	100

Note: Highlighted tests are those presented in the results section of this report. The rest are found in the appendices A-H and the digital appendix.

Figures 4.28-4.33 show susceptibility maps for corridor US30. For this corridor, small values of susceptibility are observed for the summer season (Figure 4.28), even when subjected to strong seismicity (Figure 4.29). This is likely due to relatively low soil moistures providing stabilizing suction stresses within the soil matrix (Lu and Likos, 2004). Some areas, however, begin to display a small degree of susceptibility in the central region of the corridor in Figure 4.29. For winter antecedent conditions, moderate to high levels of susceptibility are observed in multiple regions of the corridor, in very close proximity to highway US30 (Figure 4.30). In contrast to summer months, Figure 4.31 shows that moist soil conditions result in much higher sensitivity to seismic activity, as moderate to high susceptibility is observed throughout several regions within the corridor. Finally, Figures 4.32-4.33 show that as storm intensity and seismicity increase further, higher values of susceptibility are observed throughout the corridor. Note that, for all conditions, high susceptibility is concentrated into multiple regions throughout the corridor, with the highest and most widespread susceptibility values observed in the central region.

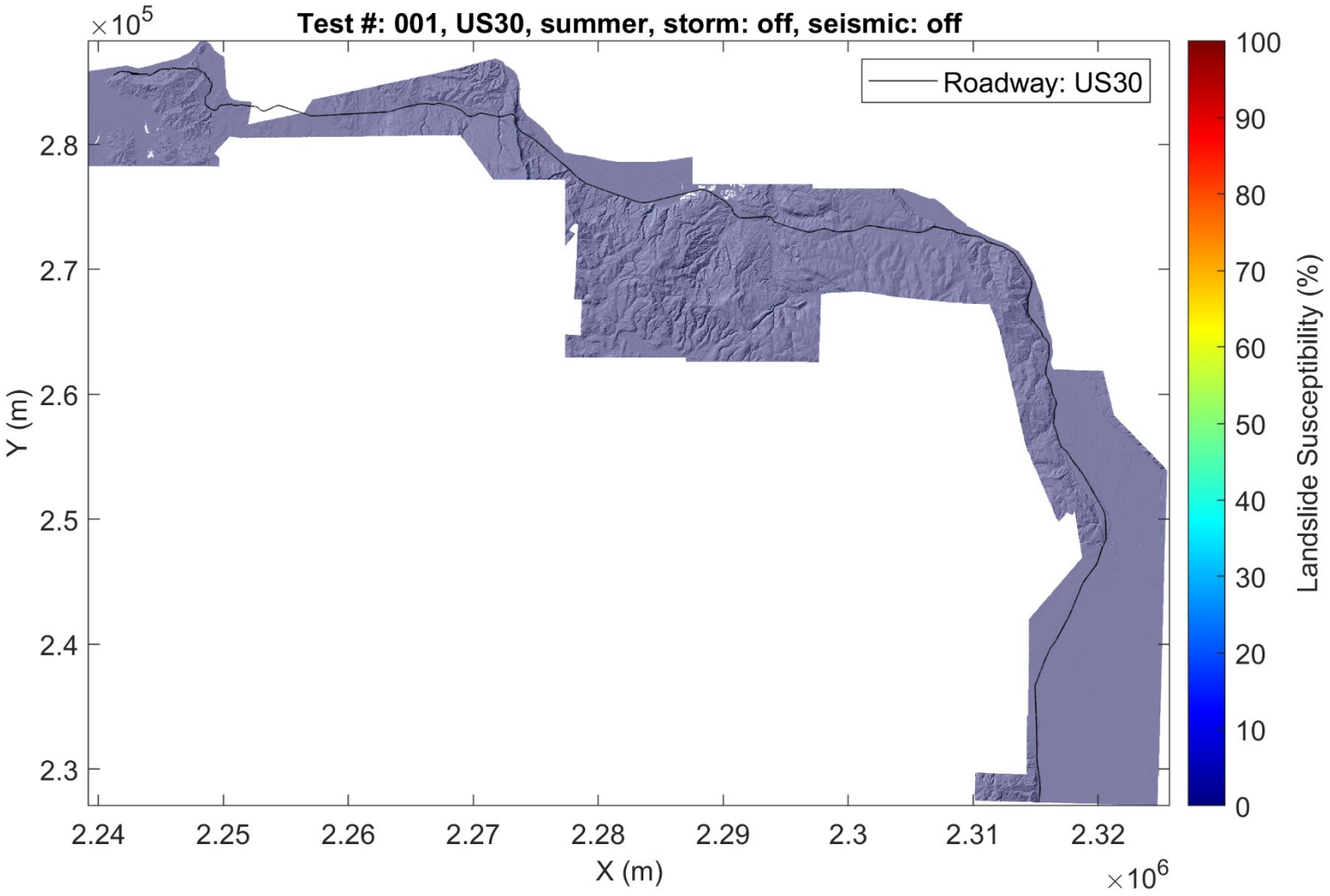

Figure 4.28: Susceptibility map for US30: summer antecedent conditions (test #: 001).

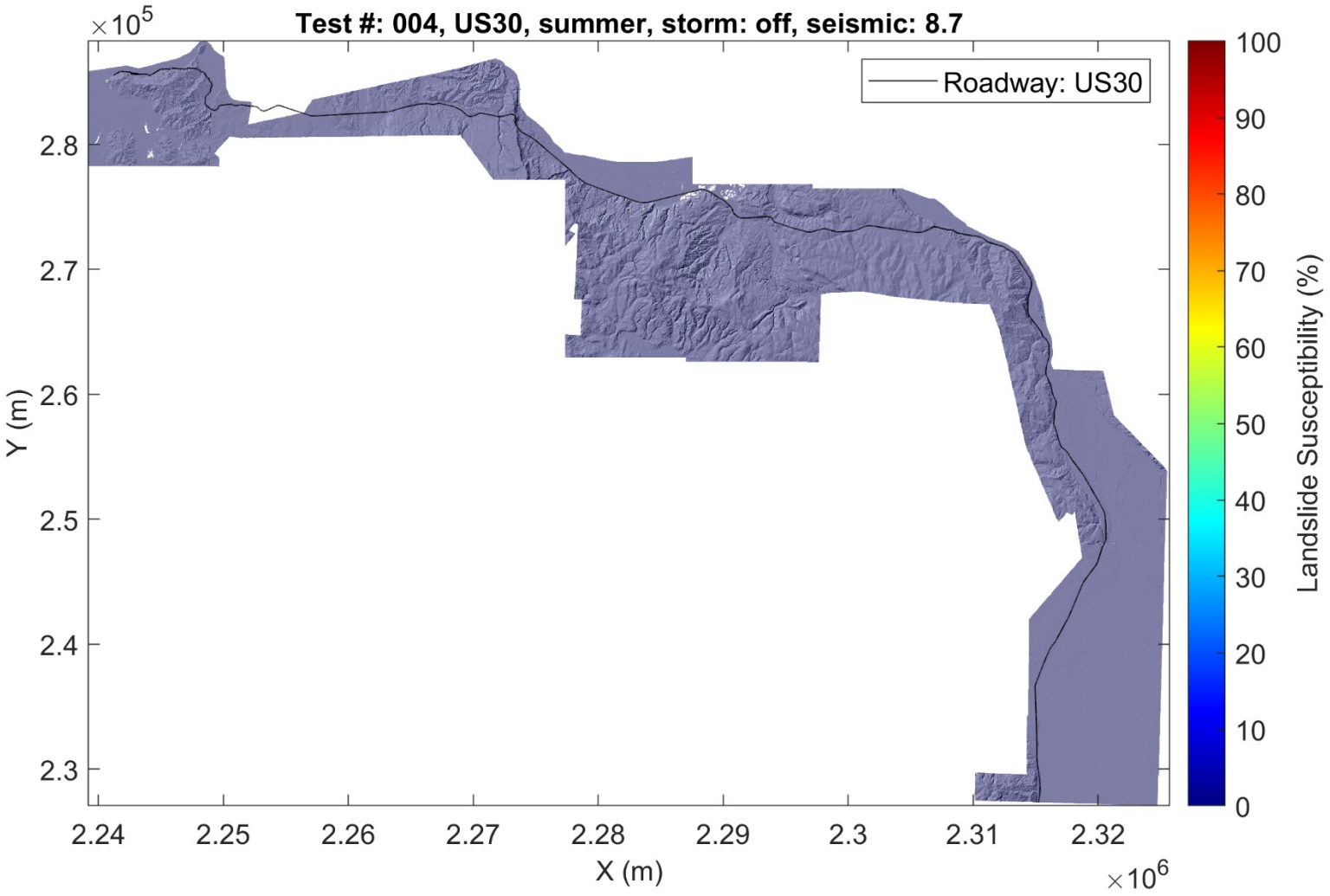

Figure 4.29: Susceptibility map for US30: summer antecedent conditions, M8.7 earthquake (test #: 004).

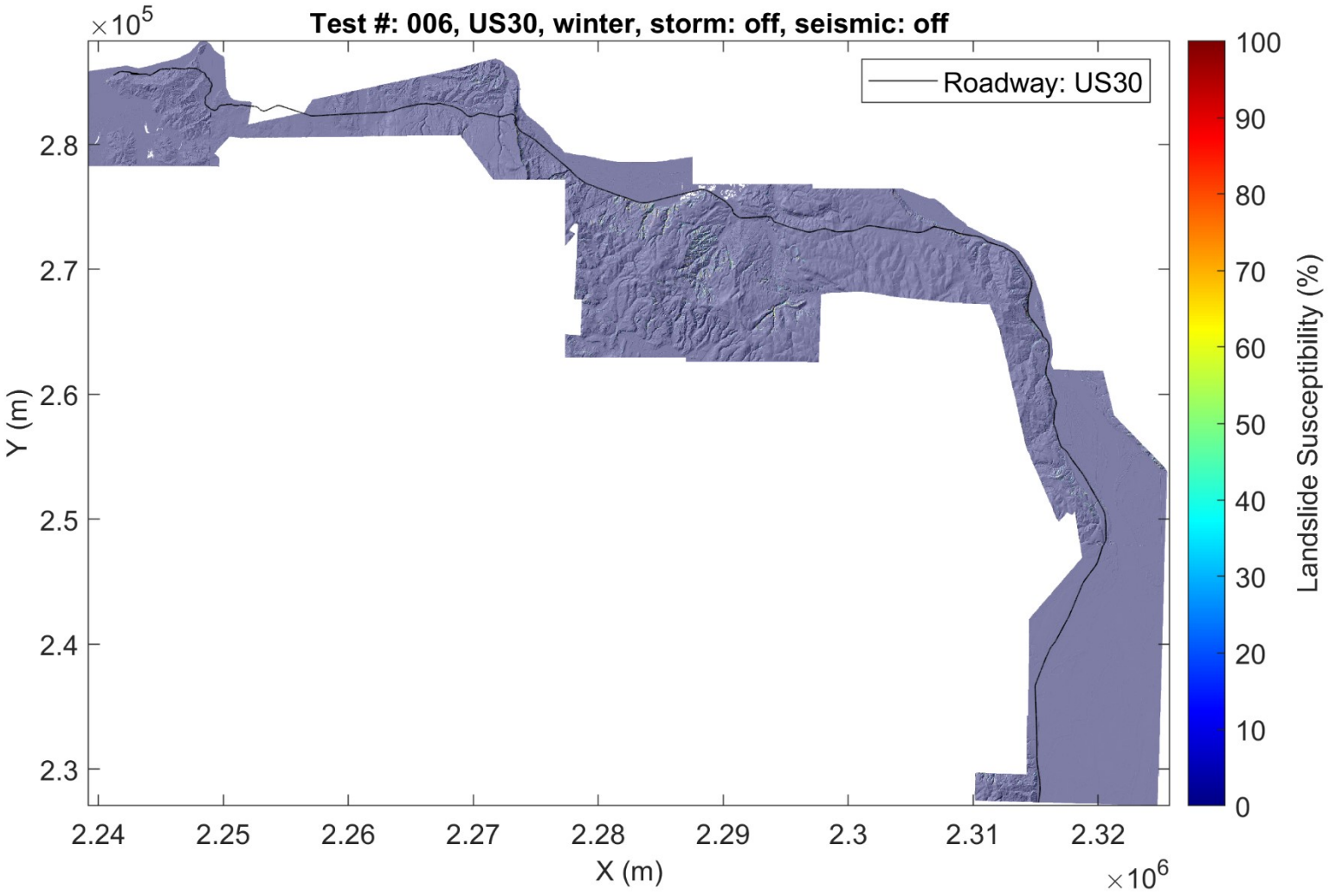

Figure 4.30: Susceptibility map for US30: winter antecedent conditions (test #: 006).

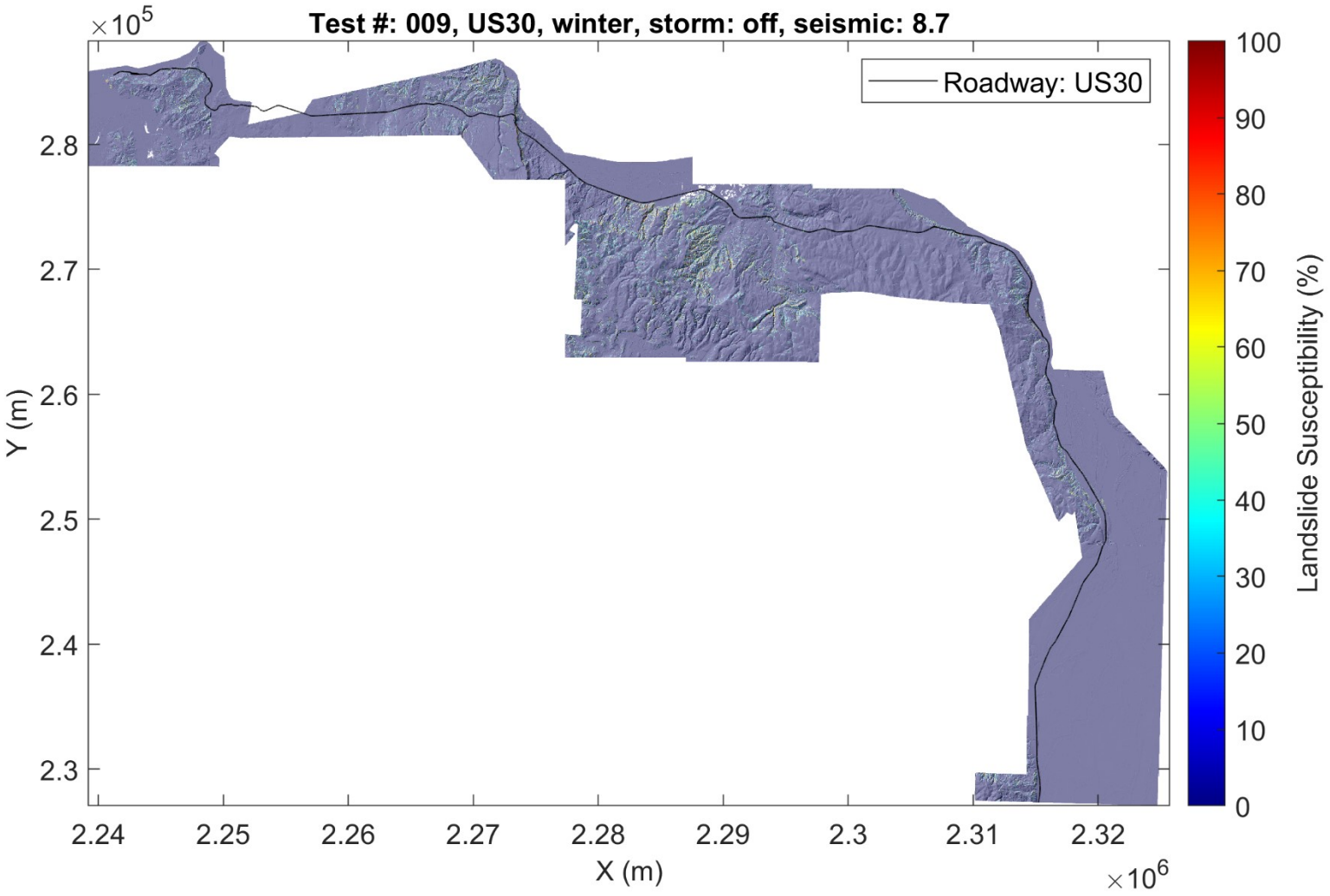

Figure 4.31: Susceptibility map for US30: winter antecedent conditions, M8.7 earthquake (test #: 009).

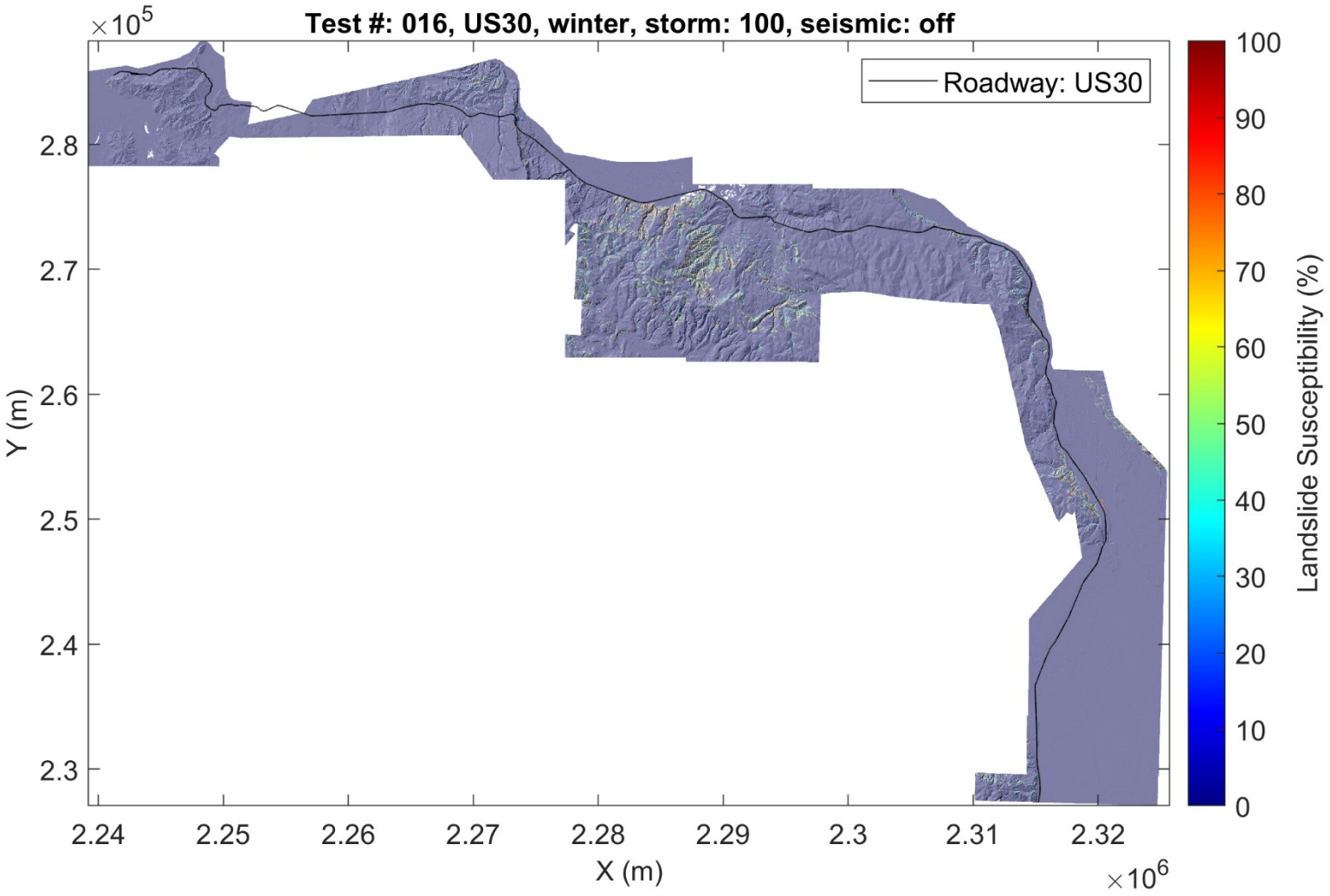

Figure 4.32: Susceptibility map for US30: winter, 100-year rainfall event (test #: 016).

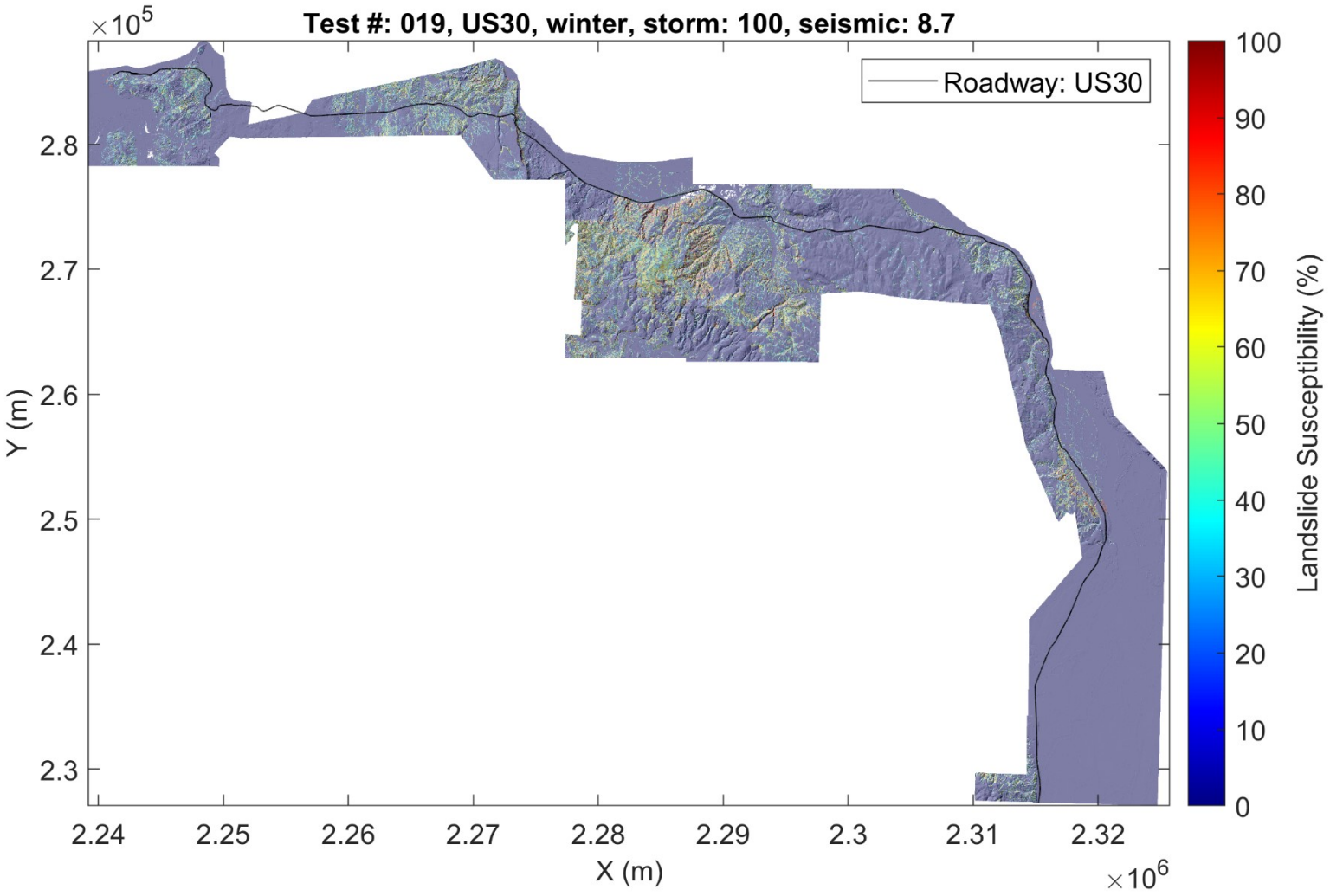

Figure 4.33: Susceptibility map for US30: winter, 100-year rainfall event, M8.7 earthquake (test #: 019).

Figures 4.34-4.39 show susceptibility maps for corridor OR06. For this corridor, very small values of susceptibility are observed for the summer season (Figure 4.34). Low to moderate of susceptibility values appear when summer conditions are subjected to strong seismicity, especially in the western region closest to the CSZ (Figure 4.35). Susceptibility gradually drops when traveling from west to east. Winter antecedent conditions (Figure 4.36) exhibit slightly higher susceptibility than those seen in Figure 4.35. In contrast to summer months, Figure 4.37 shows that moist, winter soil conditions result in higher sensitivity to strong seismic activity, as widespread moderate susceptibility, with pockets of high susceptibility are observed throughout the corridor, especially in the western region. Finally, Figures 4.38-4.39 show that as storm intensity and seismicity increase further, higher values of susceptibility are observed throughout the corridor, and an eastern region of the corridor shows increasingly higher susceptibility values. For all conditions, the central region of OR06 remains relatively low susceptibility when compared to the western and eastern regions.

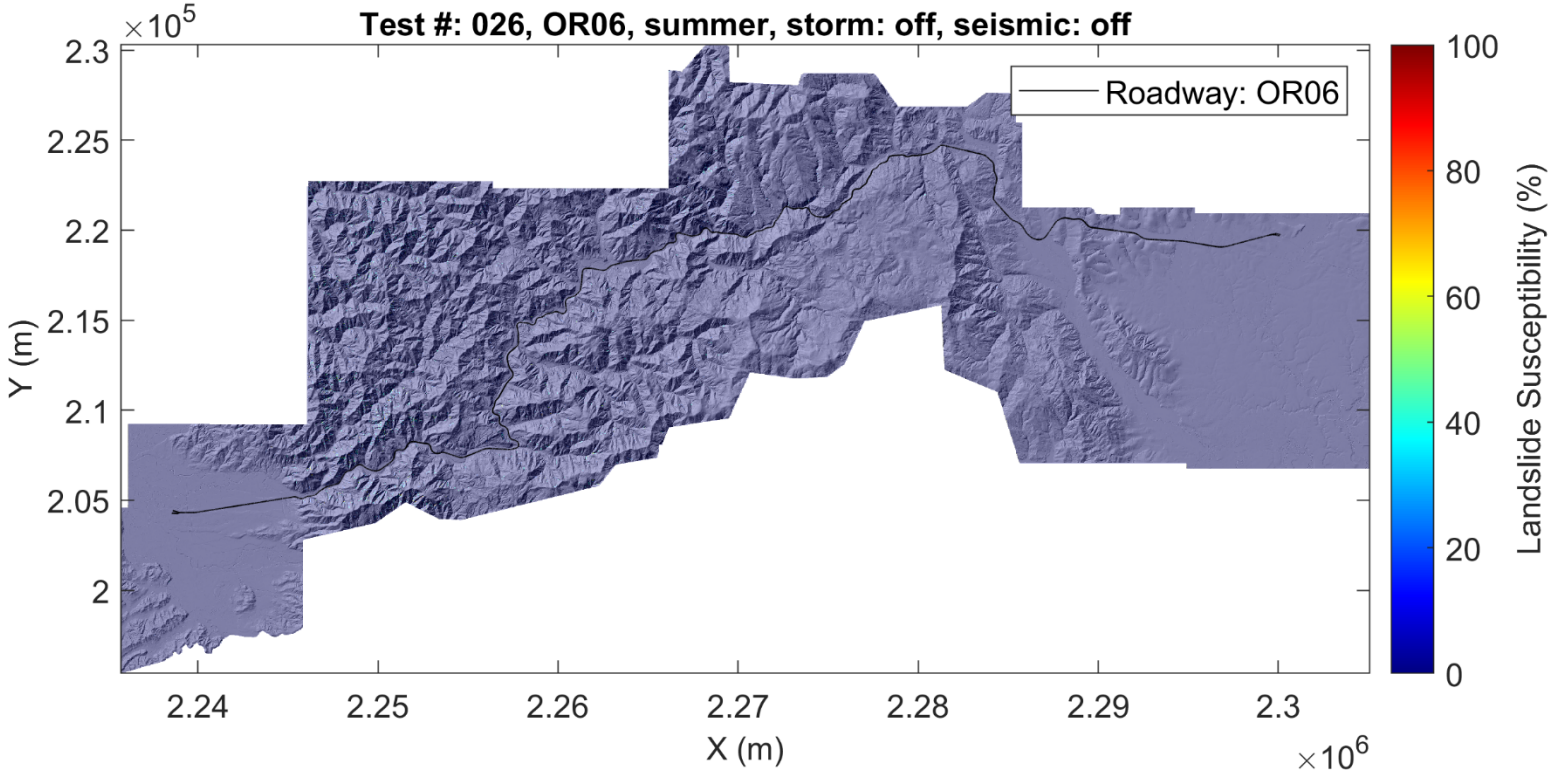

Figure 4.34: Susceptibility map for OR06: summer antecedent conditions (test #: 026).

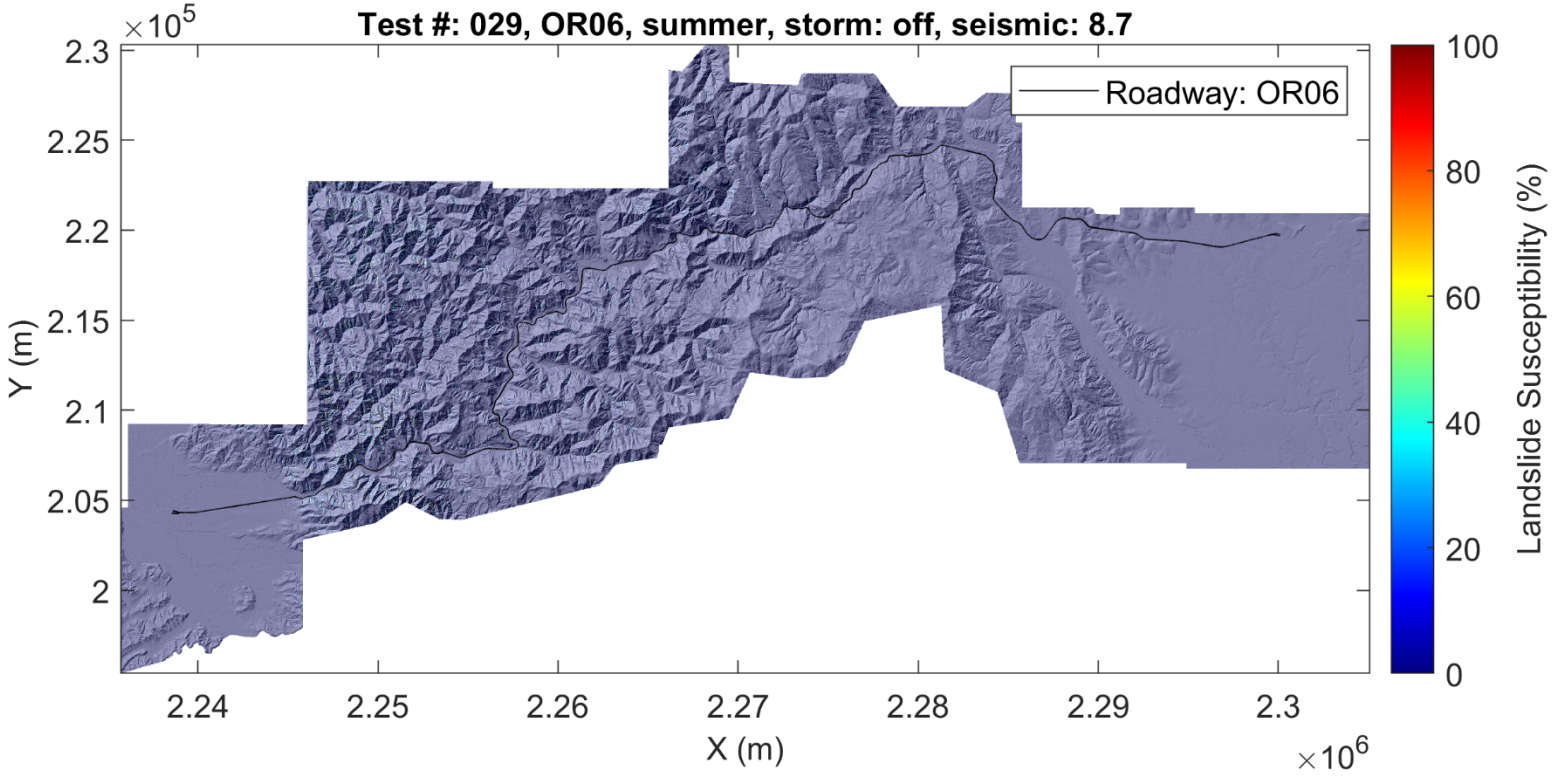

Figure 4.35: Susceptibility map for OR06: summer antecedent conditions, M8.7 earthquake (test #: 029).

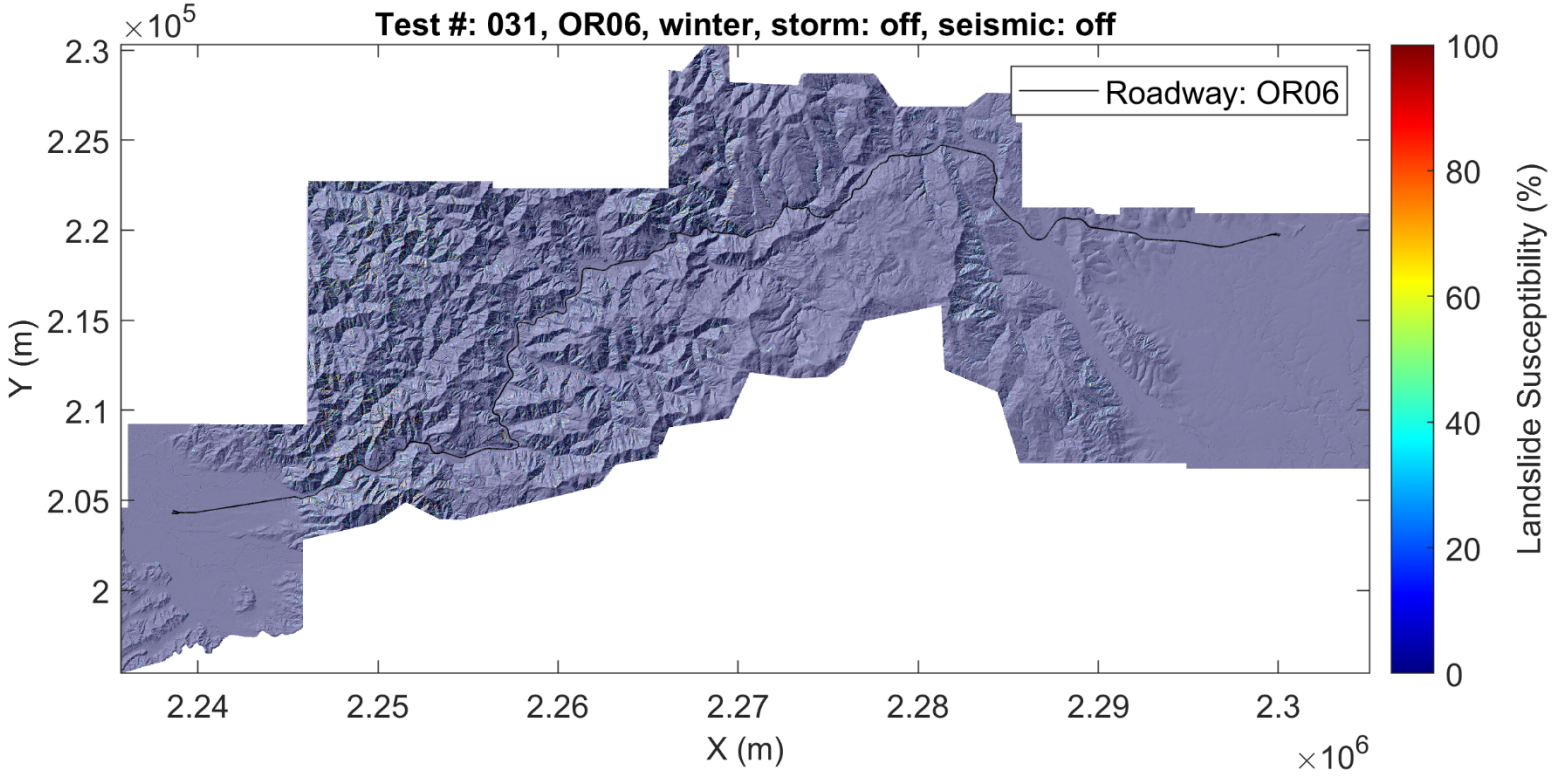

Figure 4.36: Susceptibility map for OR06: winter antecedent conditions (test #: 031).

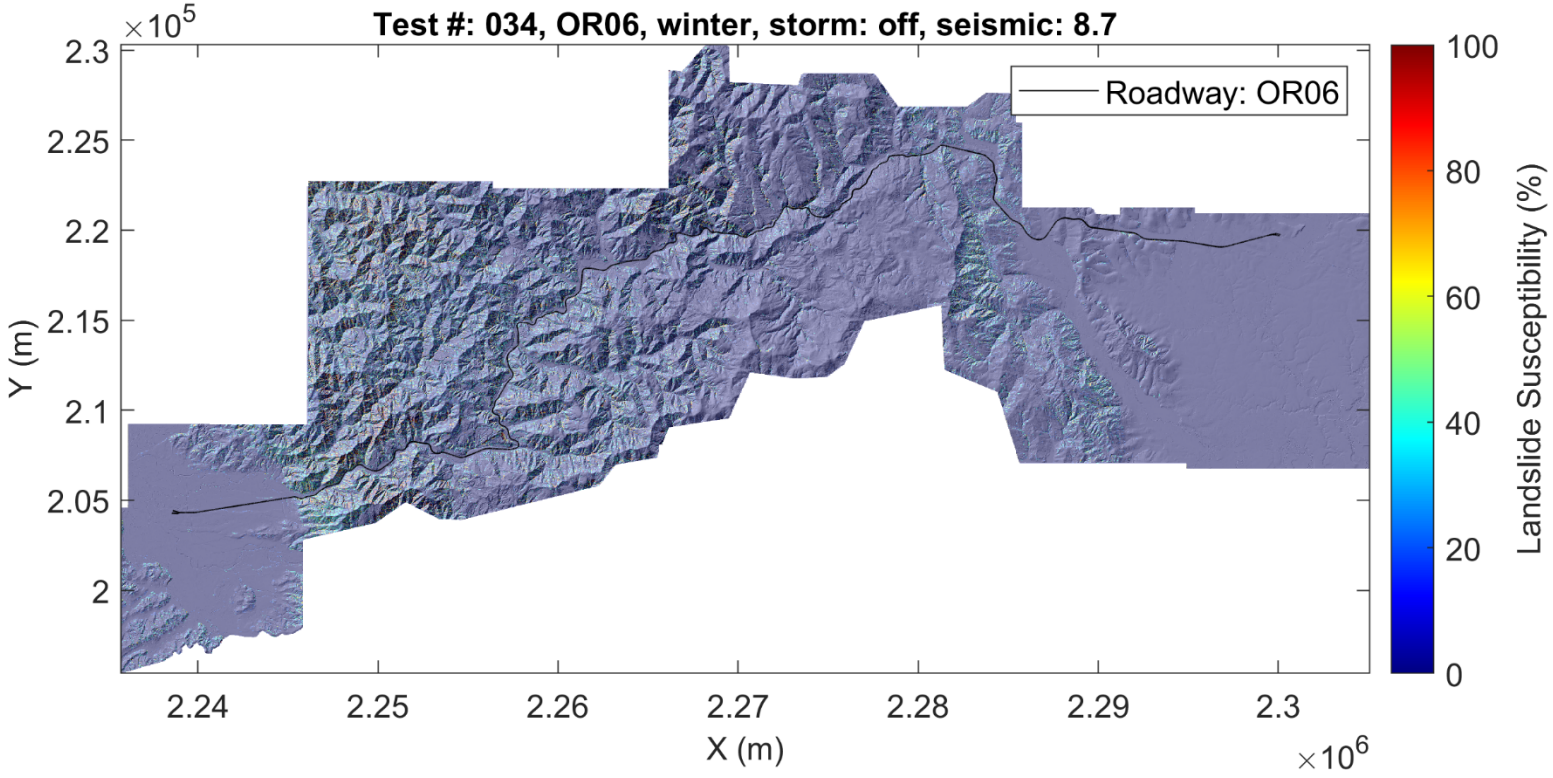

Figure 4.37: Susceptibility map for OR06: winter antecedent conditions, M8.7 earthquake (test #: 034).

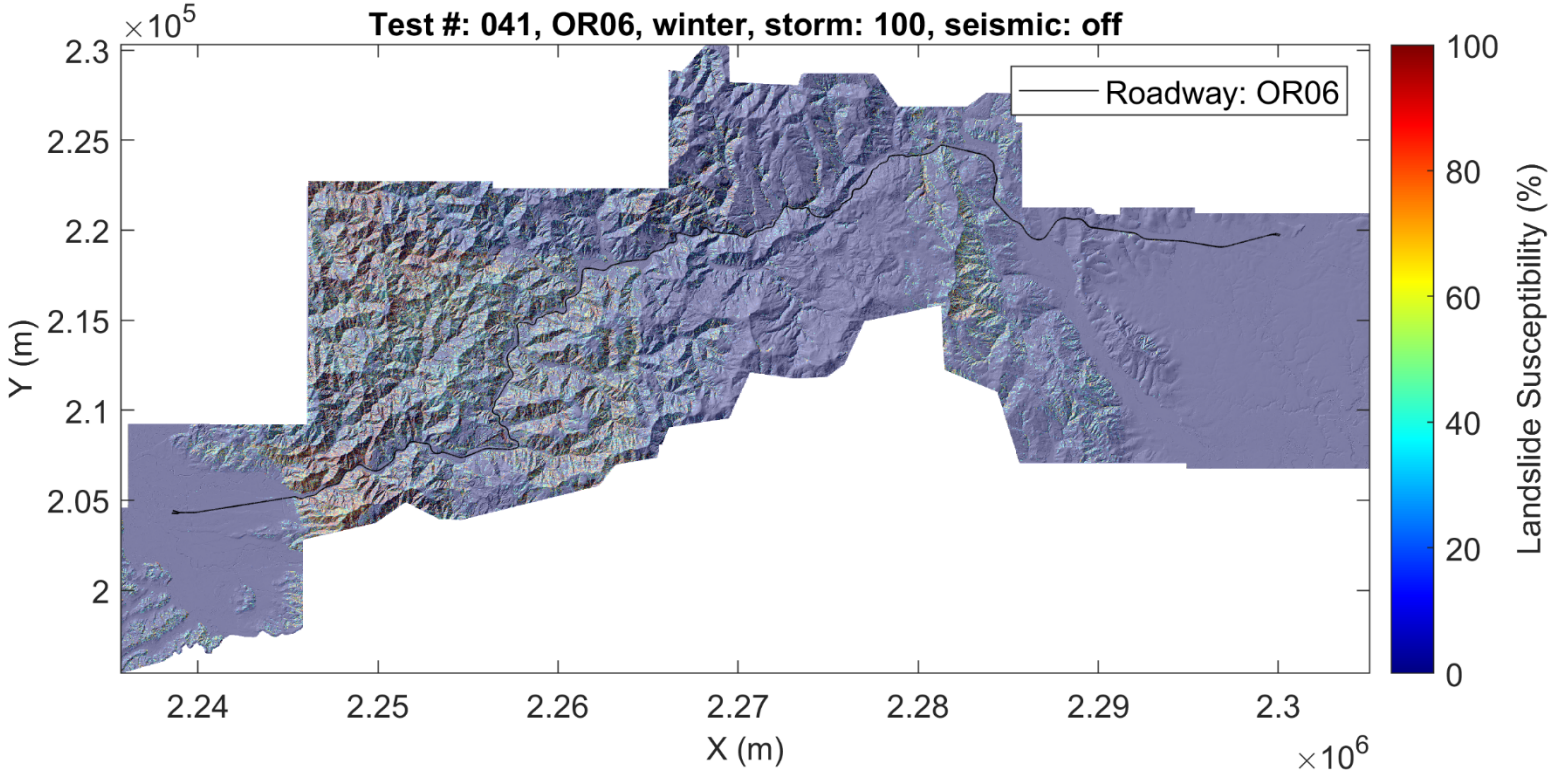

Figure 4.38: Susceptibility map for OR06: winter, 100-year rainfall event (test #: 041).

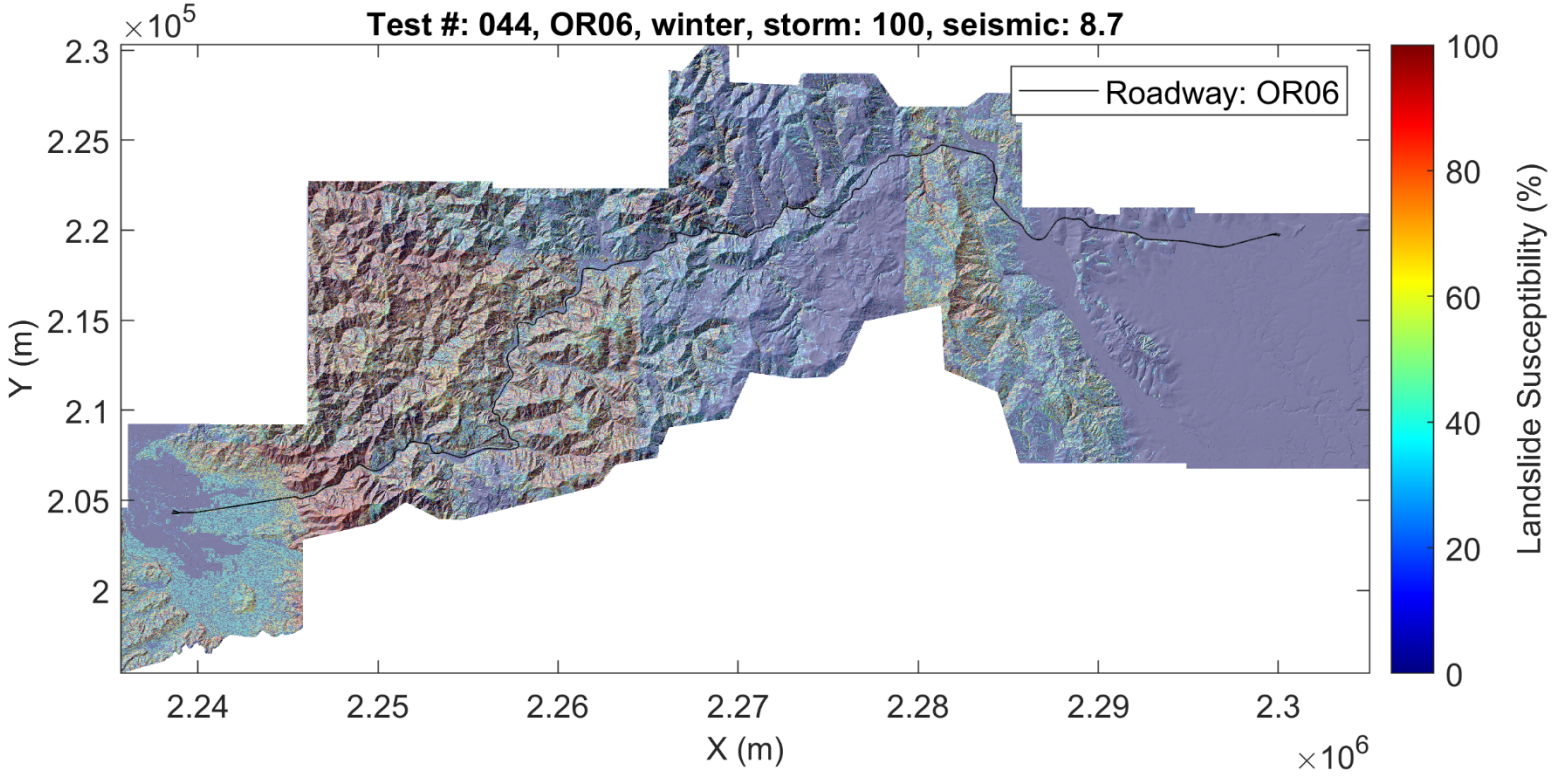

Figure 4.39: Susceptibility map for OR06: winter, 100-year rainfall event, M8.7 earthquake (test #: 044).

Figures 4.40-4.45 show susceptibility maps for corridor US20. For this corridor, very small values of susceptibility are observed for the summer season (Figure 4.40), even when subjected to strong seismicity (Figure 4.41). This entire corridor, however, exhibits high sensitivity to moisture, as demonstrated by the widespread increase in susceptibility triggered by winter antecedent conditions (Figure 4.42). This sensitivity is likely due to relatively high antecedent moisture throughout this region, in the winter, and the hydrological parameters of local soils. Figure 4.43 shows that moist soil conditions result in higher sensitivity to seismic activity, as moderate susceptibility is observed throughout the western ~2/3 of the corridor. However, Figure 4.44 shows that US20's sensitivity to seismicity is far lower than its sensitivity to increasing moisture, as a 100-year rainfall event results in very widespread values of moderate to high susceptibility throughout most of the corridor. Finally, Figure 4.45 shows that high susceptibility is further exacerbated by a M8.7 event, resulting in a widespread and severe distribution of susceptibility throughout most of the corridor. Note that PME data (discussed in Section 3.7.3) were not directly considered for the aforementioned assessments of landslide susceptibility. However, PME data was critical in validating and calibrating the forensics framework as data on only a few well-characterized landslides (both hydrologically and geometrically) were available for calibration. As this forensic analysis served as a basis for susceptibility, the PME data was invaluable.

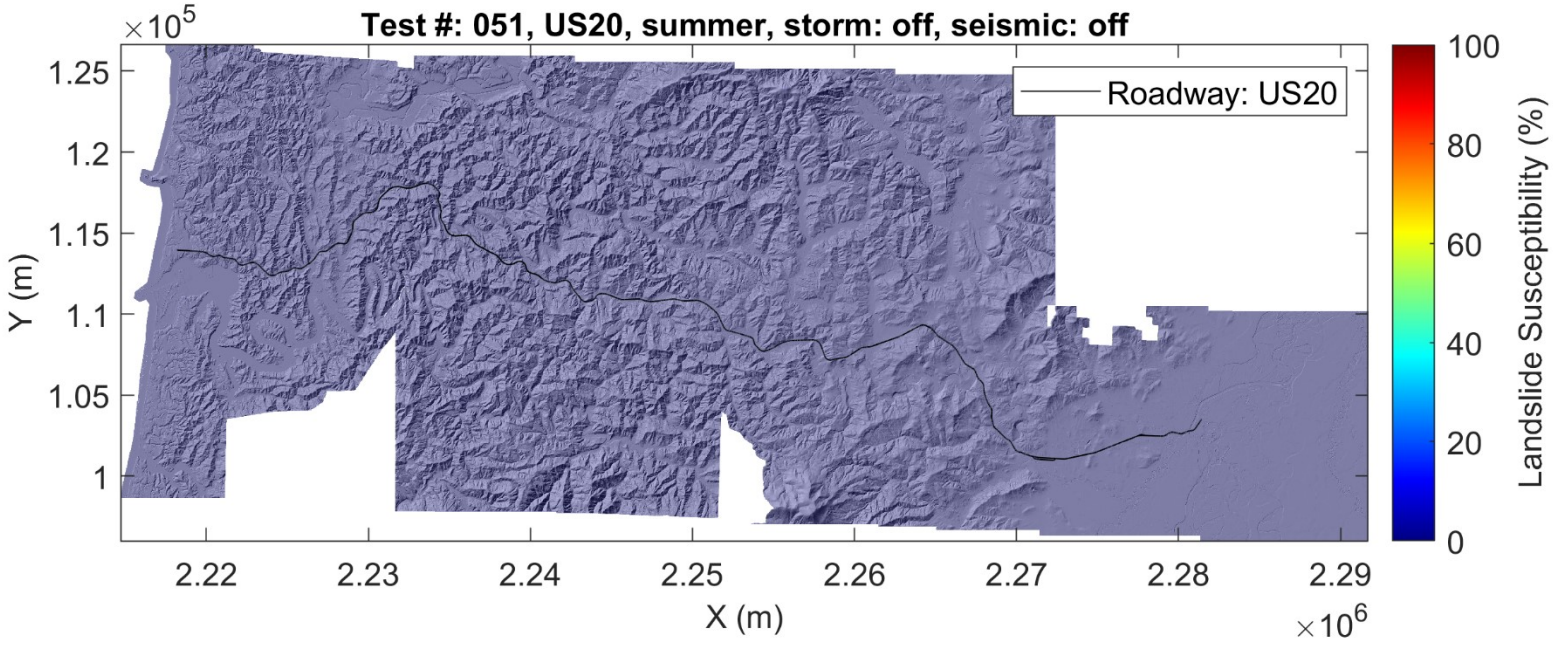

Figure 4.40: Susceptibility map for US20: summer antecedent conditions (test #: 051).

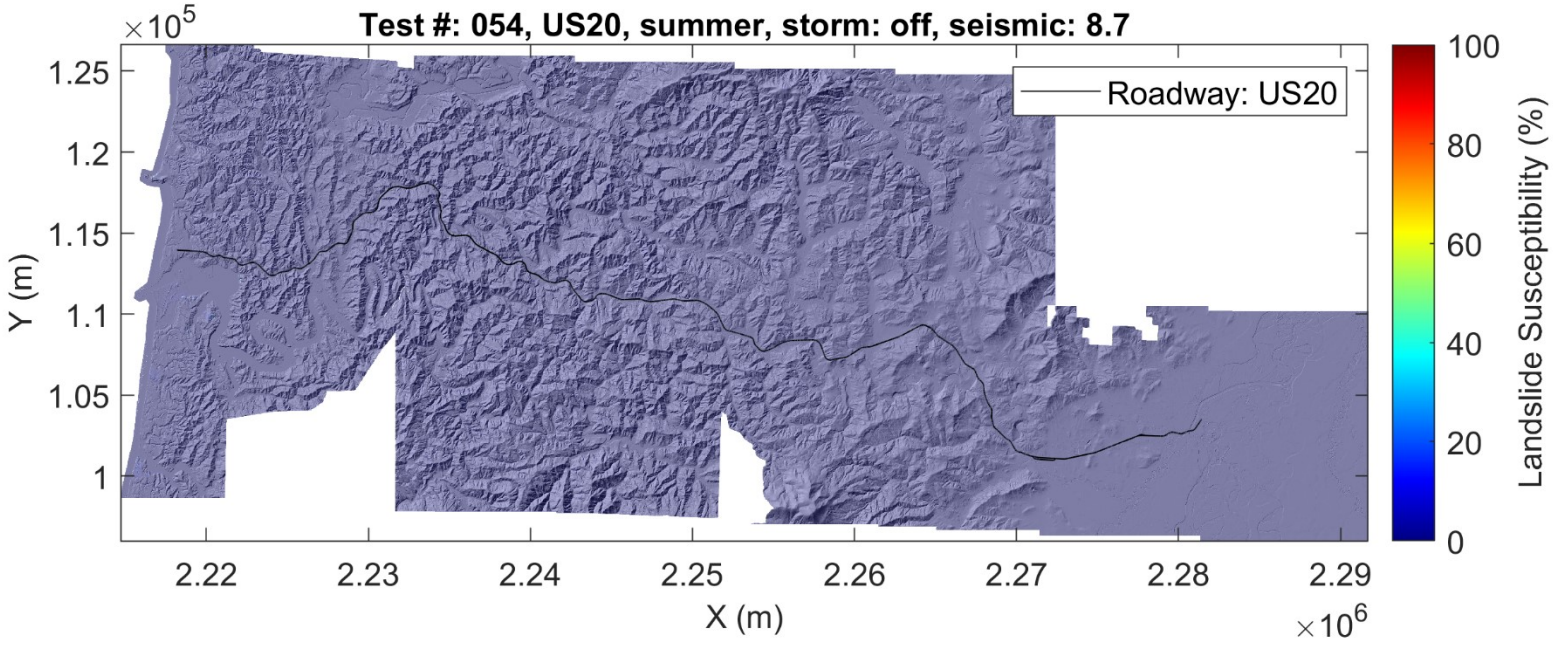

Figure 4.41: Susceptibility map for US20: summer antecedent conditions, M8.7 earthquake (test #: 054).

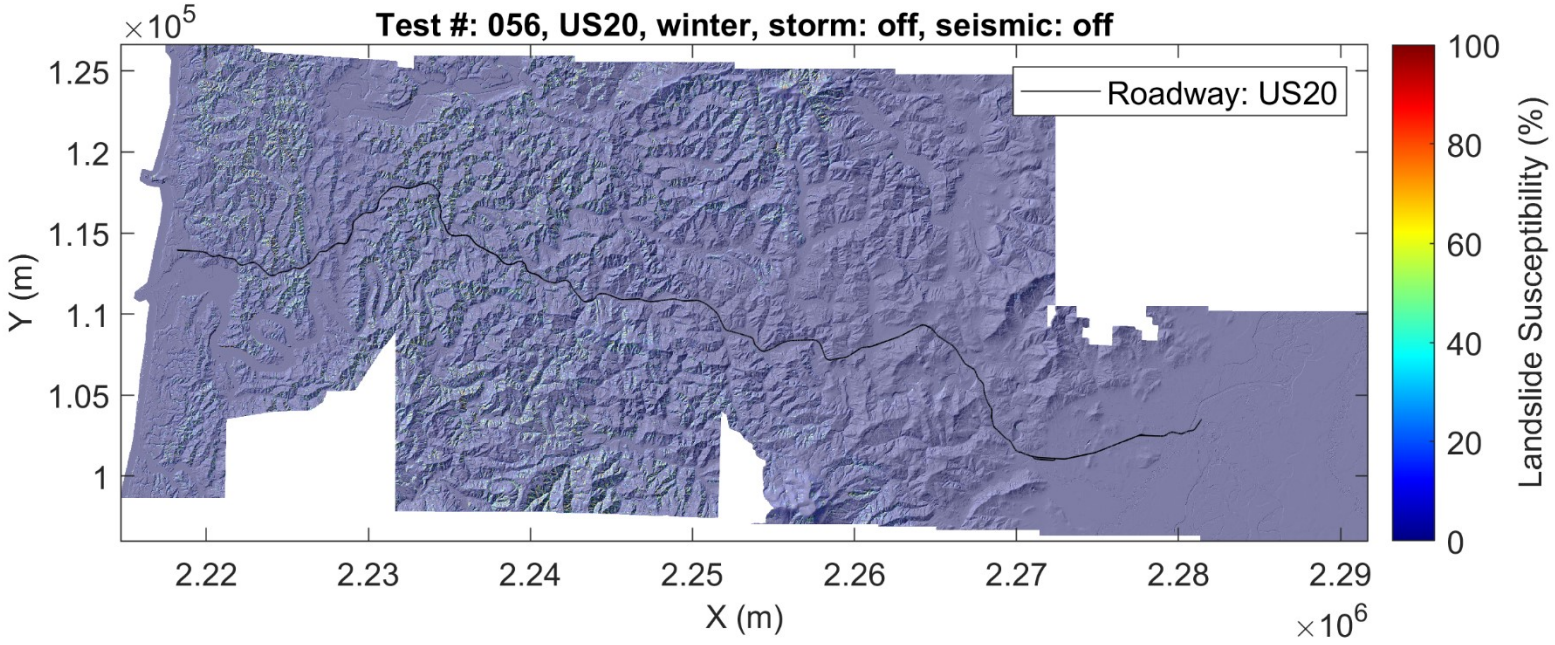

Figure 4.42: Susceptibility map for US20: winter antecedent conditions (test #: 056).

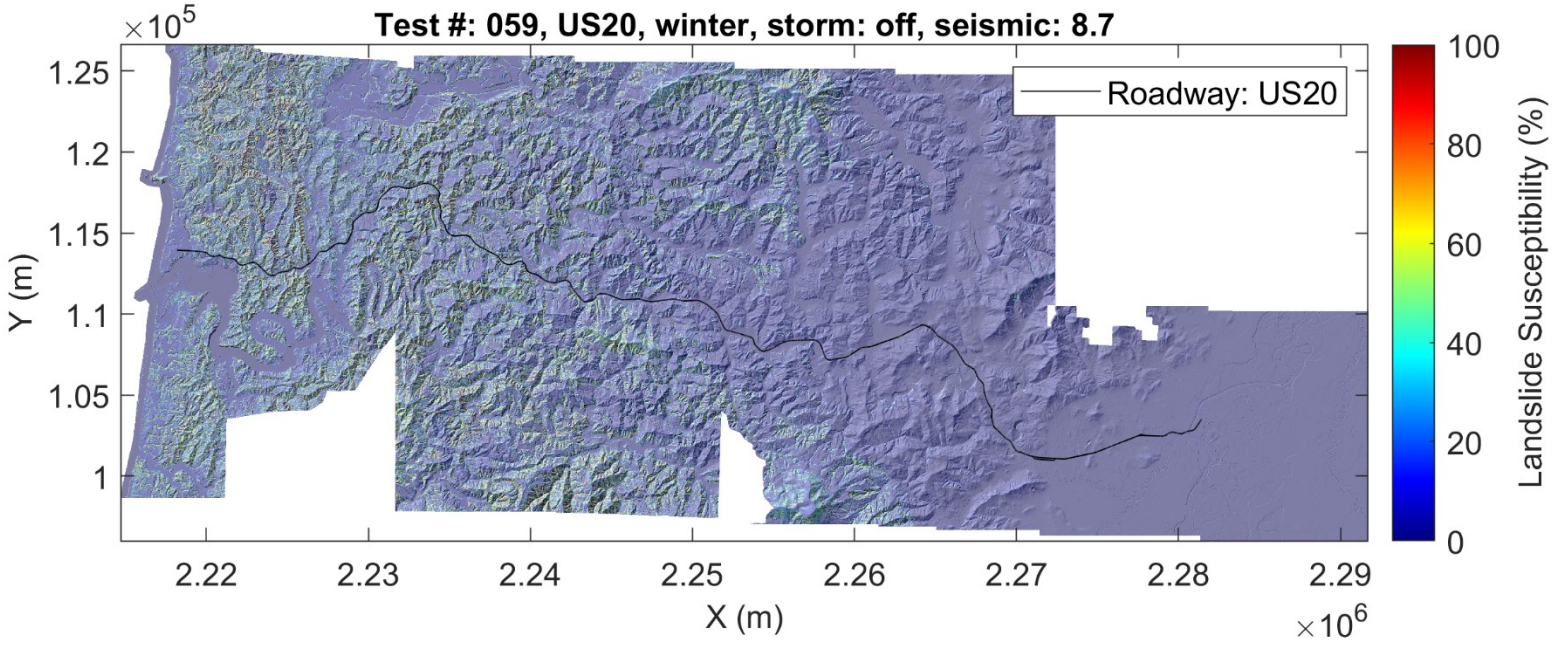

Figure 4.43: Susceptibility map for US20: winter antecedent conditions, M8.7 earthquake (test #: 059).

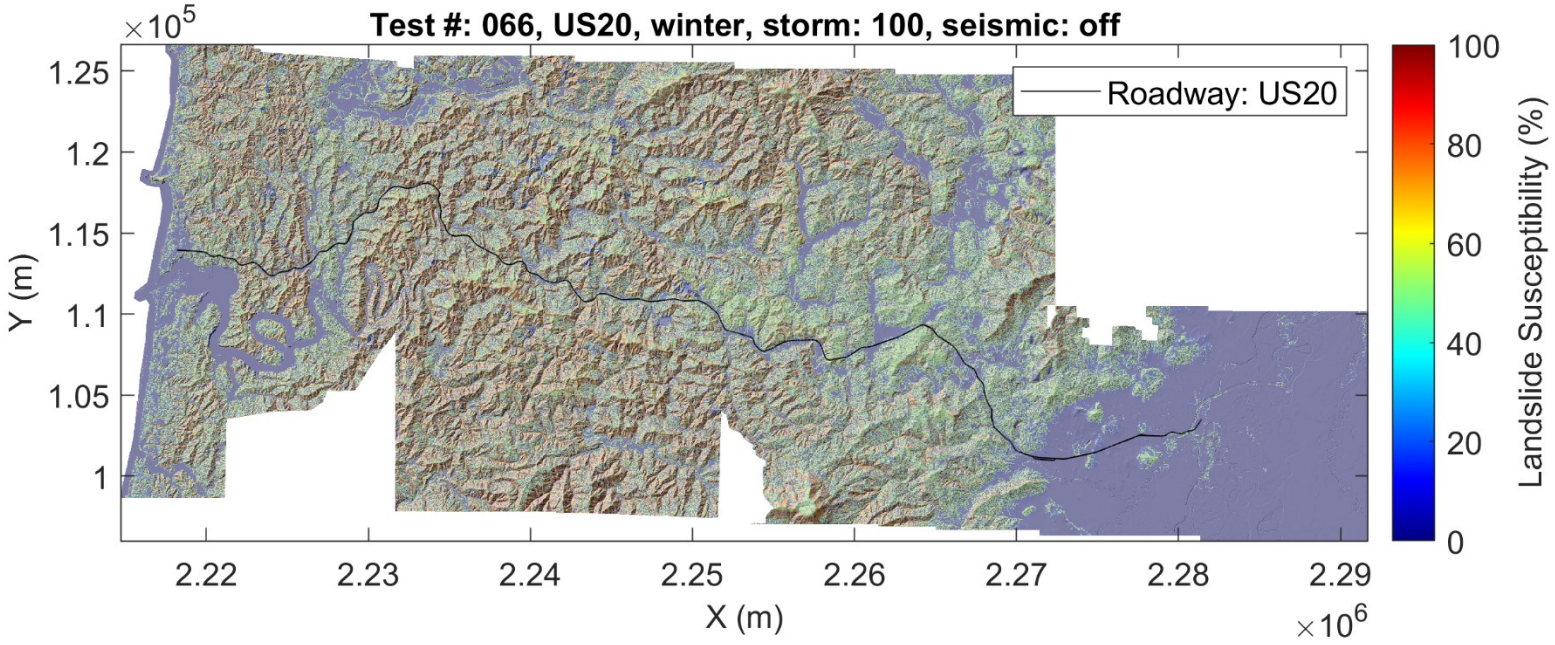

Figure 4.44: Susceptibility map for US20: winter, 100-year rainfall event (test #: 066).

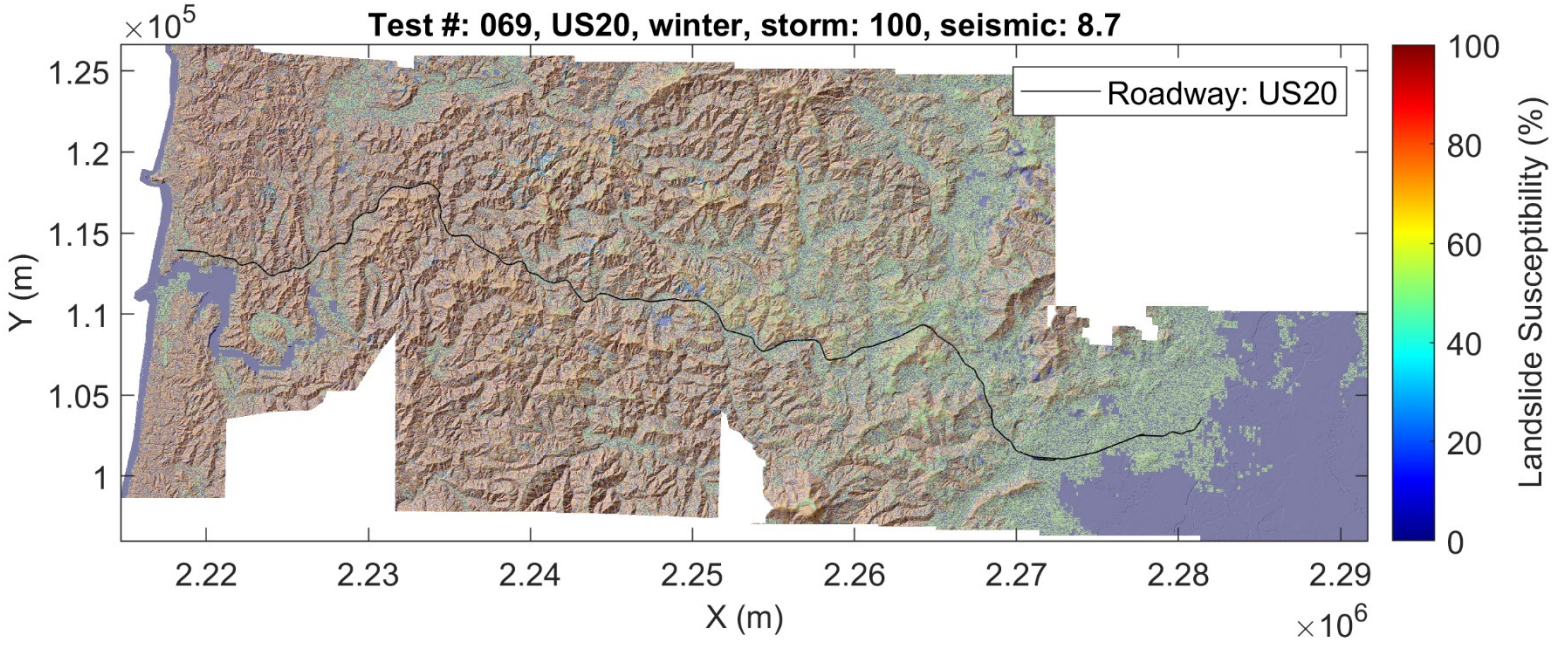

Figure 4.45: Susceptibility map for US20: winter, 100-year rainfall event, M8.7 earthquake (test #: 069).

Figures 4.46-4.51 show susceptibility maps for corridor OR42. Similarly to OR06 and US20, this corridor shows very small values of susceptibility for the summer season (Figure 4.46), even when subjected to strong seismicity (Figure 4.47). For winter antecedent conditions, slight changes in susceptibility are observed throughout the corridor, resulting in isolated pockets of low to moderate susceptibility (Figure 4.48). This contrasts with US20, which exhibited more significant sensitivity to increases in soil moisture. As seen in other corridors, Figure 4.49 shows that moist soil conditions result in higher sensitivity to seismic activity, as low susceptibility is widespread throughout the corridor, with pockets of moderate susceptibility, when subjected to strong seismicity. Finally, Figures 4.50-4.51 show that as storm intensity and seismicity increase further, higher values of susceptibility are observed throughout the corridor, with widespread moderate susceptibility, and pockets of high susceptibility, being present in Figure 4.51. OR42 exhibits more uniform susceptibility in areas of high relief, as opposed to OR30 and OR06 which exhibited more localized behaviors.

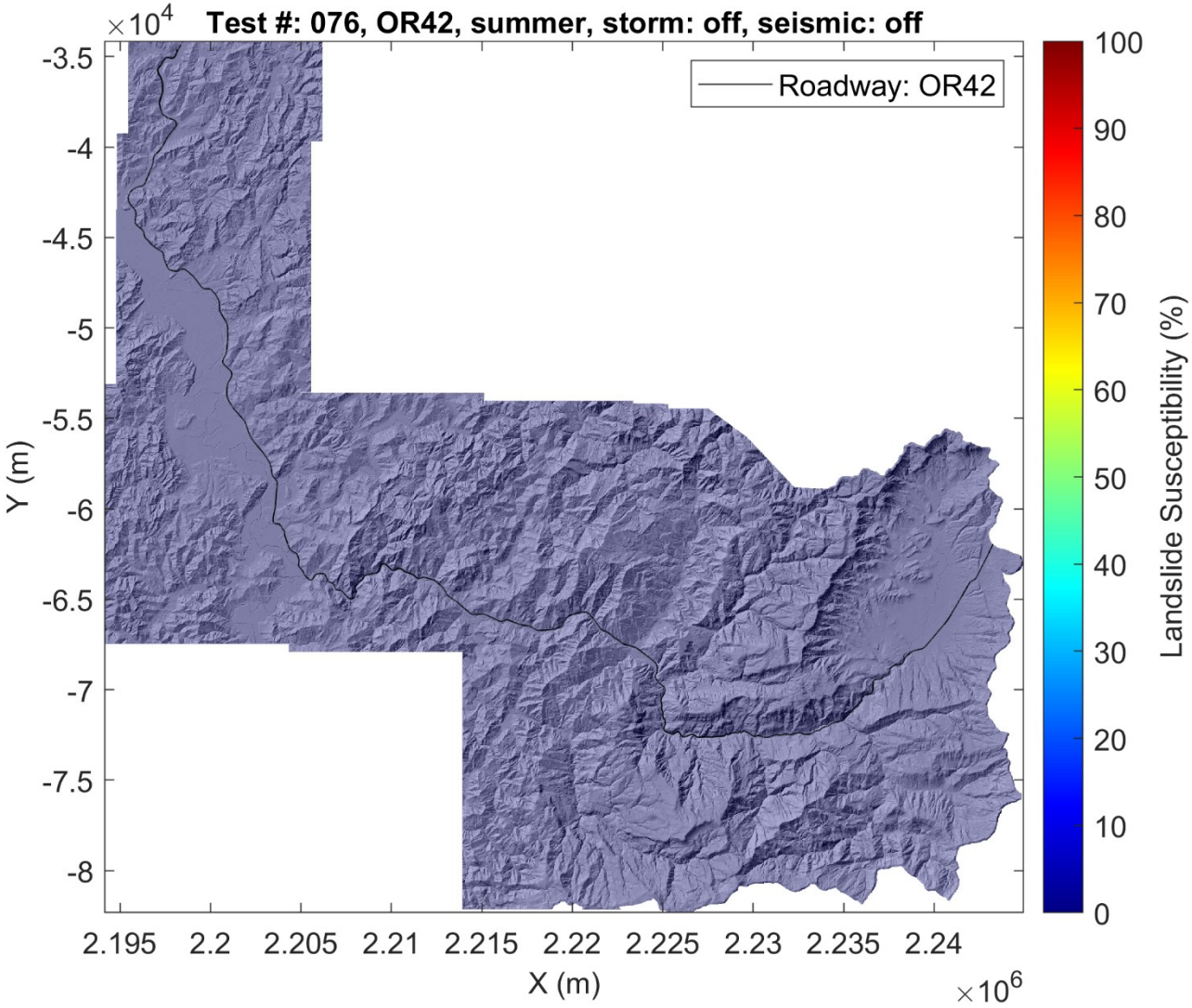

Figure 4.46: Susceptibility map for OR42: summer antecedent conditions (test #: 076).

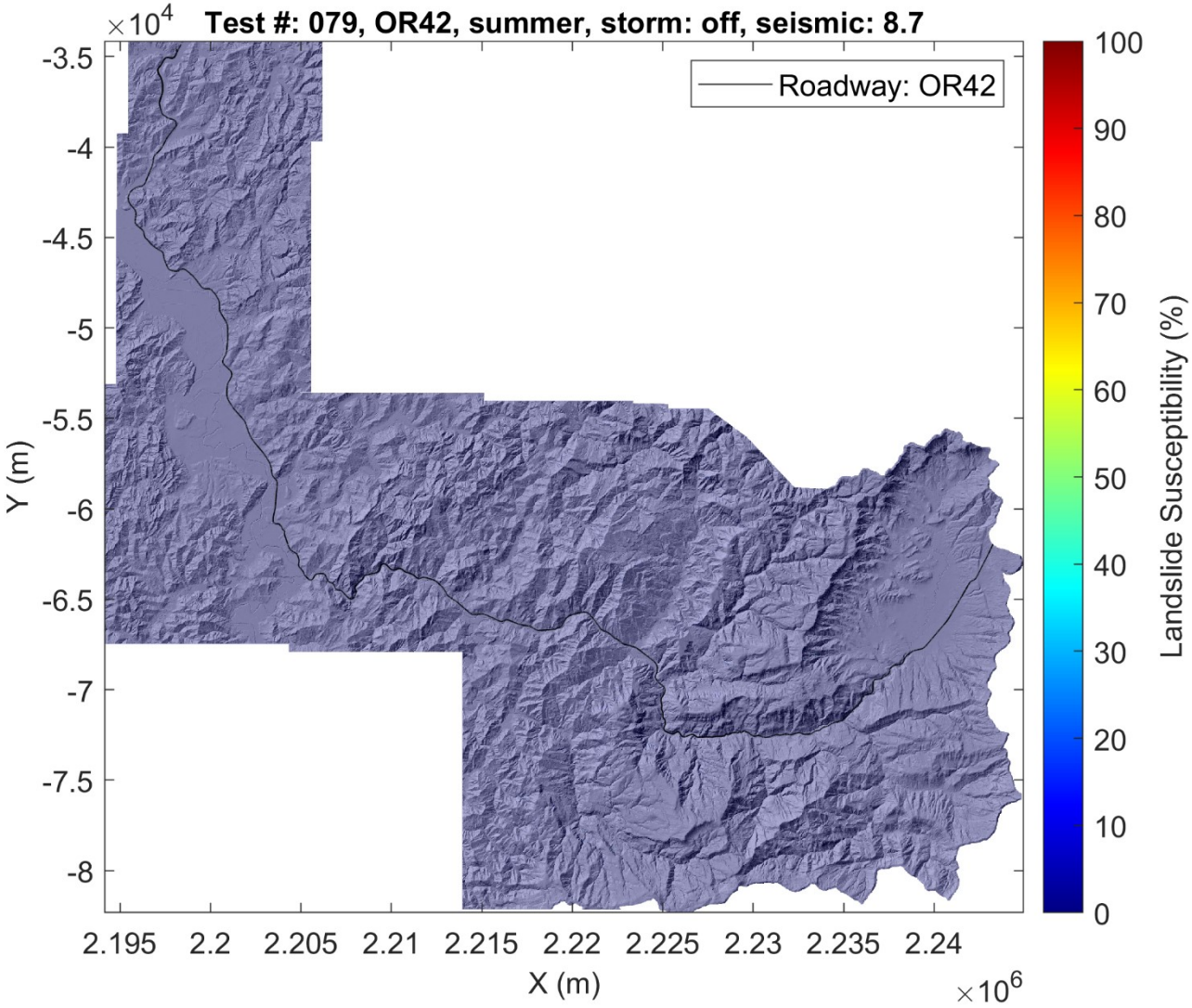

Figure 4.47: Susceptibility map for OR42: summer antecedent conditions, M8.7 earthquake (test #: 079).

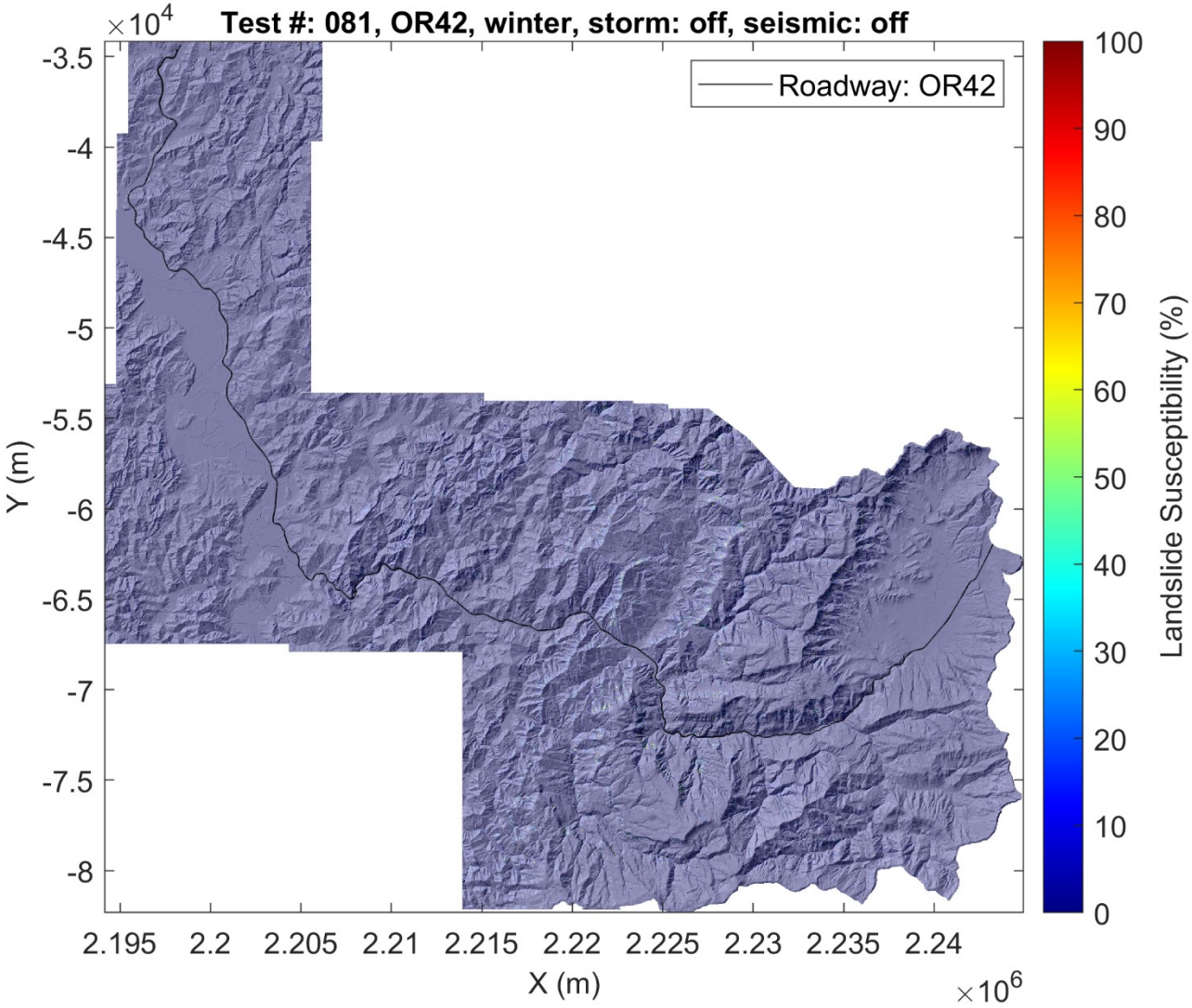

Figure 4.48: Susceptibility map for OR42: winter antecedent conditions (test #: 081).

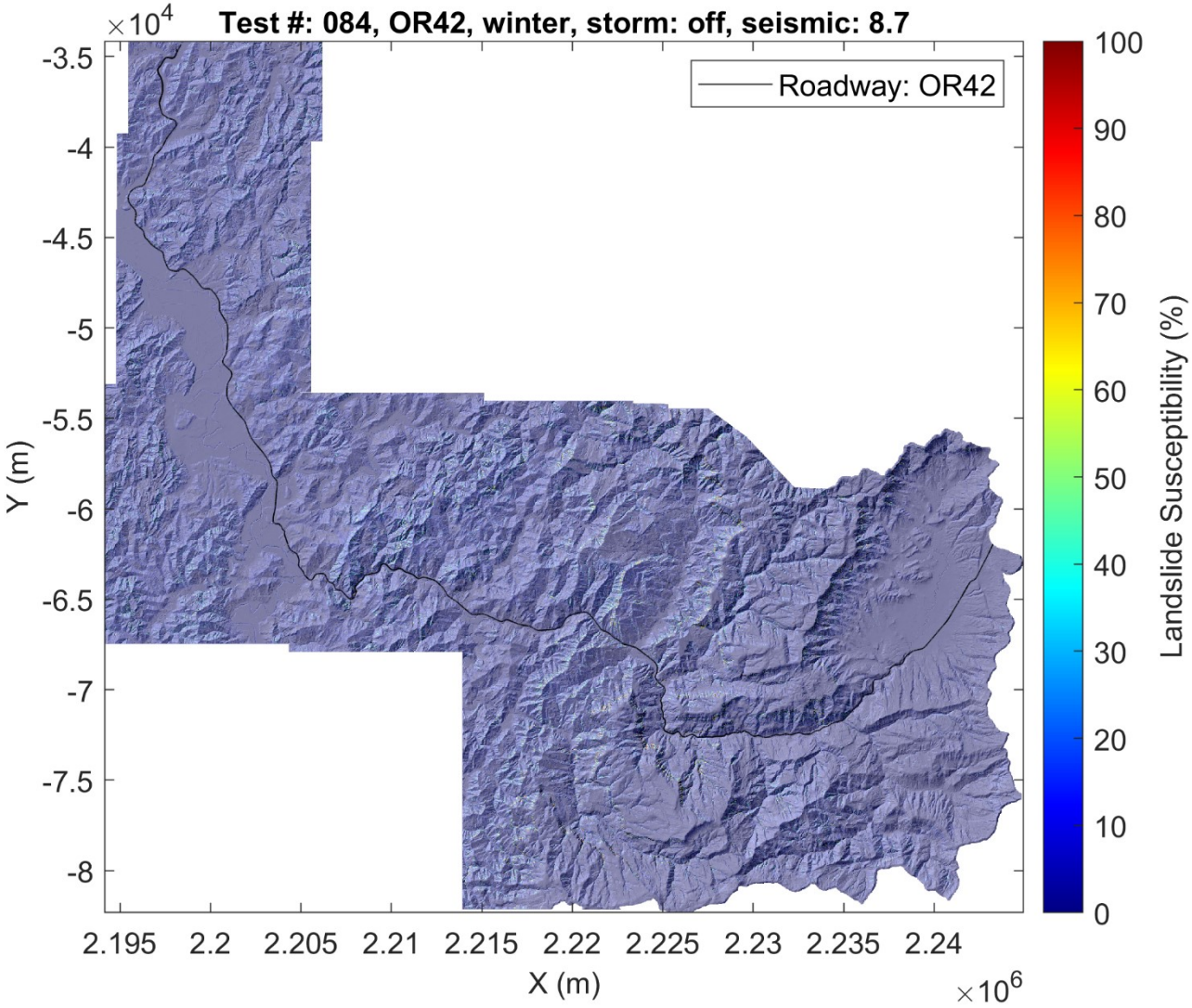

Figure 4.49: Susceptibility map for OR42: winter antecedent conditions, M8.7 earthquake (test #: 084).

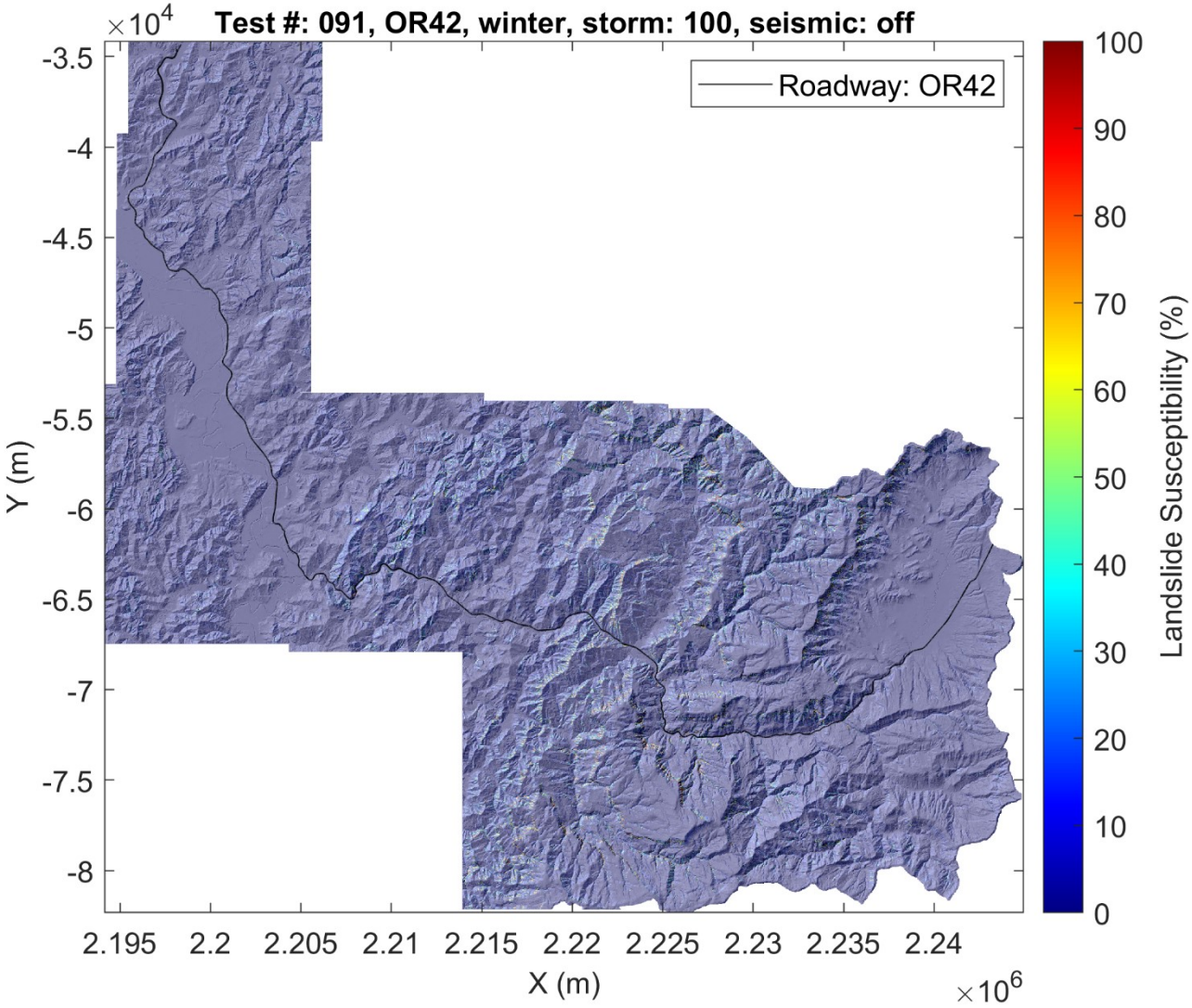

Figure 4.50: Susceptibility map for OR42: winter, 100-year rainfall event (test #: 091).

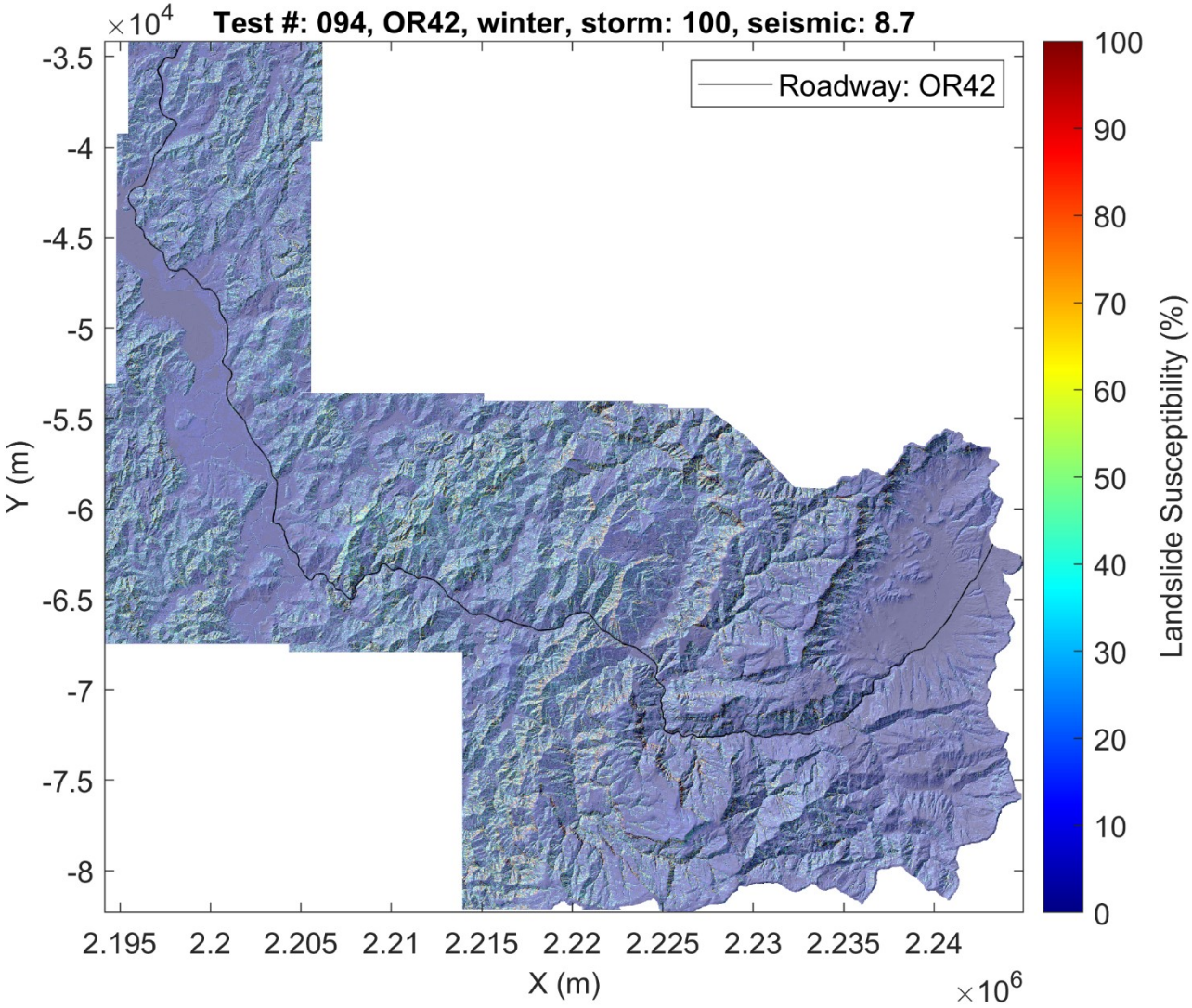

Figure 4.51: Susceptibility map for OR42: winter, 100-year rainfall event, M8.7 earthquake (test #: 094).

4.5 HAZARD

To compute hazard, the susceptibility maps shown in Section 4.4 are multiplied by the probability of their corresponding forcing events. Hazard maps expand on susceptibility maps by not only considering where landslides are likely to occur, but how likely those landslides are to occur given specific physical drivers. Probabilities for each of the tests highlighted in Table 4.4 are shown in Table 4.5 (details about these probabilities are listed in the footnotes and discussed below). Hazard maps for the tests highlighted in Table 4.4 are shown in Figures 4.52-4.75. A complete table of probabilities may be found in the supplemental data provided with this report and a full suite of hazard maps for all tests in Table 4.4 may be found in Appendix B. Note that there are no hazard maps available for M8.1 earthquake test scenarios, as to the best of the authors' knowledge, there are no published probabilities for this physical driver.

Probability is calculated differently for different types of landslide forcing events. Rainfall hazard maps reflect the probability of storm occurrence on any given year and seismic hazard maps reflect the probability of earthquake occurrence within the 50-year period 2010-2060 (Goldfinger et al., 2012). For multi-hazard events, probabilities of both the rainfall event and the seismic event on any given day are calculated, and then multiplied together. Note that since the presented hazard values vary by several orders of magnitude depending on the forcing events, the colorbars of the maps shown in Figures 4.52-4.75 range from the minimum to maximum value of hazard for each scenario. A complete table of probabilities for all tests shown in Table 4.4 may be found in the digital appendix provided with this report.

Table 4.5: Summary of Hazard Probabilities used for the Test Numbers Highlighted in Table 4.5.

Test #	*Highway*	*Season*	*Rainfall*	*Rainfall Probability*[1]	*EQ Moment Magnitude*	*EQ Mag. Probability*[2]	*Multi-Hazard Probability*[3]	*Hazard Map Probability*[4]
1	US30	summer	off	N/A	off	N/A	N/A	1
4	US30	summer	off	N/A	8.7	0.14	N/A	0.14
6	US30	winter	off	N/A	off	N/A	N/A	1
9	US30	winter	off	N/A	8.7	0.14	N/A	0.14
16	US30	winter	100-year	0.01	off	N/A	N/A	0.01
19	US30	winter	100-year	0.01	8.7	0.14	2.1017e-10	2.1017e-10
26	OR06	summer	off	N/A	off	N/A	N/A	1
29	OR06	summer	off	N/A	8.7	0.14	N/A	0.14
31	OR06	winter	off	N/A	off	N/A	N/A	1
34	OR06	winter	off	N/A	8.7	0.14	N/A	0.14
41	OR06	winter	100-year	0.01	off	N/A	N/A	0.01
44	OR06	winter	100-year	0.01	8.7	0.14	2.1017e-10	2.1017e-10
51	US20	summer	off	N/A	off	N/A	N/A	1
54	US20	summer	off	N/A	8.7	0.14	N/A	0.14
56	US20	winter	off	N/A	off	N/A	N/A	1
59	US20	winter	off	N/A	8.7	0.14	N/A	0.14
66	US20	winter	100-year	0.01	off	N/A	N/A	0.01
69	US20	winter	100-year	0.01	8.7	0.14	2.1017e-10	2.1017e-10
76	OR42	summer	off	N/A	off	N/A	N/A	1
79	OR42	summer	off	N/A	8.7	0.14	N/A	0.14
81	OR42	winter	off	N/A	off	N/A	N/A	1
84	OR42	winter	off	N/A	8.7	0.14	N/A	0.14
91	OR42	winter	100-year	0.01	off	N/A	N/A	0.01
94	OR42	winter	100-year	0.01	8.7	0.14	2.1017e-10	2.1017e-10

[1] Rainfall probability represents likelihood storm occurring on any given single year.
[2] Earthquake probability represents likelihood of event occurring within the 50-year period of 2010-2060.
[3] Multi-hazard probability based on probability of multiple events on a single day (applicable to EQ magnitudes 8.4, 8.7, and 9.0 only).
[4] Probability multiplied by susceptibility to calculate hazard maps.

Figures 4.52-4.57 show hazard maps for corridor US30. Figure 4.52 shows hazard for the summer, with no applied physical drivers. In this case, hazard is equal to susceptibility, as the probability of summer occurring is 100%. For these conditions, there is a sparse distribution of hazard, with only small localized pockets of higher hazard occurring in some areas. Figure 4.53 shows that under seismic forcing, there more widespread hazard with maximum values of around 12%. Figure 4.54 shows hazard for antecedent winter conditions. In this case, hazard is equal to susceptibility, as antecedent conditions have a 100% chance of occurrence. Figure 4.54 shows more widespread hazard than summer conditions, with pockets of higher susceptibility. Figure 4.55 shows more widespread and uniform hazard when strong seismic forcing is applied. In comparison, application of a heavy rainfall event results in hazard values more concentrated into the central region of US30 (Figure 4.56). Finally, Figure 4.57 shows widespread, but low, values of hazard throughout the corridor, with the highest values concentrated into the central region. Note that while this multi-hazard event produced very high values of susceptibility, the probability of the two hazard events occurring on the same day is quite low, resulting in relatively low values of hazard.

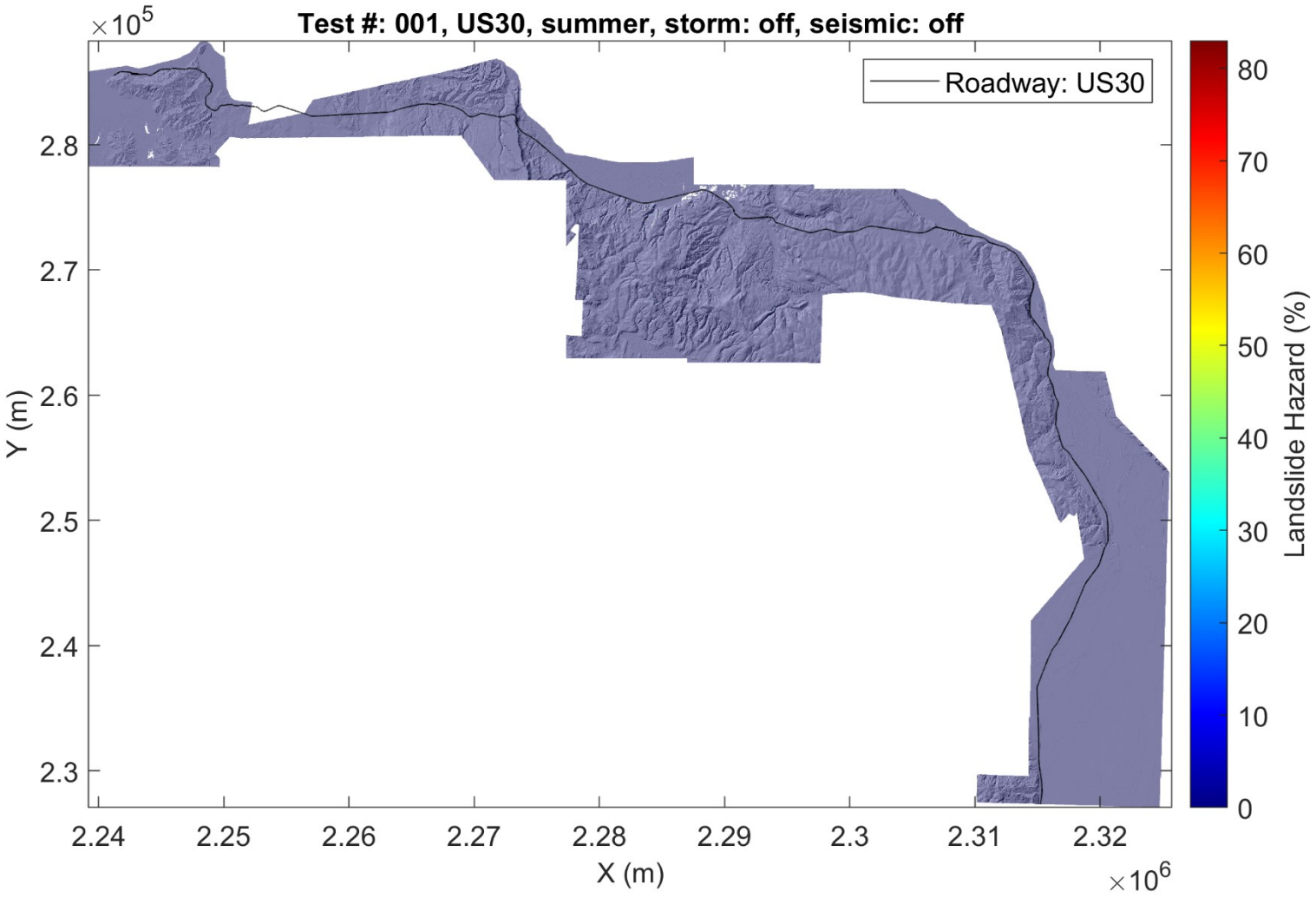

Figure 4.52: Hazard map for US30: summer antecedent conditions (test #: 001).

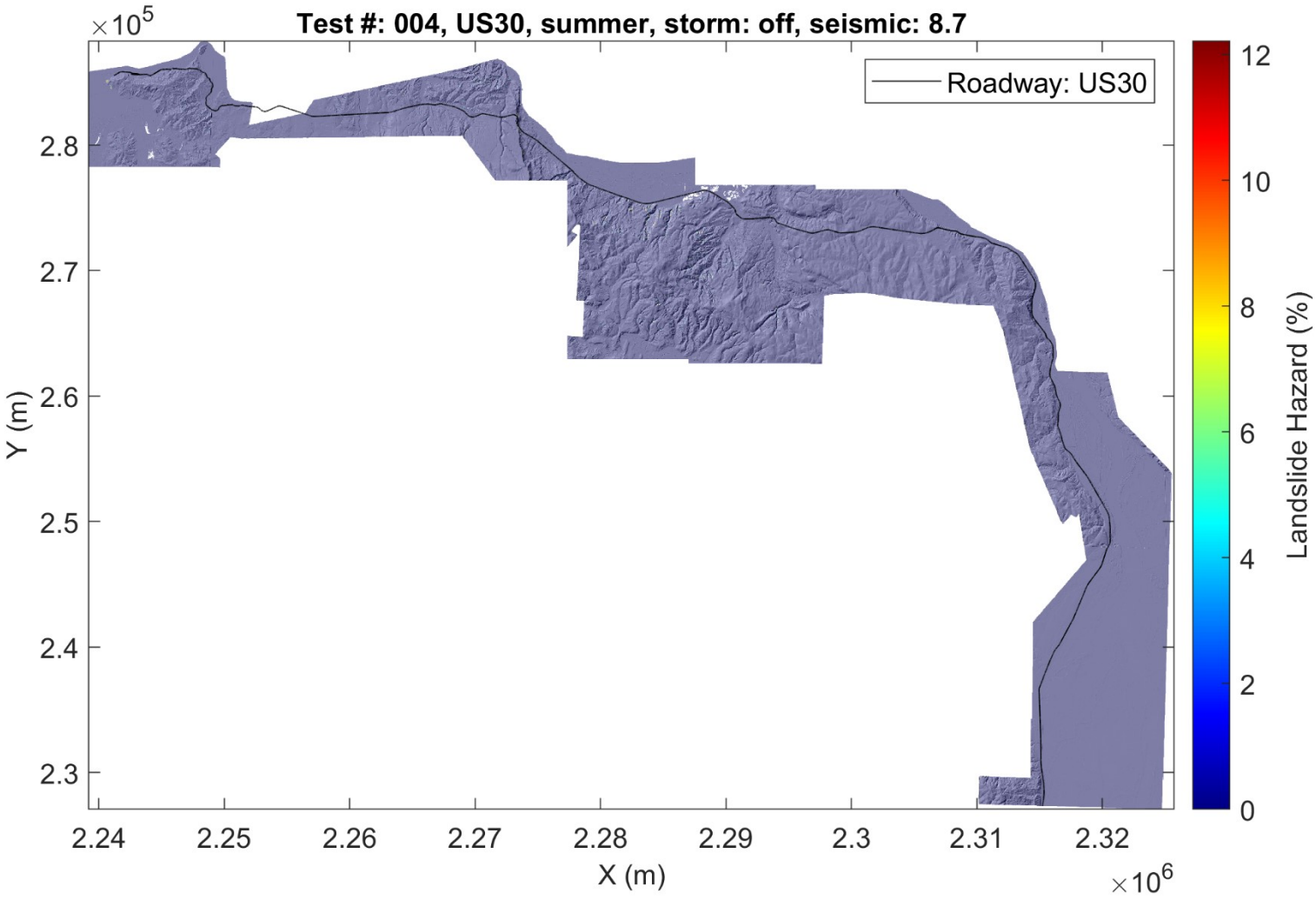

Figure 4.53: Hazard map for US30: summer antecedent conditions, M8.7 earthquake (test #: 004).

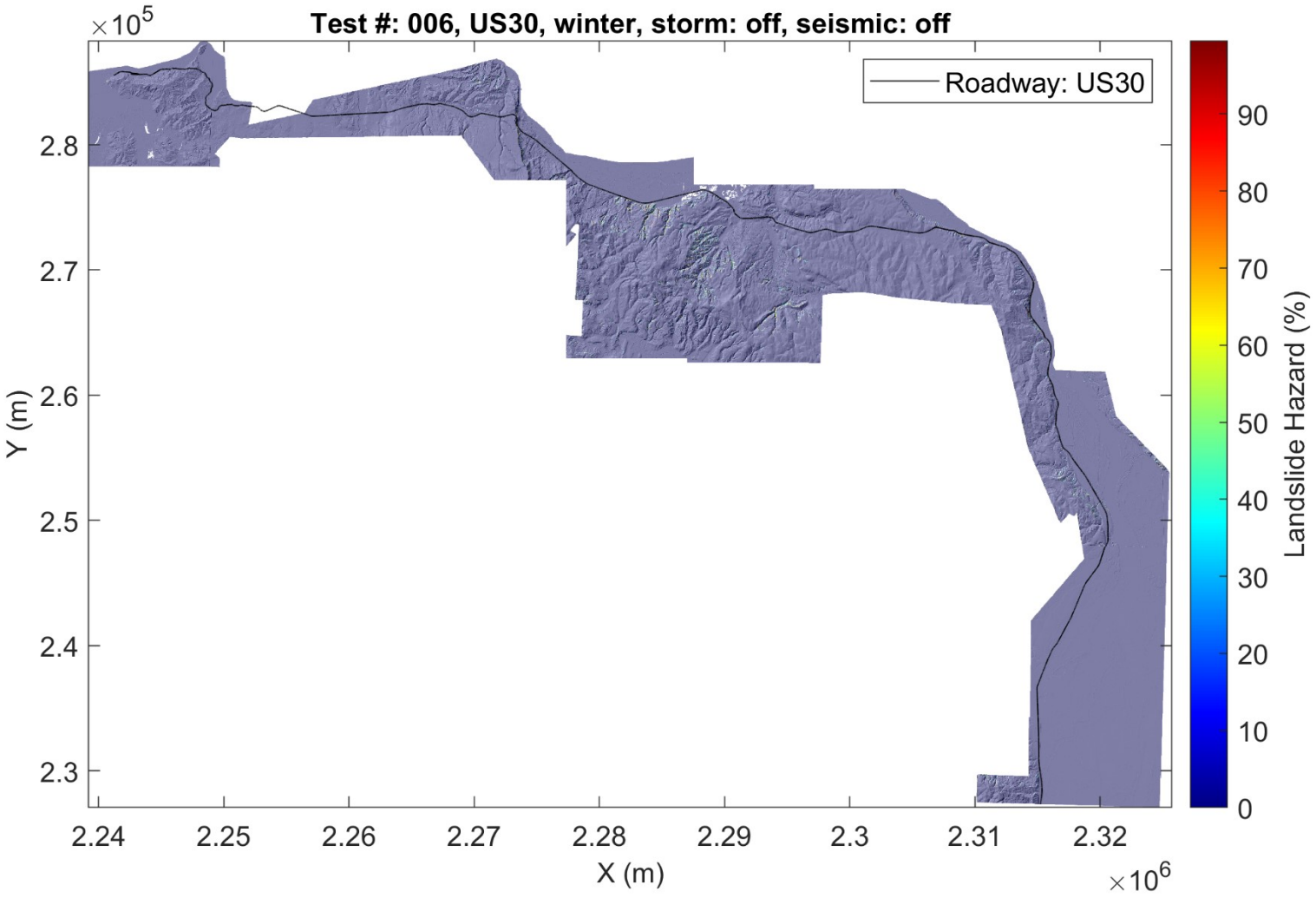

Figure 4.54: Hazard map for US30: winter antecedent conditions (test #: 006).

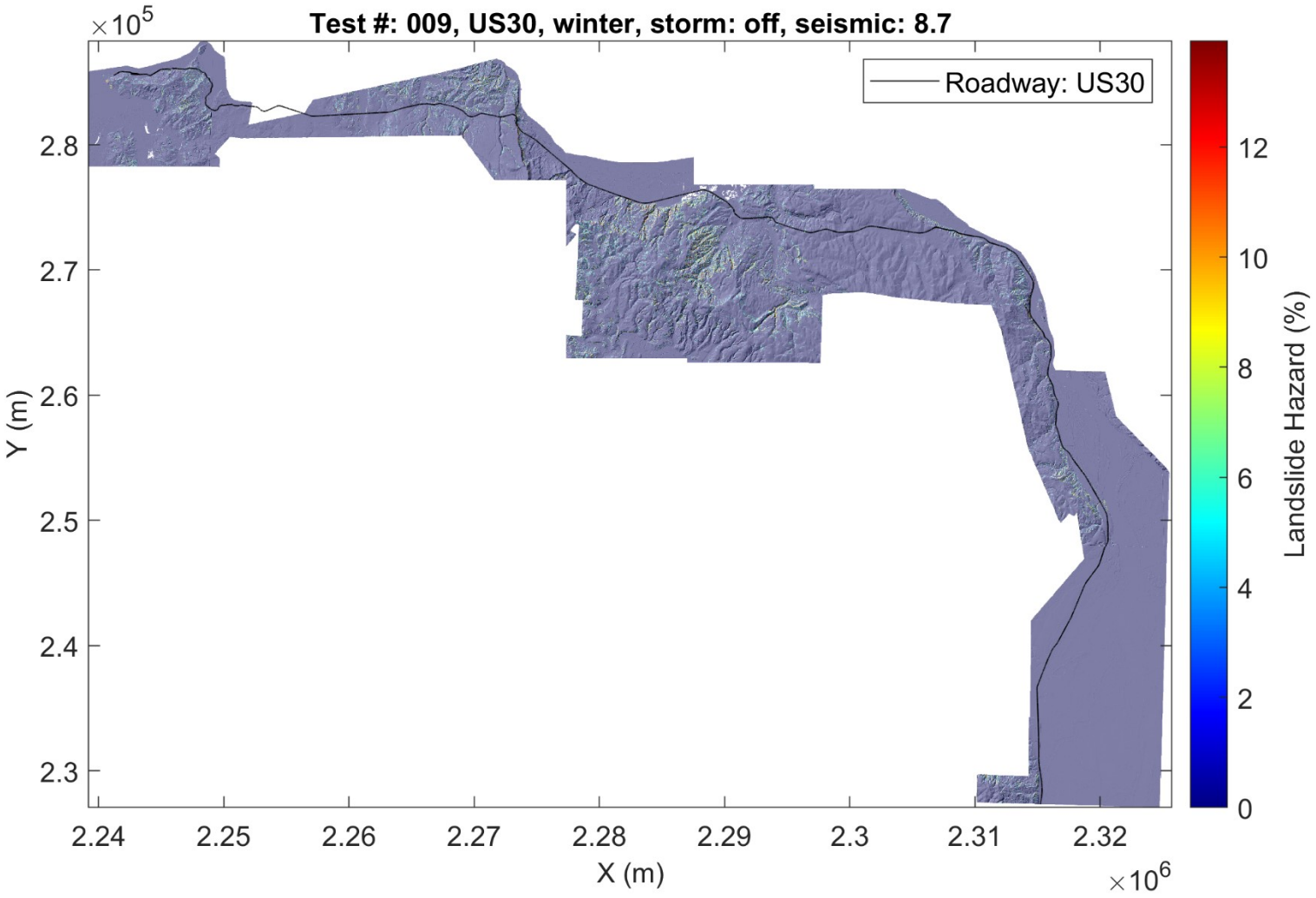

Figure 4.55: Hazard map for US30: winter antecedent conditions, M8.7 earthquake (test #: 009).

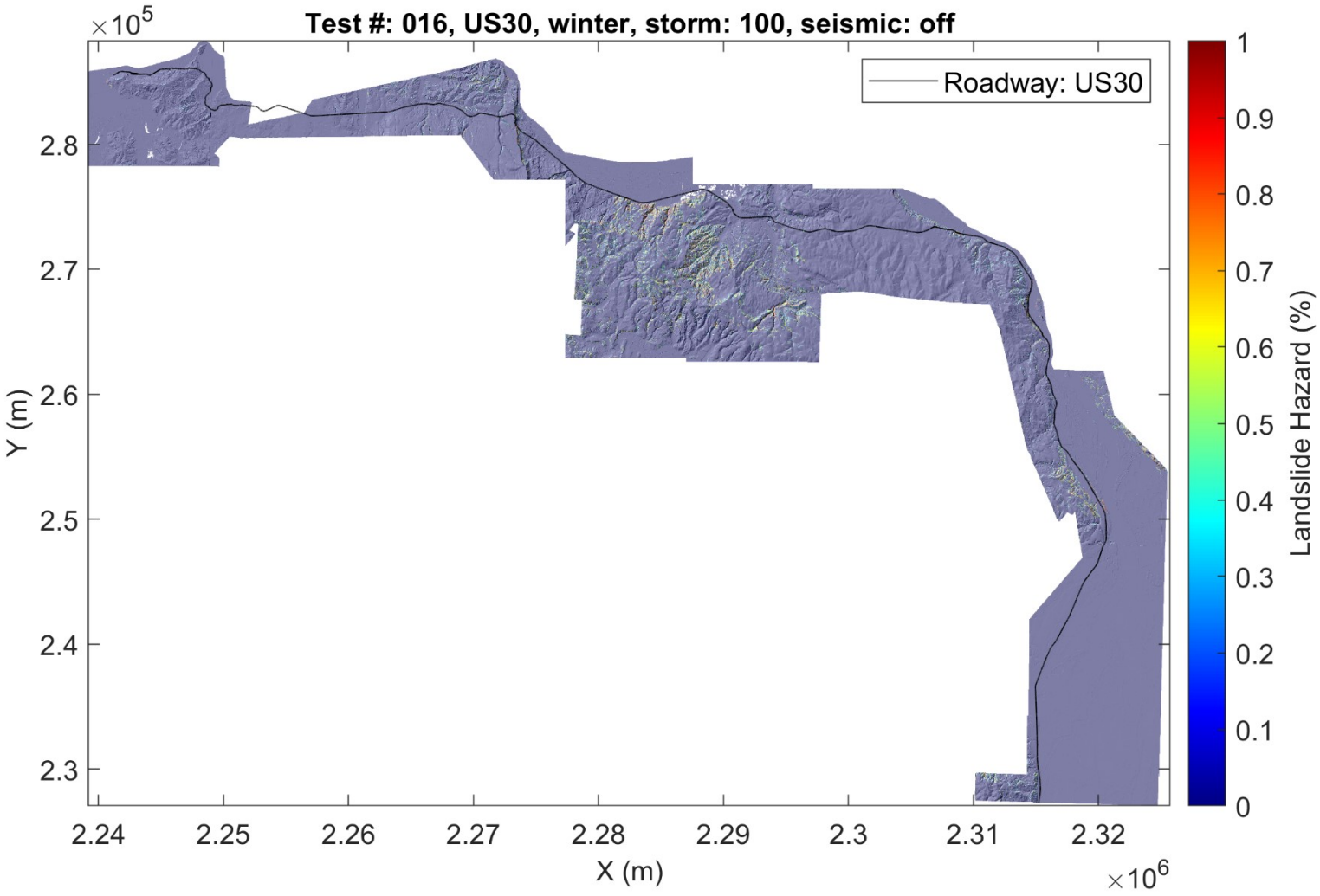

Figure 4.56: Hazard map for US30: winter, 100-year rainfall event (test #: 016).

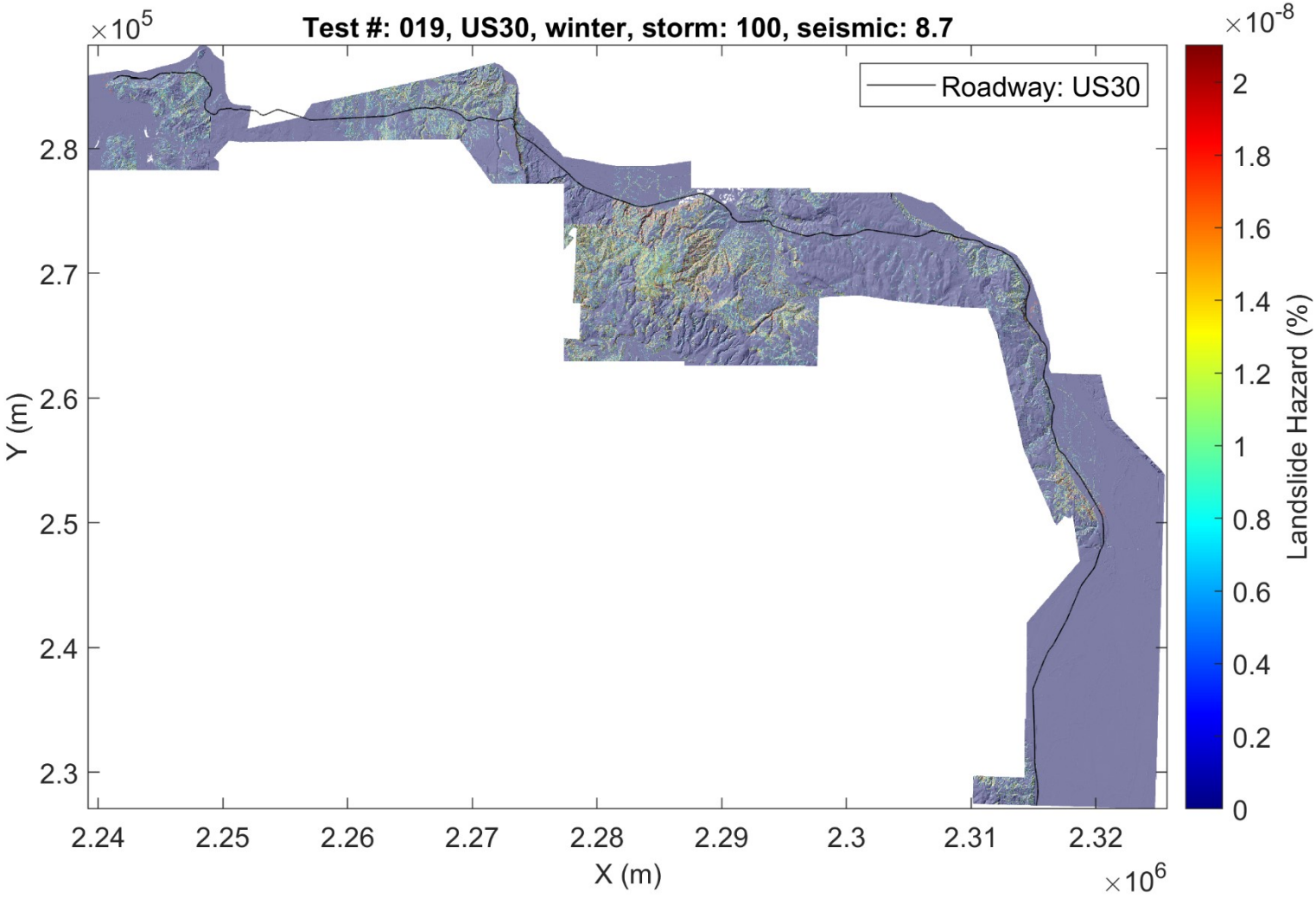

Figure 4.57: Hazard map for US30: winter, 100-year rainfall event, M8.7 earthquake (test #: 019).

Figures 4.58-4.63 show hazard maps for corridor OR06. Figure 4.58 shows hazard for the summer, with no applied physical drivers. In this case, hazard is equal to susceptibility, as the probability of summer occurring is 100%. Similar to US30, there is a sparse distribution of hazard, with only small localized pockets of higher hazard occurring in some areas. Figure 4.59 shows that under seismic forcing, there is slightly more widespread hazard, concentrated in the western region, with maximum values of around 13%. Figure 4.60 shows hazard for antecedent winter conditions. In this case, hazard is equal to susceptibility, as antecedent conditions have a 100% chance of occurrence. Figure 4.60 shows more widespread hazard than summer conditions, with pockets of higher susceptibility. Although the maximum value of hazard in Figure 4.61 is similar to that in Figure 4.59, Figure 4.61 shows more widespread and uniform hazard when strong seismic forcing is applied in the winter. Figure 4.62 shows concentrated distributions in the eastern and western regions of the corridor. However, hazard values are slightly lower due to the probability of a 100-year rainfall event. Finally, Figure 4.63 shows widespread, but low, values of hazard throughout the corridor, with the highest values concentrated into the eastern and western regions. As mentioned for corridor US30, the probability of these two hazard events occurring on the same day is quite low, resulting in relatively low values of hazard.

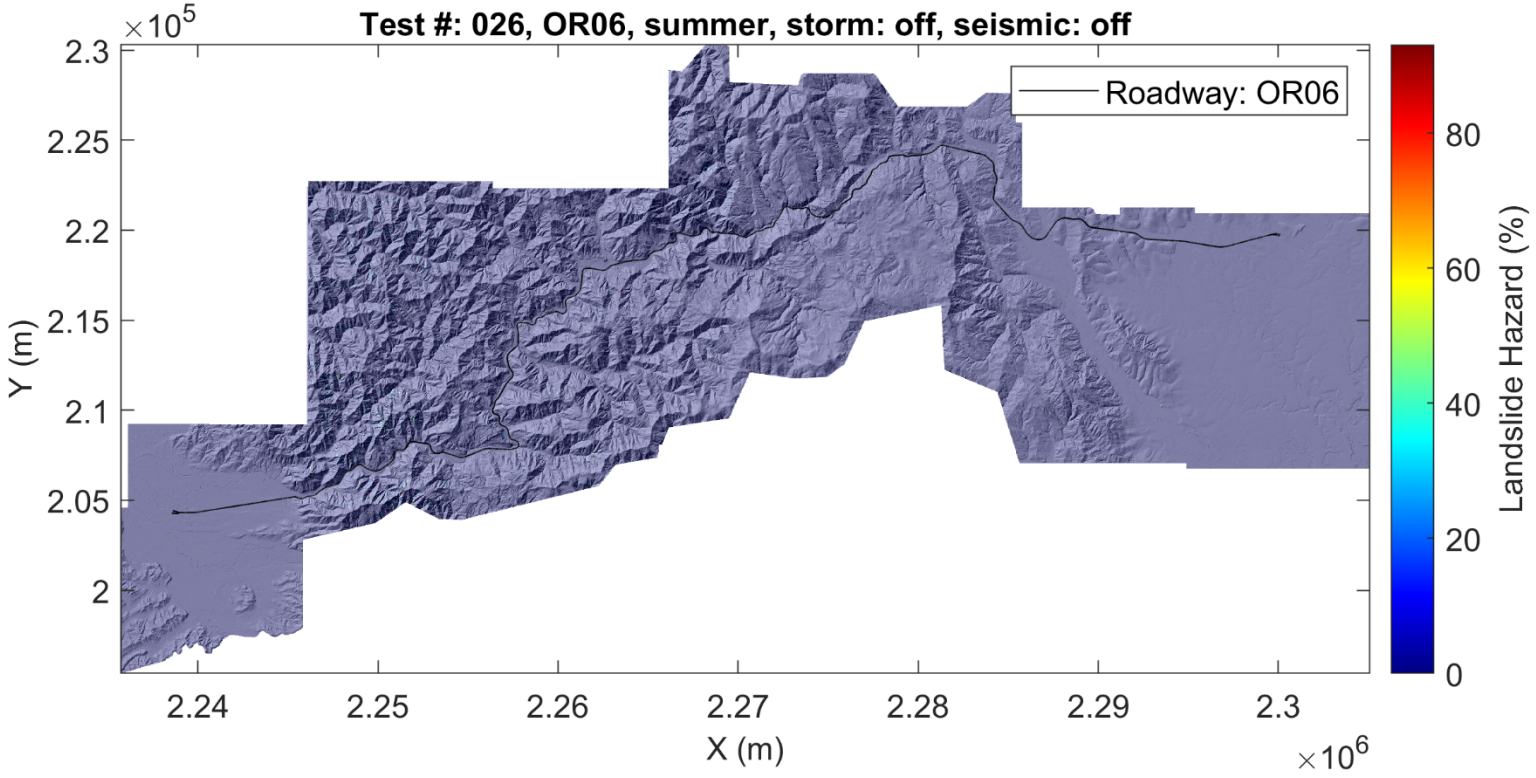

Figure 4.58: Hazard map for OR06: summer antecedent conditions (test #: 026).

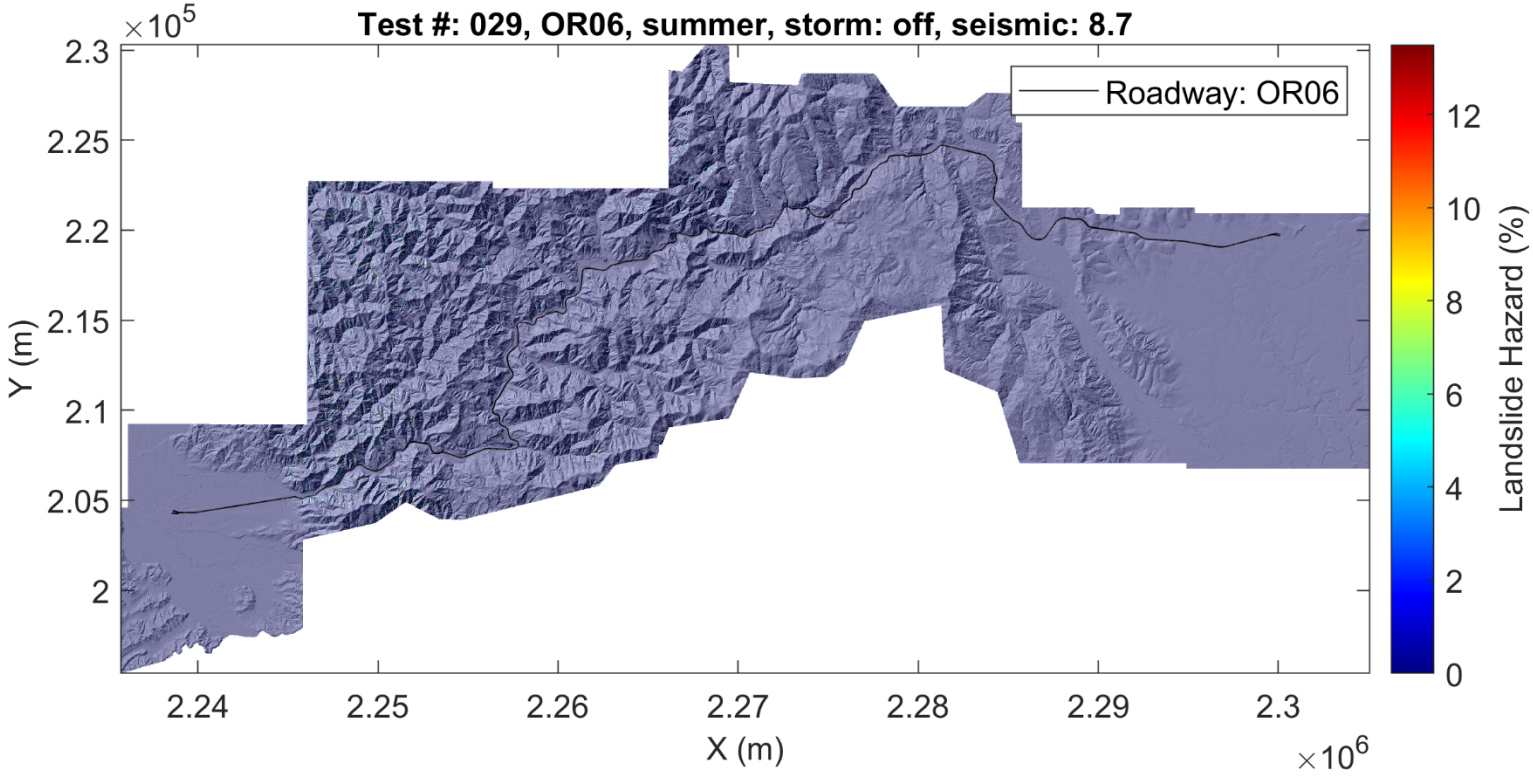

Figure 4.59: Hazard map for OR06: summer antecedent conditions, M8.7 earthquake (test #: 029).

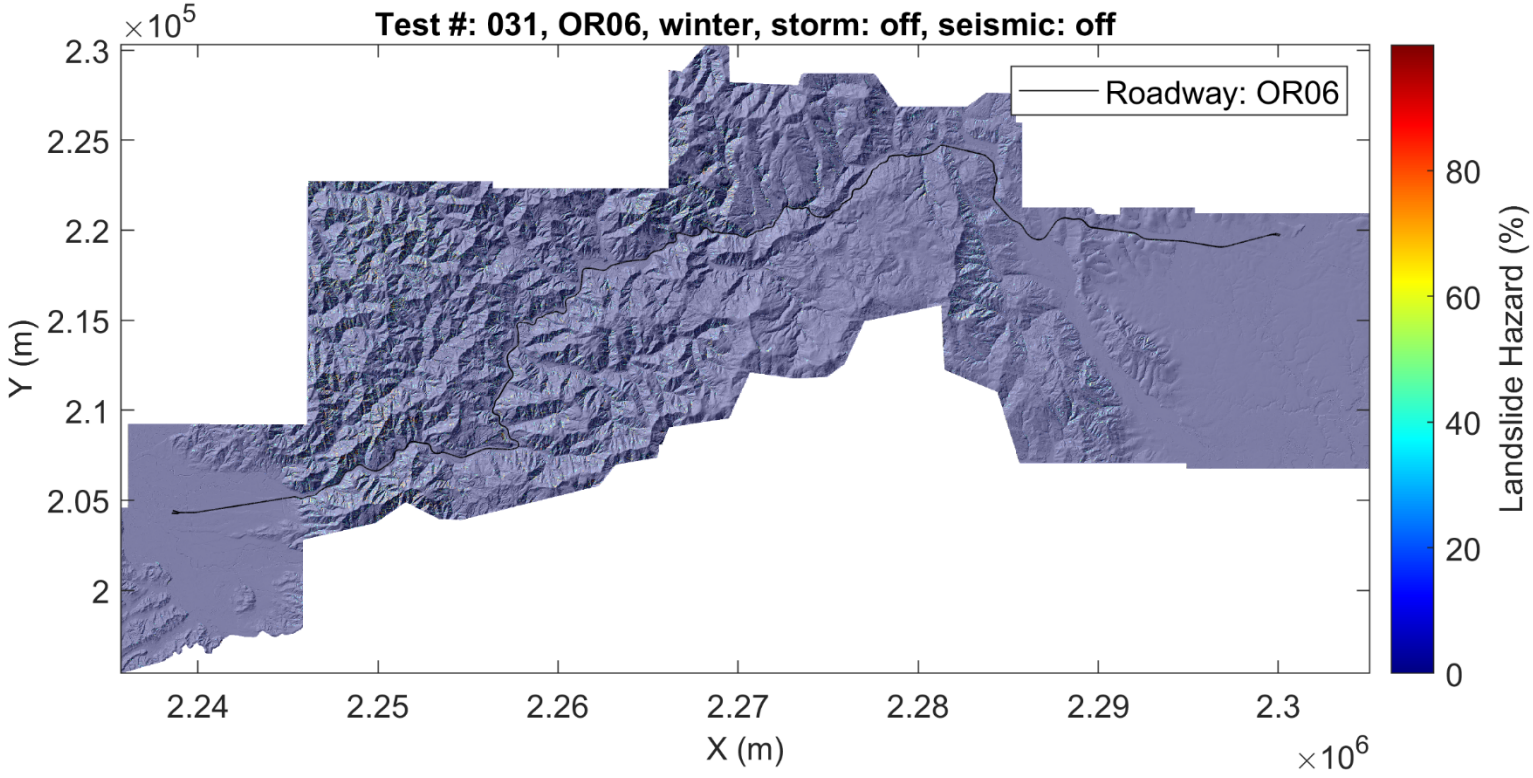

Figure 4.60: Hazard map for OR06: winter antecedent conditions (test #: 031).

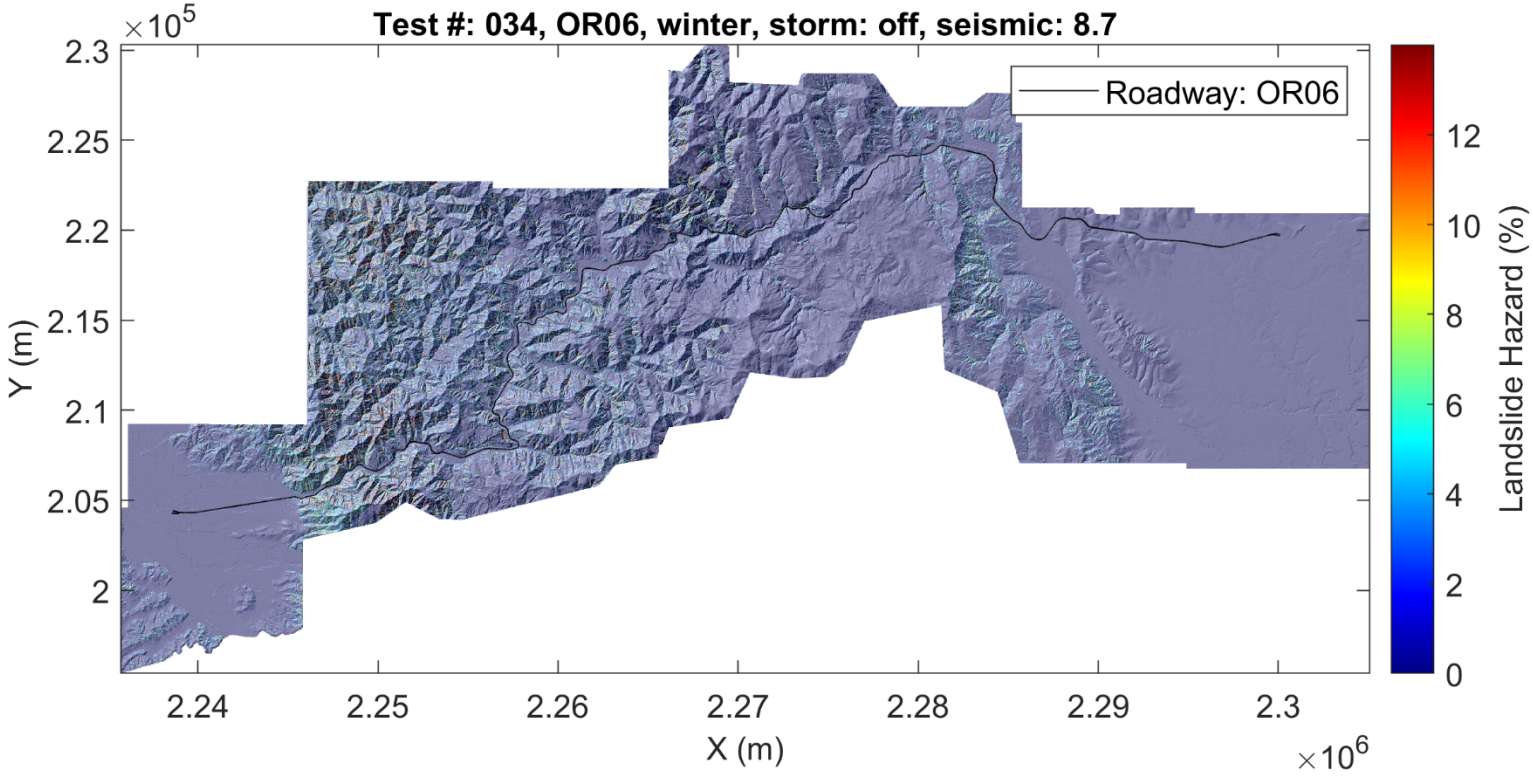

Figure 4.61: Hazard map for OR06: winter antecedent conditions, M8.7 earthquake (test #: 034).

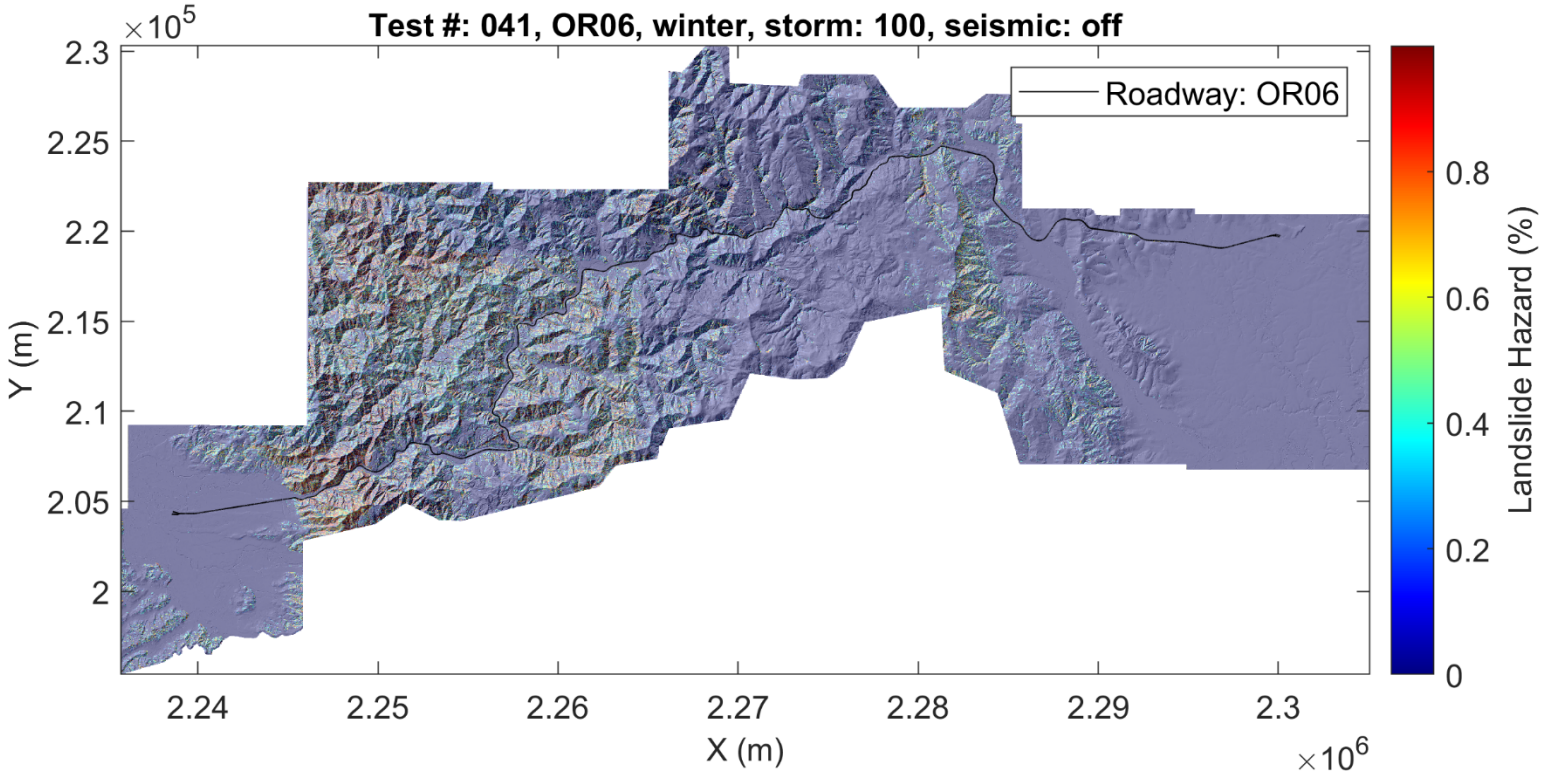

Figure 4.62: Hazard map for OR06: winter, 100-year rainfall event (test #: 041).

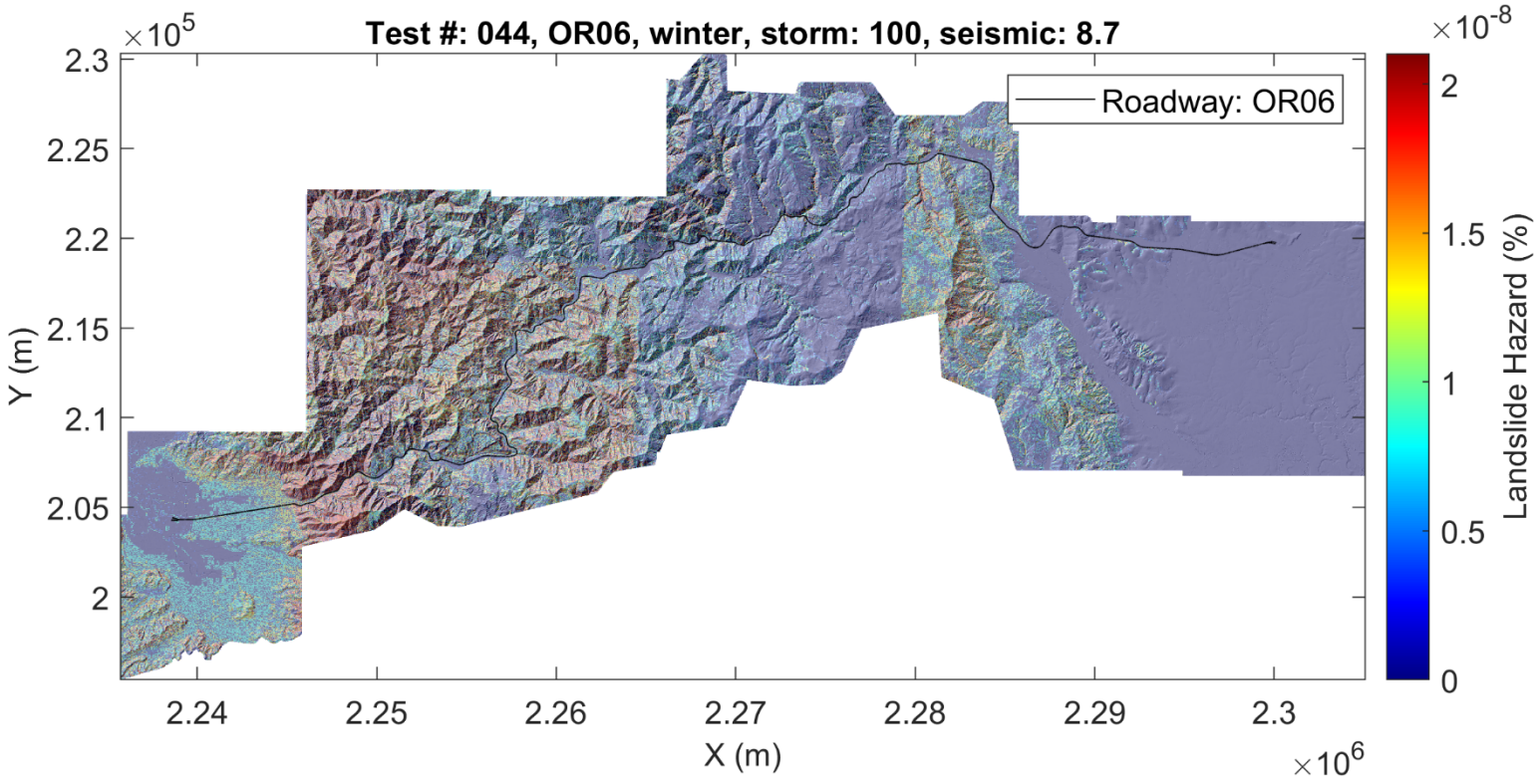

Figure 4.63: Hazard map for OR06: winter, 100-year rainfall event, M8.7 earthquake (test #: 044).

Figures 4.64-4.69 show hazard maps for corridor US20. Figure 4.64 shows hazard for the summer, with no applied physical drivers. For these conditions, there is a sparse distribution of hazard, with only small localized pockets of moderate hazard occurring in isolated areas. Figure 4.65 shows that under seismic forcing, hazard remains fairly sparse, with isolated hazard values up to about 11%. Figure 4.66 shows hazard for antecedent winter conditions, which is equal to susceptibility for this scenario. As seen for previous corridors, there is more widespread hazard than for antecedent summer conditions. Figure 4.67 shows a stark increase in the distribution of hazard from antecedent summer conditions subjected to strong seismicity, especially in the western region closest to the CSZ. As demonstrated in Section 4.4, Figure 4.68 highlights corridor US20's sensitivity to rainfall events. While hazard values are slightly lower due to the probability of a 100-year rainfall event, it is widespread throughout the corridor. Finally, Figure 4.69 shows low, but widespread and relatively uniform, values of hazard throughout the corridor.

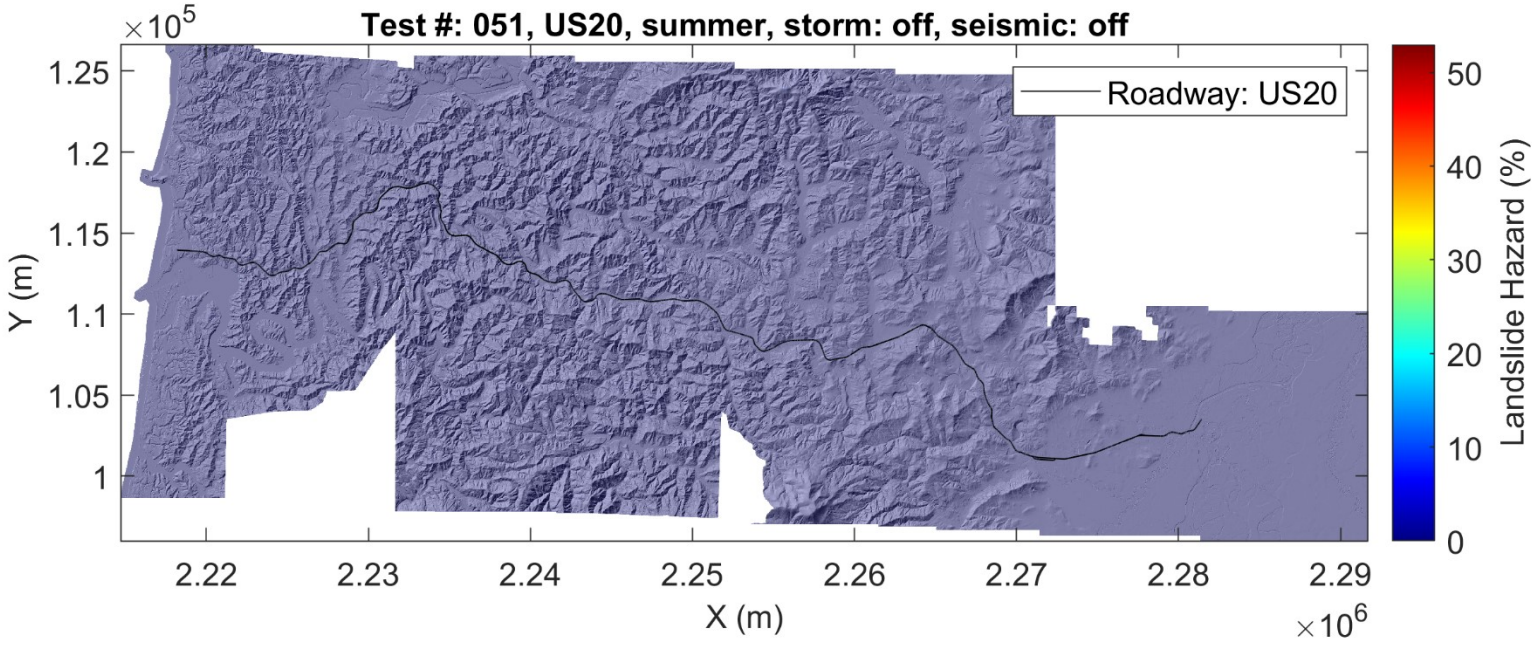

Figure 4.64: Hazard map for US20: summer antecedent conditions (test #: 051).

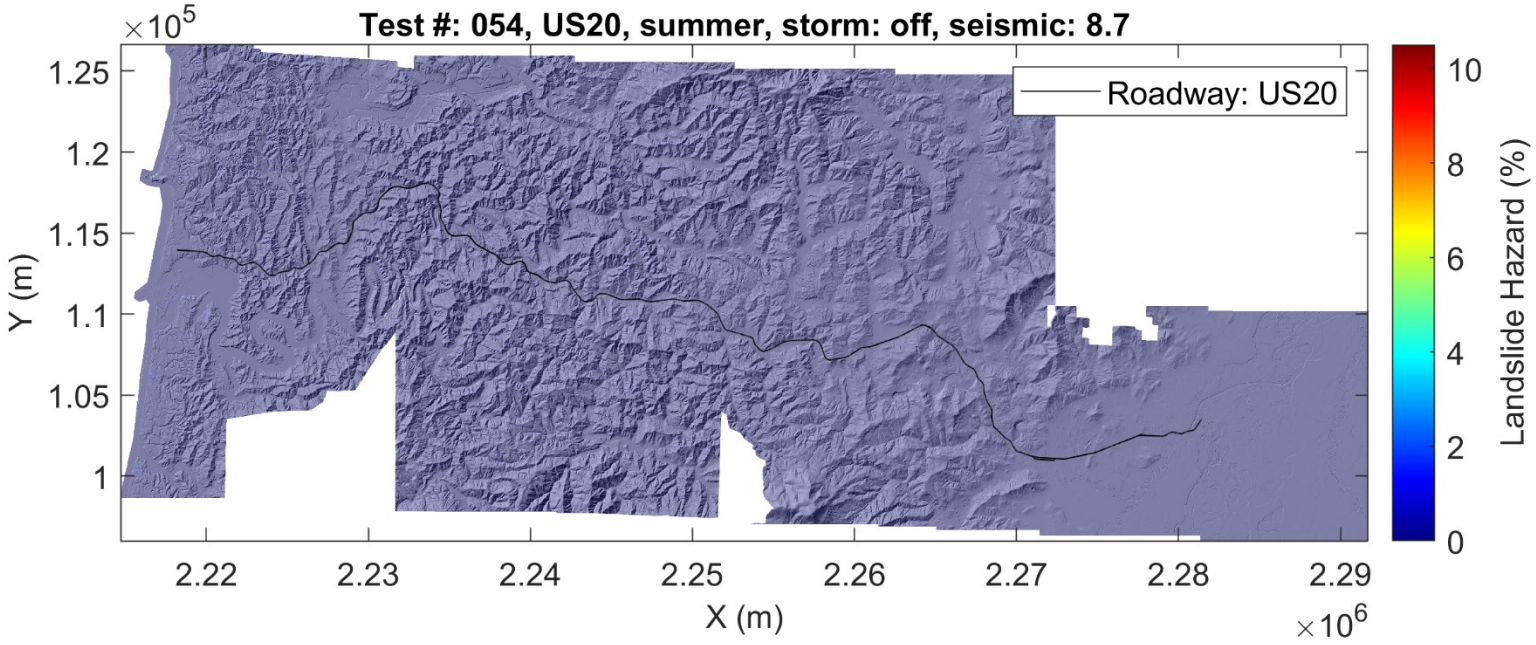

Figure 4.65: Hazard map for US20: summer antecedent conditions, M8.7 earthquake (test #: 054).

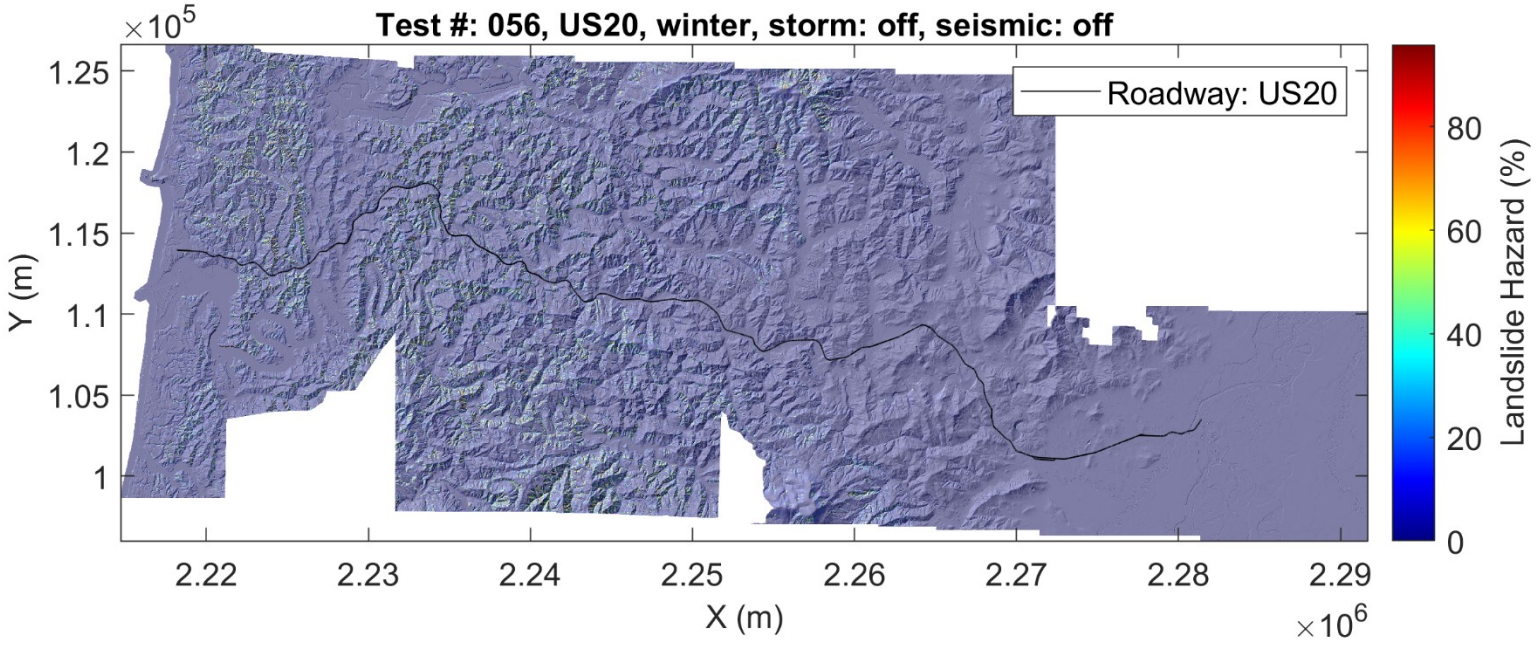

Figure 4.66: Hazard map for US20: winter antecedent conditions (test #: 056).

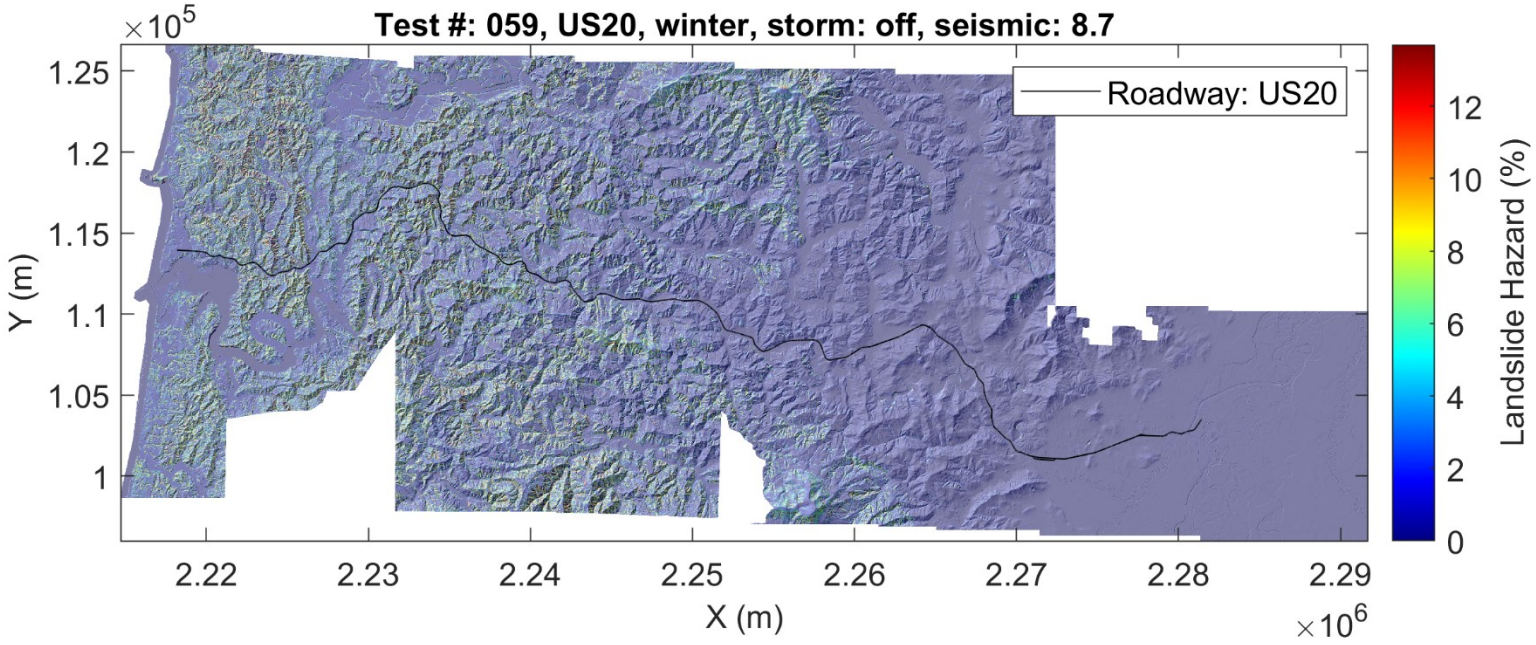

Figure 4.67: Hazard map for US20: winter antecedent conditions, M8.7 earthquake (test #: 059).

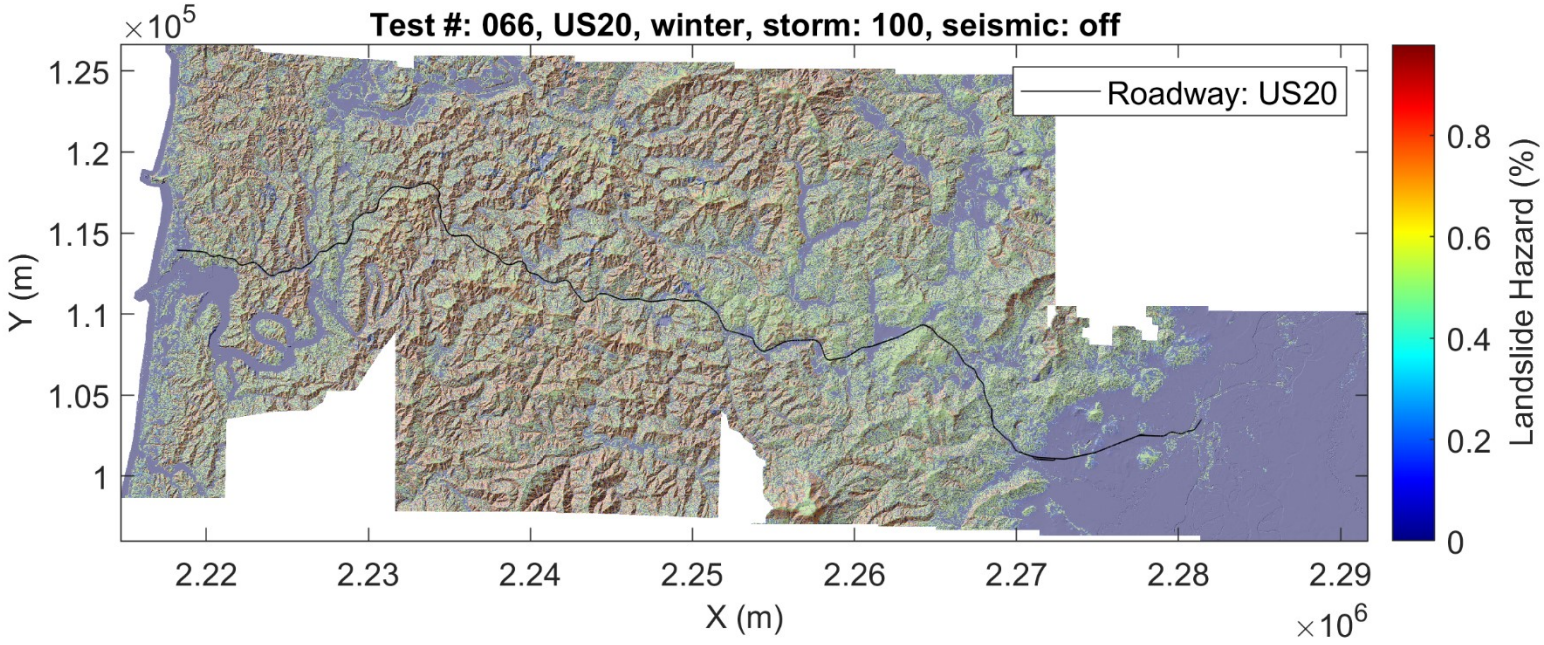

Figure 4.68: Hazard map for US20: winter, 100-year rainfall event (test #: 066).

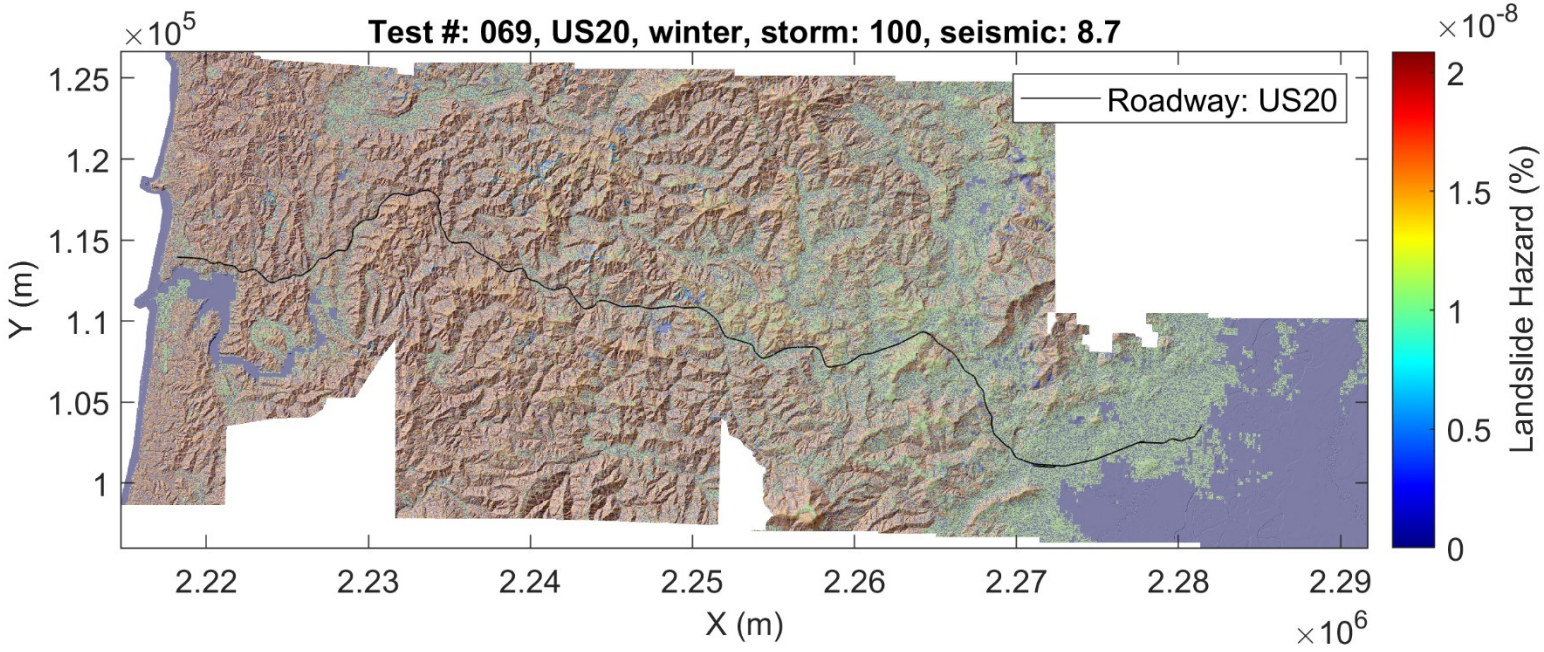

Figure 4.69: Hazard map for US20: winter, 100-year rainfall event, M8.7 earthquake (test #: 069).

Figures 4.70-4.75 show hazard maps for corridor OR42. Figure 4.70 shows hazard for the summer, with no applied physical drivers. For these conditions, there is a sparse distribution of hazard, with only small localized pockets of low hazard occurring in isolated areas. Figure 4.71 shows that under seismic forcing, hazard remains fairly sparse, with isolated hazard values up to about 7%. Figure 4.72 shows hazard for antecedent winter conditions, which is equal to susceptibility for this scenario. Antecedent winter hazard remains relatively low compared to other corridors, but there are some isolated pockets of high hazard. Figure 4.73 shows widespread hazard throughout the corridor, with regions of higher hazard throughout the corridor. Figure 4.74 shows a similar distribution of hazard as Figure 4.73, but with isolated pockets of relatively high hazard appearing on individual hillslopes. Finally, Figure 4.75 shows low, but slightly more homogeneous, values of hazard throughout the corridor. Again, these low values of hazard are tied to the low probability of these two forcing events occurring on the same day.

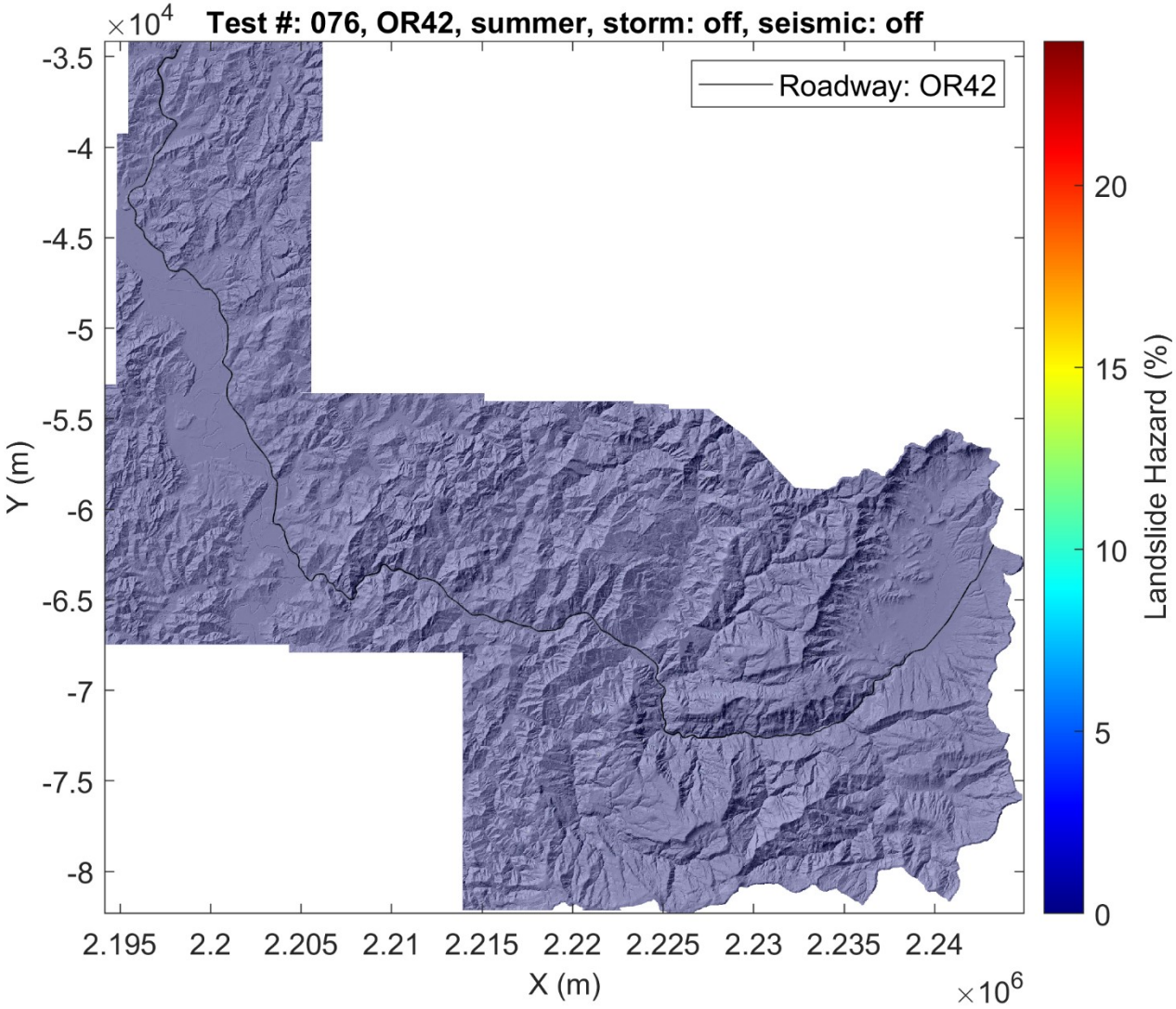

Figure 4.70: Hazard map for OR42: summer antecedent conditions (test #: 076).

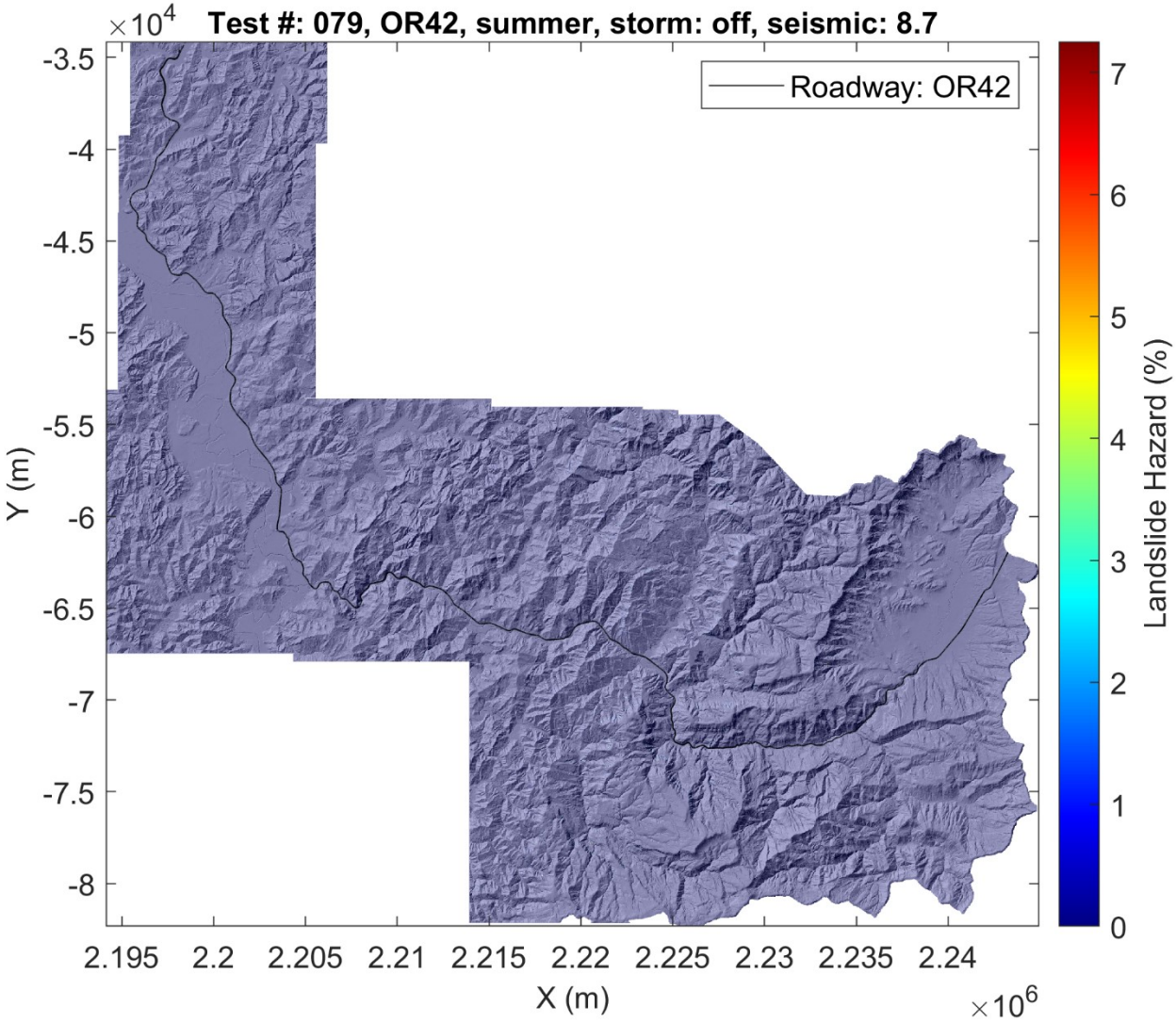

Figure 4.71: Hazard map for OR42: summer antecedent conditions, M8.7 earthquake (test #: 079).

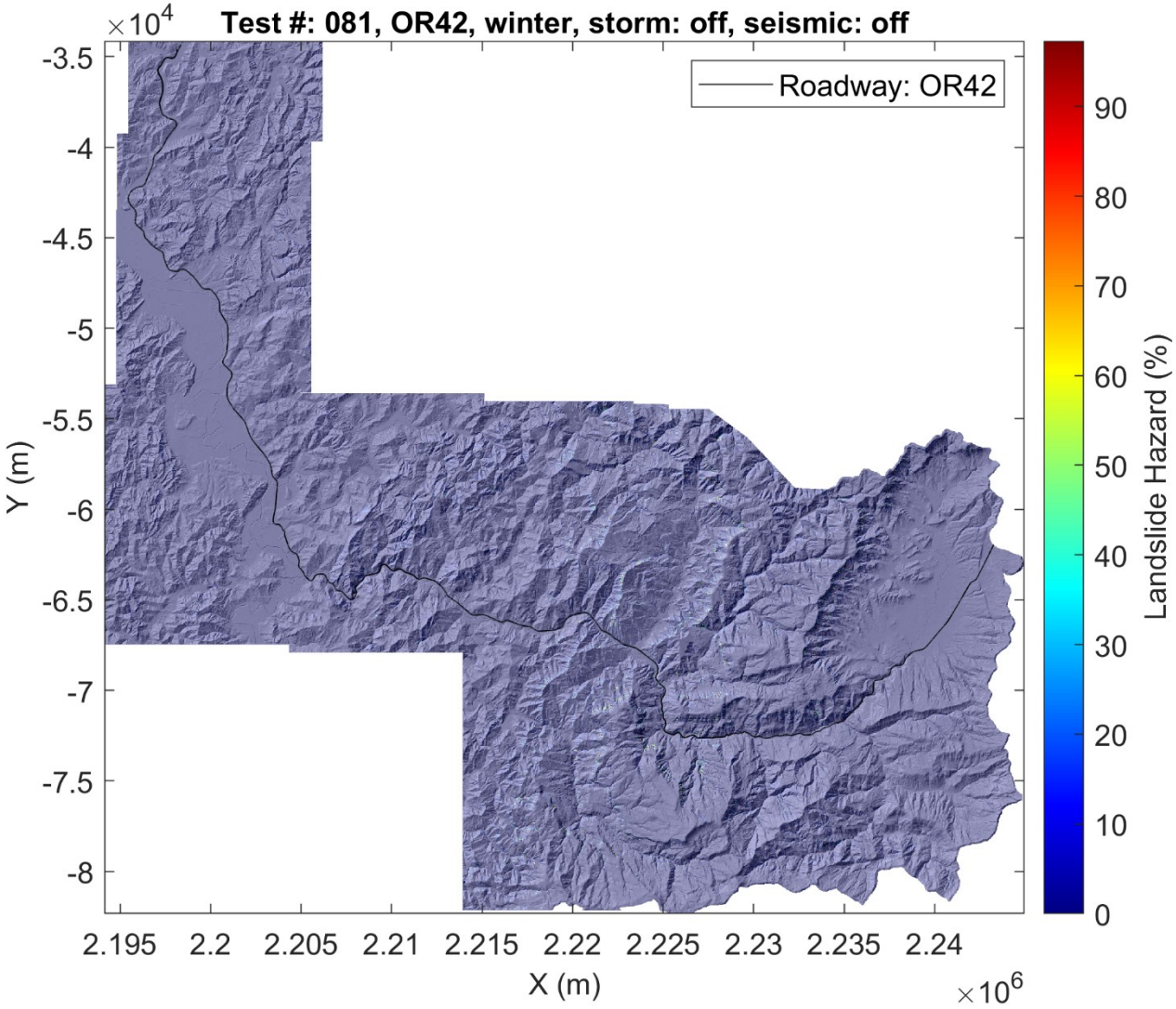

Figure 4.72: Hazard map for OR42: winter antecedent conditions (test #: 081).

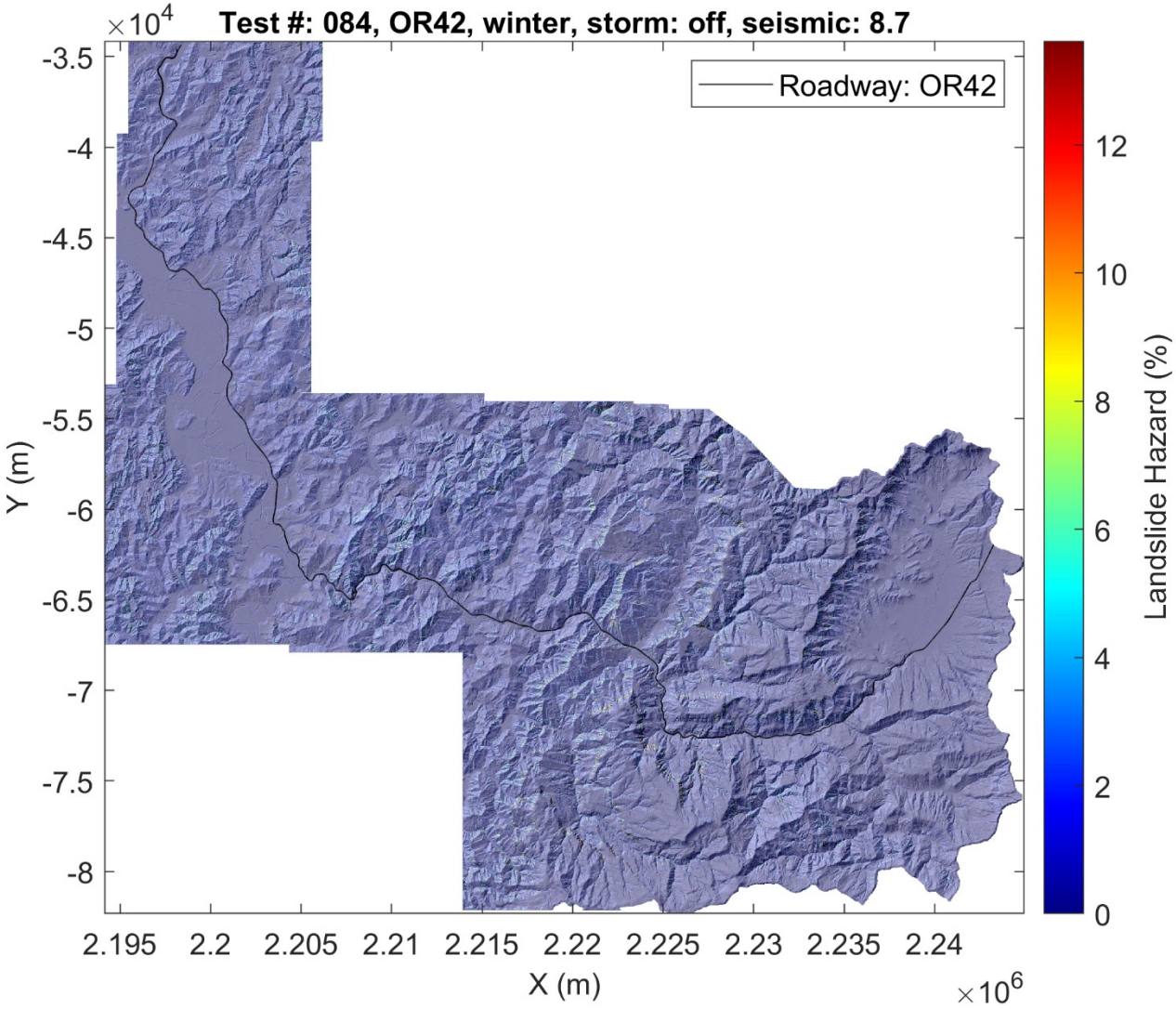

Figure 4.73: Hazard map for OR42: winter antecedent conditions, M8.7 earthquake (test #: 084).

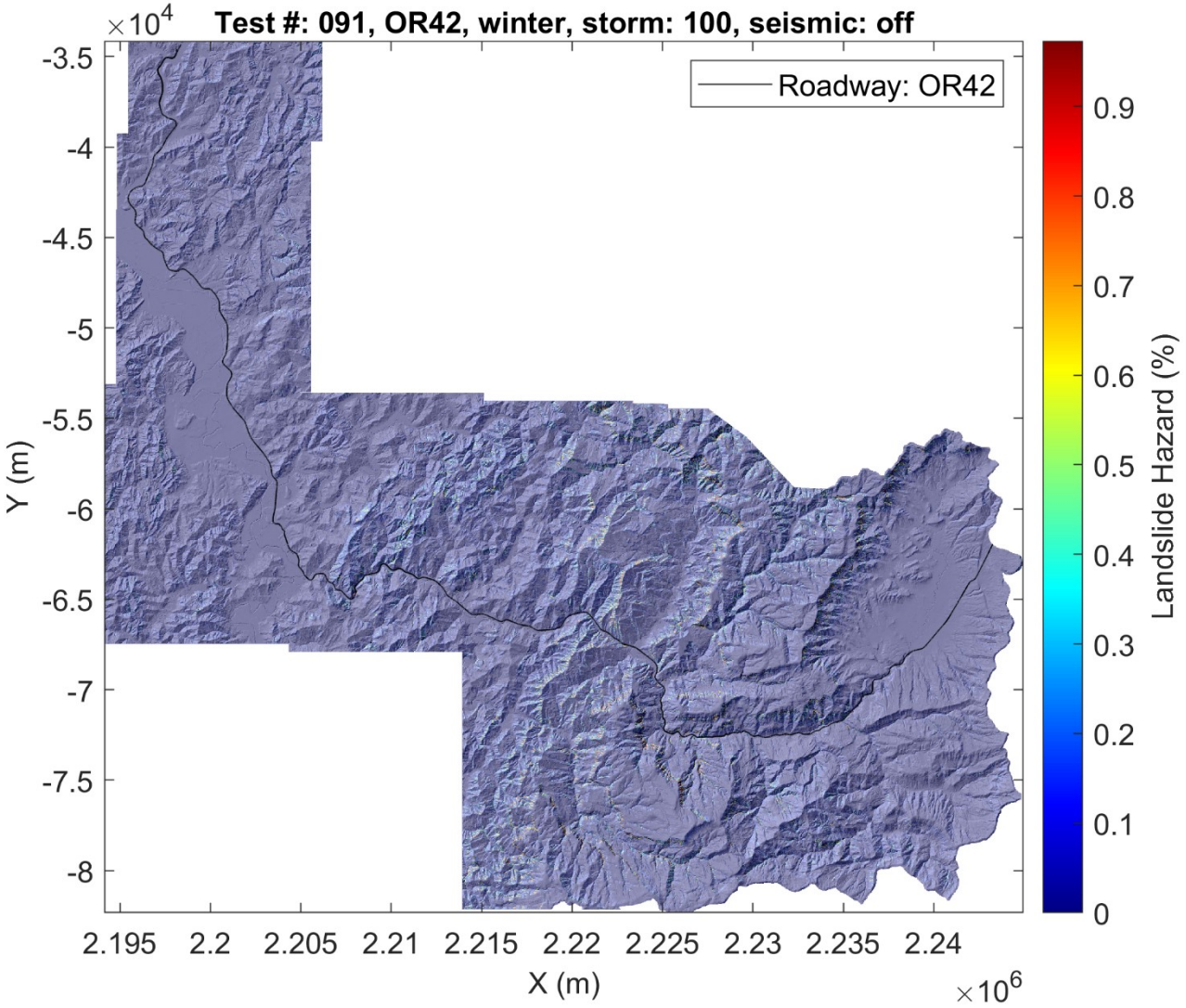

Figure 4.74: Hazard map for OR42: winter, 100-year rainfall event (test #: 091).

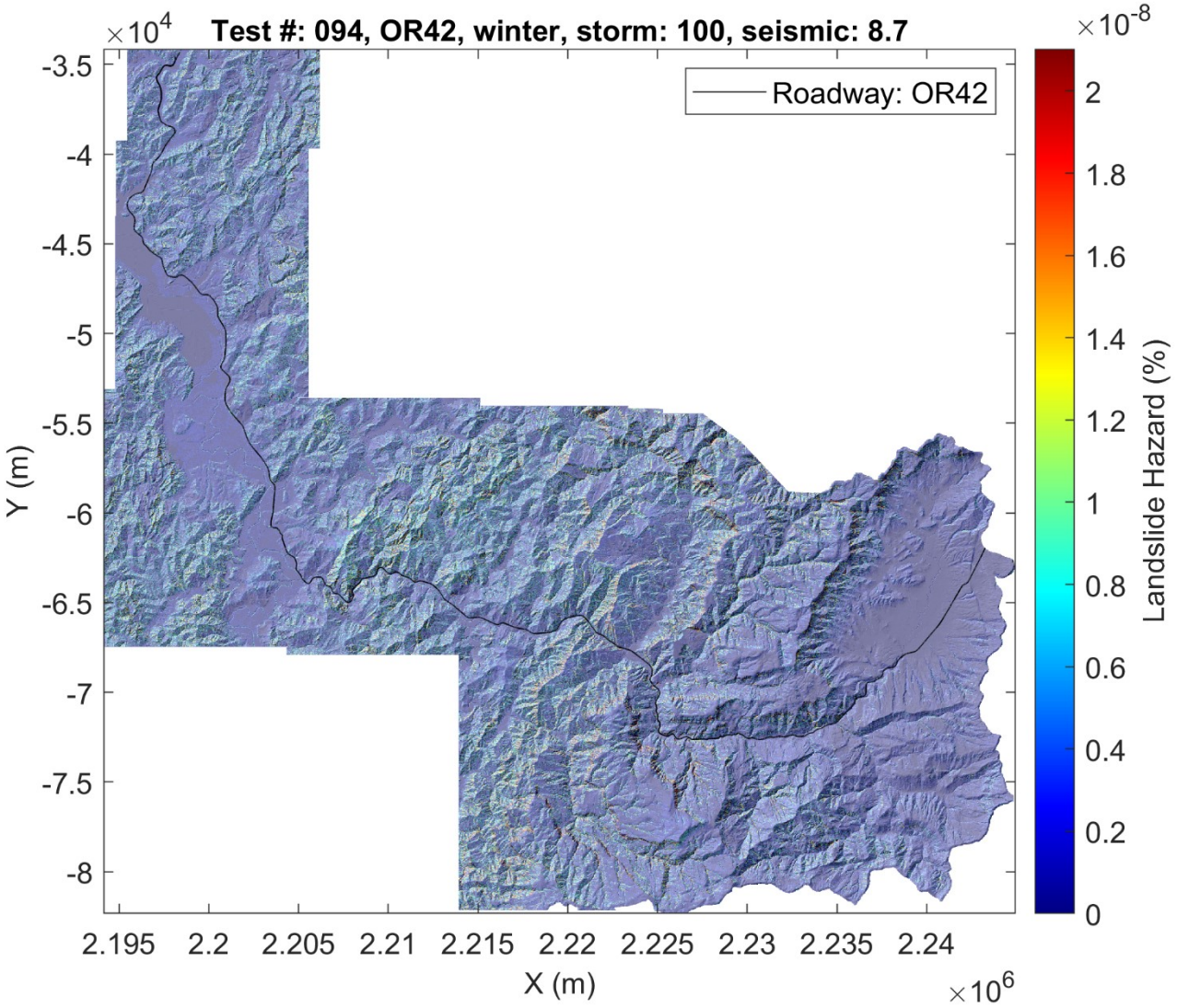

Figure 4.75: Hazard map for OR42: winter, 100-year rainfall event, M8.7 earthquake (test #: 094).

4.6 RISK

In this section, the susceptibility maps shown in Section 4.4 are used to generate course risk metrics, such as total closure times and costs assuming different landslide and road geometries, maps showing the closure times of ODOT ROW, and plots showing time associated with highway repair as a function of milepost.

4.6.1 Total Closure Times and Costs Associated with Impacted Infrastructure

In this section, three costs associated with highway closure time are considered. First are the costs of repairing impacted sections of highway, as discussed in section 3.10.3. These costs are tied to the time and materials required to excavate landslide debris and to construct cut slopes or retaining walls, depending on the geometry of settled landslide debris. Also considered are the costs associated with lost commodity flow. Estimates of the daily value of commodities traveling through the corridors analyzed herein (generated using TPAU), along with computed closure times of those corridors, are used to estimate the total loss of commodity flow for each corridor. Finally, the daily costs of rerouting traffic and computed closure times are used to estimate the total costs of rerouting traffic following a hazard-induced highway closure. Table 4.6 contains a summary of closure times and associated costs corresponding with the tests highlighted in Table 4.4. Note that these values assume a 40-foot wide roadway and do not include a landslide buffer in their calculation. Further, these costs are likely an underestimate, as they do not include various other construction expenses beyond excavation. A complete table of closure times and costs, for all tests, can be found in the digital appendix included with this report. Additionally, shapefiles containing attribute tables of closure times, closure cost, mileposts, and other relevant data may be found in the digital appendix; this data may be sorted, viewed, and used in a GIS platform.

Note that, generally, closure times increase as seismicity or rainfall increases. However, in some cases, the opposite can be true (e.g. tests #2 and #3 in Table 4.6). This is mainly due to slight changes in landslide debris angles for similar sections of closure along the corridor. Seismicity can increase the size of a given landslide polygon, entraining more cells and potentially lowering the average angle of the landslide debris covering the road. As a result, the cross-sectional area of the debris prism may increase significantly, in turn increasing the volume of debris and closure time.

Table 4.6: Table of Course Risk Metrics for Tests Highlighted in Table 4.4.

Test Information					Closure and Costs (40 ft Road Width)				Closure and Costs (24 ft Road Width)			
Test #	***High-way***	***Season***	***Rainfall***	***EQ Moment Magnitude***	***Closure Duration (days)***	***Total Repair Cost ($)***	***Commodity Loss ($)***	***Rerouting Loss ($)***	***Closure Duration (days)***	***Total Repair Cost ($)***	***Commodity Loss ($)***	***Rerouting Loss ($)***
1	US30	summer	off	off	7.47	$411,091	$17,105,522	$1,669,133	2.69	$211,745	$6,157,988	$600,888
4	US30	summer	off	8.7	33.03	$1,818,072	$75,650,136	$7,381,835	11.89	$722,501	$27,234,046	$2,657,460
6	US30	winter	off	off	125.22	$6,968,623	$286,832,704	$27,988,736	45.08	$2,763,962	$103,259,768	$10,075,943
9	US30	winter	off	8.7	131.93	$7,528,488	$302,182,880	$29,486,582	47.49	$3,017,910	$108,785,832	$10,615,168
16	US30	winter	100-yr	off	122.65	$7,261,696	$280,935,552	$27,413,298	44.15	$2,855,909	$101,136,792	$9,868,785
19	US30	winter	100-yr	8.7	172.72	$9,947,466	$395,614,336	$38,603,492	62.18	$3,946,541	$142,421,152	$13,897,256
26	OR06	summer	off	off	0.76	$41,637	$732,822	$82,943	0.27	$14,989	$263,816	$29,860
29	OR06	summer	off	8.7	1.65	$90,703	$1,596,401	$180,686	0.59	$32,653	$574,704	$65,047
31	OR06	winter	off	off	6.48	$356,719	$6,278,347	$710,603	2.33	$128,419	$2,260,205	$255,817
34	OR06	winter	off	8.7	52.17	$3,089,513	$50,546,760	$5,721,043	18.78	$1,312,383	$18,196,832	$2,059,576
41	OR06	winter	100-yr	off	83.77	$4,737,137	$81,165,760	$9,186,600	30.16	$1,840,754	$29,219,676	$3,307,176
44	OR06	winter	100-yr	8.7	147.53	$8,121,059	$142,932,512	$16,177,555	53.11	$2,923,581	$51,455,704	$5,823,921
51	US20	summer	off	off	0.00	$0	$0	$0	0.00	$0	$0	$0
54	US20	summer	off	8.7	0.00	$0	$0	$0	0.00	$0	$0	$0
56	US20	winter	off	off	6.47	$355,918	$8,953,142	$1,208,077	2.33	$128,130	$3,223,131	$434,908
59	US20	winter	off	8.7	60.57	$3,334,091	$83,869,328	$11,316,762	21.80	$1,200,273	$30,192,956	$4,074,035
66	US20	winter	100-yr	off	166.89	$9,187,027	$231,100,416	$31,183,140	60.08	$3,307,330	$83,196,152	$11,225,926
69	US20	winter	100-yr	8.7	205.86	$11,332,334	$285,065,728	$38,464,848	74.11	$4,079,640	$102,623,664	$13,847,351
76	OR42	summer	off	off	0.00	$0	$0	$0	0.00	$0	$0	$0
79	OR42	summer	off	8.7	0.00	$0	$0	$0	0.00	$0	$0	$0
81	OR42	winter	off	off	3.22	$177,348	$9,187,228	$404,586	1.16	$63,845	$3,307,402	$145,651
84	OR42	winter	off	8.7	17.25	$949,750	$49,200,264	$2,166,675	6.21	$341,910	$17,712,096	$780,003
91	OR42	winter	100-yr	off	29.07	$1,600,519	$82,912,344	$3,651,284	10.47	$576,187	$29,848,444	$1,314,462
94	OR42	winter	100-yr	8.7	42.15	$2,320,117	$120,189,992	$5,292,911	15.17	$835,242	$43,268,392	$1,905,448

4.6.2 Maps of Landslide Polygons and Risk Metrics along ODOT Right-of-Way

Total values of closure may be discretized into impacted sections along each ODOT highway analyzed in this study. Spatial distributions of highway closure metrics, presented using maps, are important tools for planning and resilience following landslide-driving events, such as earthquakes or rainstorms. Figures 4.76-4.99 show initial landslide shapes (prior to runout estimation), final landslide shapes (following runout estimation), and a 60-foot (18.3 m) buffer applied to the perimeter of those final landslide shapes for the 24 tests highlighted in Table 4.4. Additionally, Figures 4.76-4.99 show ODOT ROW colored to illustrate values of closure time along the highway. Note that the select scenarios shown in this section assume a 40-foot (12.2 m) wide roadway and show closure times associated with the overlap of initial shapes and estimated runout only (60-foot buffers do not contribute to closure). A full suite of maps illustrating closure times for initial landslide shapes and estimated runouts, assuming a 40-foot wide roadway, may be found in Appendix C. A full suite of maps illustrating closure times associated with overlap of the 60-foot applied buffer, in addition to initial landslide shapes and runouts, assuming a 40-foot wide roadway, may be found in Appendix D. Further, rasters containing all landslide polygons – initial, final, and buffered – may be found in the digital appendix accompanying this report, along with shapefiles containing highway closure data for each corridor. These shapefiles contain closure data (closure times and associated costs) for assumed highway widths of both 40 feet (12.2 m) and 24 feet (7.3 m). There are also additional shapefiles containing closure data assuming a 60-foot buffer around the final landslide shapes.

Figures 4.76-4.81 show closure times for corridor US30. Figure 4.76 shows that for summer conditions, there are some areas at risk of closure, with closed sections occurring in the central region of the corridor and within a steep area in the west-central region of the corridor. When strong seismicity is applied, higher values of closure are observed in these same areas (Figure 4.77). For winter antecedent conditions, higher values of closure are observed ranging from the west-central to eastern regions of the corridor (Figure 4.78). When seismicity is applied during winter conditions, more widespread closure is observed, and hot spots begin to appear in the far western region of the corridor (Figure 4.79). Figure 4.80 shows closure corresponding to a 100-year rain event. Here, high values of closure time are observed, mainly concentrated in the central region of the corridor. Finally, when a 100-year rainfall event and a M8.7 earthquake are applied, high closure times are observed throughout the corridor with hot spots appearing throughout its extents (Figure 4.81).

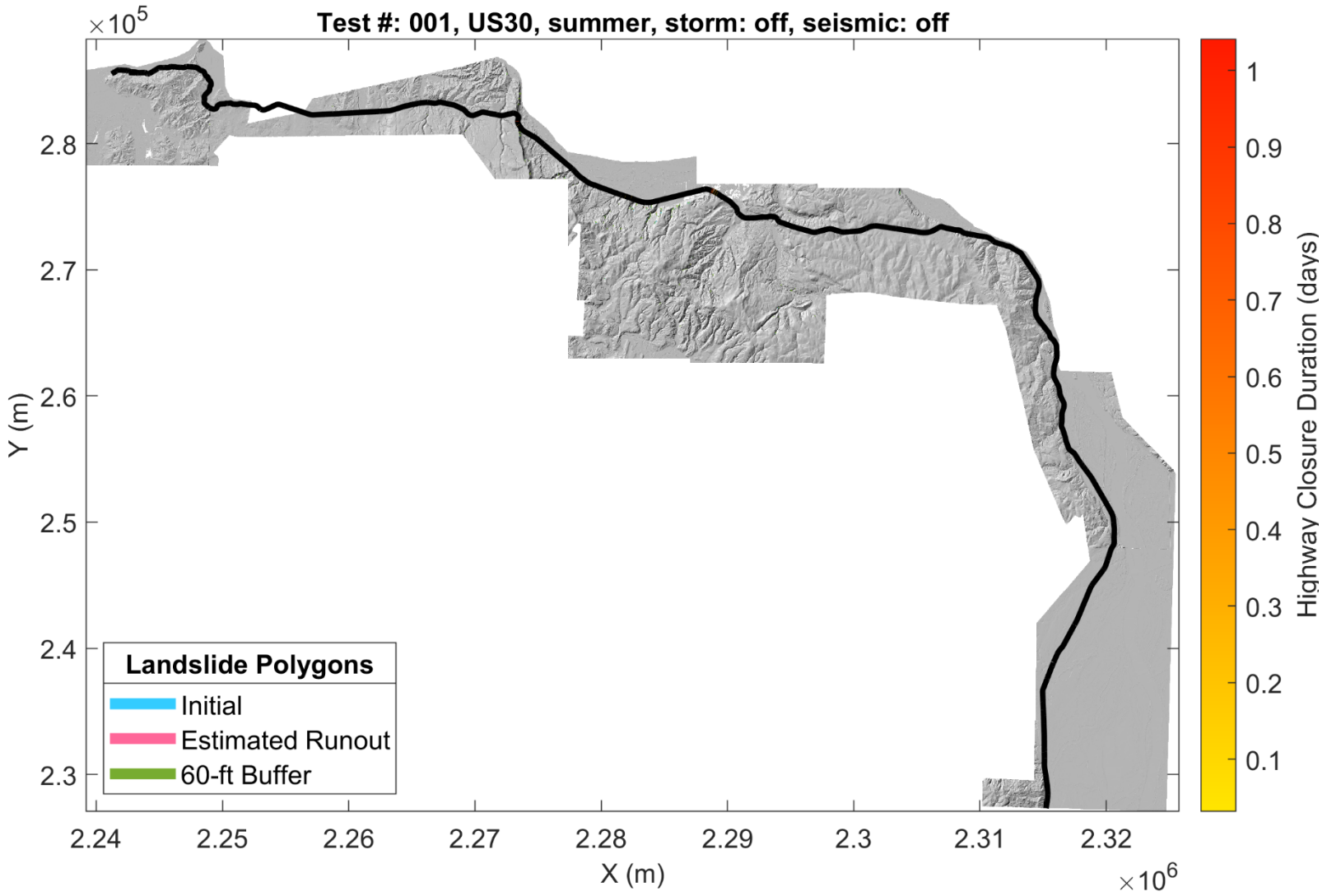

Figure 4.76: Map of landslide polygons, estimated runout, landslide buffers, and ROW closure for US30: summer antecedent conditions (test #: 001).

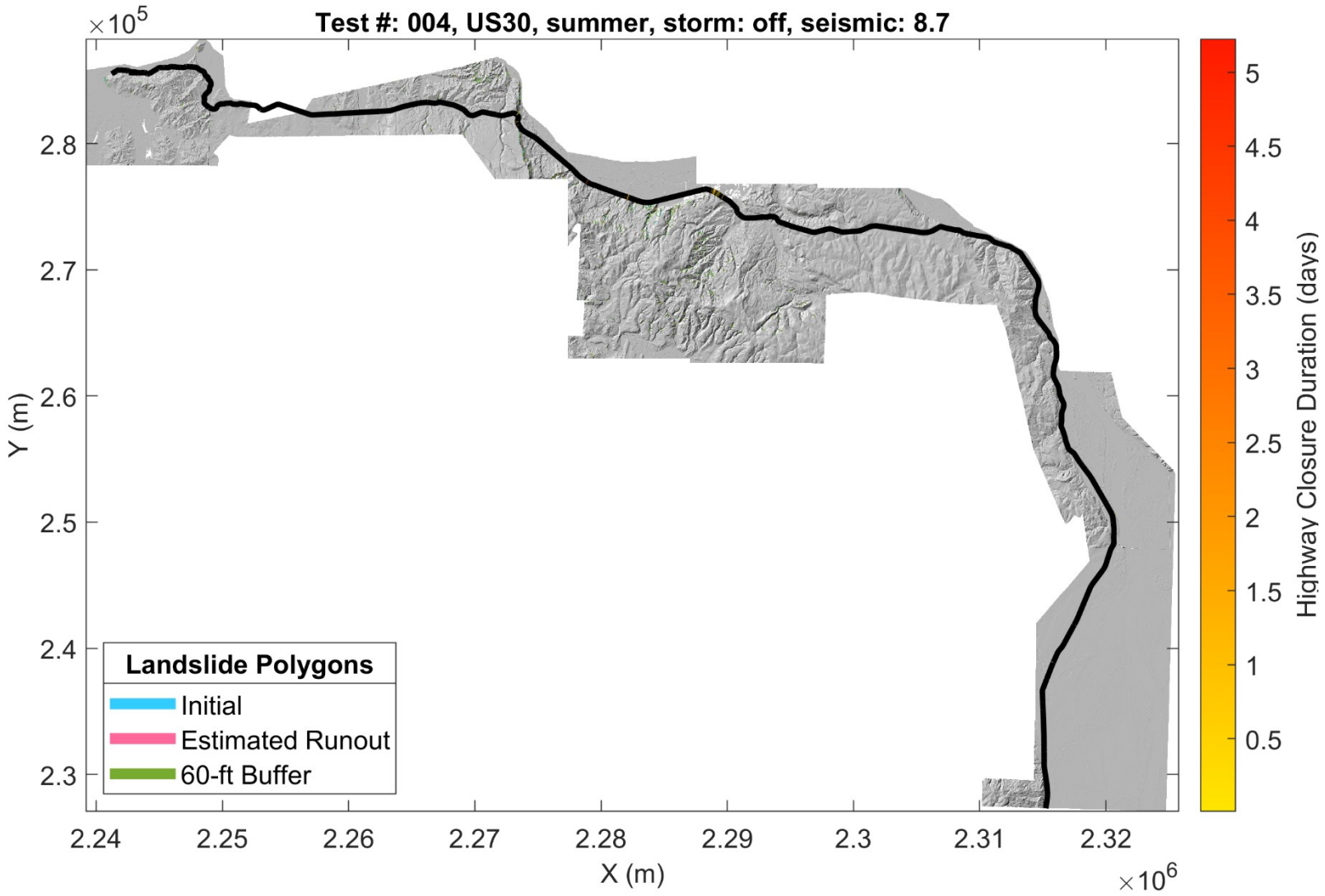

Figure 4.77: Map of landslide polygons, estimated runout, landslide buffers, and ROW closure for US30: summer antecedent conditions, M8.7 earthquake (test #: 004).

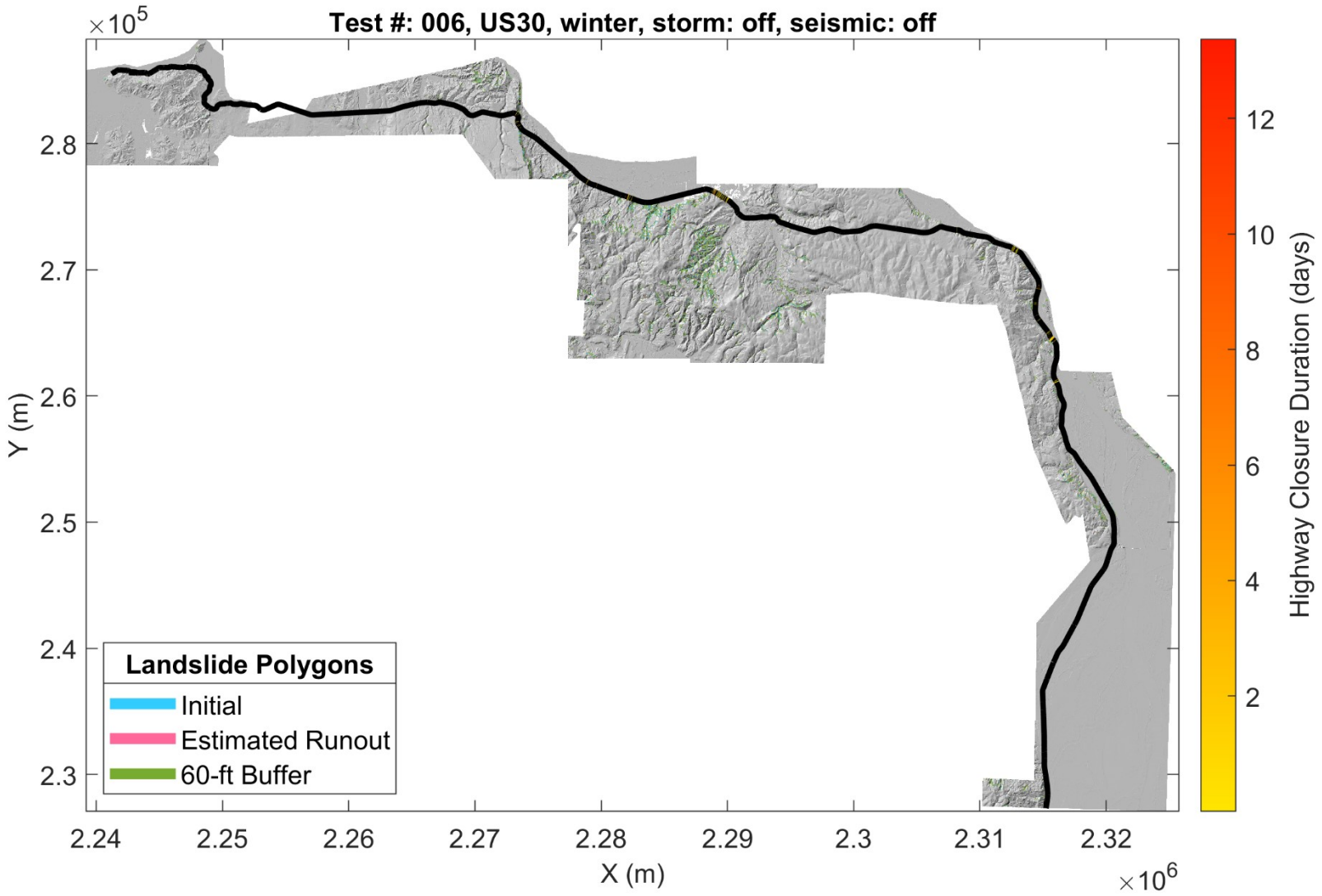

Figure 4.78: Map of landslide polygons, estimated runout, landslide buffers, and ROW closure for US30: winter antecedent conditions (test #: 006).

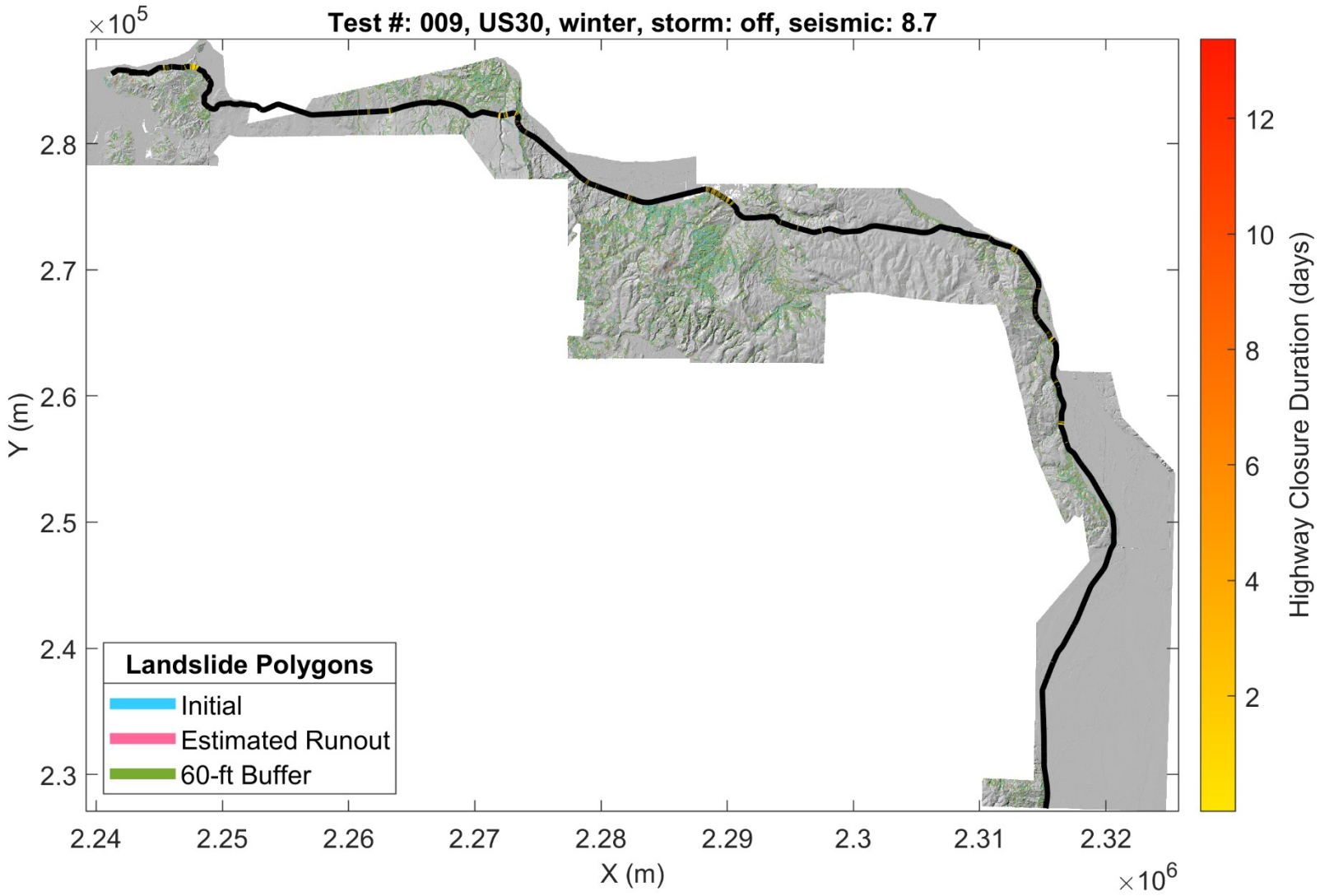

Figure 4.79: Map of landslide polygons, estimated runout, landslide buffers, and ROW closure for US30: winter antecedent conditions, M8.7 earthquake (test #: 009).

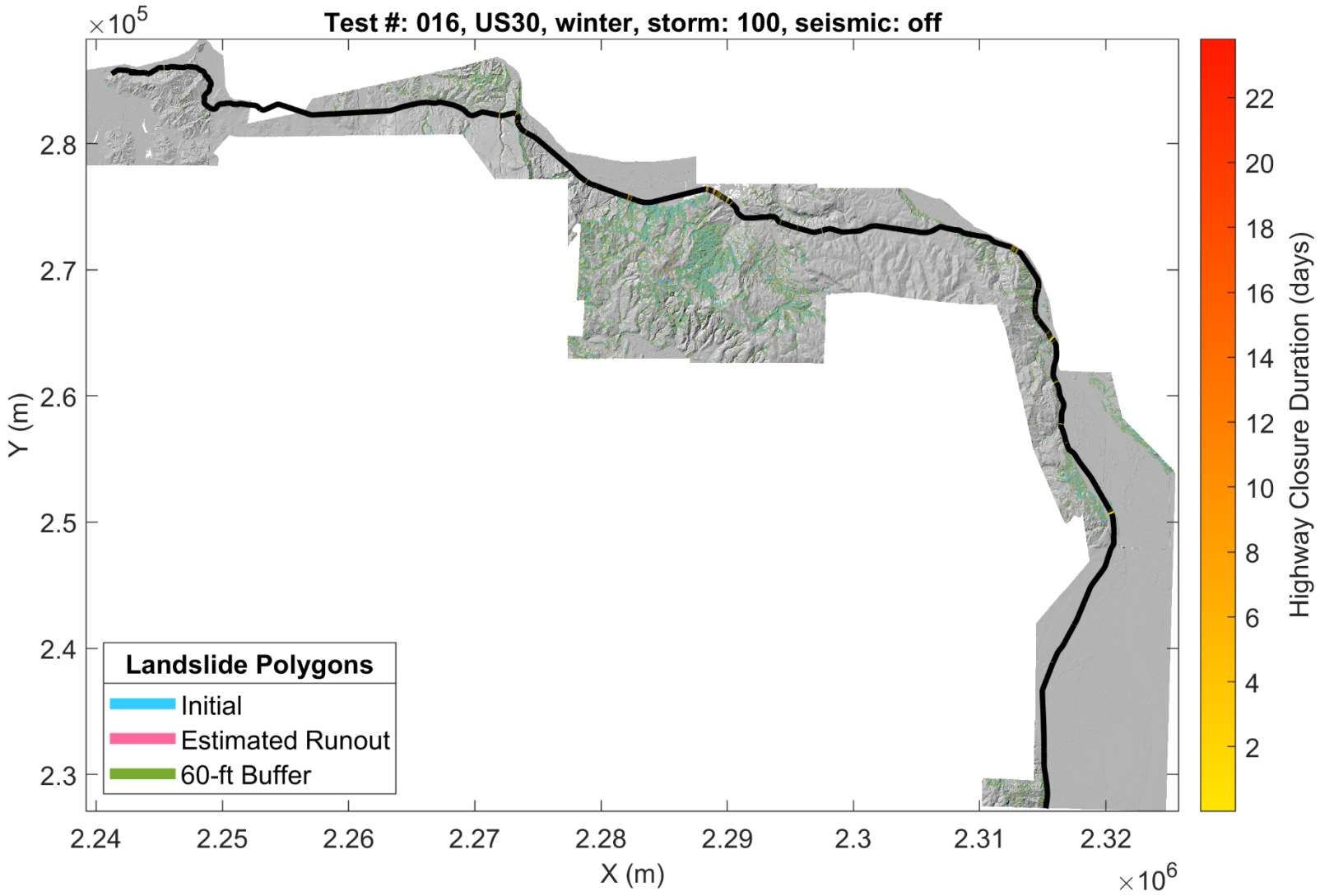

Figure 4.80: Map of landslide polygons, estimated runout, landslide buffers, and ROW closure for US30: winter, 100-year rainfall event (test #: 016).

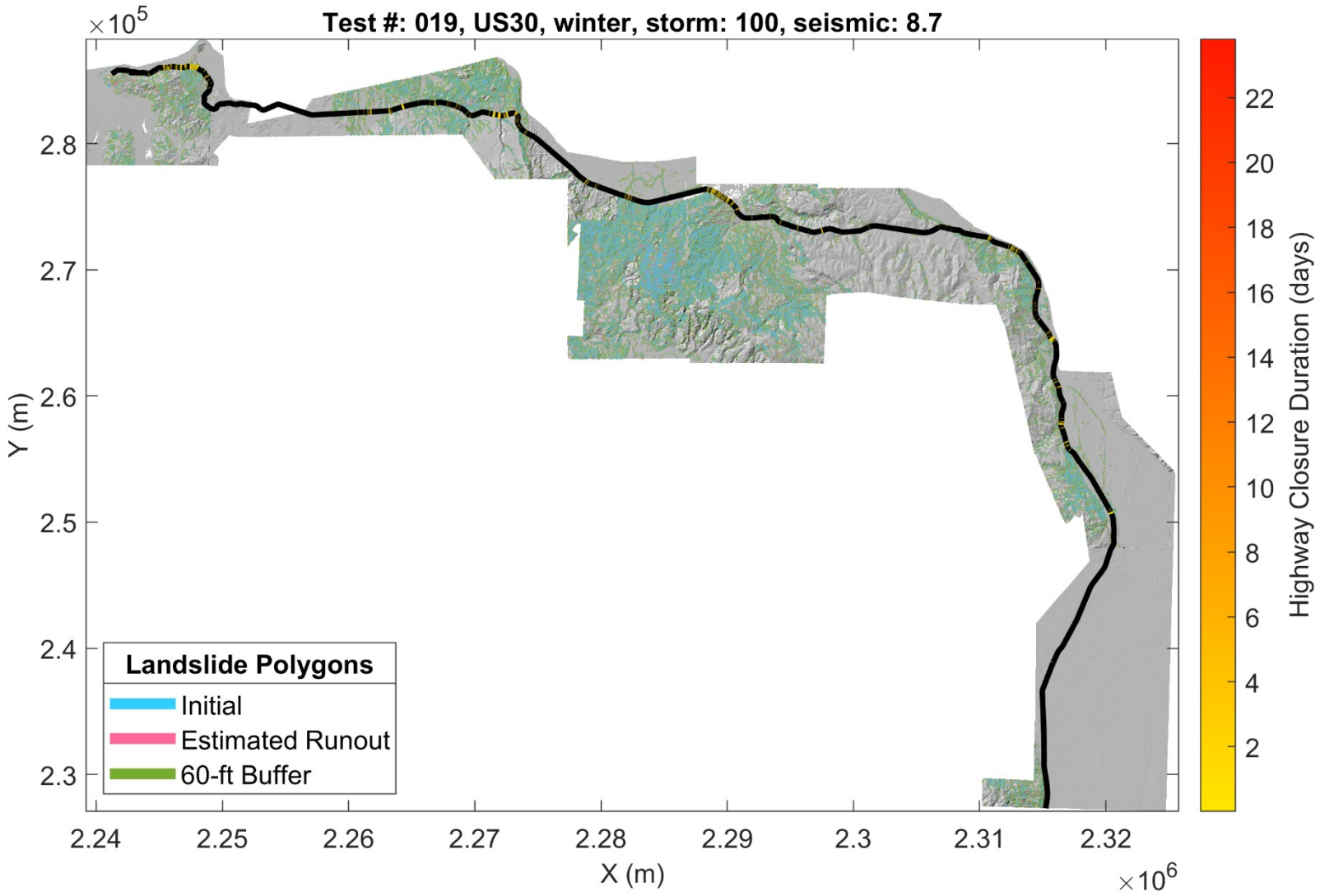

Figure 4.81: Map of landslide polygons, estimated runout, landslide buffers, and ROW closure for US30: winter, 100-year rainfall event, M8.7 earthquake (test #: 019).

Figures 4.82-4.87 show closure times for corridor OR06. Figure 4.82 shows that for summer conditions, the corridor is at very low risk of closure, with only sparse areas of low closure time appearing. When strong seismicity is applied, higher values of closure are observed in the central and far west regions of the corridor (Figure 4.83). For winter antecedent conditions, slightly higher closure times are observed throughout the corridor (Figure 4.84). When seismicity is applied during winter conditions, more widespread and severe closure times are observed, with hot spots in the west-central and western regions of the corridor (Figure 4.85). Figure 4.86 shows closure corresponding to a 100-year rain event. Here, high values of closure time are observed throughout the corridor. Finally, when a 100-year rainfall event and a M8.7 earthquake are applied, widespread closure is observed throughout the corridor with hot spots becoming much longer in their extents (Figure 4.87).

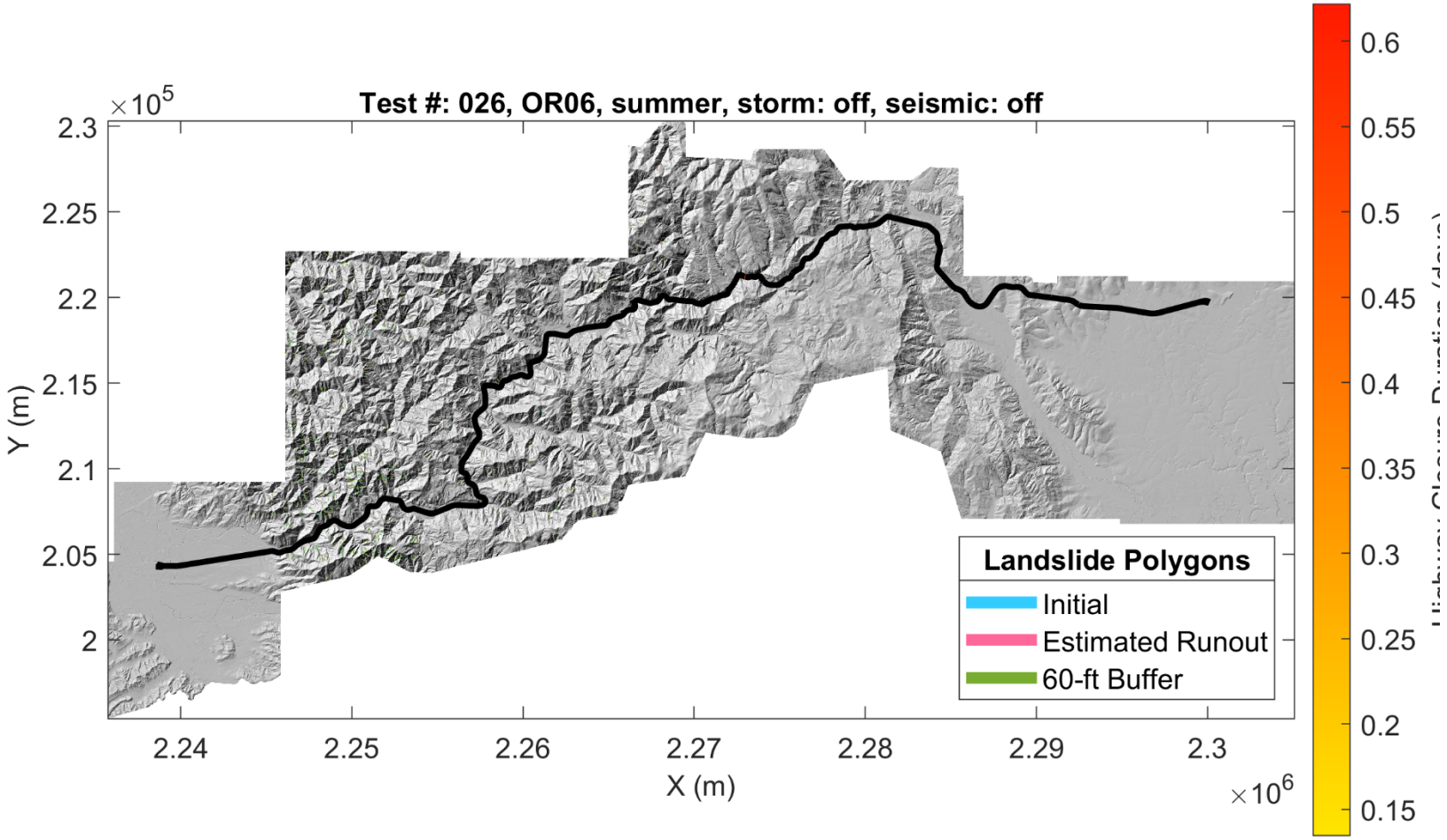

Figure 4.82: Map of landslide polygons, estimated runout, landslide buffers, and ROW closure for OR06: summer antecedent conditions (test #: 026).

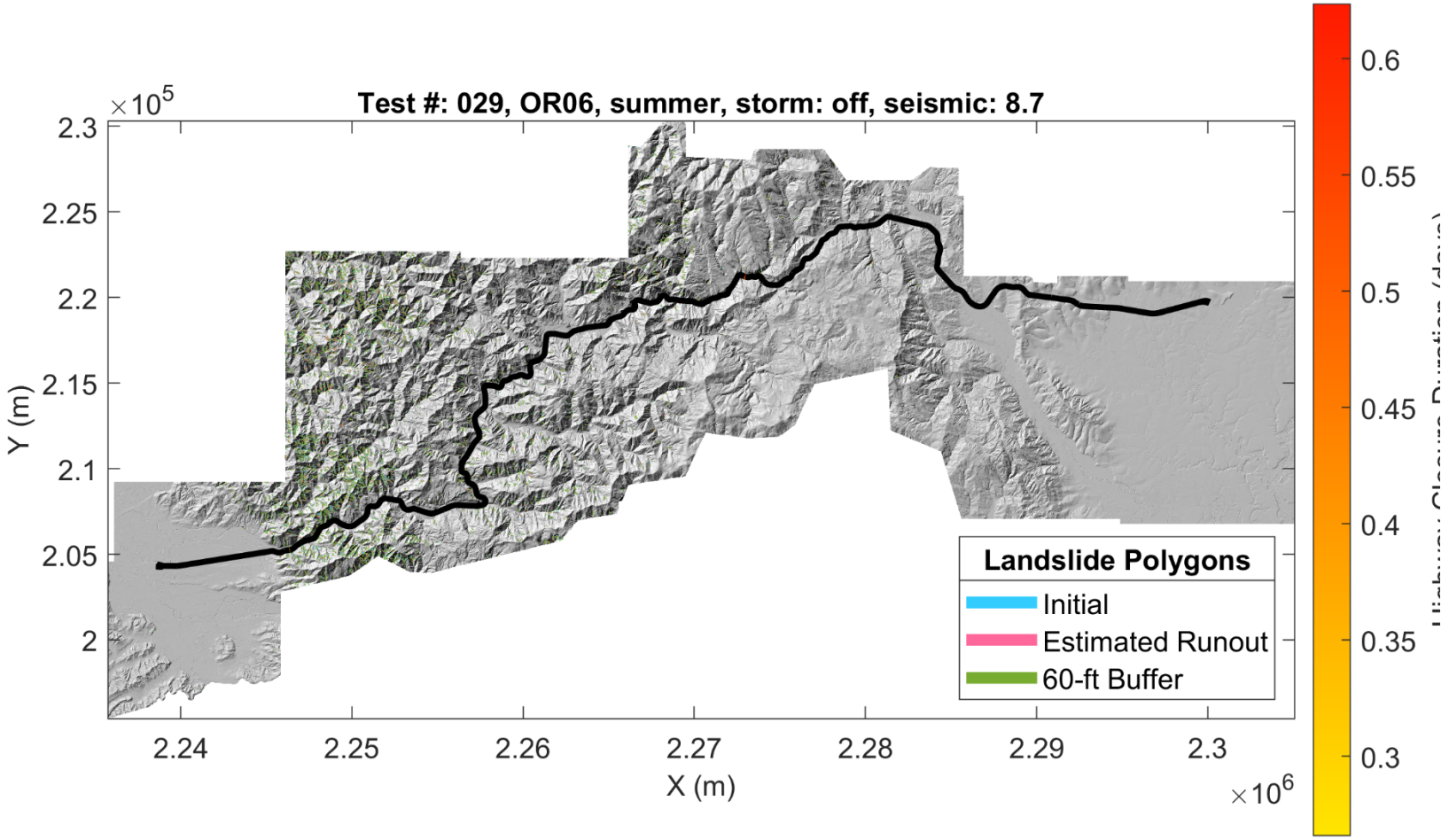

Figure 4.83: Map of landslide polygons, estimated runout, landslide buffers, and ROW closure for OR06: summer antecedent conditions, M8.7 earthquake (test #: 029).

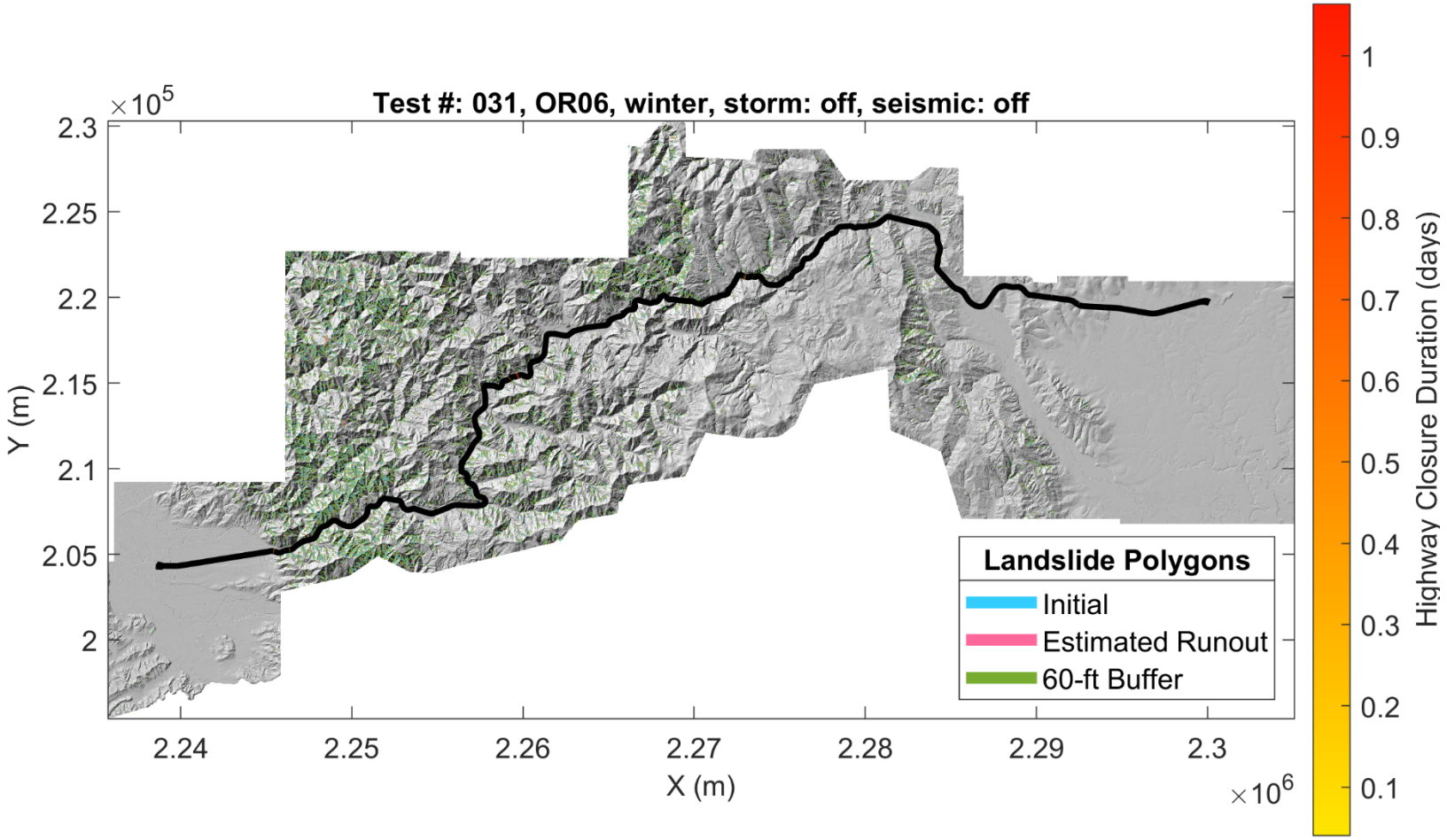

Figure 4.84: Map of landslide polygons, estimated runout, landslide buffers, and ROW closure for OR06: winter antecedent conditions (test #: 031).

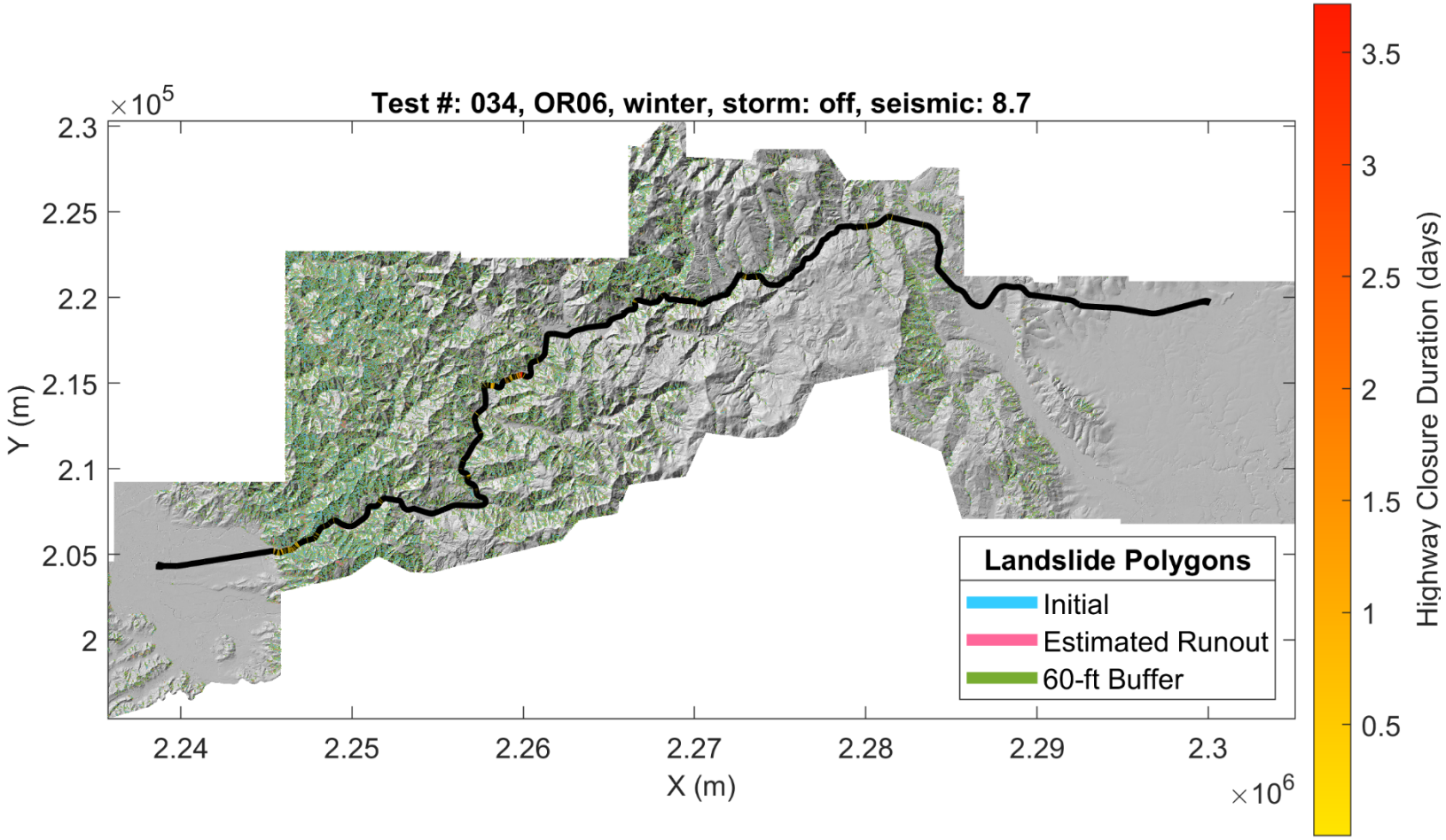

Figure 4.85: Map of landslide polygons, estimated runout, landslide buffers, and ROW closure for OR06: winter antecedent conditions, M8.7 earthquake (test #: 034).

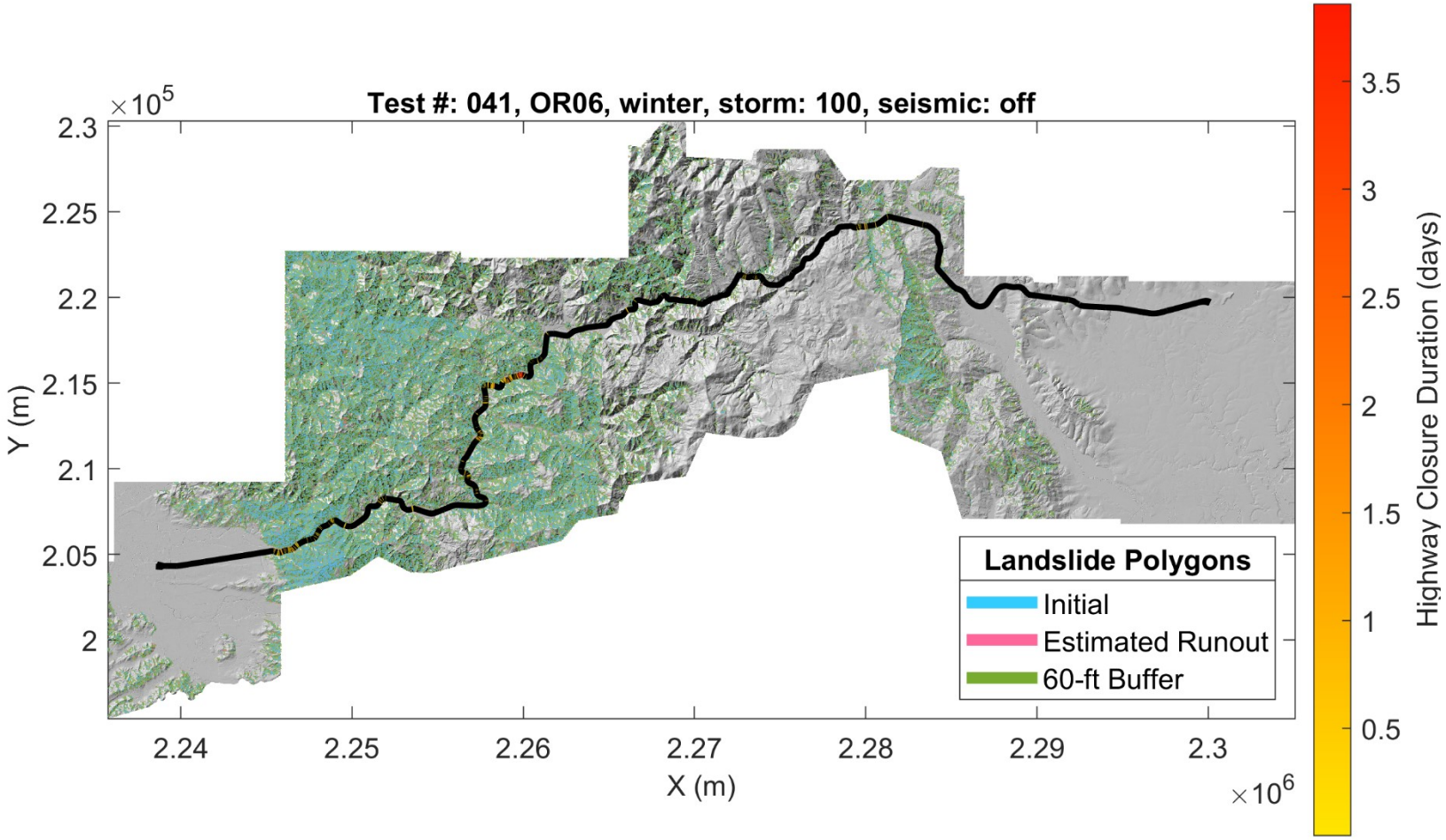

Figure 4.86: Map of landslide polygons, estimated runout, landslide buffers, and ROW closure for OR06: winter, 100-year rainfall event (test #: 041).

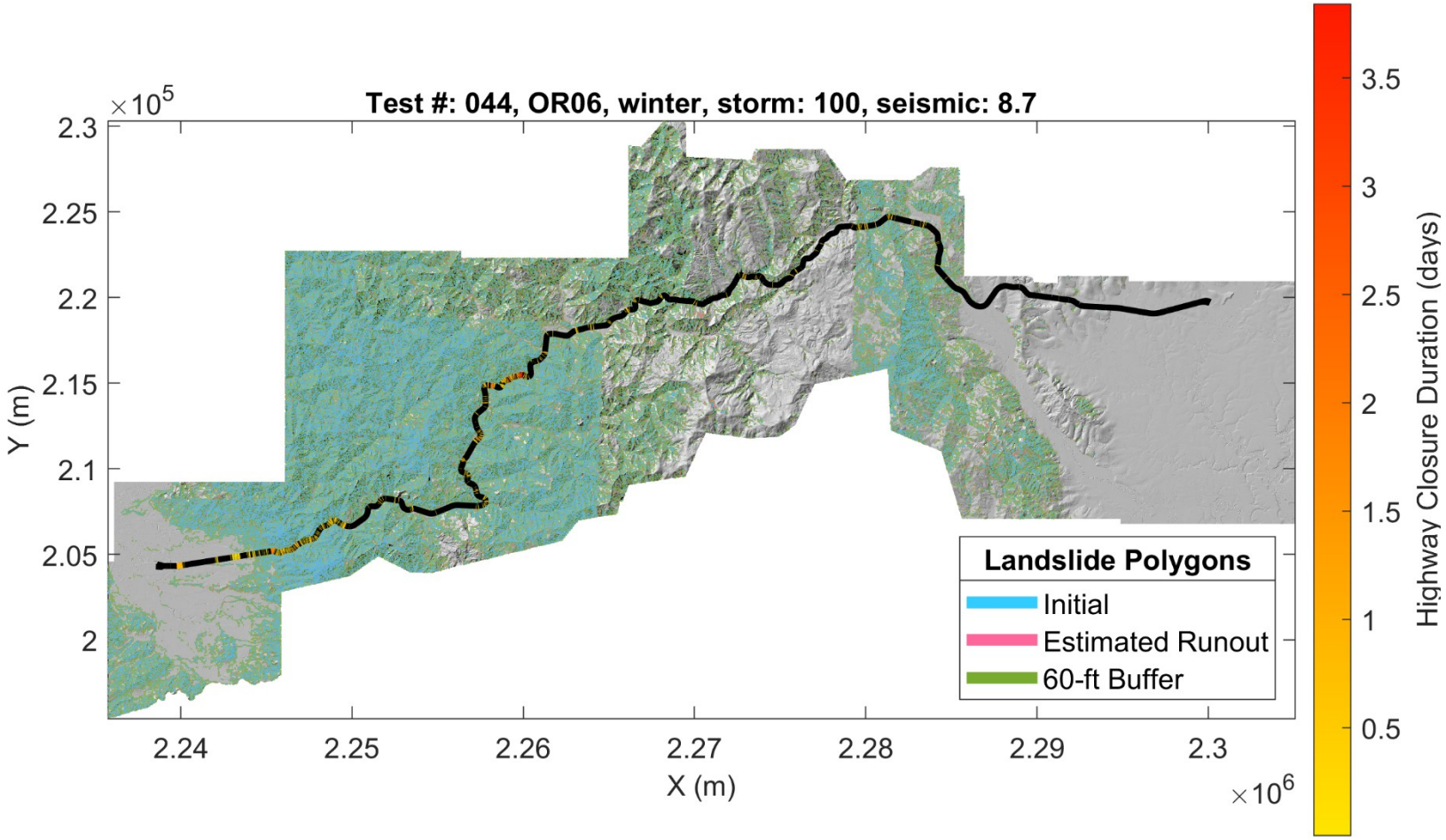

Figure 4.87: Map of landslide polygons, estimated runout, landslide buffers, and ROW closure for OR06: winter, 100-year rainfall event, M8.7 earthquake (test #: 044).

Figures 4.88-4.93 show closure times for corridor US20. For summer conditions, zero days of closure are observed throughout the corridor (Figure 4.88), even when seismicity is applied (Figure 4.89). However, closure for US20 is found to be highly sensitive to increased soil moisture. For winter antecedent conditions, closed sections begin appearing in the western region of the corridor (Figure 4.90). When seismicity is applied during antecedent winter conditions, more widespread and severe closure times are observed, with hot spots in the west-central region and slightly less severe hot spots in the western region of the corridor (Figure 4.91). When a 100-year rainstorm is applied, very widespread closure activity is observed throughout the corridor (Figure 4.92), becoming increasingly widespread and severe when seismicity is applied (Figure 4.93).

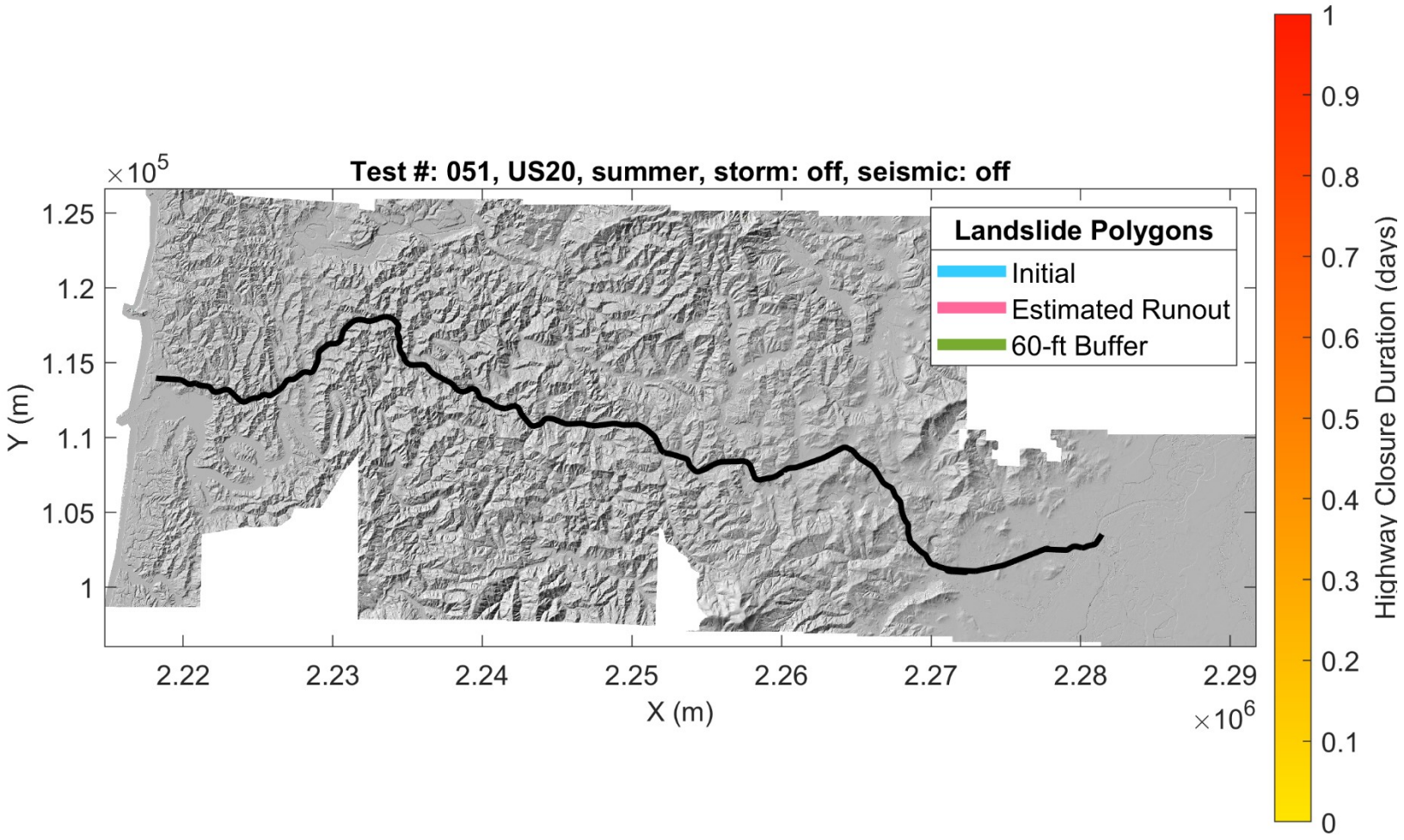

Figure 4.88: Map of landslide polygons, estimated runout, landslide buffers, and ROW closure for US20: summer antecedent conditions (test #: 051).

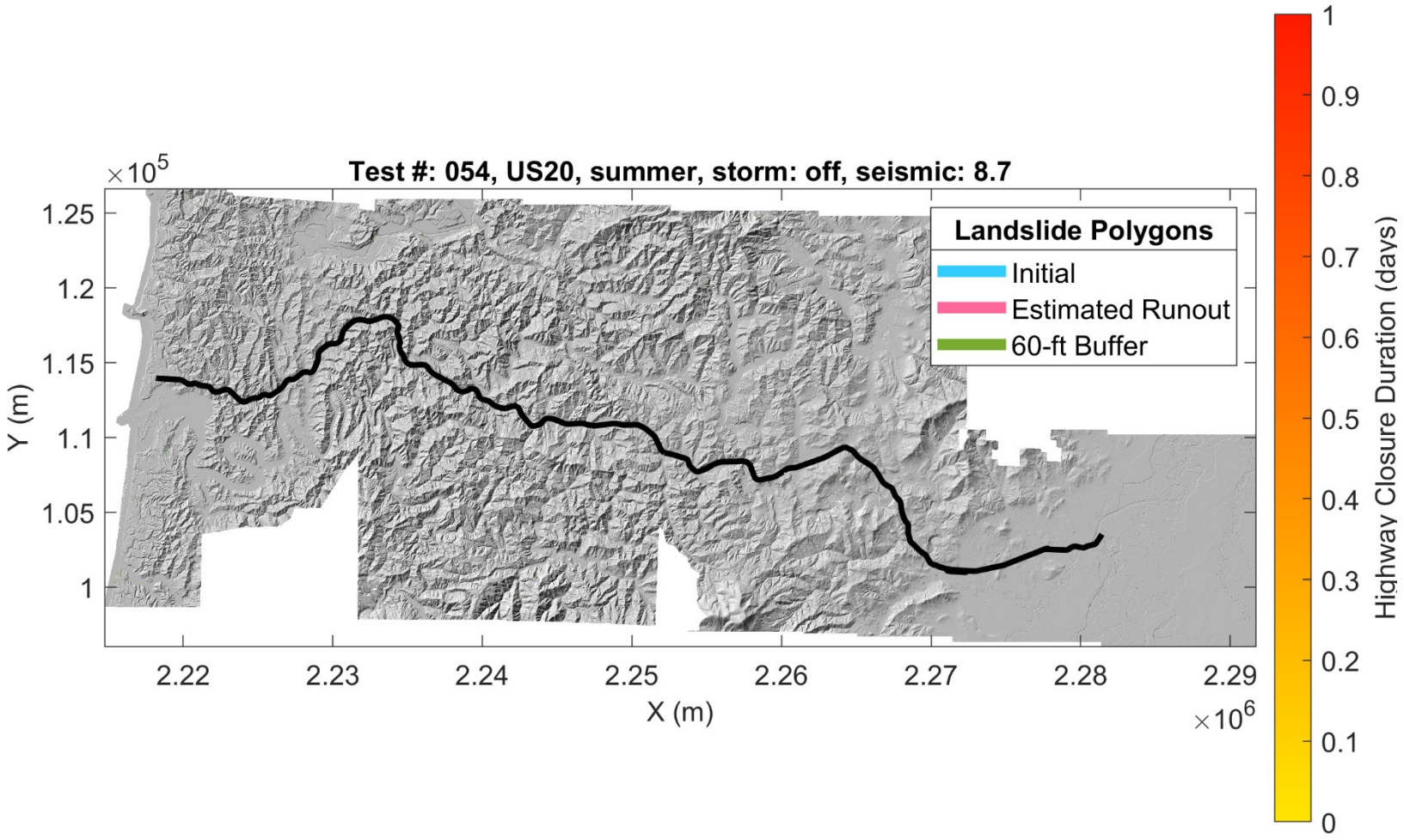

Figure 4.89: Map of landslide polygons, estimated runout, landslide buffers, and ROW closure for US20: summer antecedent conditions, M8.7 earthquake (test #: 054).

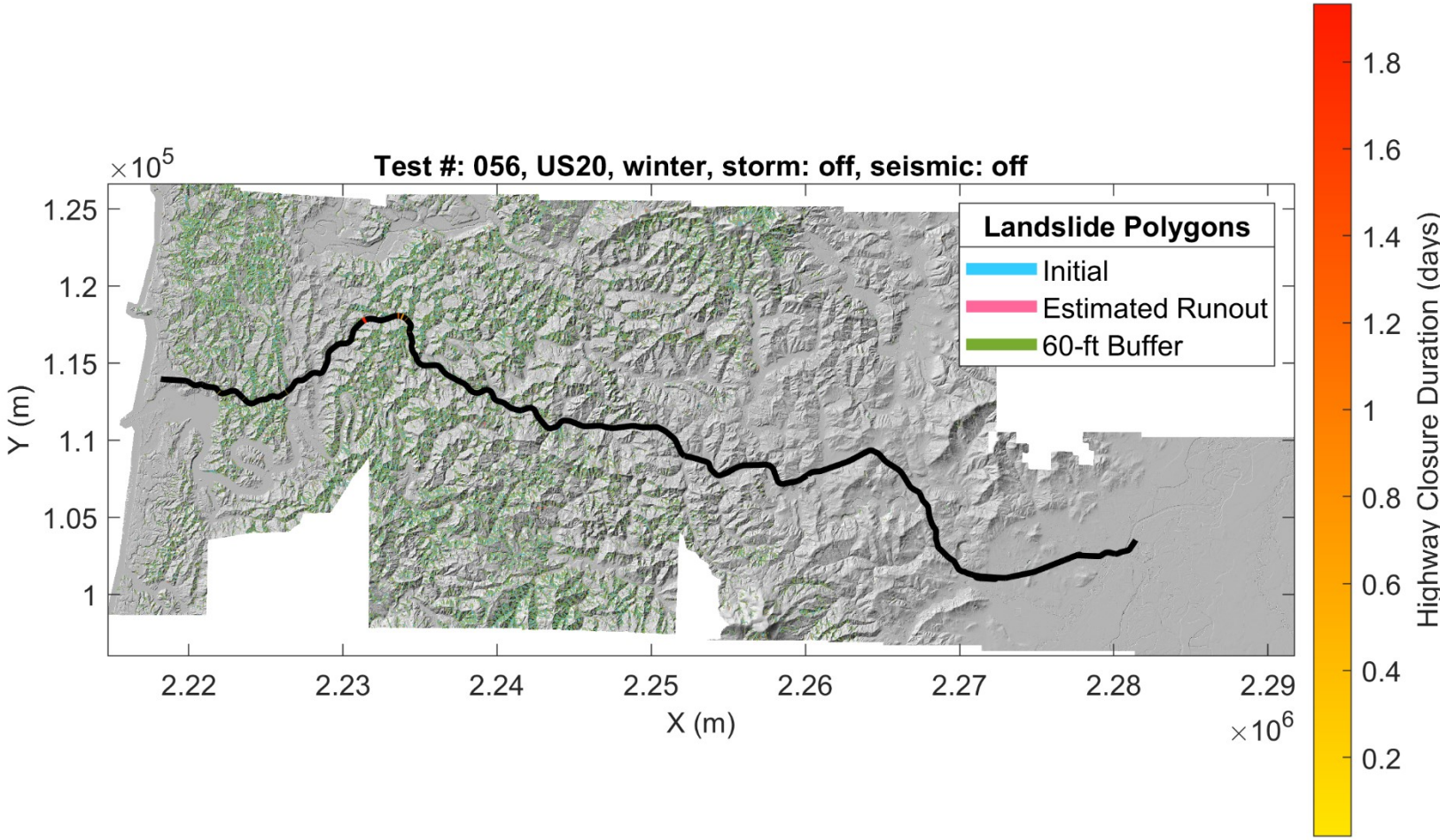

Figure 4.90: Map of landslide polygons, estimated runout, landslide buffers, and ROW closure for US20: winter antecedent conditions (test #: 056).

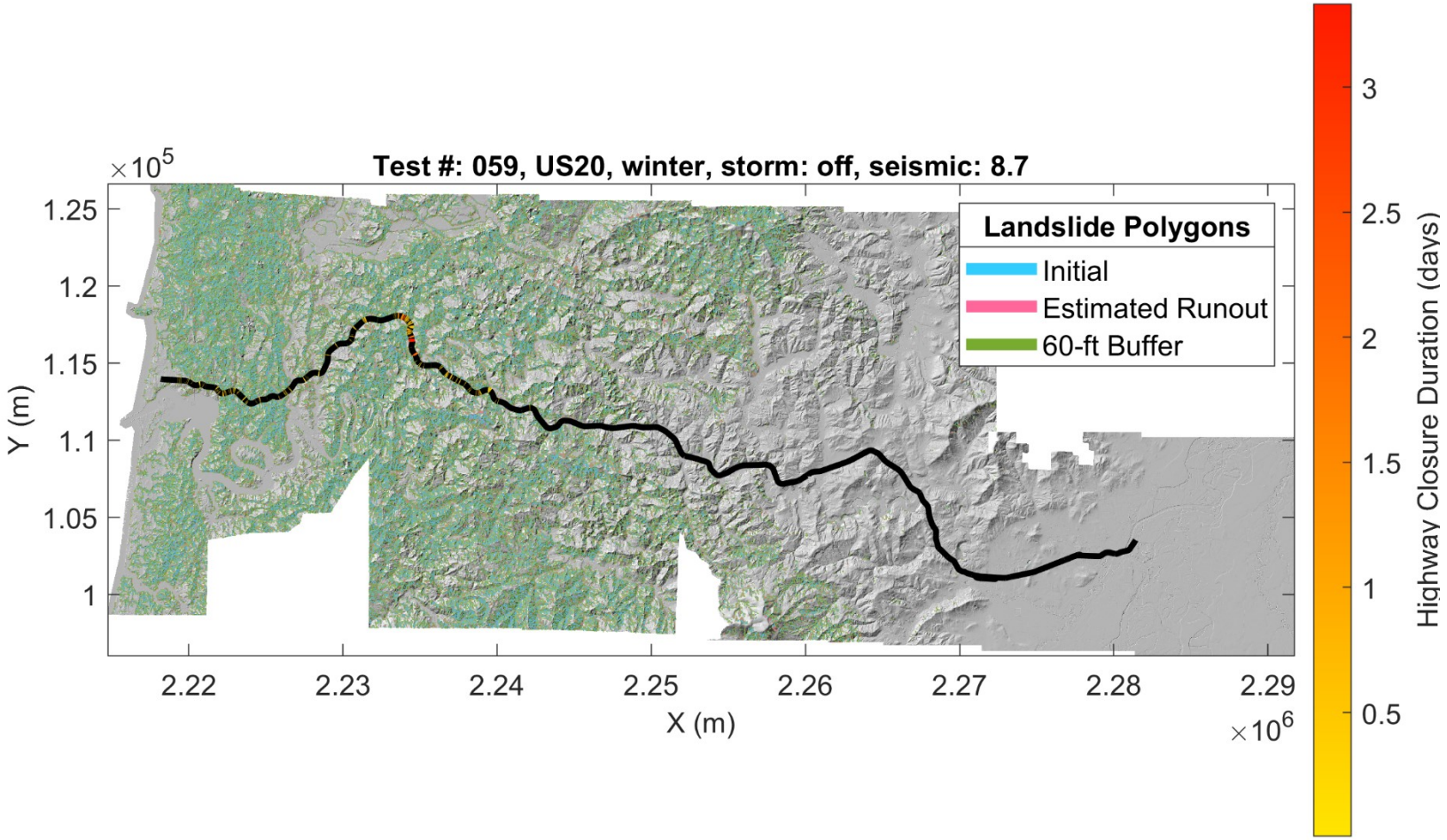

Figure 4.91: Map of landslide polygons, estimated runout, landslide buffers, and ROW closure for US20: winter antecedent conditions, M8.7 earthquake (test #: 059).

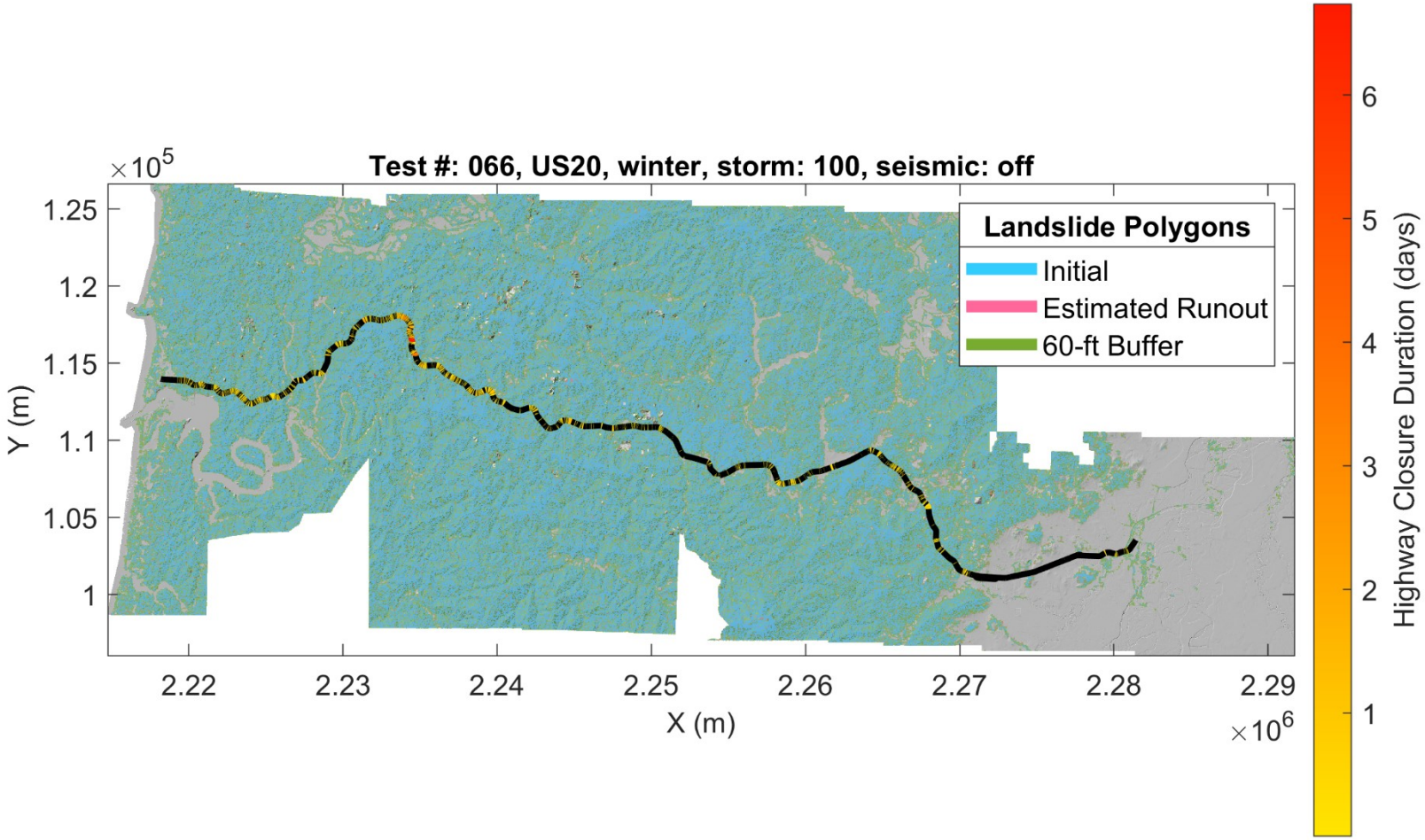

Figure 4.92: Map of landslide polygons, estimated runout, landslide buffers, and ROW closure for US20: winter, 100-year rainfall event (test #: 066).

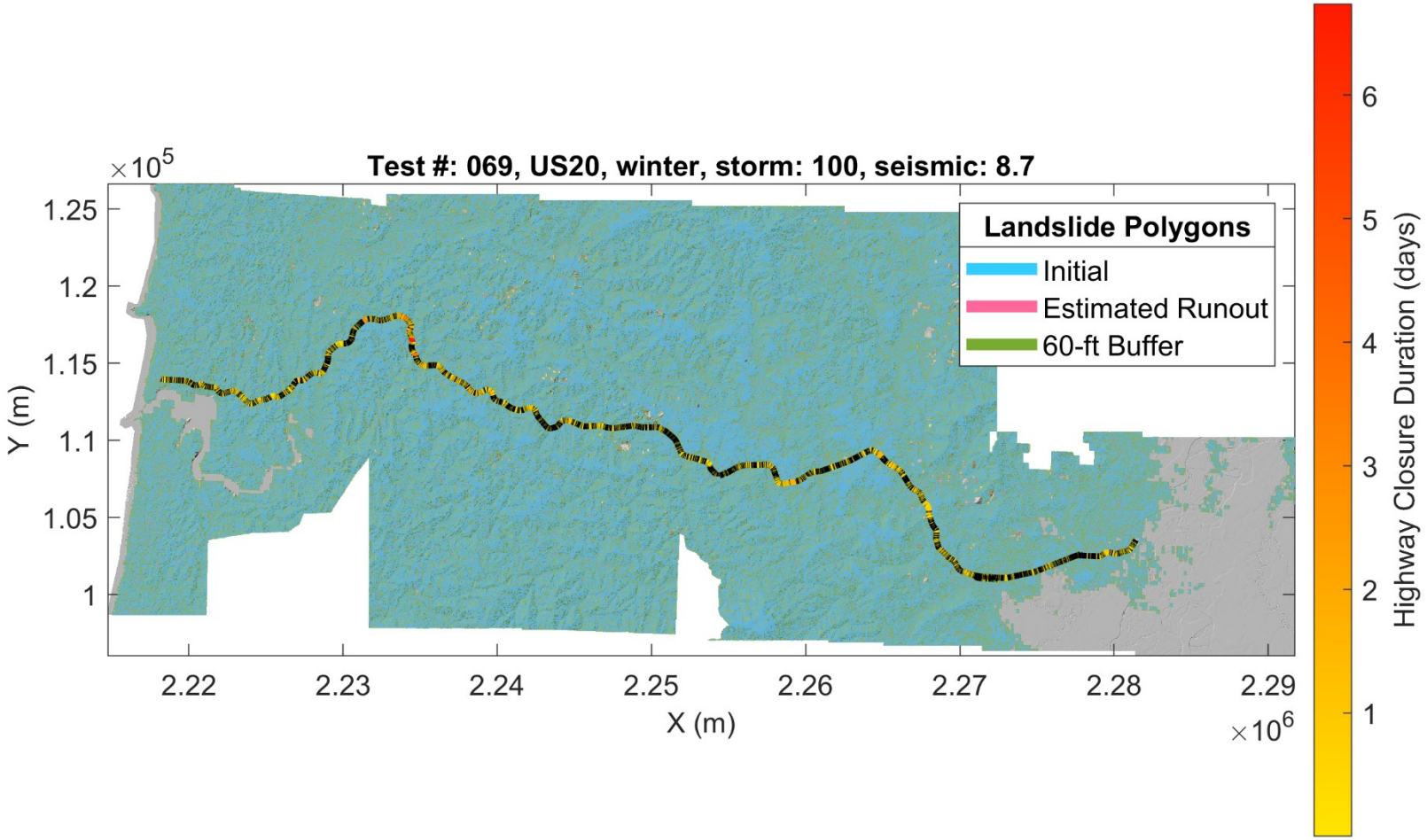

Figure 4.93: Map of landslide polygons, estimated runout, landslide buffers, and ROW closure for US20: winter, 100-year rainfall event, M8.7 earthquake (test #: 069).

Figures 4.94-4.99 show closure times for corridor OR42. For summer conditions, zero days of closure are observed throughout the corridor (Figure 4.94), even when seismicity is applied (Figure 4.95). For winter antecedent conditions, closed sections begin appearing in the east-central region of the corridor (Figure 4.96). When seismicity is applied during antecedent winter conditions, the east-central region exhibits slightly more severe closure times (Figure 4.97). Closure times increase again when a 100-year storm is applied (Figure 4.98), with high closure times still mainly concentrated in the east-central region. Finally, applied seismicity with a 100-year storm event results in more widespread closure throughout the corridor (Figure 4.99).

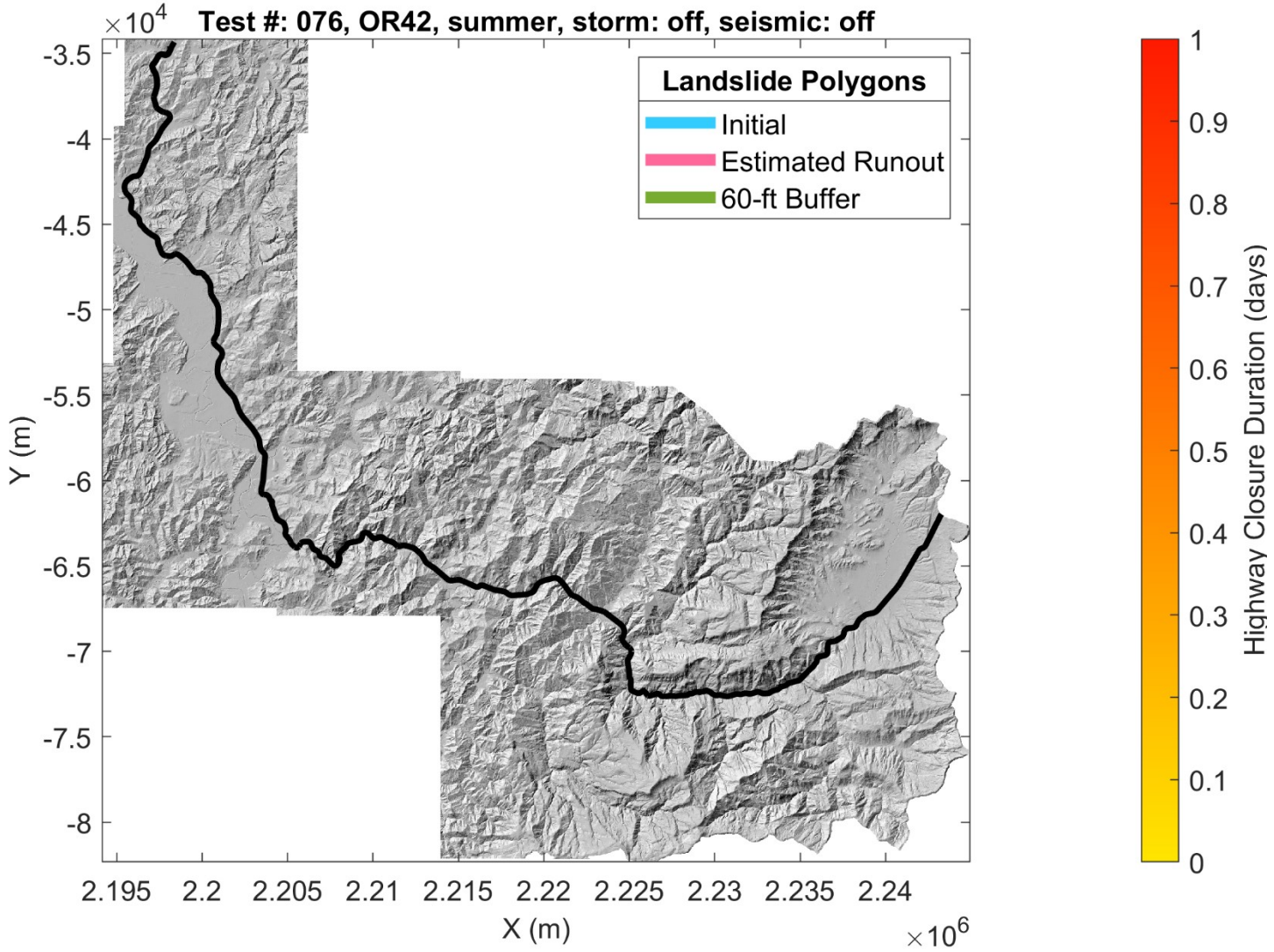

Figure 4.94: Map of landslide polygons, estimated runout, landslide buffers, and ROW closure for OR42: summer antecedent conditions (test #: 076).

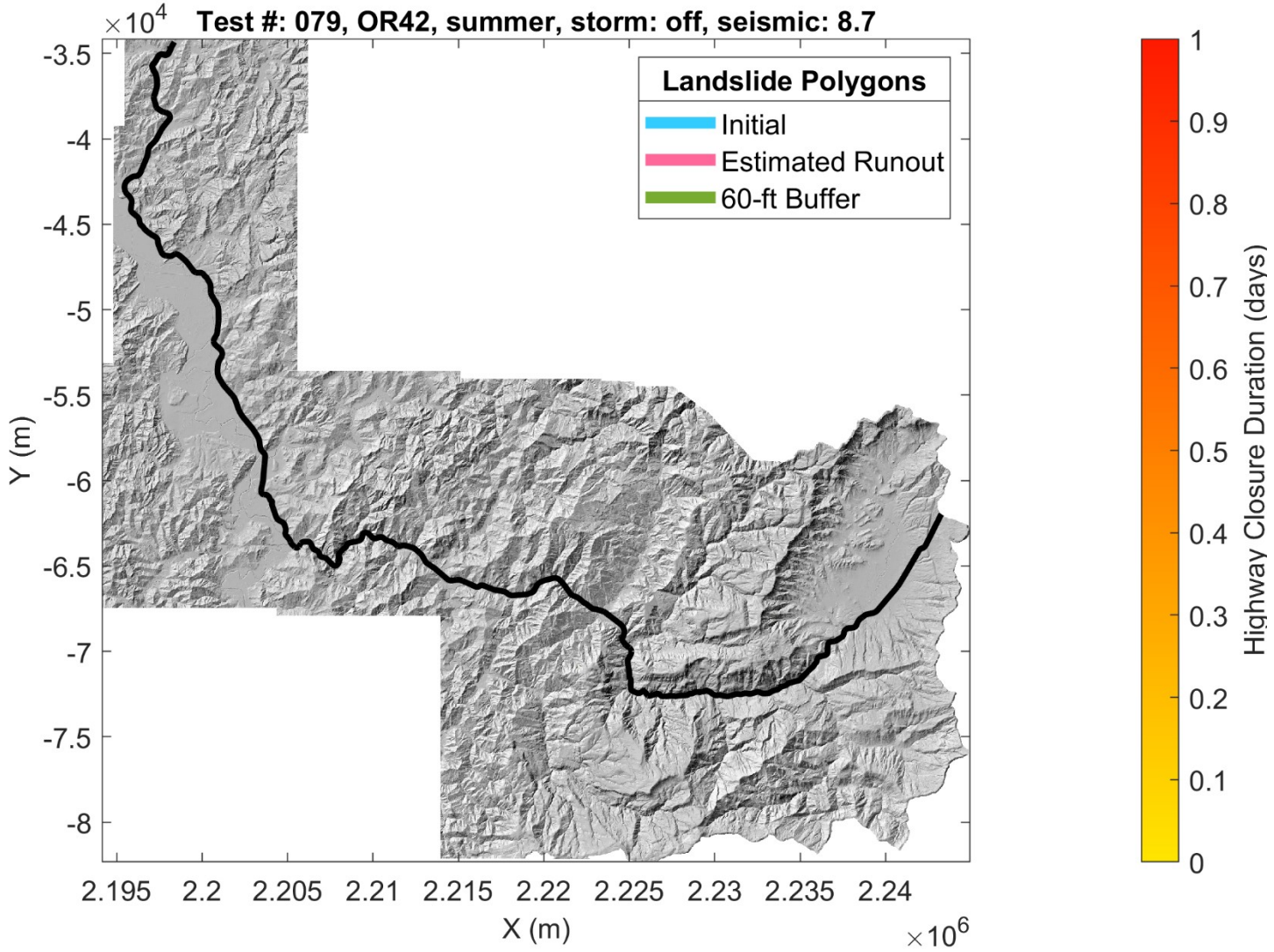

Figure 4.95: Map of landslide polygons, estimated runout, landslide buffers, and ROW closure for OR42: summer antecedent conditions, M8.7 earthquake (test #: 079).

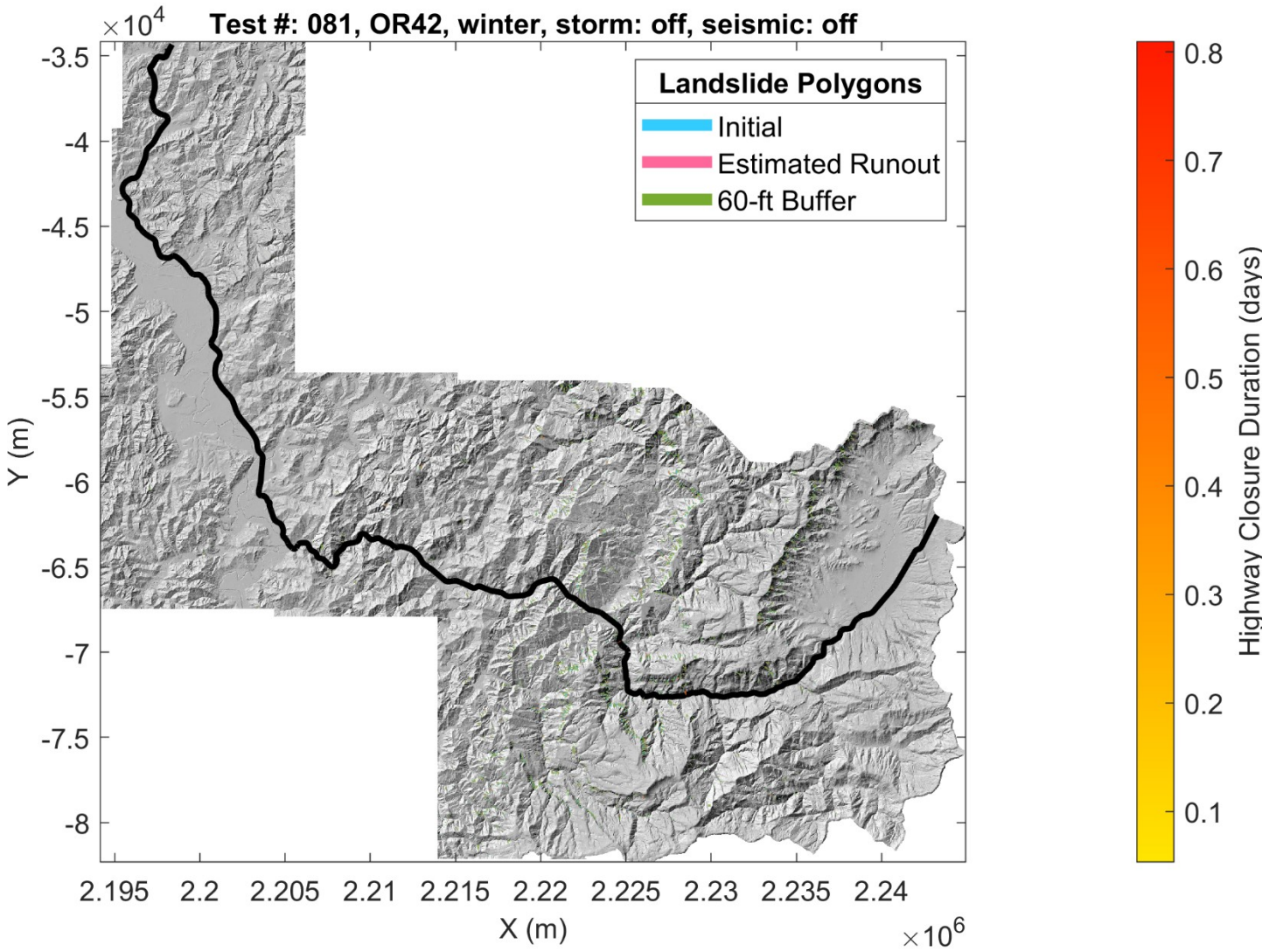

Figure 4.96: Map of landslide polygons, estimated runout, landslide buffers, and ROW closure for OR42: winter antecedent conditions (test #: 081).

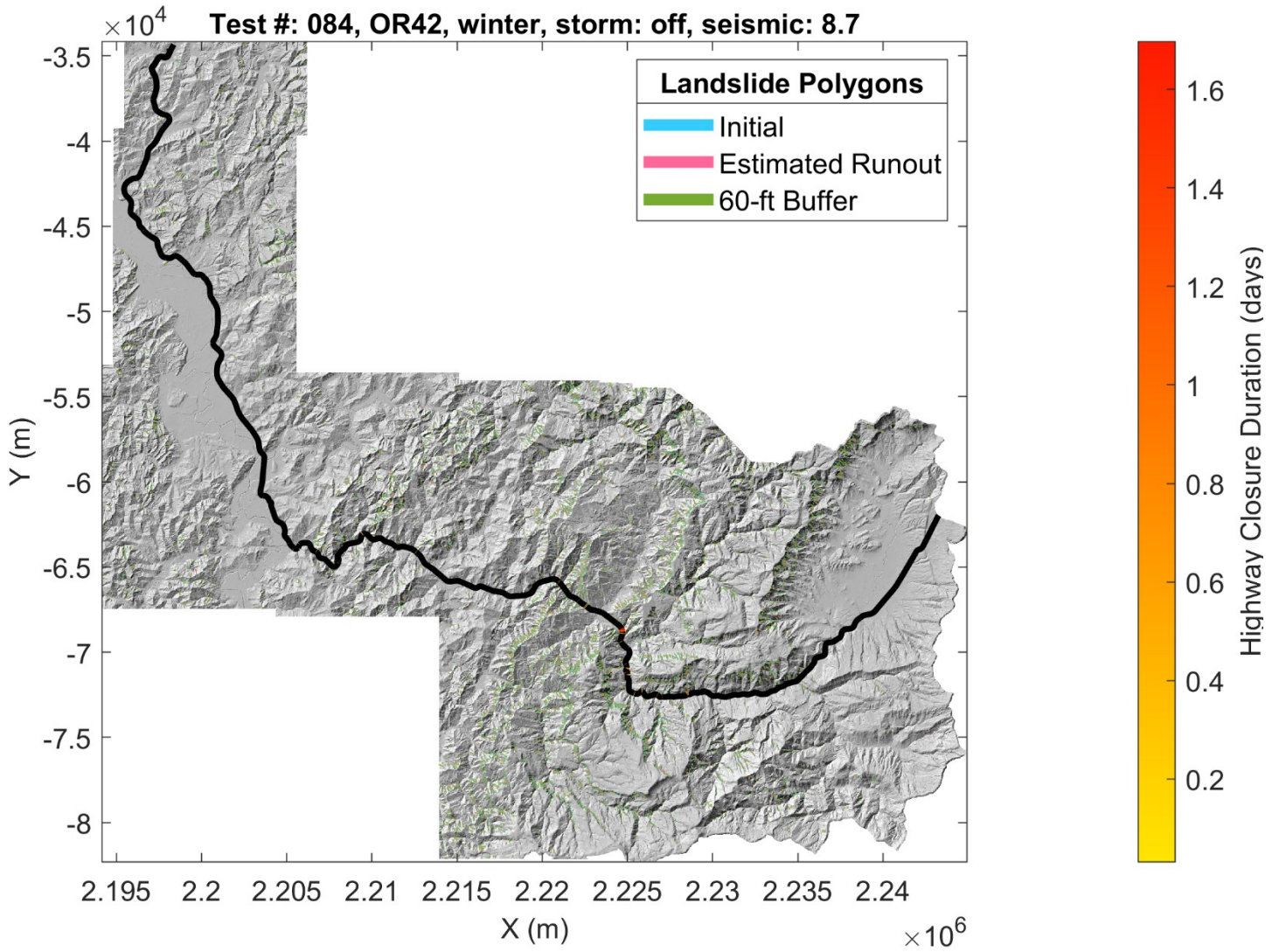

Figure 4.97: Map of landslide polygons, estimated runout, landslide buffers, and ROW closure for OR42: winter antecedent conditions, M8.7 earthquake (test #: 084).

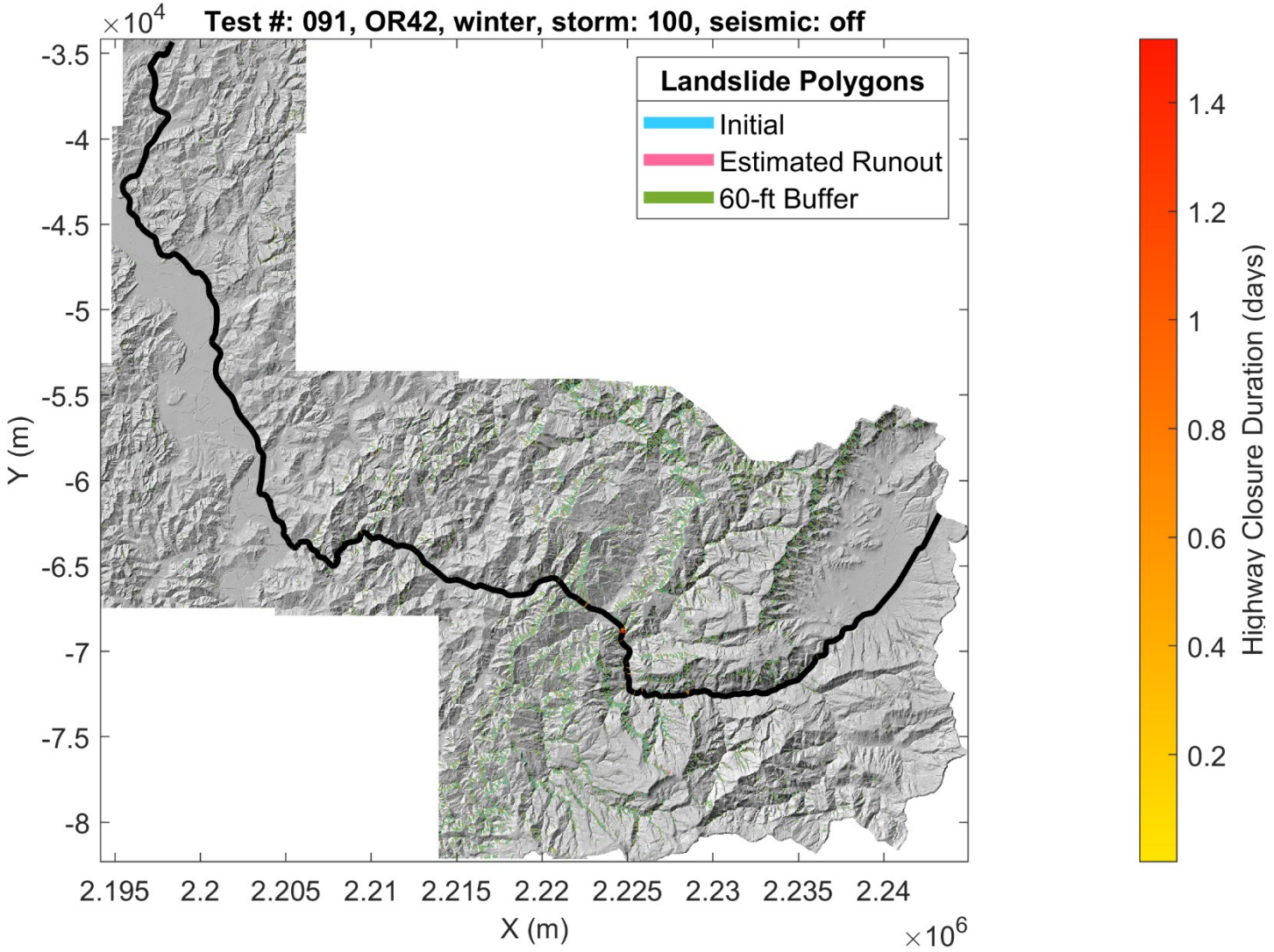

Figure 4.98: Map of landslide polygons, estimated runout, landslide buffers, and ROW closure for OR42: winter, 100-year rainfall event (test #: 091).

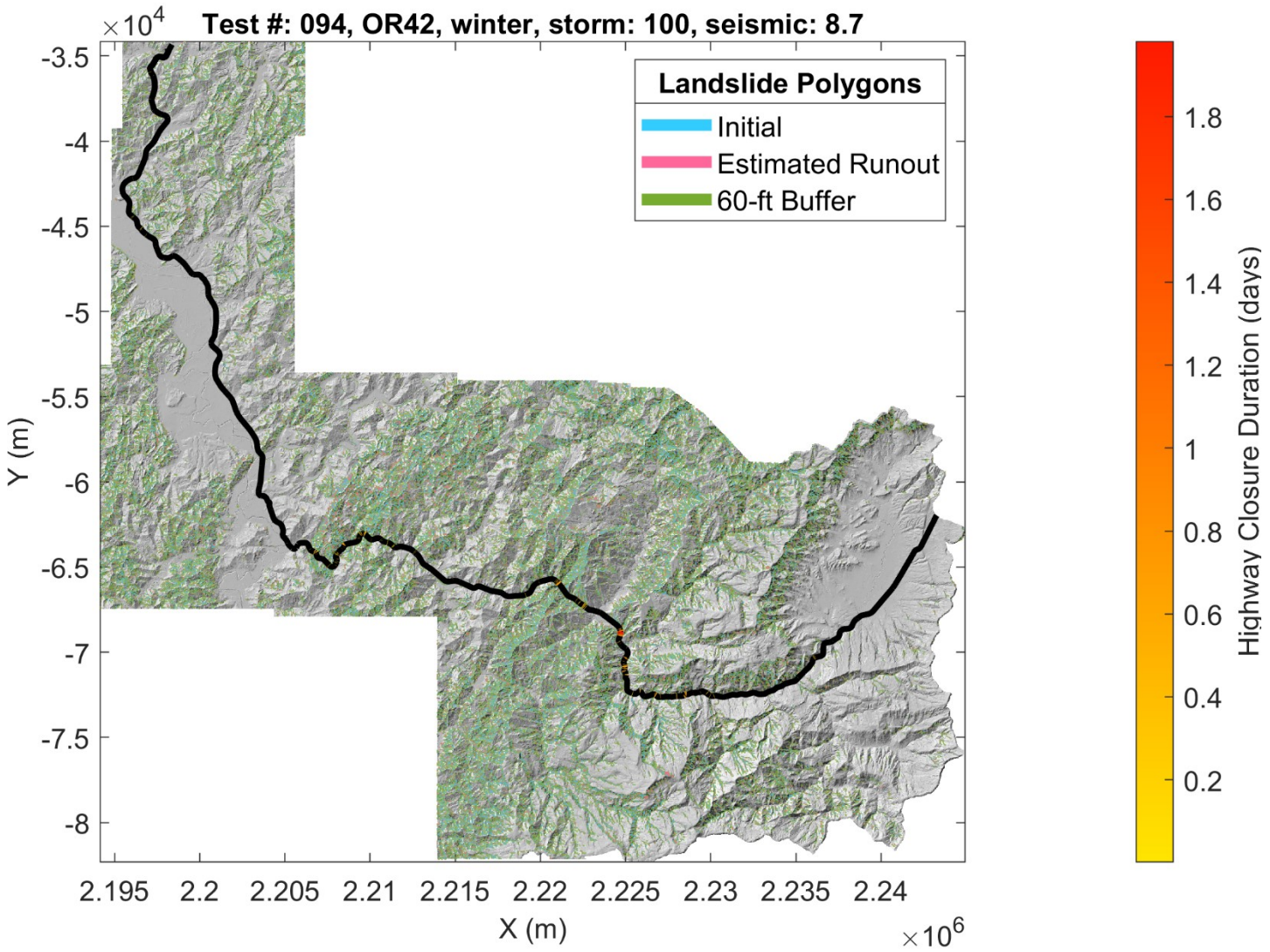

Figure 4.99: Map of landslide polygons, estimated runout, landslide buffers, and ROW closure for OR42: winter, 100-year rainfall event, M8.7 earthquake (test #: 094).

4.6.3 Profiles of Highway Closure Times and Associated Repair Costs

To supplement the maps shown in Section 4.6.2, highway closure data is used to create profiles of cumulative closure times and associated repair costs, with respect to highway milepost. Note that these closure metrics are cumulative; in other words, while traversing the corridor, closure times and costs are added to the total time and cost as they are encountered. This allows planners an additional means of visualizing closure metrics along each corridor of ODOT ROW. For the test numbers highlighted in Table 4.4, profiles of highway milepost vs. closure time are shown in Figures 4.100-4.123 and profiles of milepost vs. repair cost are shown in Figures 4.124-4.147. Note that for Figures 4.100-4.123, the dashed curves represent the possibility of beginning repairs on both ends of each analyzed highway, which given sufficient resources, theoretically divides the total repair time by two. A full suite of figures showing highway milepost vs. closure time and milepost vs. repair cost, for all tests in Table 4.4, may be found in Appendices E and F, respectively. Similar full suites of profiles considering a 60-foot (18.3 m) buffer around landslide shapes may be found in Appendices G (milepost vs. closure time) and H (milepost vs. repair cost). Similar to the values shown in Table 4.6, note that these costs and times are likely an underestimate, as they do not include various other expenses tied to construction beyond excavation.

4.6.3.1 ***Milepost vs. Closure Time***

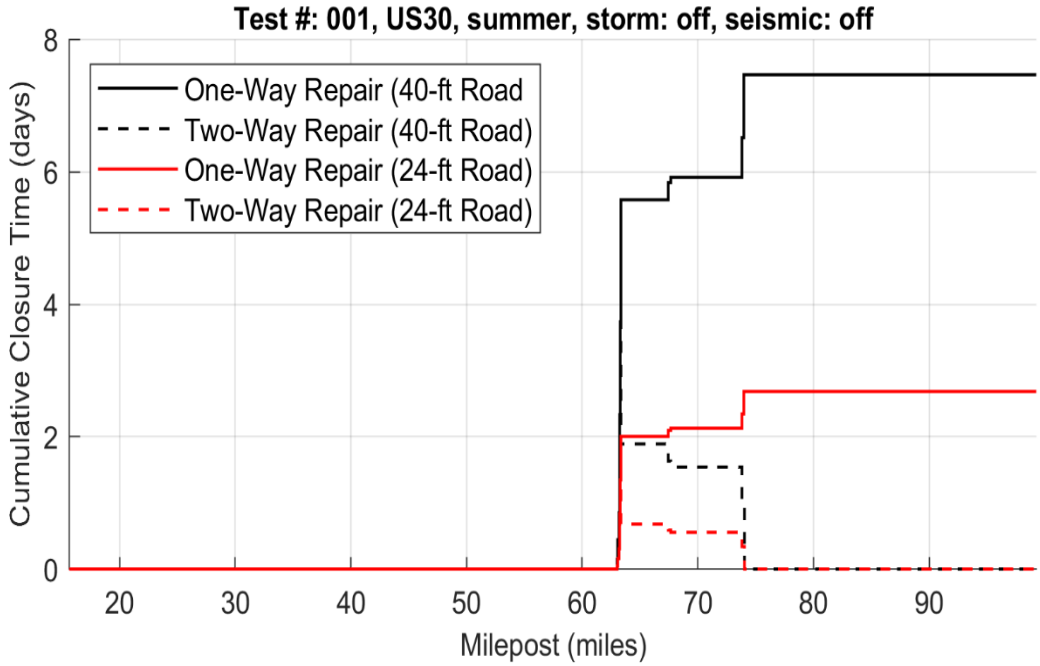

Figure 4.100: Profile of cumulative closure time for US30: summer antecedent conditions (test #: 001).

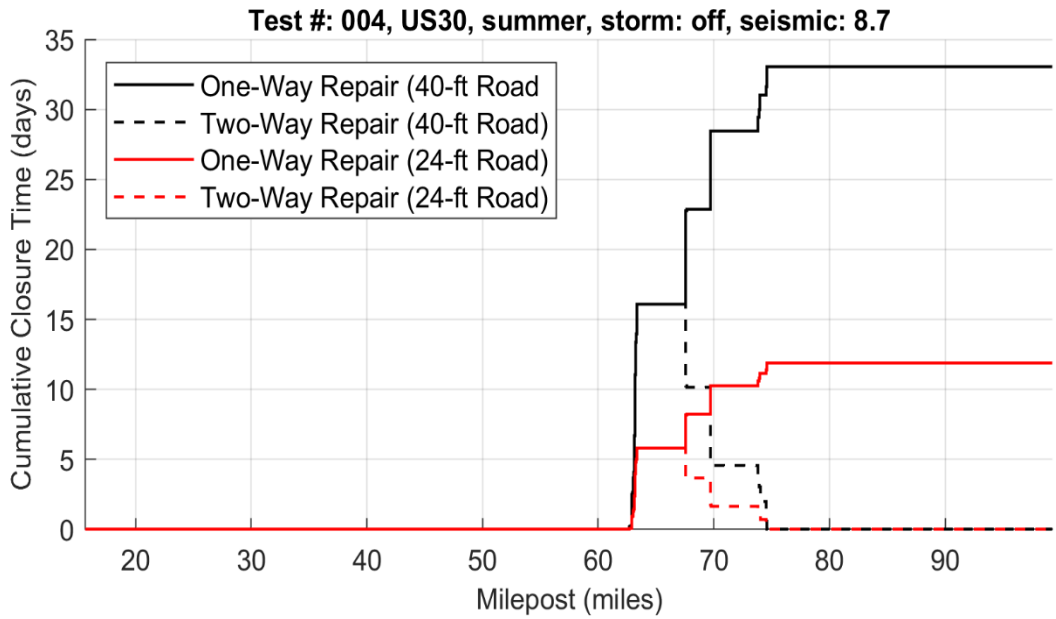

Figure 4.101: Profile of cumulative closure time for US30: summer antecedent conditions, M8.7 earthquake (test #: 004).

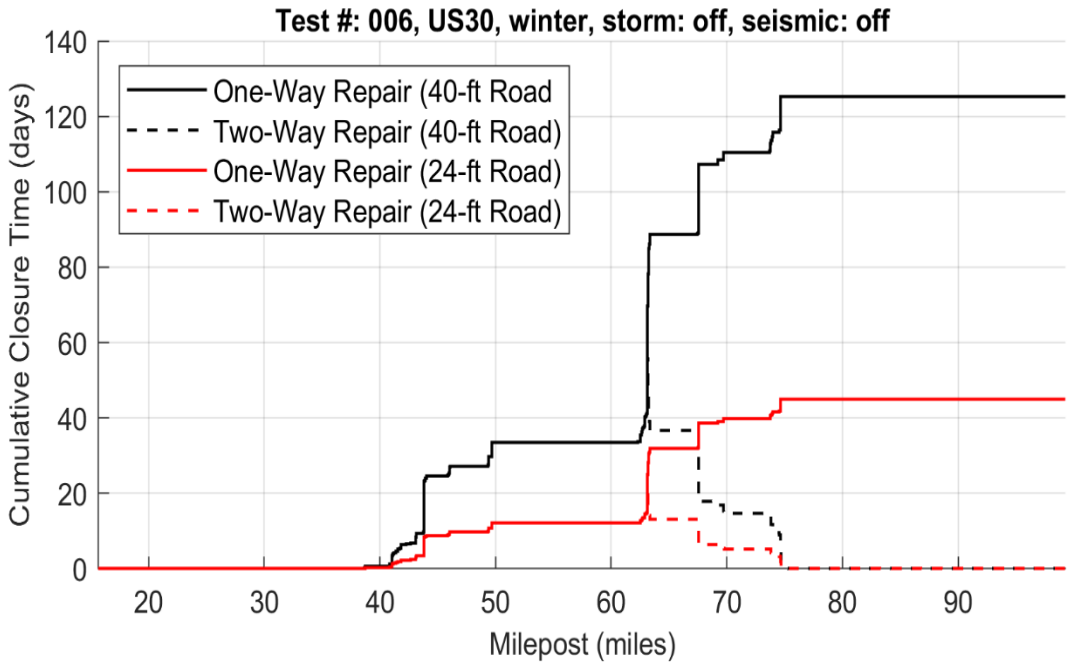

Figure 4.102: Profile of cumulative closure time for US30: winter antecedent conditions (test #: 006).

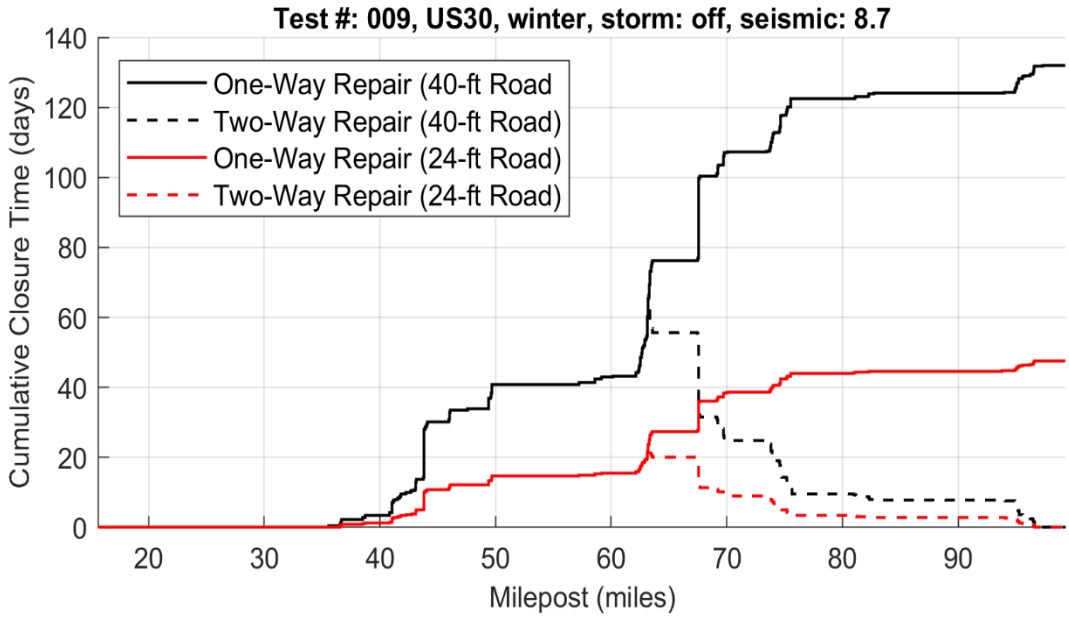

Figure 4.103: Profile of cumulative closure time for US30: winter antecedent conditions, M8.7 earthquake (test #: 009).

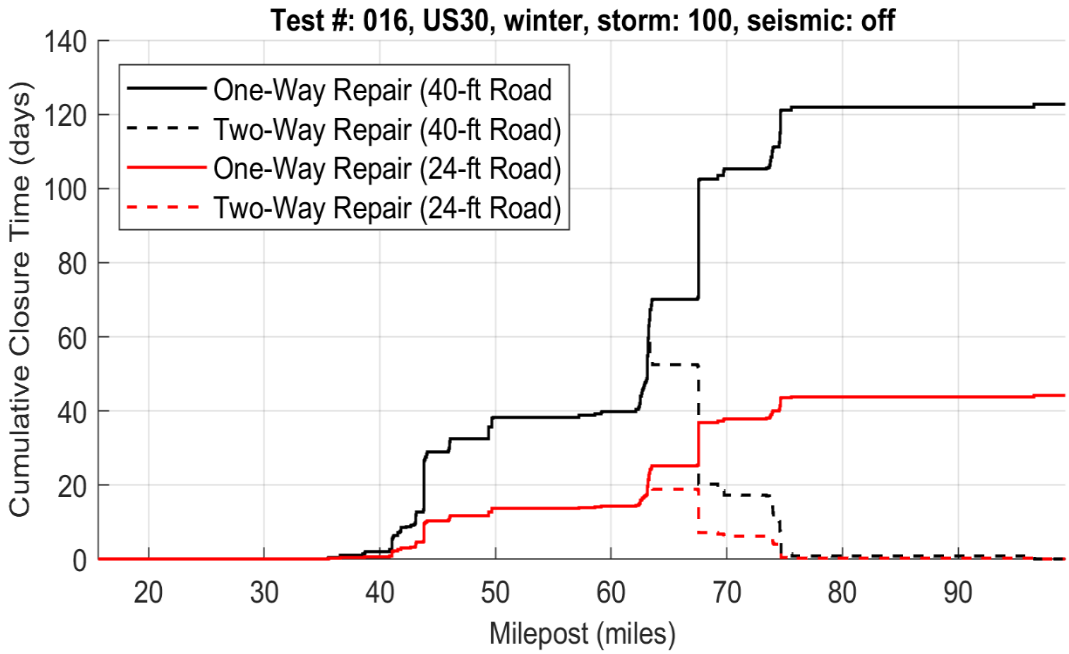

Figure 4.104: Profile of cumulative closure time for US30: winter, 100-year rainfall event (test #: 016).

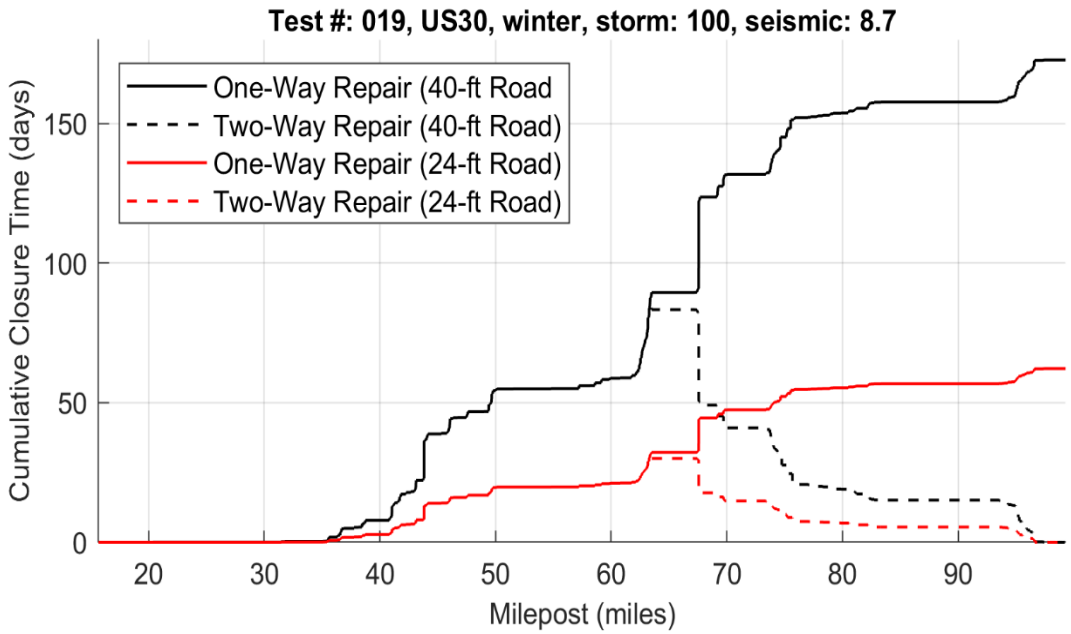

Figure 4.105: Profile of cumulative closure time for US30: winter, 100-year rainfall event, M8.7 earthquake (test #: 019).

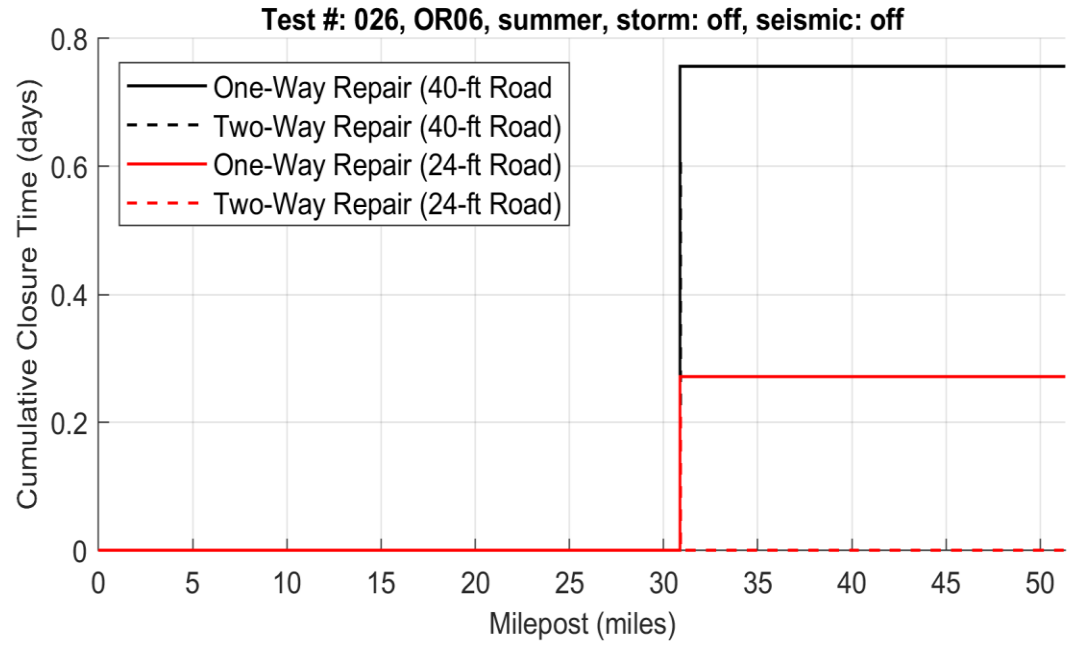

Figure 4.106: Profile of cumulative closure time for OR06: summer antecedent conditions (test #: 026).

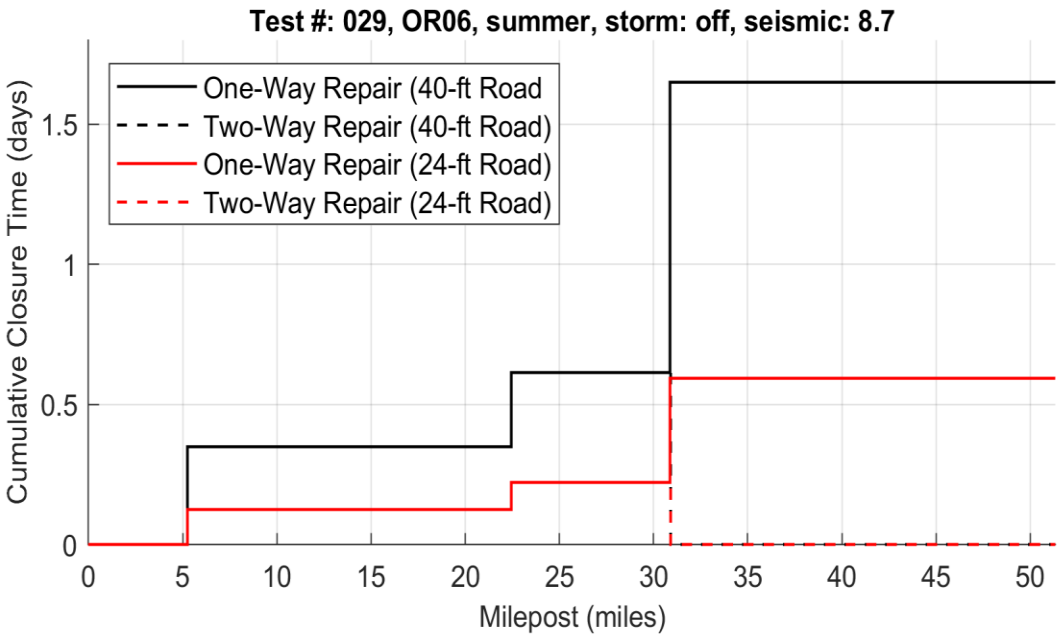

Figure 4.107: Profile of cumulative closure time for OR06: summer antecedent conditions, M8.7 earthquake (test #: 029).

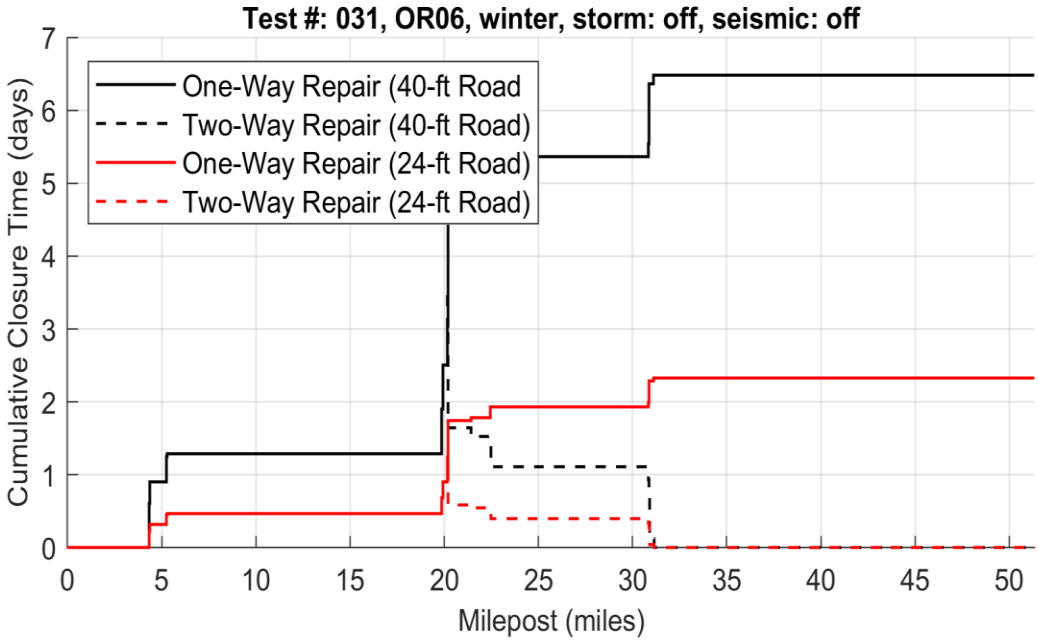

Figure 4.108: Profile of cumulative closure time for OR06: winter antecedent conditions (test #: 031).

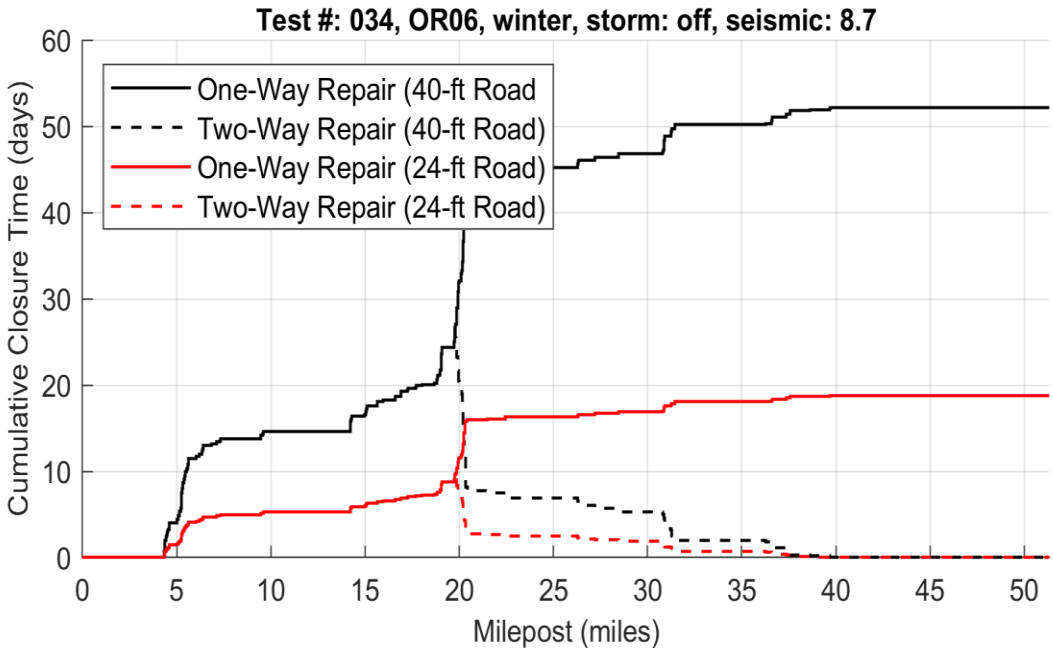

Figure 4.109: Profile of cumulative closure time for OR06: winter antecedent conditions, M8.7 earthquake (test #: 034).

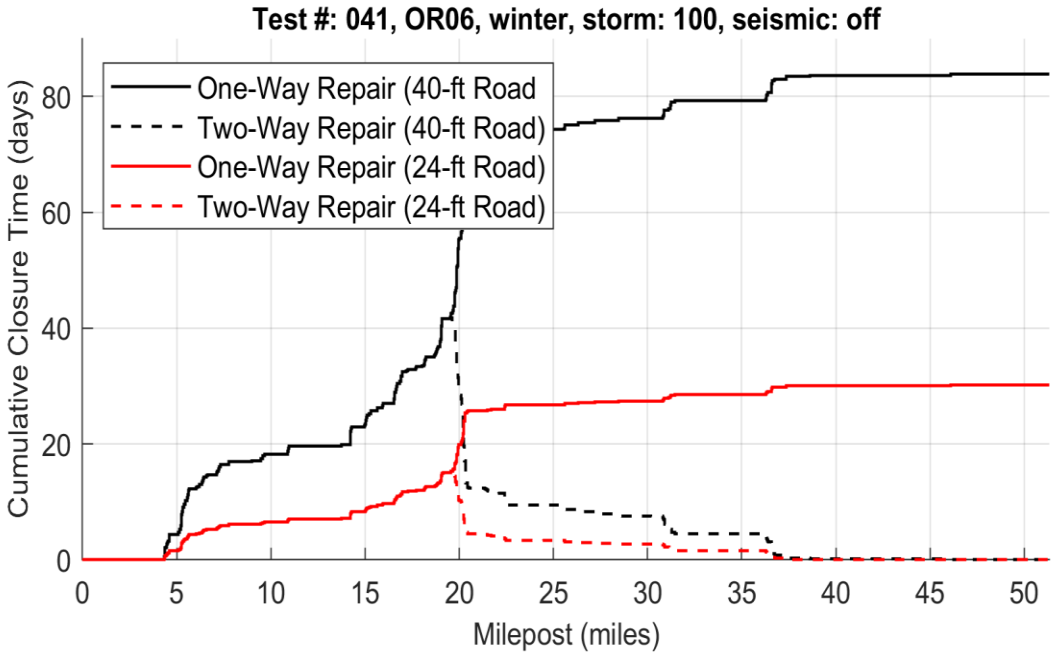

Figure 4.110: Profile of cumulative closure time for OR06: winter, 100-year rainfall event (test #: 041).

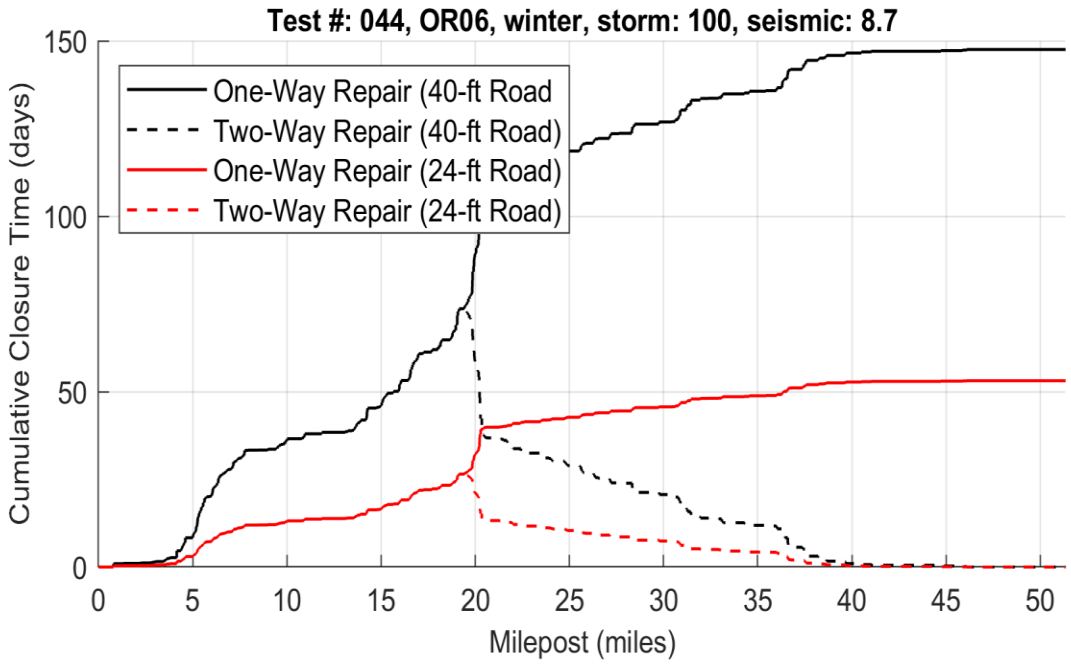

Figure 4.111: Profile of cumulative closure time for OR06: winter, 100-year rainfall event, M8.7 earthquake (test #: 044).

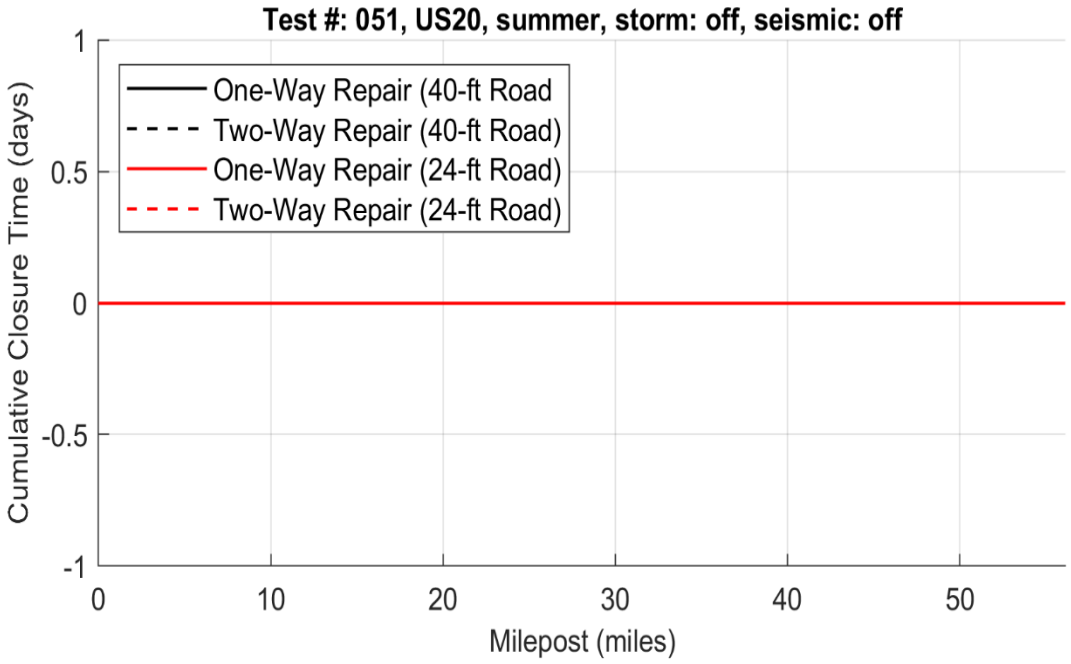

Figure 4.112: Profile of cumulative closure time for US20: summer antecedent conditions (test #: 051).

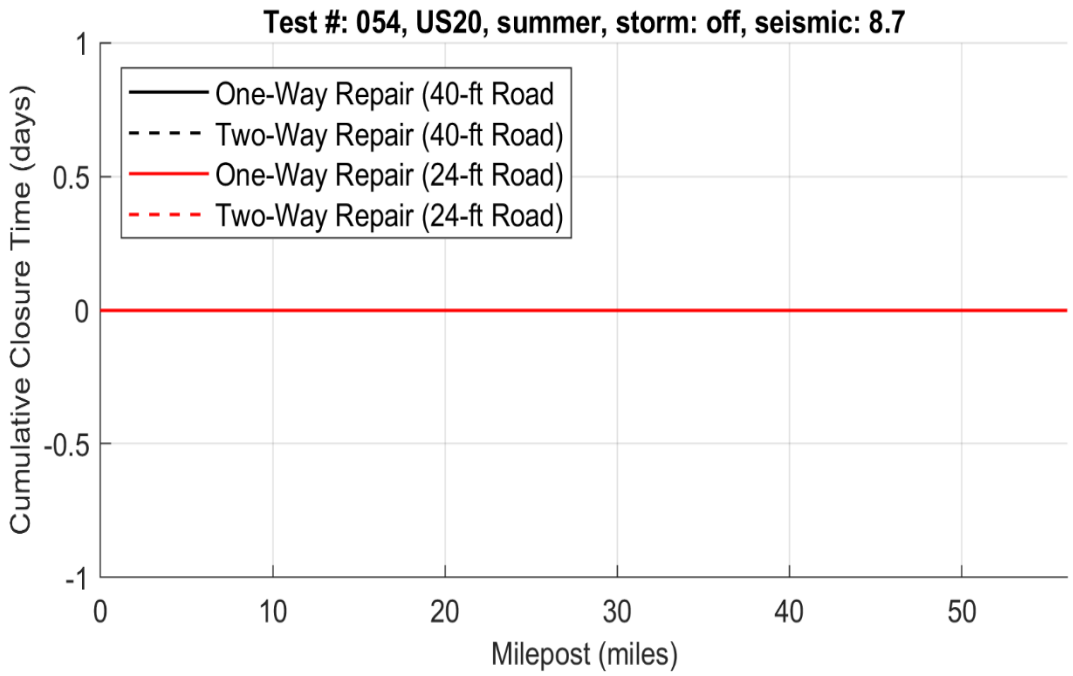

Figure 4.113: Profile of cumulative closure time for US20: summer antecedent conditions, M8.7 earthquake (test #: 054).

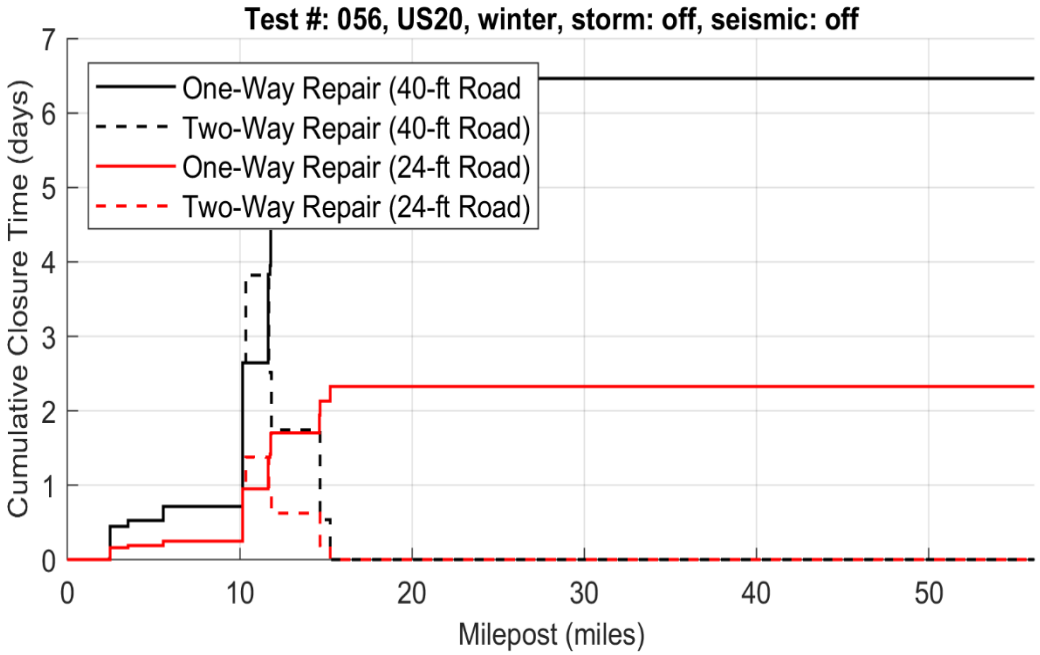

Figure 4.114: Profile of cumulative closure time for US20: winter antecedent conditions (test #: 056).

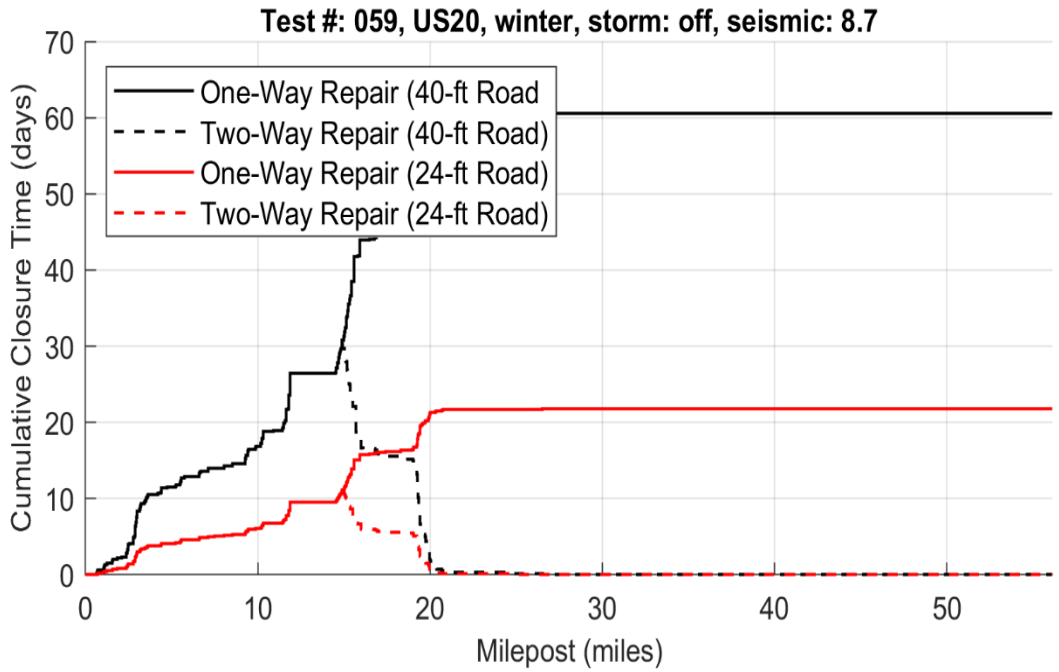

Figure 4.115: Profile of cumulative closure time for US20: winter antecedent conditions, M8.7 earthquake (test #: 059).

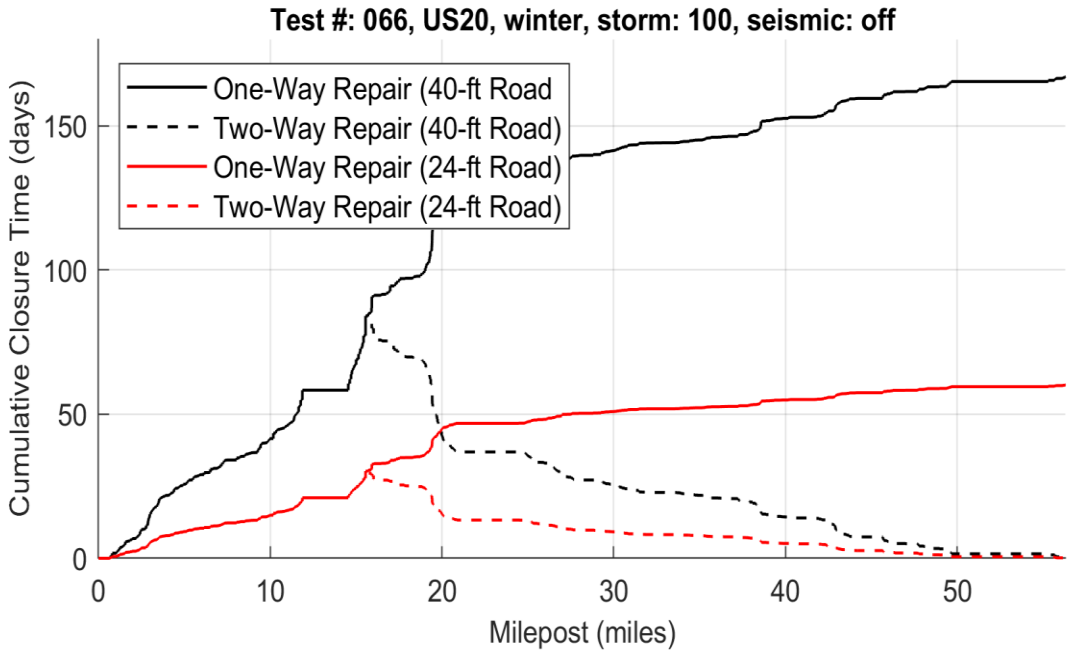

Figure 4.116: Profile of cumulative closure time for US20: winter, 100-year rainfall event (test #: 066).

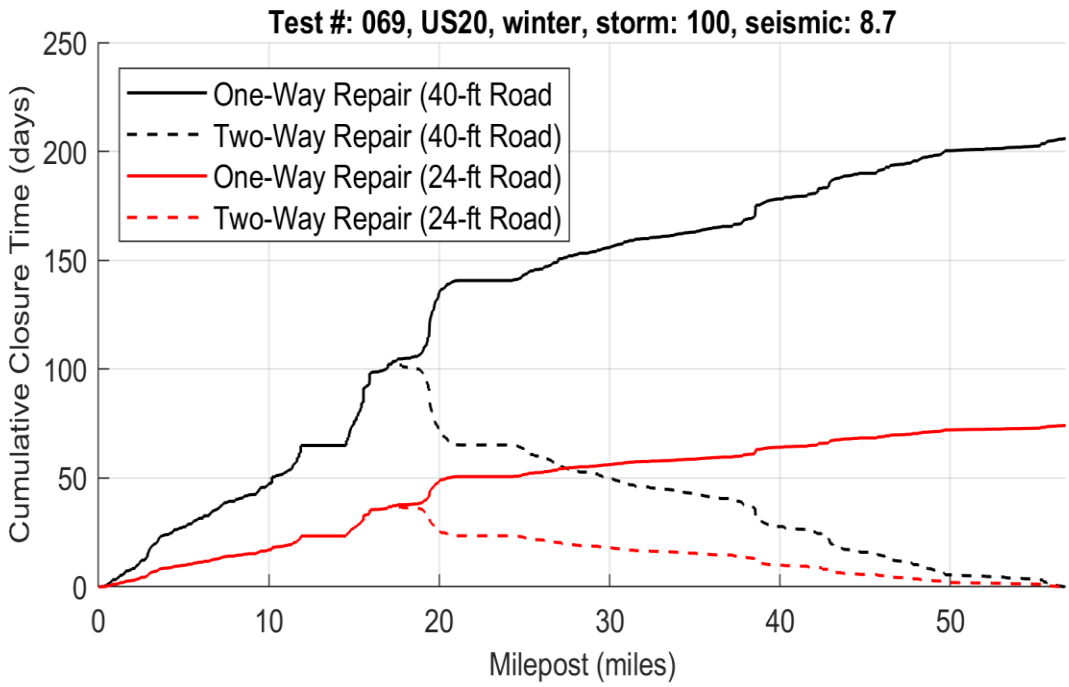

Figure 4.117: Profile of cumulative closure time for US20: winter, 100-year rainfall event, M8.7 earthquake (test #: 069).

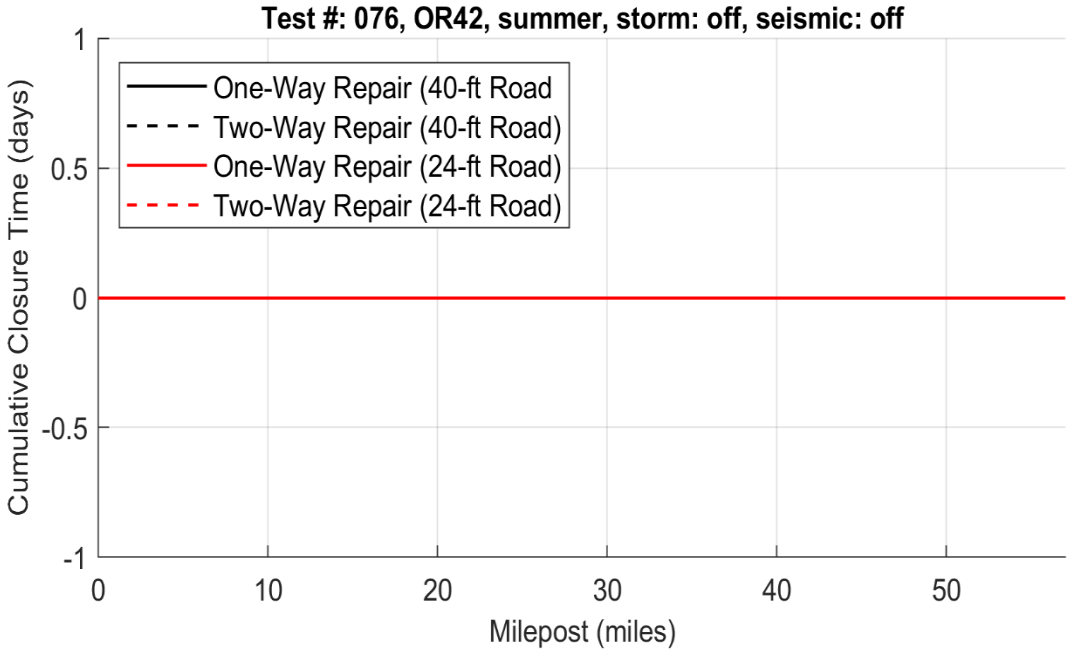

Figure 4.118: Profile of cumulative closure time for OR42: summer antecedent conditions (test #: 076).

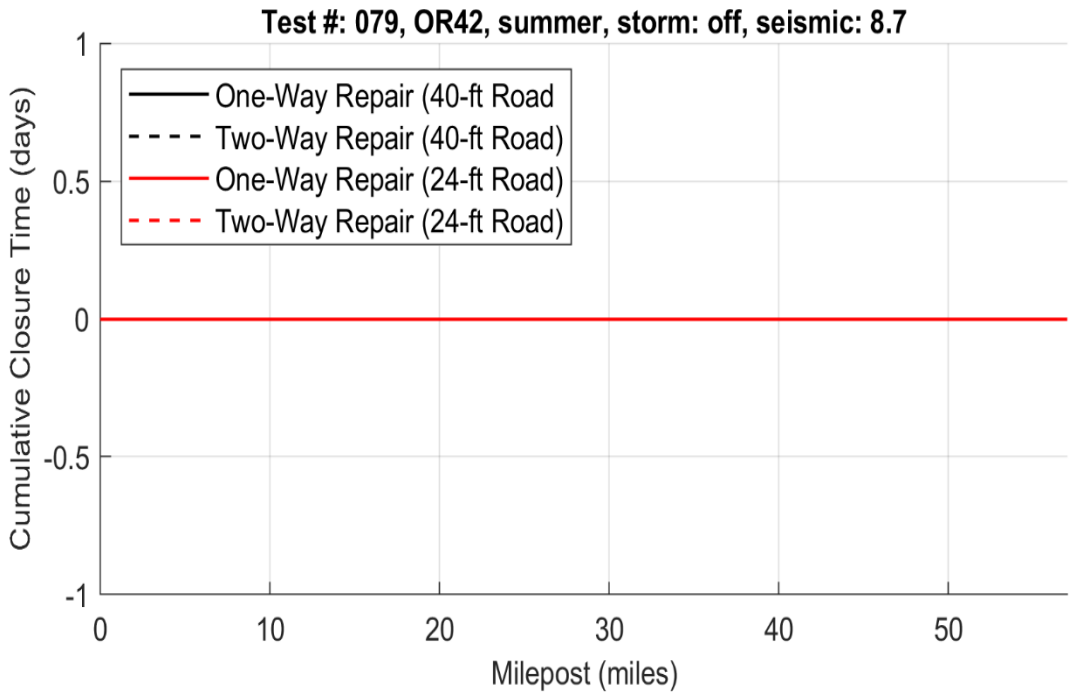

Figure 4.119: Profile of cumulative closure time for OR42: summer antecedent conditions, M8.7 earthquake (test #: 079).

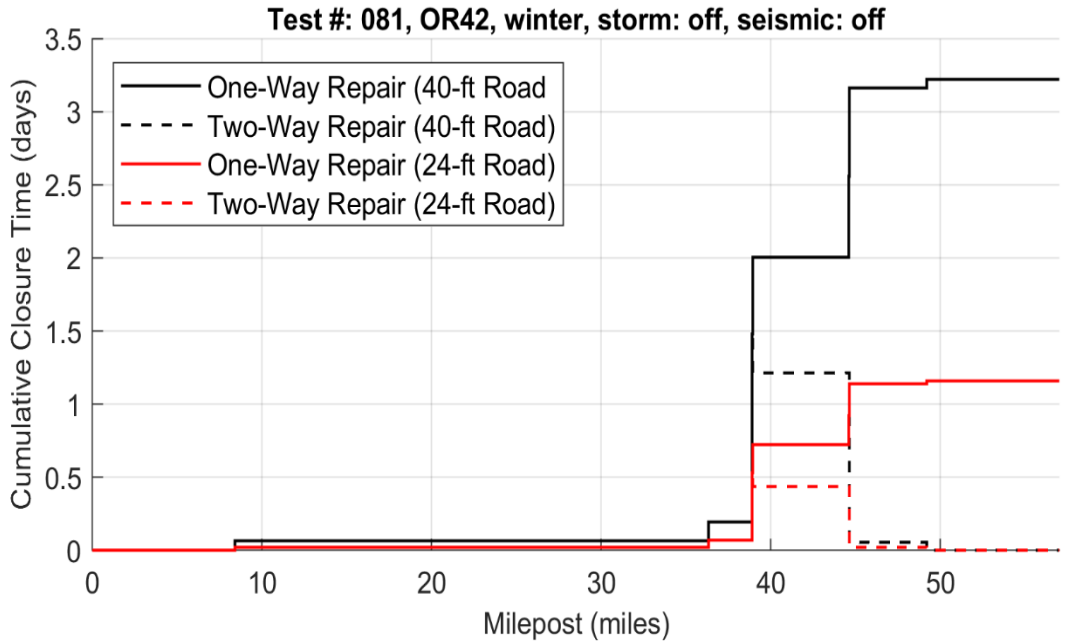

Figure 4.120: Profile of cumulative closure time for OR42: winter antecedent conditions (test #: 081).

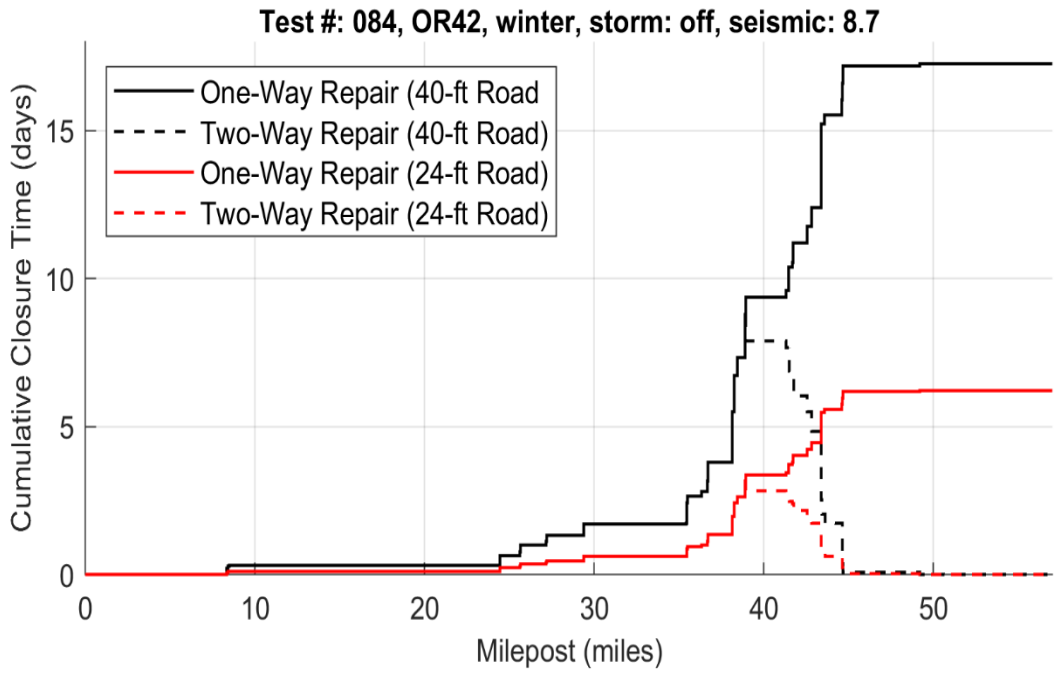

Figure 4.121: Profile of cumulative closure time for OR42: winter antecedent conditions, M8.7 earthquake (test #: 084).

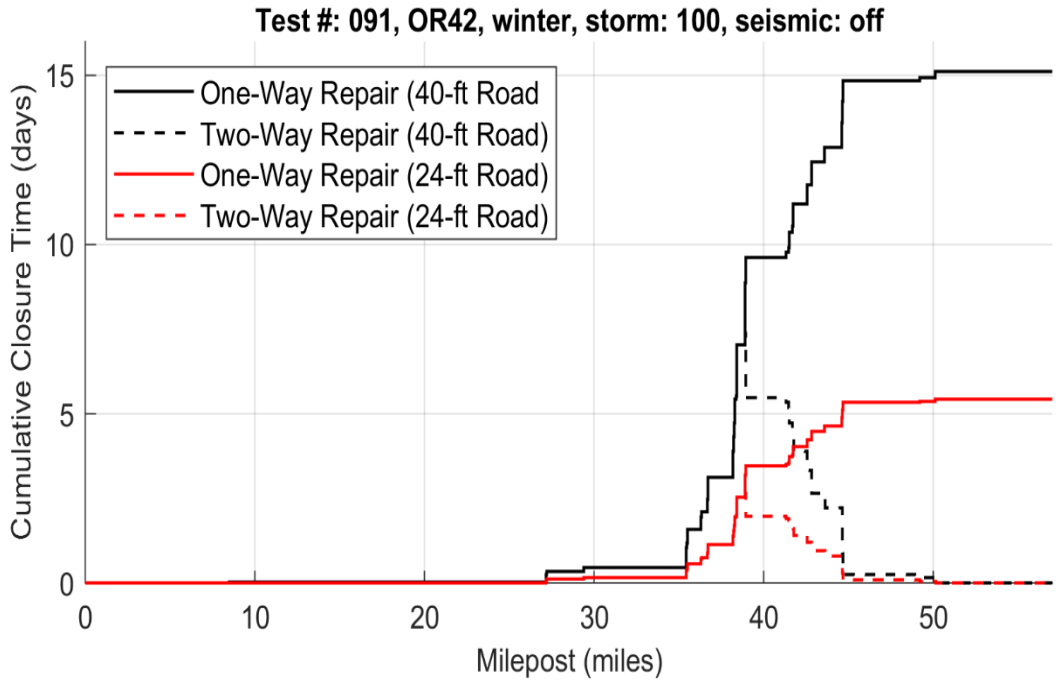

Figure 4.122: Profile of cumulative closure time for OR42: winter, 100-year rainfall event (test #: 091).

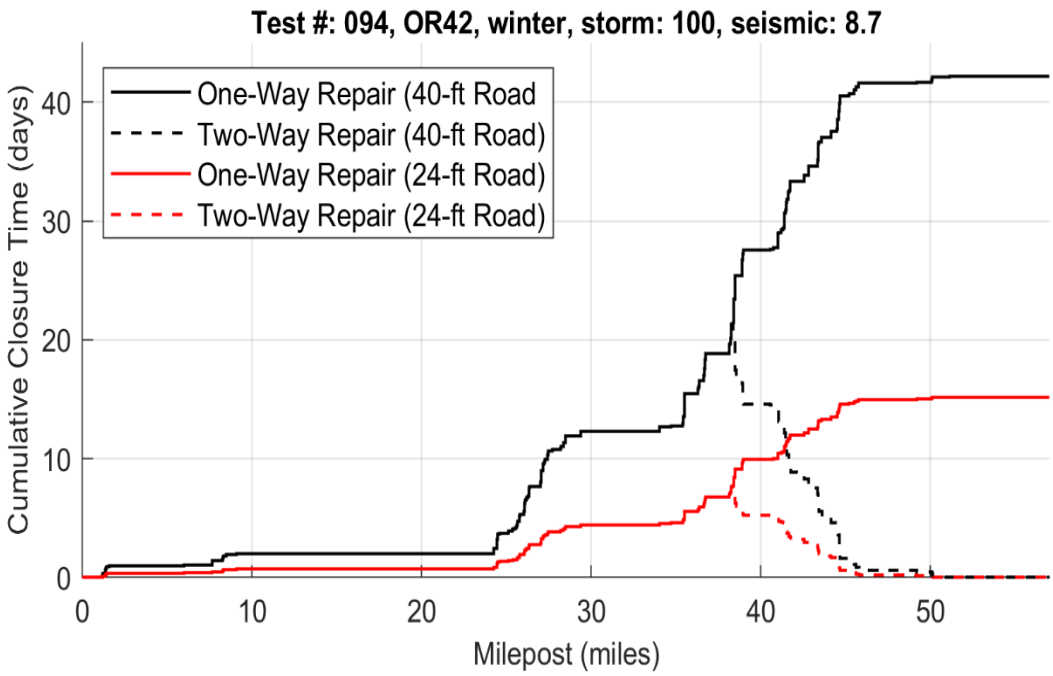

Figure 4.123: Profile of cumulative closure time for OR42: winter, 100-year rainfall event, M8.7 earthquake (test #: 094).

4.6.3.2 ***Milepost vs. Cumulative Repair Cost***

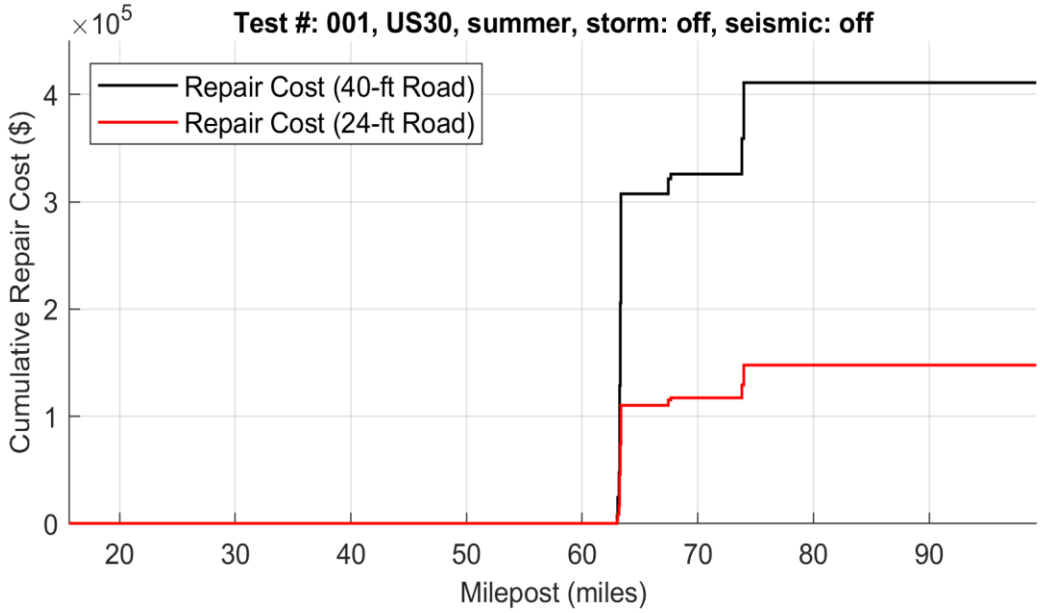

Figure 4.124: Profile of cumulative repair cost for US30: summer antecedent conditions (test #: 001).

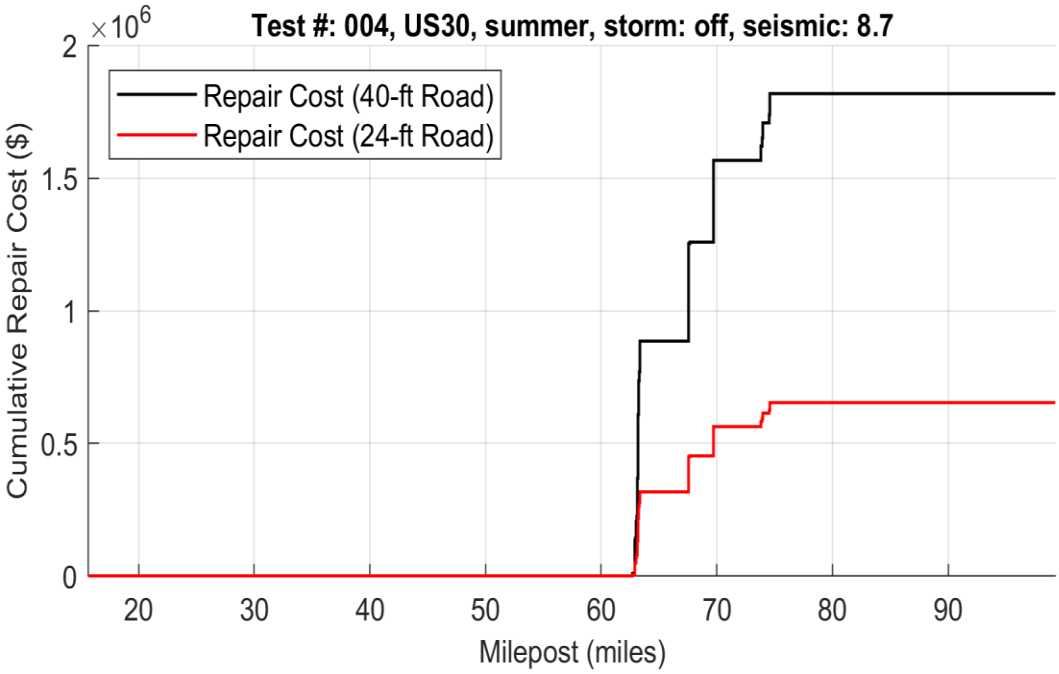

Figure 4.125: Profile of cumulative repair cost for US30: summer antecedent conditions, M8.7 earthquake (test #: 004).

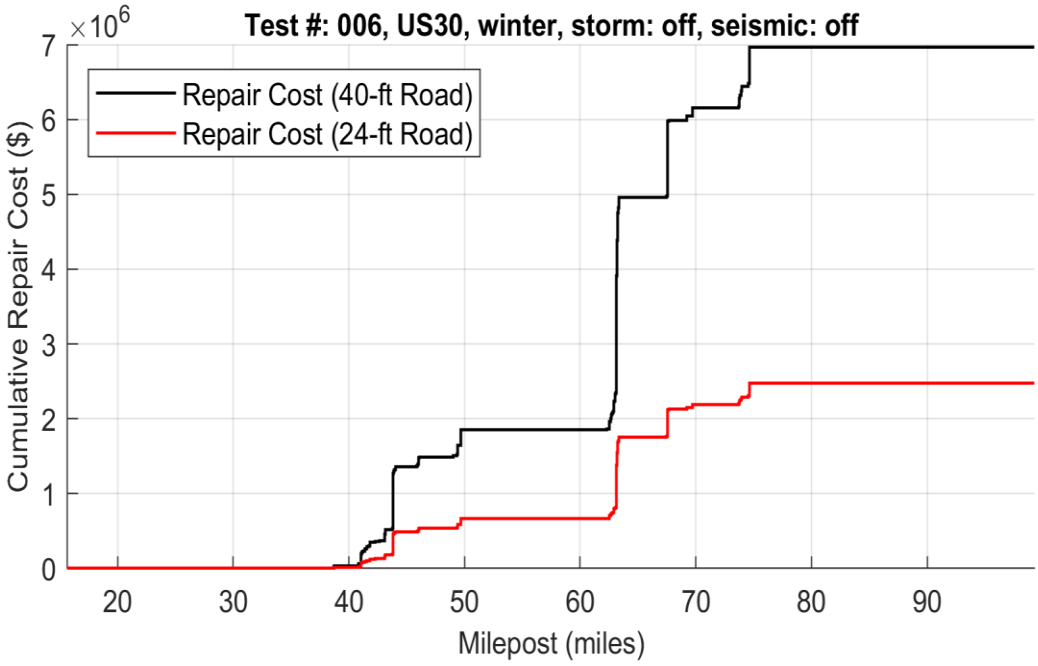

Figure 4.126: Profile of cumulative repair cost for US30: winter antecedent conditions (test #: 006).

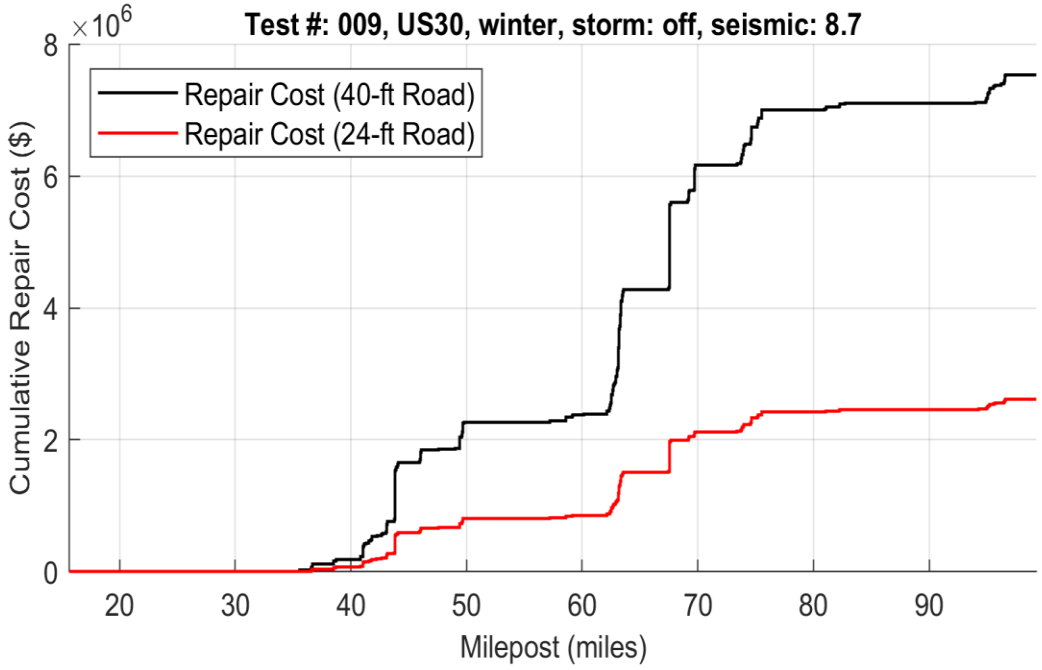

Figure 4.127: Profile of cumulative repair cost for US30: winter antecedent conditions, M8.7 earthquake (test #: 009).

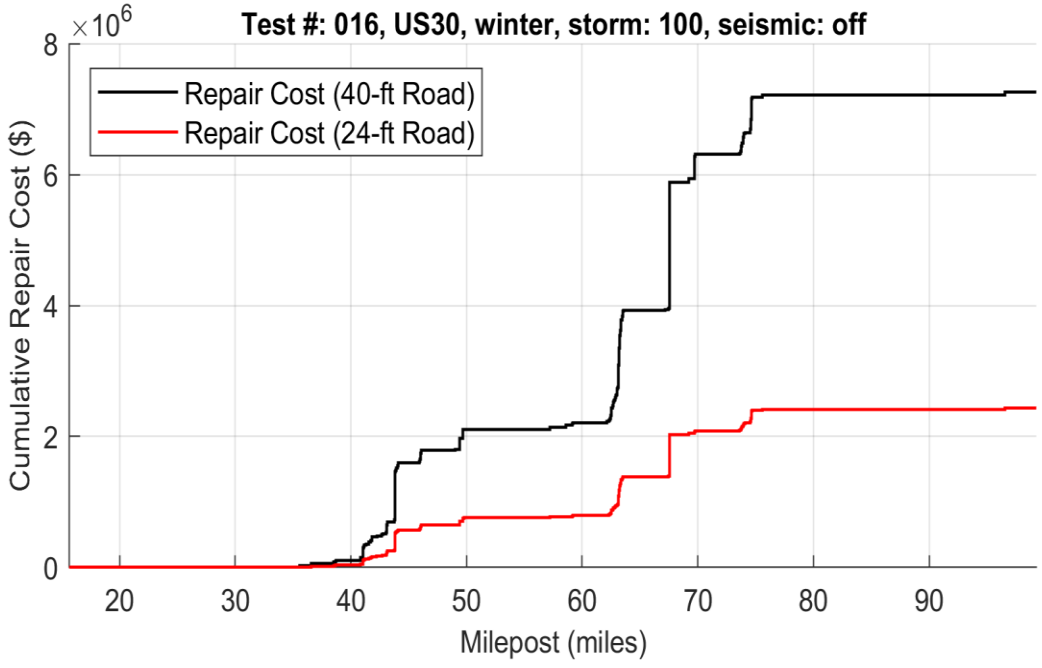

Figure 4.128: Profile of cumulative repair cost for US30: winter, 100-year rainfall event (test #: 016).

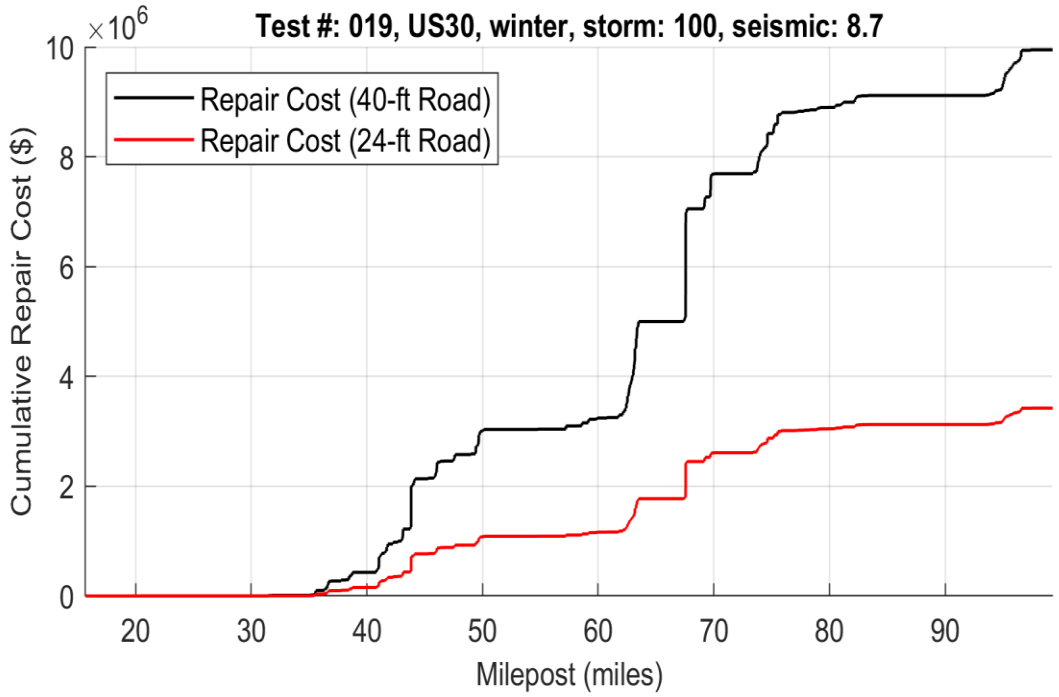

Figure 4.129: Profile of cumulative repair cost for US30: winter, 100-year rainfall event, M8.7 earthquake (test #: 019).

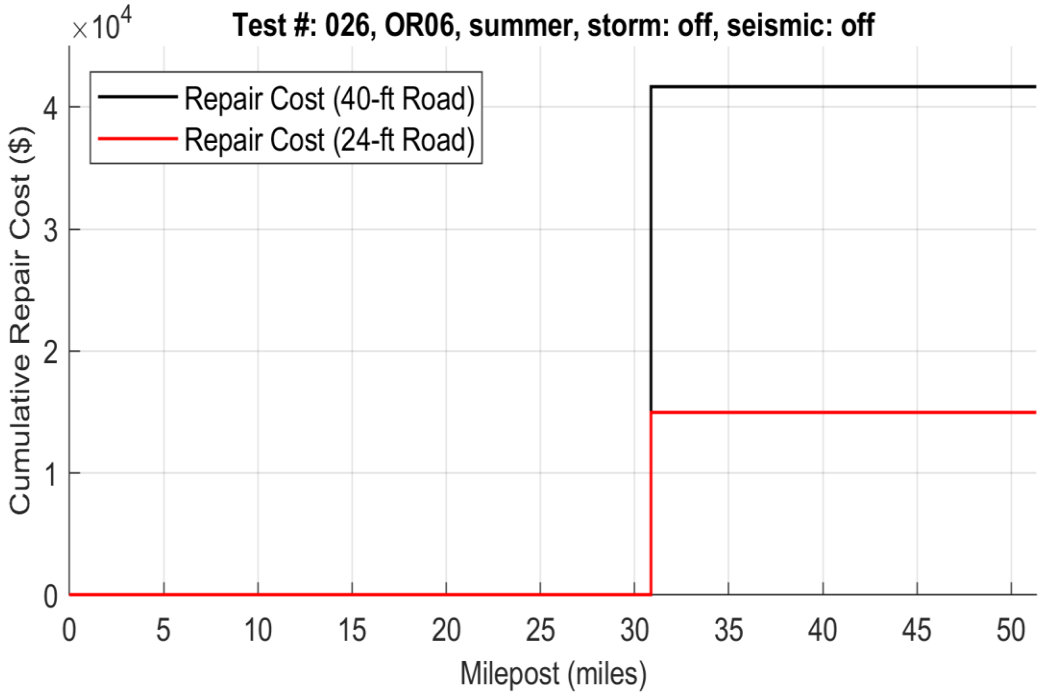

Figure 4.130: Profile of cumulative repair cost for OR06: summer antecedent conditions (test #: 026).

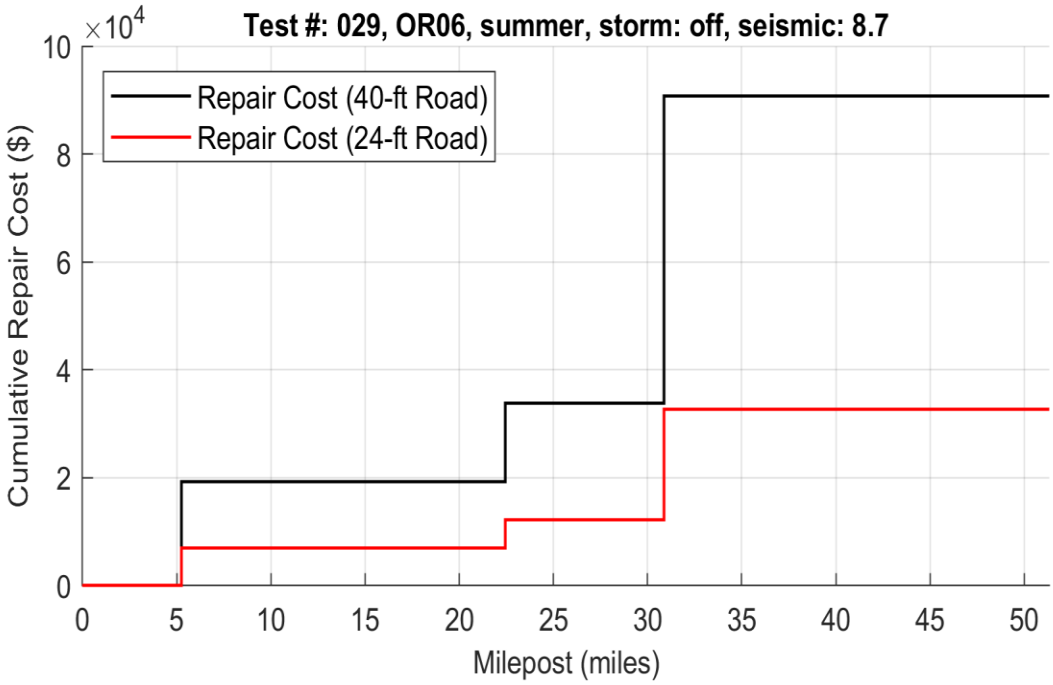

Figure 4.131: Profile of cumulative repair cost for OR06: summer antecedent conditions, M8.7 earthquake (test #: 029).

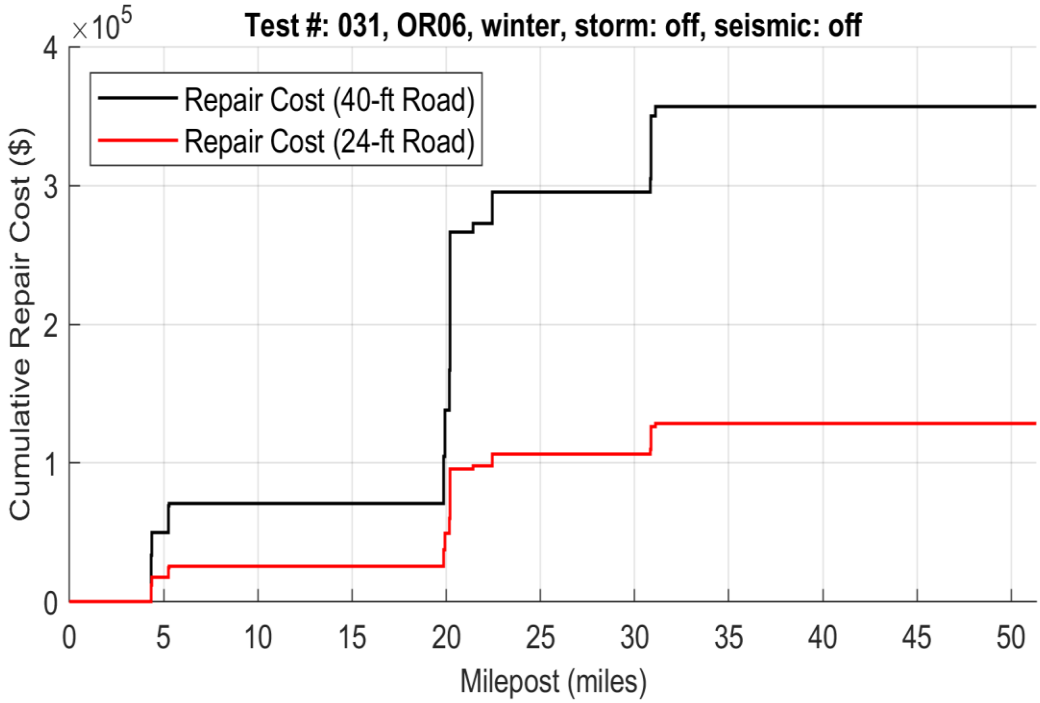

Figure 4.132: Profile of cumulative repair cost for OR06: winter antecedent conditions (test #: 031).

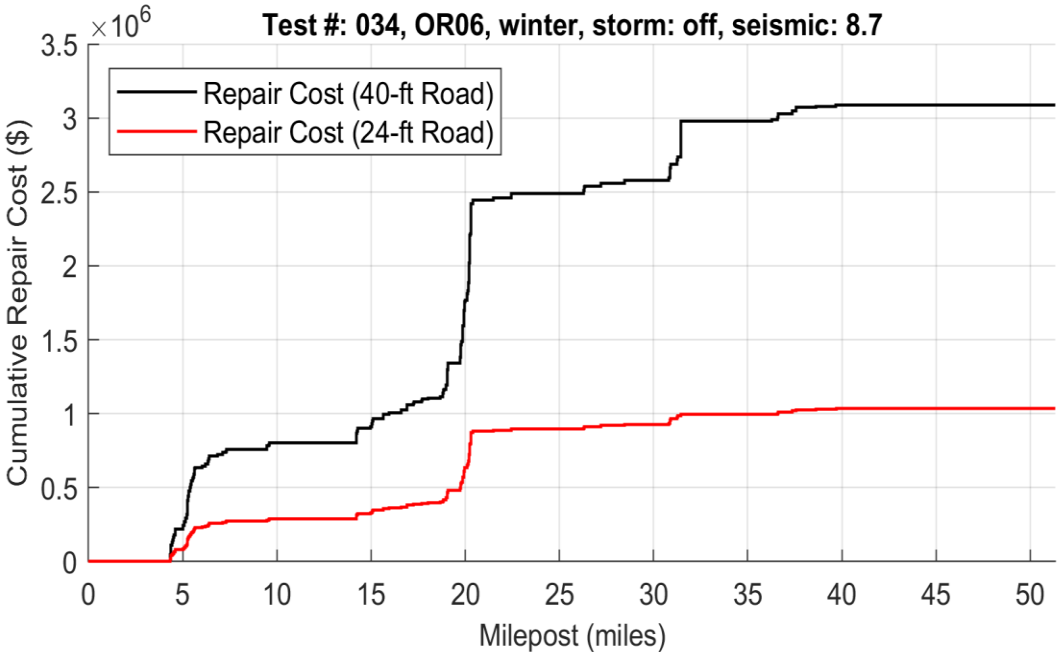

Figure 4.133: Profile of cumulative repair cost for OR06: winter antecedent conditions, M8.7 earthquake (test #: 034).

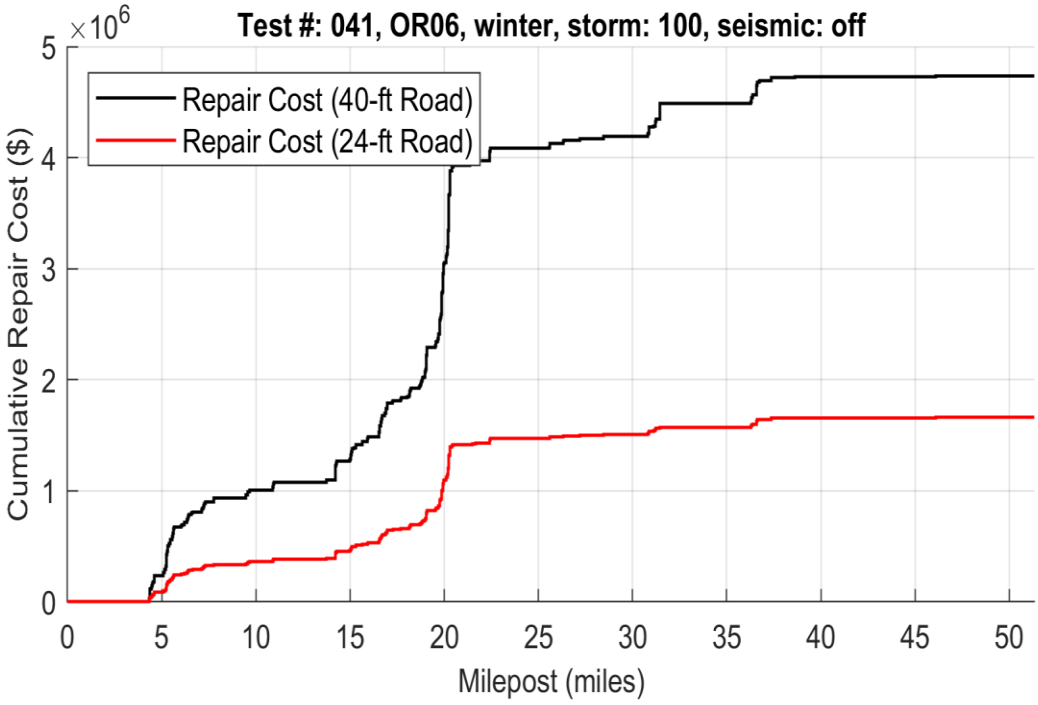

Figure 4.134: Profile of cumulative repair cost for OR06: winter, 100-year rainfall event (test #: 041).

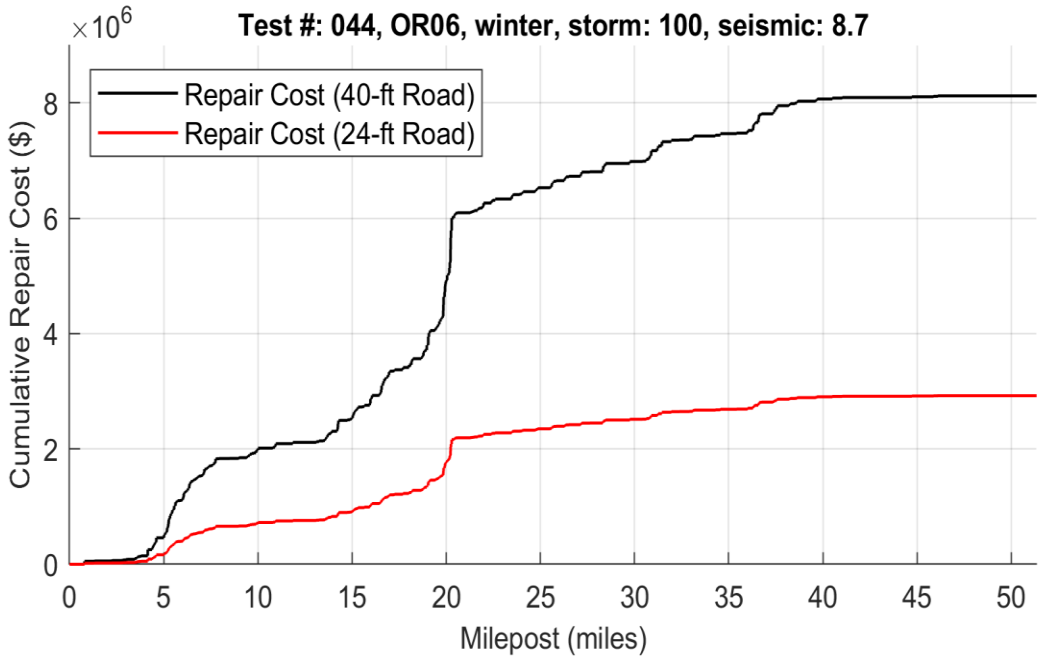

Figure 4.135: Profile of cumulative repair cost for OR06: winter, 100-year rainfall event, M8.7 earthquake (test #: 044).

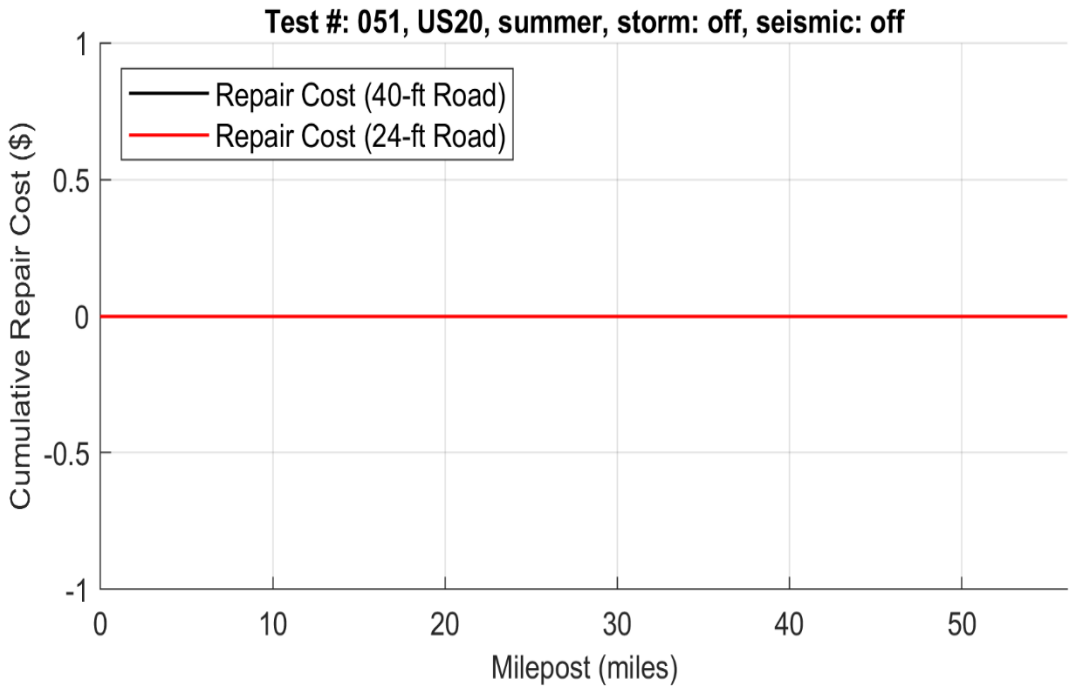

Figure 4.136: Profile of cumulative repair cost for US20: summer antecedent conditions (test #: 051).

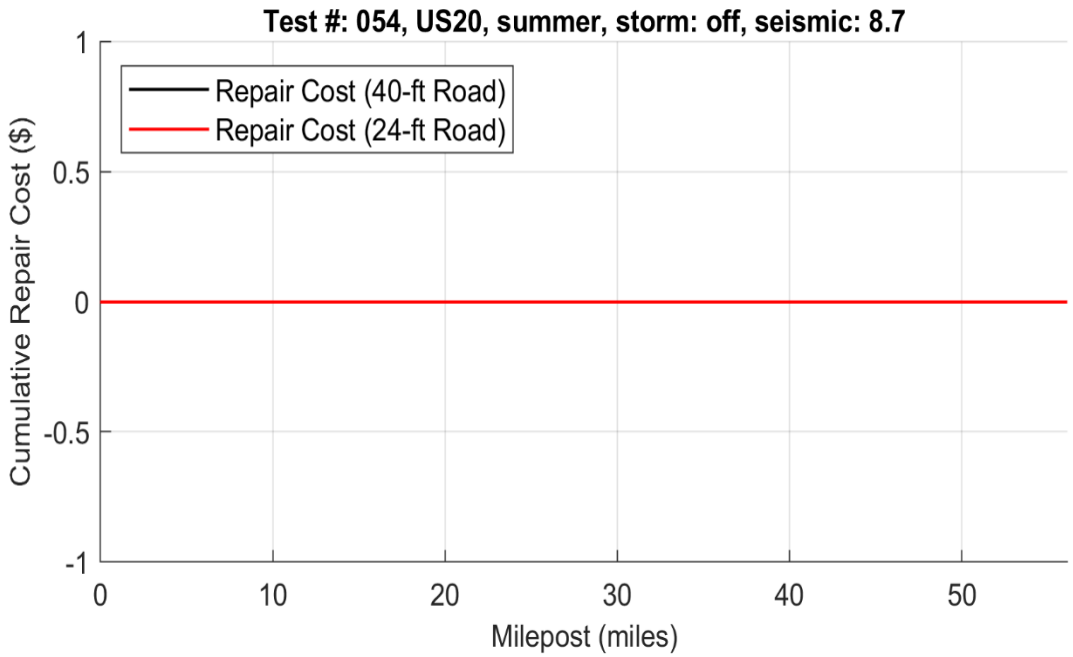

Figure 4.137: Profile of cumulative repair cost for US20: summer antecedent conditions, M8.7 earthquake (test #: 054).

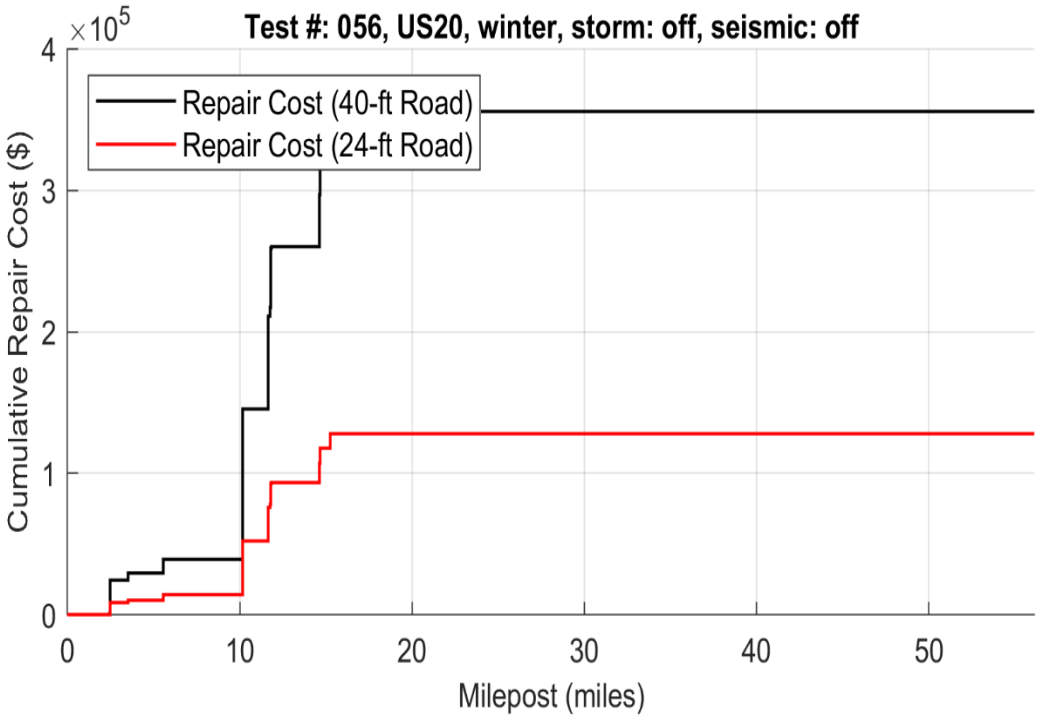

Figure 4.138: Profile of cumulative repair cost for US20: winter antecedent conditions (test #: 056).

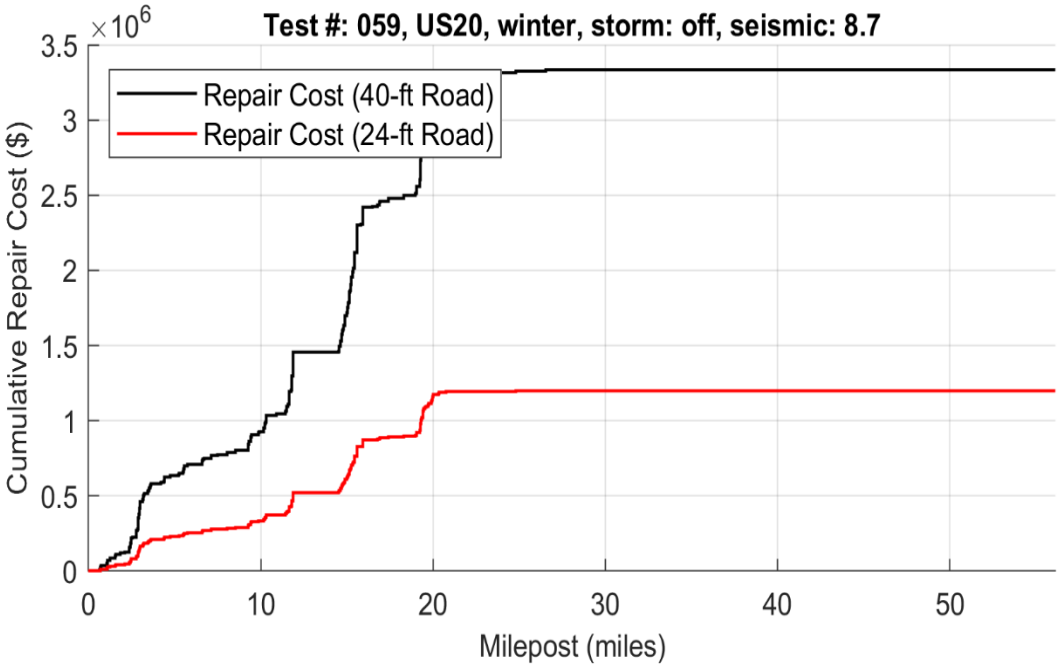

Figure 4.139: Profile of cumulative repair cost for US20: winter antecedent conditions, M8.7 earthquake (test #: 059).

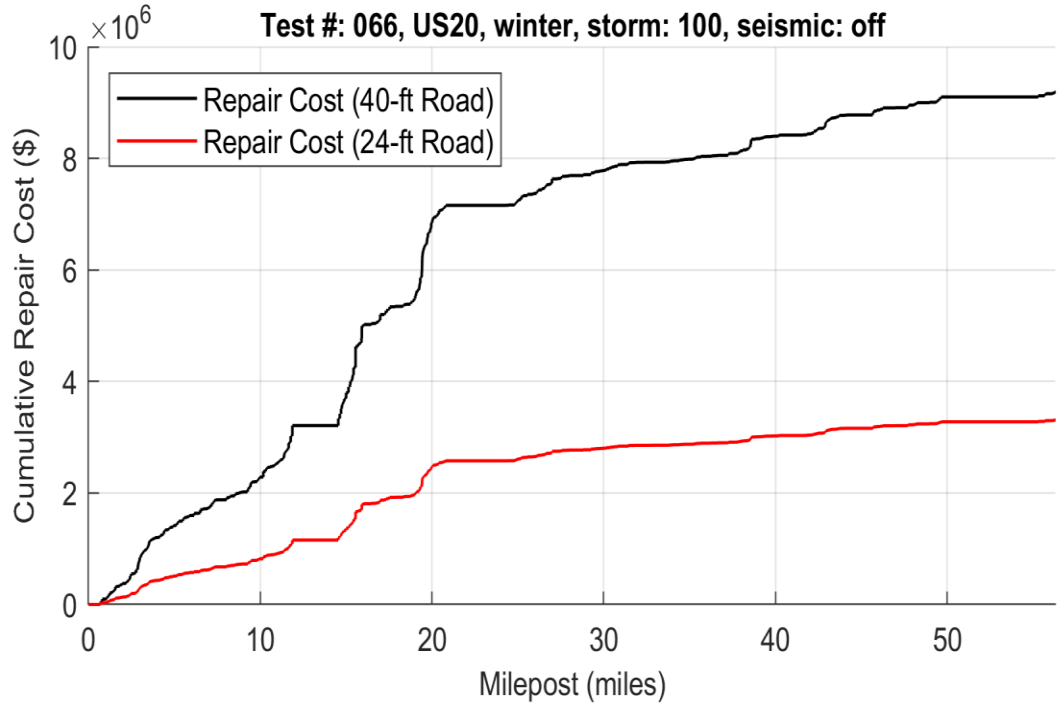

Figure 4.140: Profile of cumulative repair cost for US20: winter, 100-year rainfall event (test #: 066).

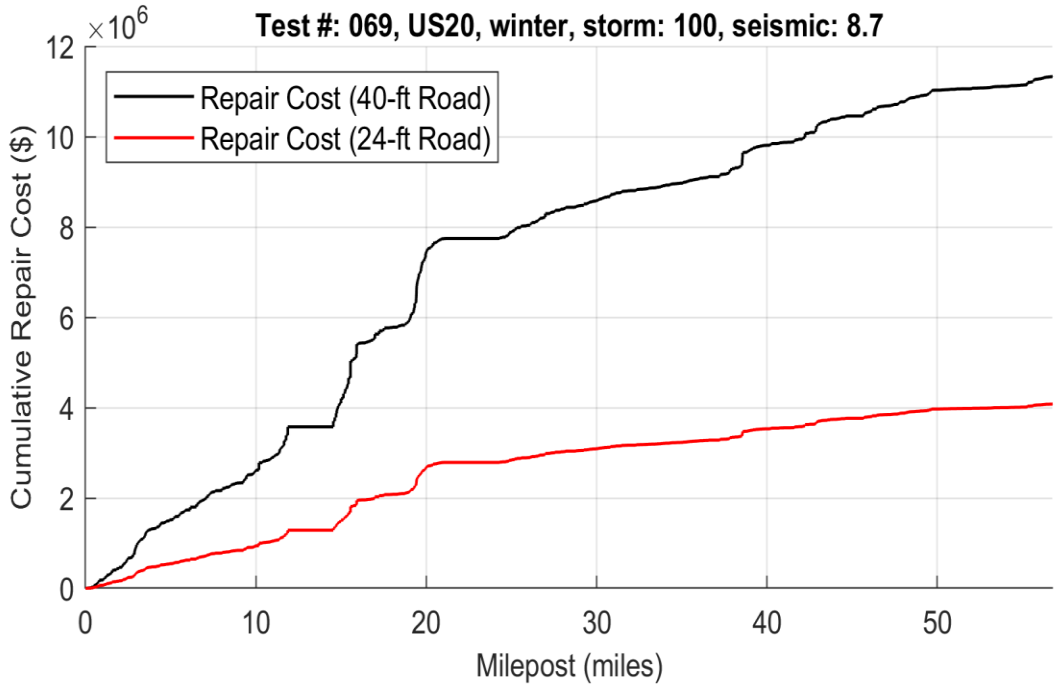

Figure 4.141: Profile of cumulative repair cost for US20: winter, 100-year rainfall event, M8.7 earthquake (test #: 069).

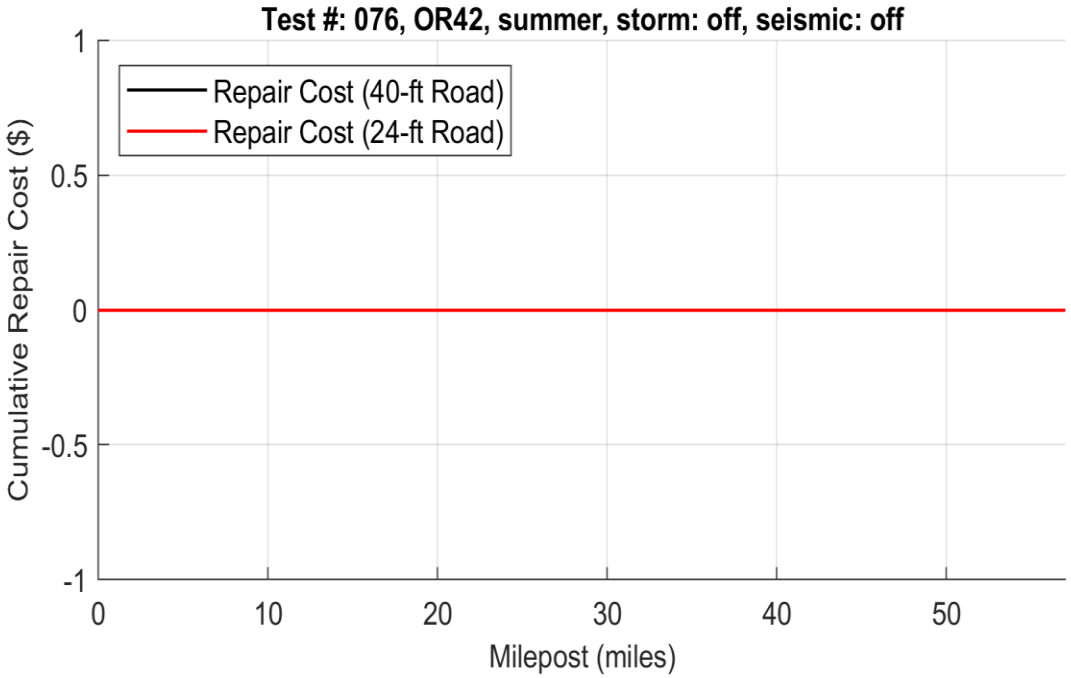

Figure 4.142: Profile of cumulative repair cost for OR42: summer antecedent conditions (test #: 076).

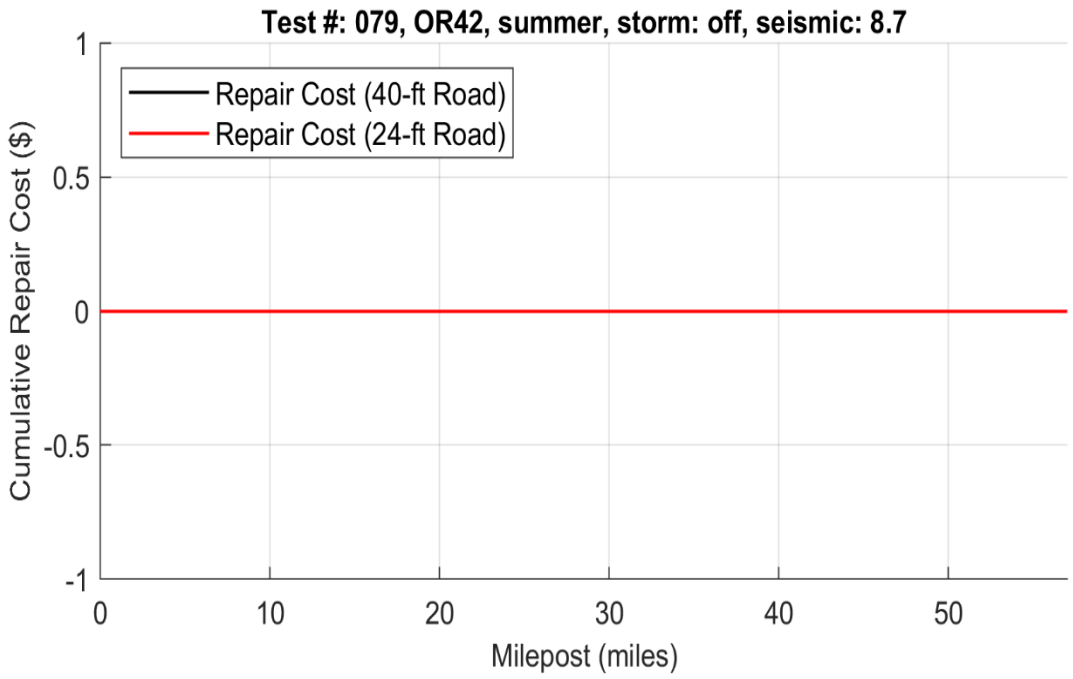

Figure 4.143: Profile of cumulative repair cost for OR42: summer antecedent conditions, M8.7 earthquake (test #: 079).

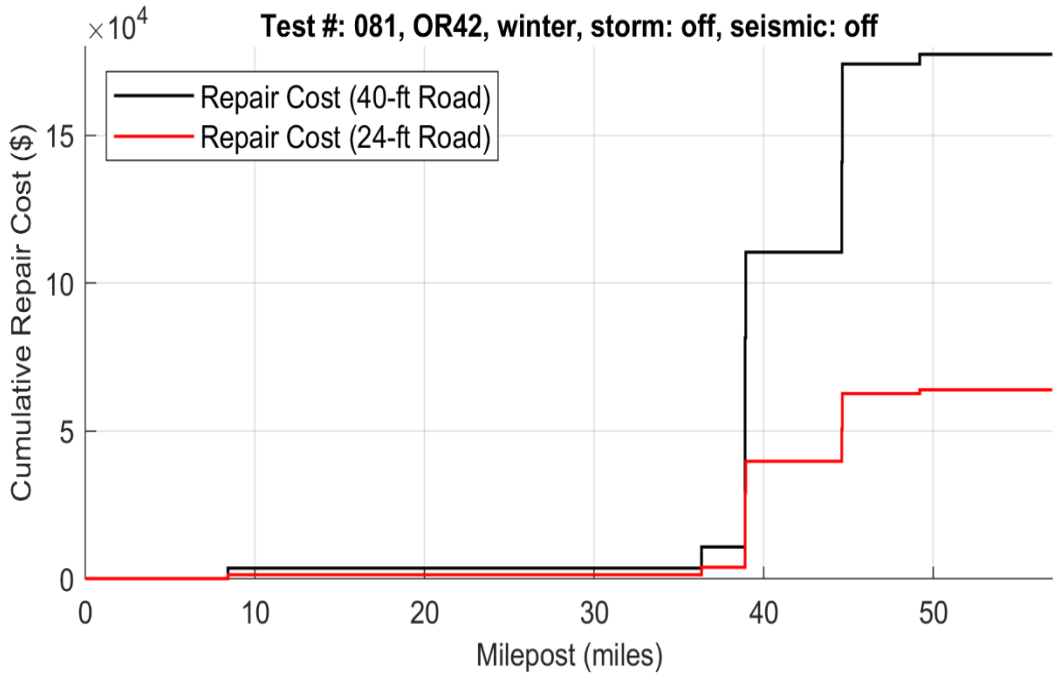

Figure 4.144: Profile of cumulative repair cost for OR42: winter antecedent conditions (test #: 081).

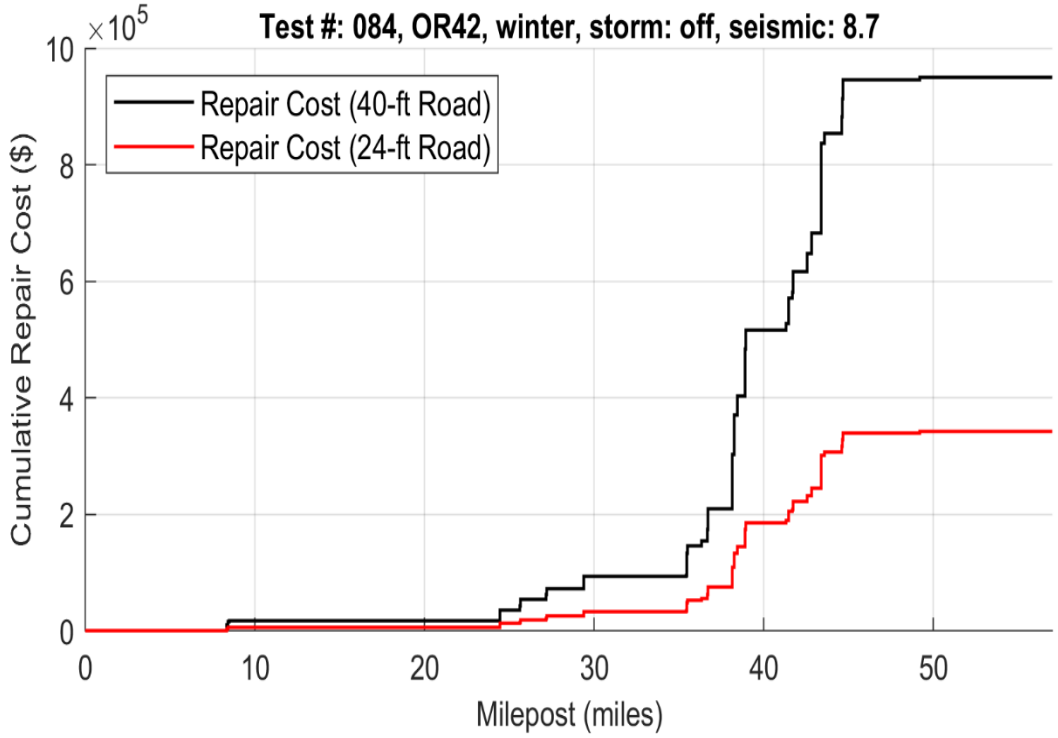

Figure 4.145: Profile of cumulative repair cost for OR42: winter antecedent conditions, M8.7 earthquake (test #: 084).

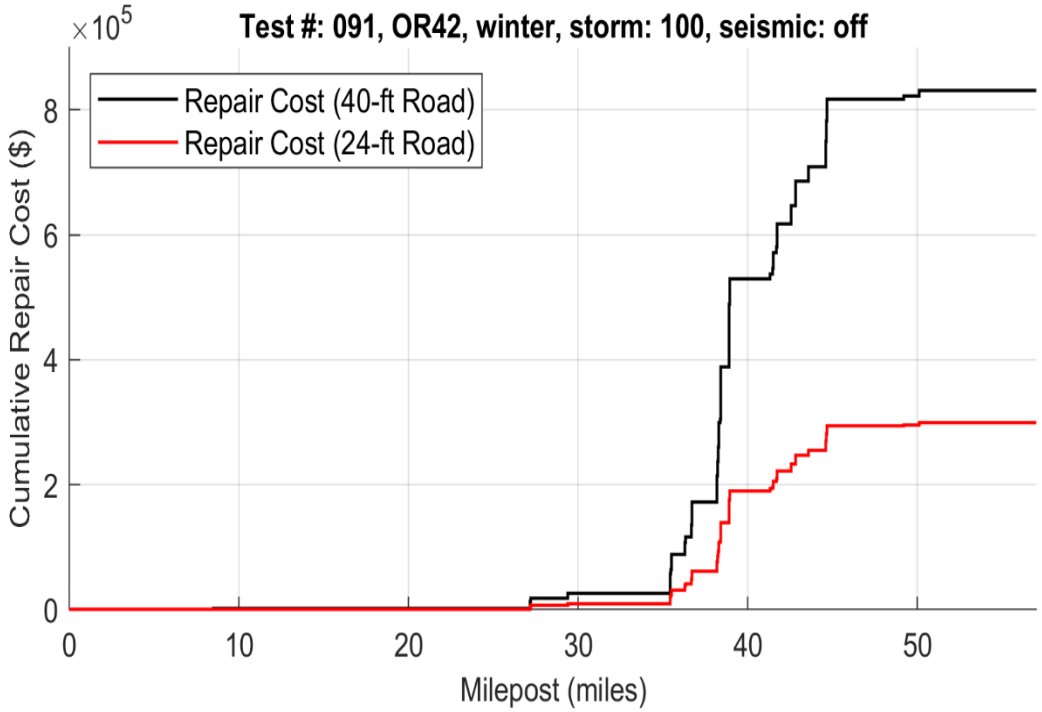

Figure 4.146: Profile of cumulative repair cost for OR42: winter, 100-year rainfall event (test #: 091).

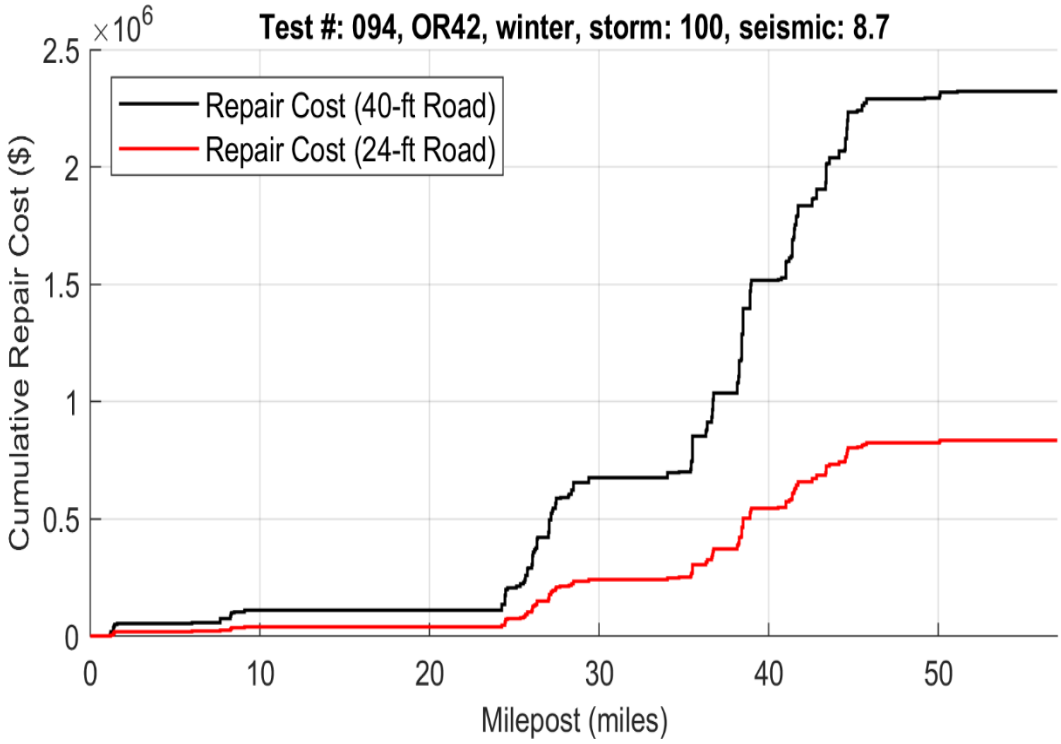

Figure 4.147: Profile of cumulative repair cost for OR42: winter, 100-year rainfall event, M8.7 earthquake (test #: 094).

4.7 EFFECTS OF CLIMATE CHANGE ON SUSCEPTIBILITY AND RISK

The effects of changing climate are evaluated for a select suite of tests by multiplying 24-hour rainfall rasters by a raster of future rainfall anomaly (Figure 4.148) and examining the effects of changes in rainfall on susceptibility and select risk metrics. A directory describing all scenarios with climate anomaly applied is shown in Table 4.7. The assumed anomaly for this study is representative of projected changes in precipitation for the period of 2040-2069, assuming the RCP 8.5 projection scenario (Riahi et al., 2011). For the examples in this section, extents of incipient failure and susceptibility outputs are compared for each corridor, assuming two different precipitation rasters: 10-year rainfall for current climatic conditions and 10-year rainfall scaled by the assumed anomaly raster, or future rainfall:

$$\boldsymbol{future\ rainfall = current\ rainfall * \left(1 + \frac{anomaly}{100}\right)} \quad \textbf{(4-2)}$$

Where:

$anomaly$ is the percent increase in mean precipitation.

Maps of rainfall anomaly, current 24-hour rainfall, and future 24-hour rainfall are shown in Figures 4.148a, 4.148b, and 4.148c, respectively. It should be noted that this method presents a rough estimate of future extreme rainfall events, as extreme events may not scale directly with changes in mean rainfall over a given period of time (Ragno et al., 2018). Similar to those presented in Section 4.4, all susceptibility analyses in this section assume antecedent winter conditions before rainfall is applied.

To compute incipient failure, susceptibility maps, computed using the methodology in Section 3.8, are subjected to a 50% susceptibility threshold. As described in Section 3.10.1, all cells above 50% susceptibility are assumed to be in a state of incipient failure. Note that for the comparisons of incipient failure herein, estimated runout is not calculated or included. Comparisons of the extent of incipient failure for each corridor, subject to 10-year rainfall for each climatic setting (current and future), are shown in Figures 4.149, 4.151, 4.153, and 4.155. Note that the orange cells show additional failed cells due to increased rainfall, and that all current climate cells (blue) should be included in those areas of future-climate failures. These figures show that, for all corridors, increased levels of rainfall increase the size of many existing clusters of failed cells, while also producing new clusters of failed cells in previously stable areas. While this behavior is seen throughout the corridors, inset images in Figures 4.149, 4.151, 4.153, and 4.155 show regions where this is exemplified. Further, inset images in Figures 4.149 and 4.151 show sections of ROW directly affected by climate-change induced landslide activity, previously unaffected in current climatic conditions. This behavior shows that higher values of extreme rainfall, due to climate change, may exacerbate existing landslide risk, and in some cases create new zones of potential risk.

Figures 4.150, 4.152, 4.154, and 4.156 show the difference in susceptibility maps for current and future rainfall. Note that these maps compare raw values of susceptibility, computed as described in Section 3.8, without a 50% filter applied. All corridors show that increased rainfall, due to climate change, results in higher distributions of susceptibility throughout the corridor. Inset images in Figures 4.150, 4.152, 4.154, and 4.156 all highlight regions in which increased susceptibility is observed near sections of ODOT ROW, further demonstrating that increased rainfall may result in an increase of landslide problems in these regions. The insets also show that hillslopes may experience different changes in susceptibility, even within a relatively small region of the corridor, when increased values of rainfall are applied. This is likely due to the spatial variability of soil types, rainfall magnitude, and rainfall anomaly, as well as variations in local topography.

Informed by the maps shown in Figures 4.149, 4.151, 4.153, and 4.155, Table 4.8 summarizes the total planform areas exhibiting incipient failure and percent increases in these areas. Percent increases in incipient failure area support observations from Figures 4.149, 4.151, 4.153, and 4.155, while also quantifying the effects of additional rainfall. From an incipient failure perspective, OR06 is shown to be most affected by rainfall anomaly with a 13.63% increase in area of failed cells, and US20 is shown to be the least affected by rainfall anomaly with a 1.87% increase in area of failed cells. The low increase for US20 is likely because incipient failure was already widespread prior to applying increased values of rainfall (Figure 4.153). Table 4.8 also shows increases in total repair costs corresponding with future climate, stemming from increased closure times. Note that inflation is not included in the reported values of future climate repair

cost and that all costs correspond with closure from incipient failure with estimated runouts (see Section 3.10.2); 60-foot (18.3 m) landslide buffers are not applied for cost comparisons.

A full suite of susceptibility maps, hazard maps, risk maps, and risk metrics corresponding to future climate scenarios (tests 101-112; Table 4.7) may be found in Appendices A-H. Rasters of landslide shapes and shapefiles containing highway closure for these tests may be found in the digital appendix.

Table 4.7: Directory of Tests with Rainfall Anomaly Applied.

Season	Seismic	Rainfall Anomaly	Corridor	Storm Recurrence Interval	Test #
winter	off	RCP 8.5 (2040-2069)	US30	10-year	101
				100-year	102
				1000-year	103
			OR06	10-year	104
				100-year	105
				1000-year	106
			US20	10-year	107
				100-year	108
				1000-year	109
			OR42	10-year	110
				100-year	111
				1000-year	112

Table 4.8: Effects of ClimateCchange on Incipient Failure and Repair Costs for each Corridor.

Test #	Rainfall	Climatic Scenario	Failed Cell Area (km^2)[1]	% Increase in Failed Cell Area	Total Repair Cost[2,3]
			US30		
11	10-year	current	15.848	10.46%	$6,142,627
101		RCP 8.5 (2040-2069)	17.505		$6,187,891
			OR06		
36	10-year	current	56.380	13.63%	$3,026,188
104		RCP 8.5 (2040-2069)	64.064		$3,234,754
			US20		
61	10-year	current	810.898	1.87%	$8,402,748
107		RCP 8.5 (2040-2069)	826.080		$8,485,809
			OR42		
86	10-year	current	6.260	9.25%	$581,940
110		RCP 8.5 (2040-2069)	6.839		$628,128

[1] Only incipient failure counted (landslide runout and buffer not included in count).
[2] Closure cost estimate includes estimated runout in analysis, but excludes landslide buffer.
[3] Closure cost analysis assumes 40-foot (12.2-m) wide roadway.

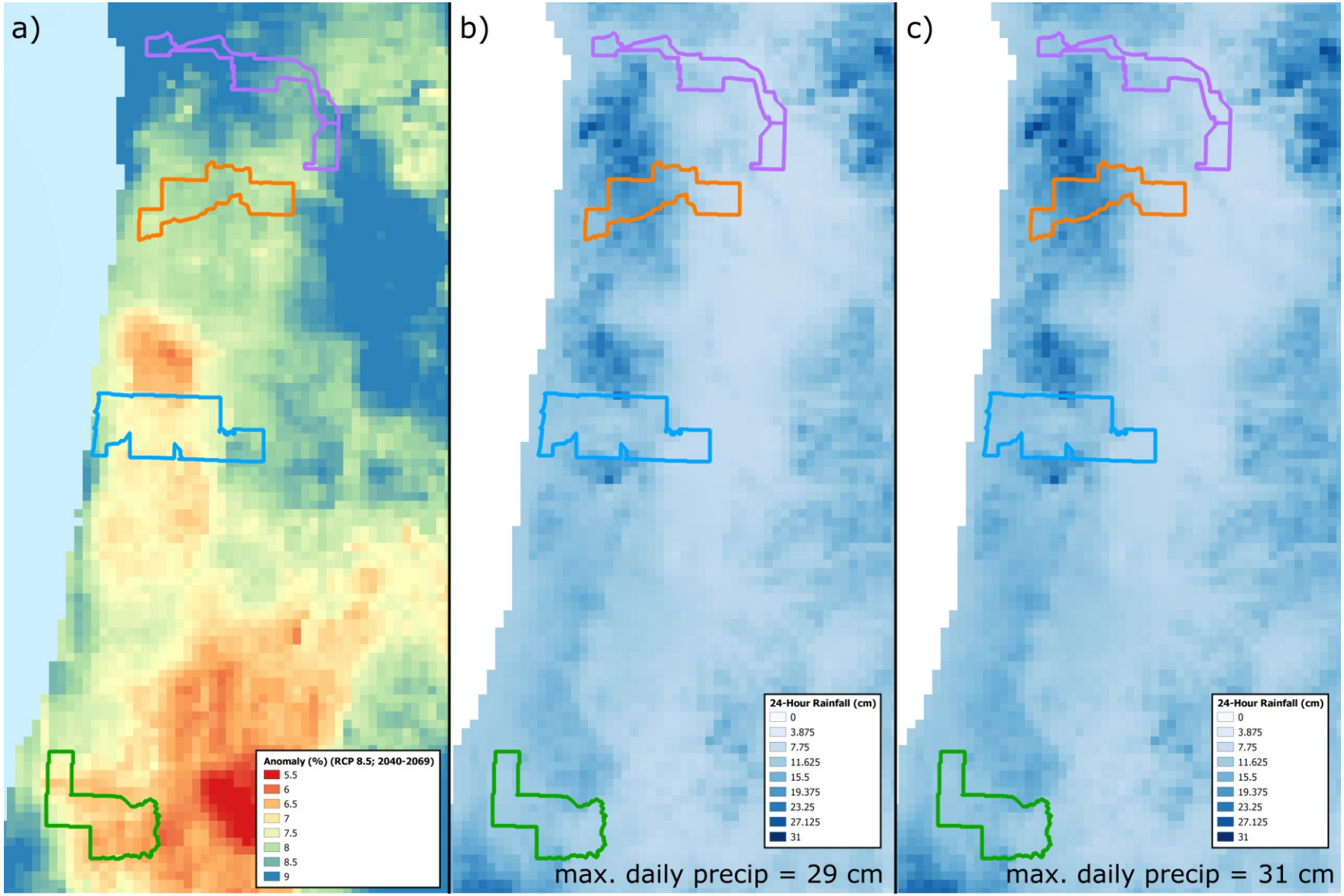

Figure 4.148: Maps showing affects precipitation anomaly: a) precipitation anomaly (RCP 8.5; 2040-2069); b) 10-year 24-hour precipitation without anomaly; c) 10-year, 24-hour precipitation scaled by precipitation anomaly.

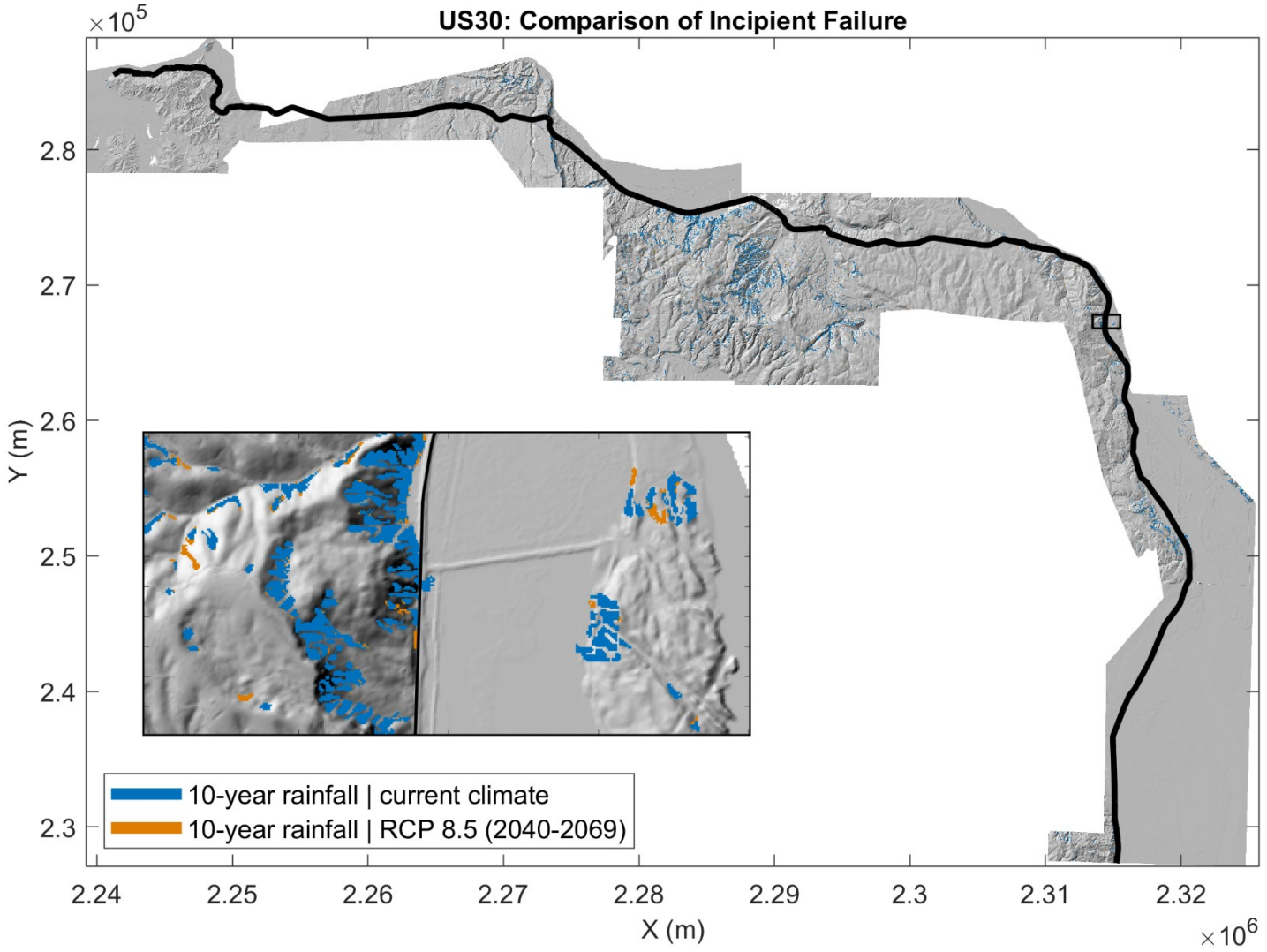

Figure 4.149: Comparison of cells exhibiting incipient failure, for corridor US30, during a 10-year rainfall event for the current climate and future climate (RCP 8.5; 2040-2069).

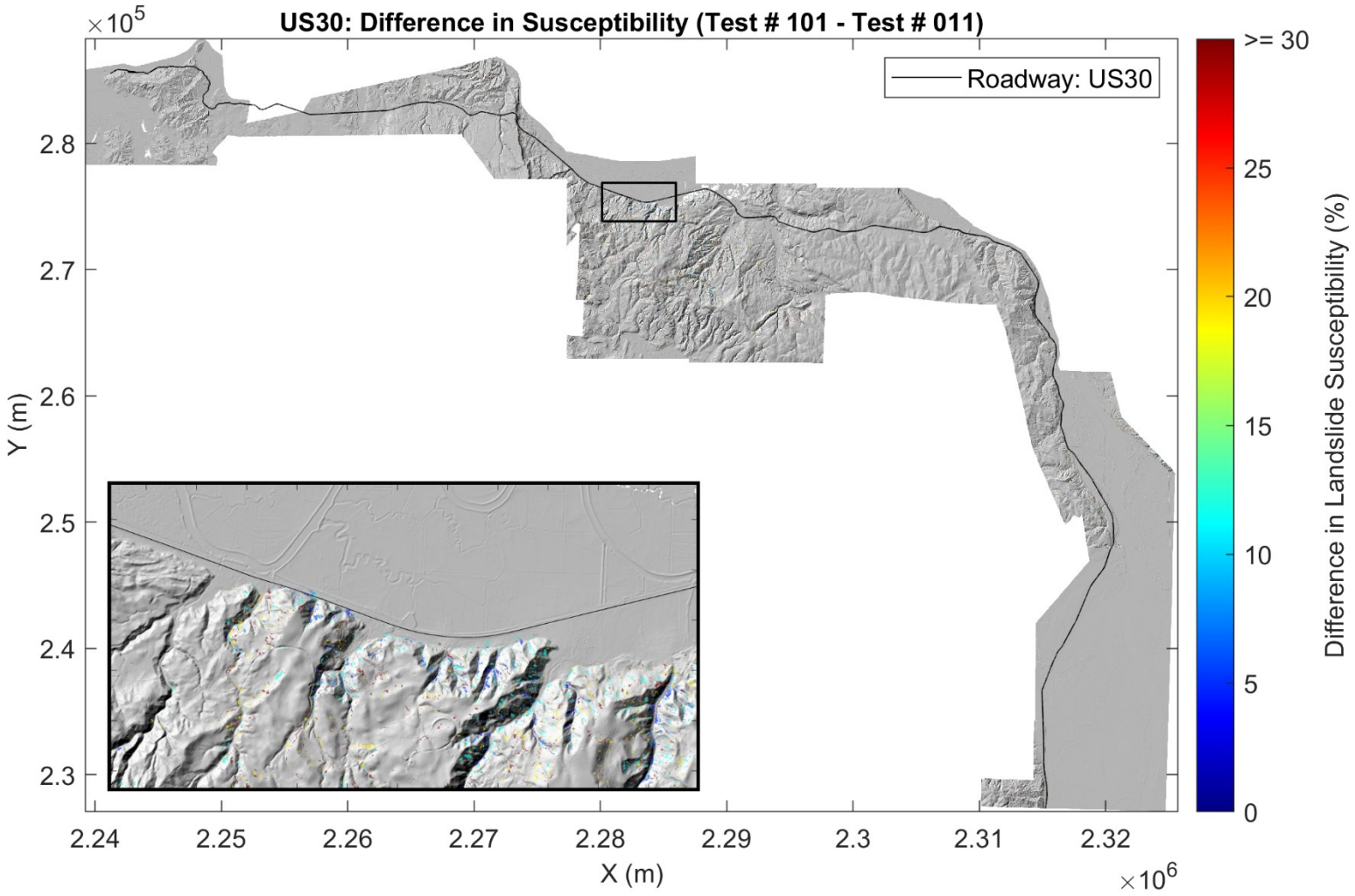

Figure 4.150: Increase in susceptibility for corridor US30 when a future climate 10-year rainfall event is applied (RCP 8.5; 2040-2069), in comparison to a current climate 10-year rainfall event.

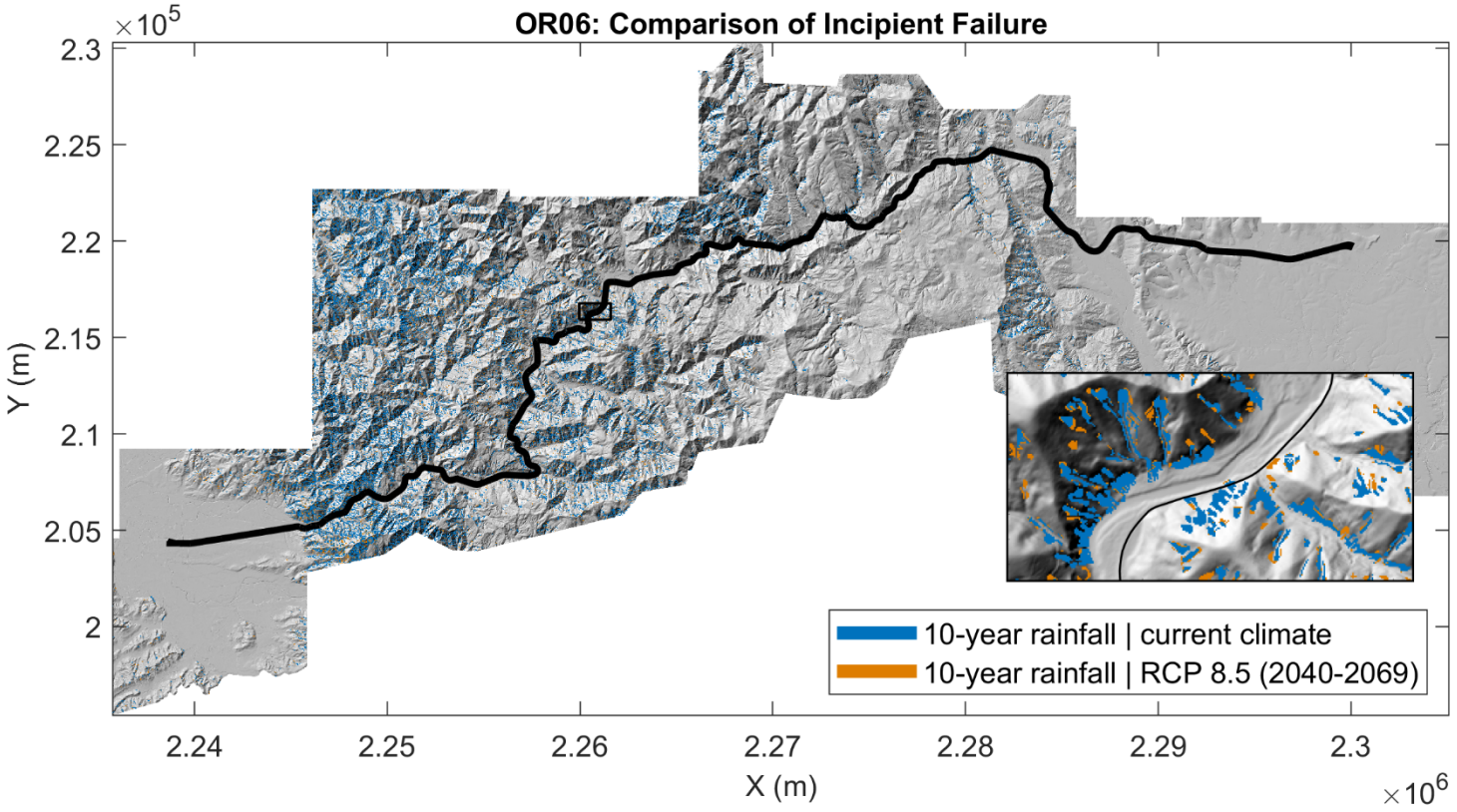

Figure 4.151: Comparison of cells exhibiting incipient failure, for corridor OR06, during a 10-year rainfall event for the current climate and future climate (RCP 8.5; 2040-2069).

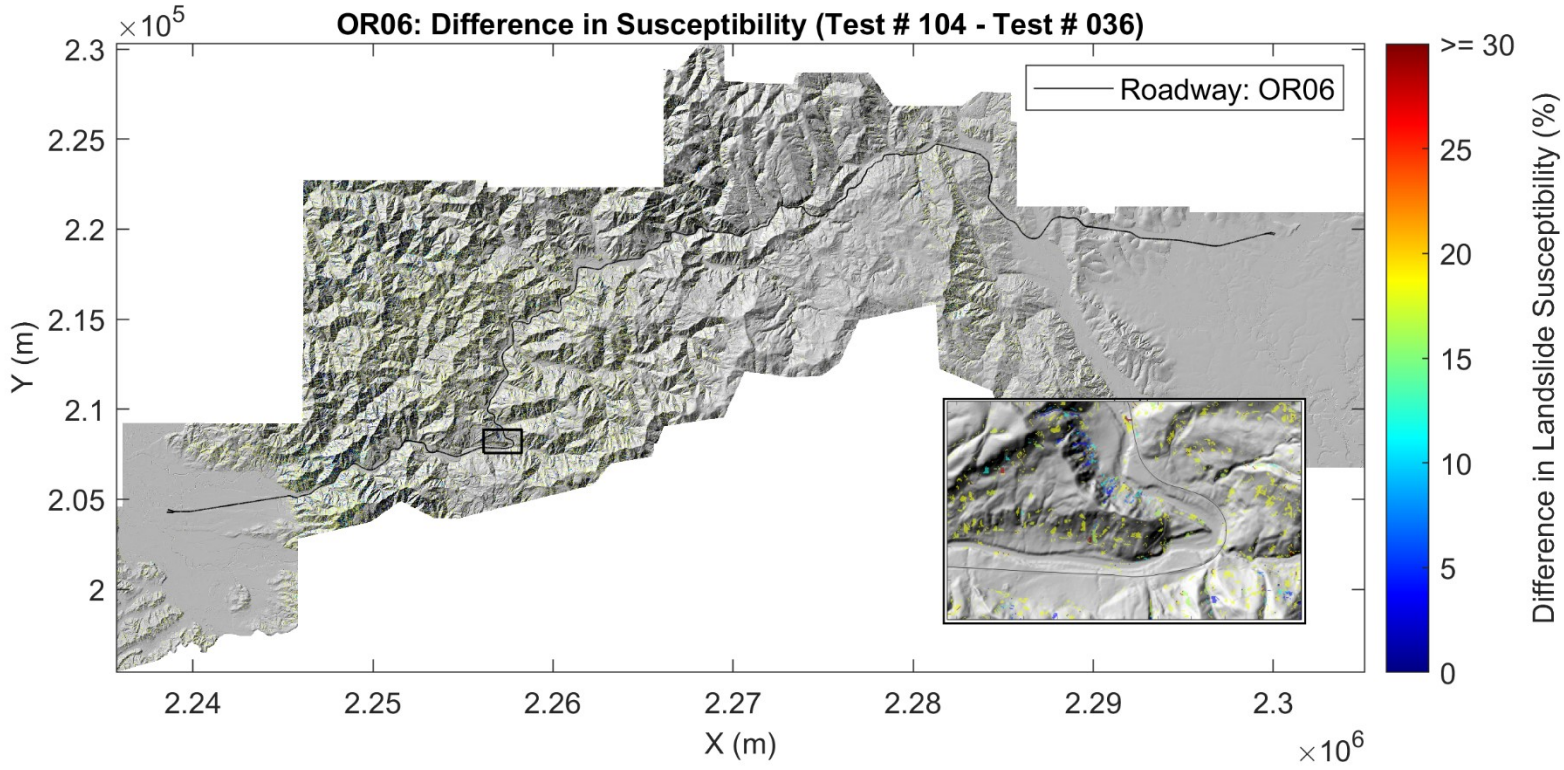

Figure 4.152: Increase in susceptibility for corridor OR06 when a future climate 10-year rainfall event is applied (RCP 8.5; 2040-2069), in comparison to a current climate 10-year rainfall event.

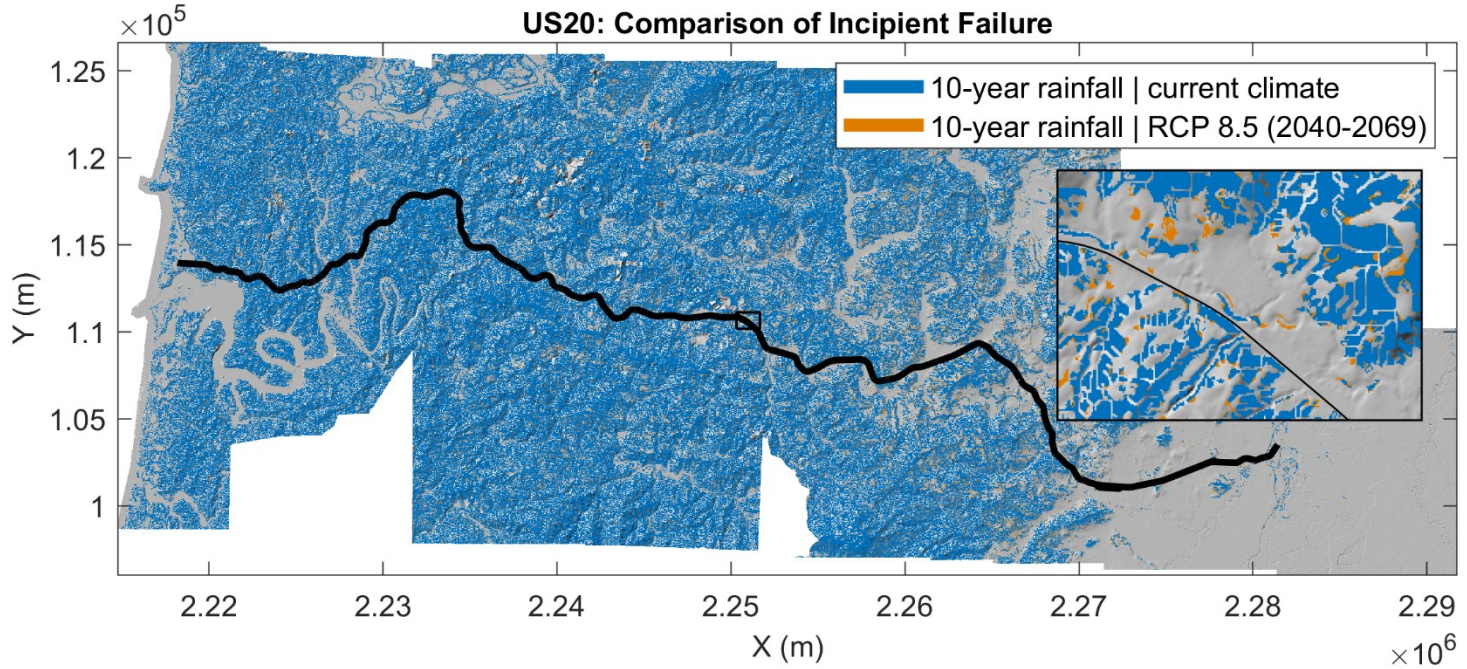

Figure 4.153: Comparison of cells exhibiting incipient failure, for corridor US20, during a 10-year rainfall event for the current climate and future climate (RCP 8.5; 2040-2069).

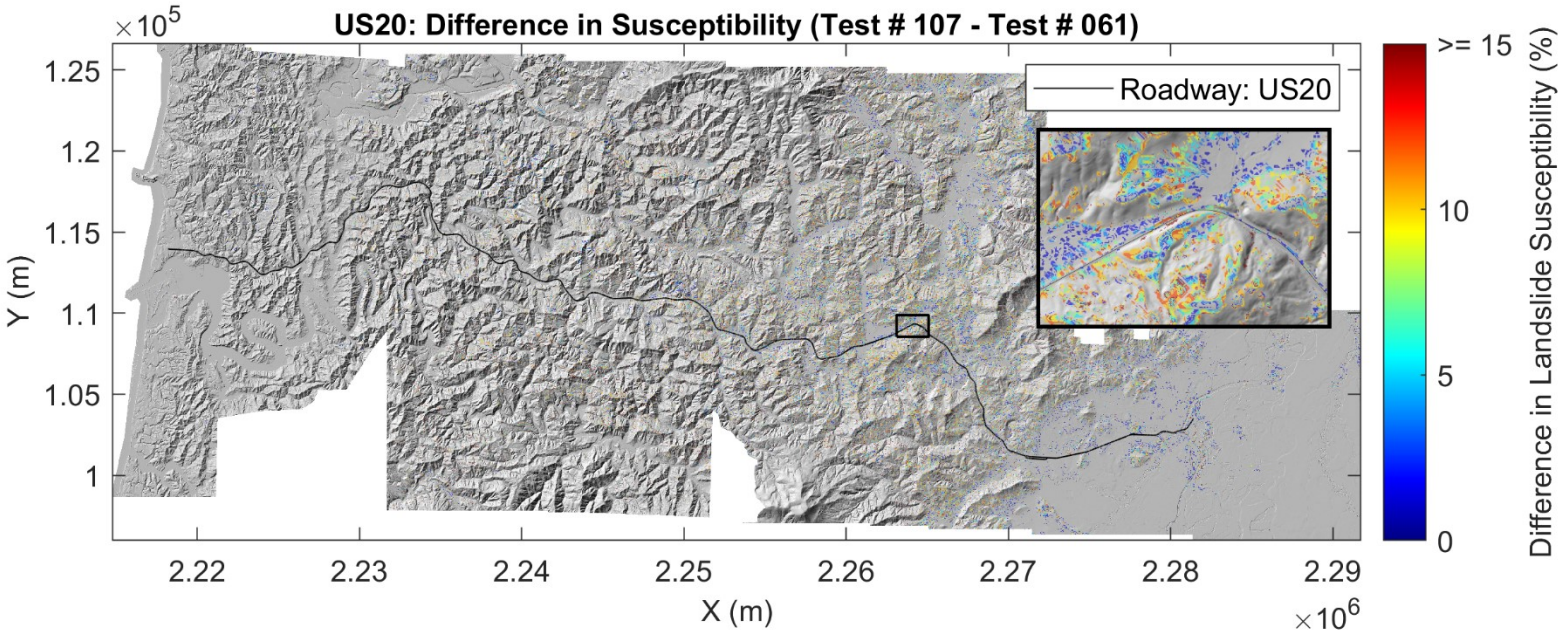

Figure 4.154: Increase in susceptibility for corridor US20 when a future climate 10-year rainfall event is applied (RCP 8.5; 2040-2069), in comparison to a current climate 10-year rainfall event.

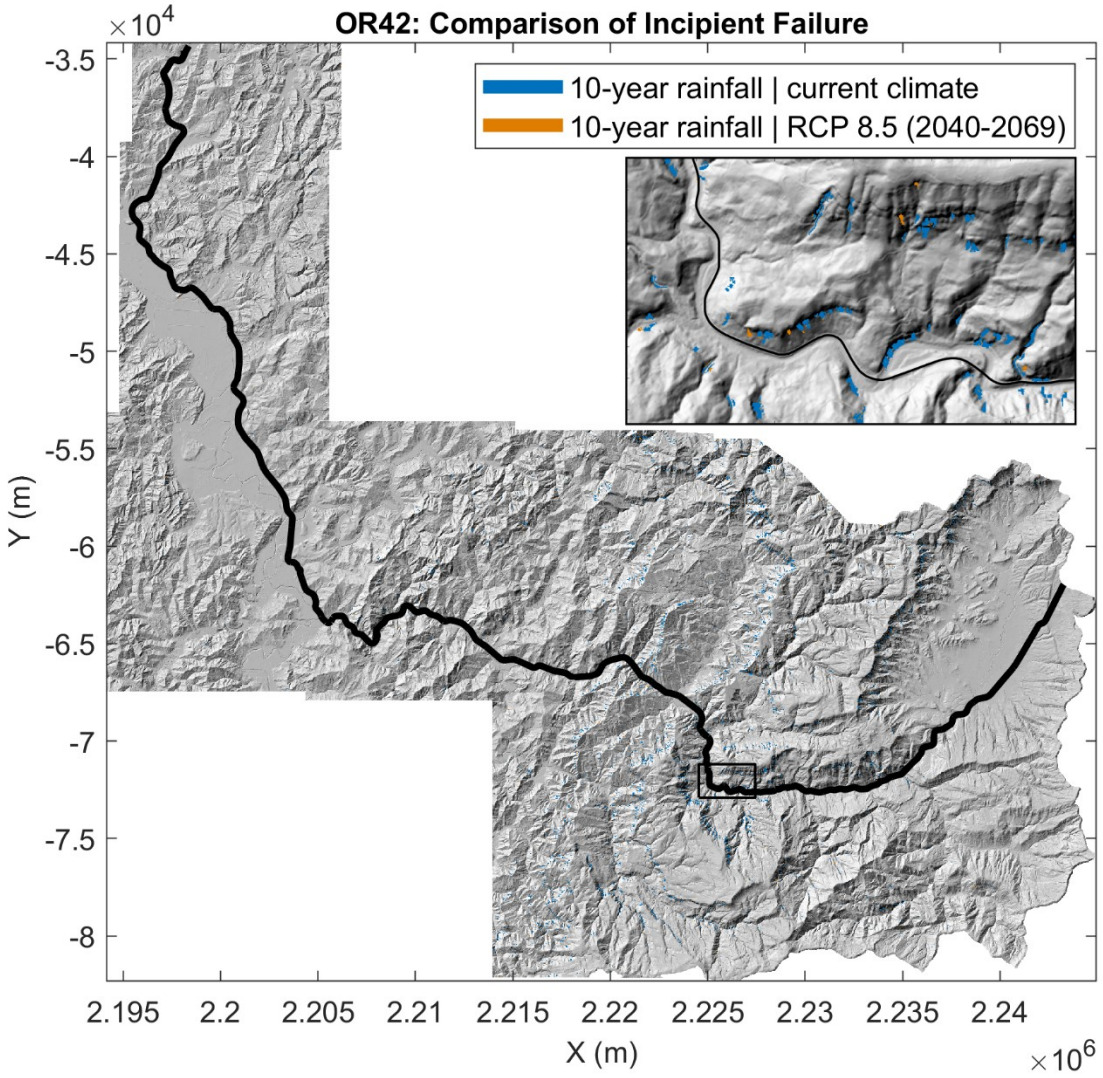

Figure 4.155: Comparison of cells exhibiting incipient failure, for corridor OR42, during a 10-year rainfall event for the current climate and future climate (RCP 8.5; 2040-2069).

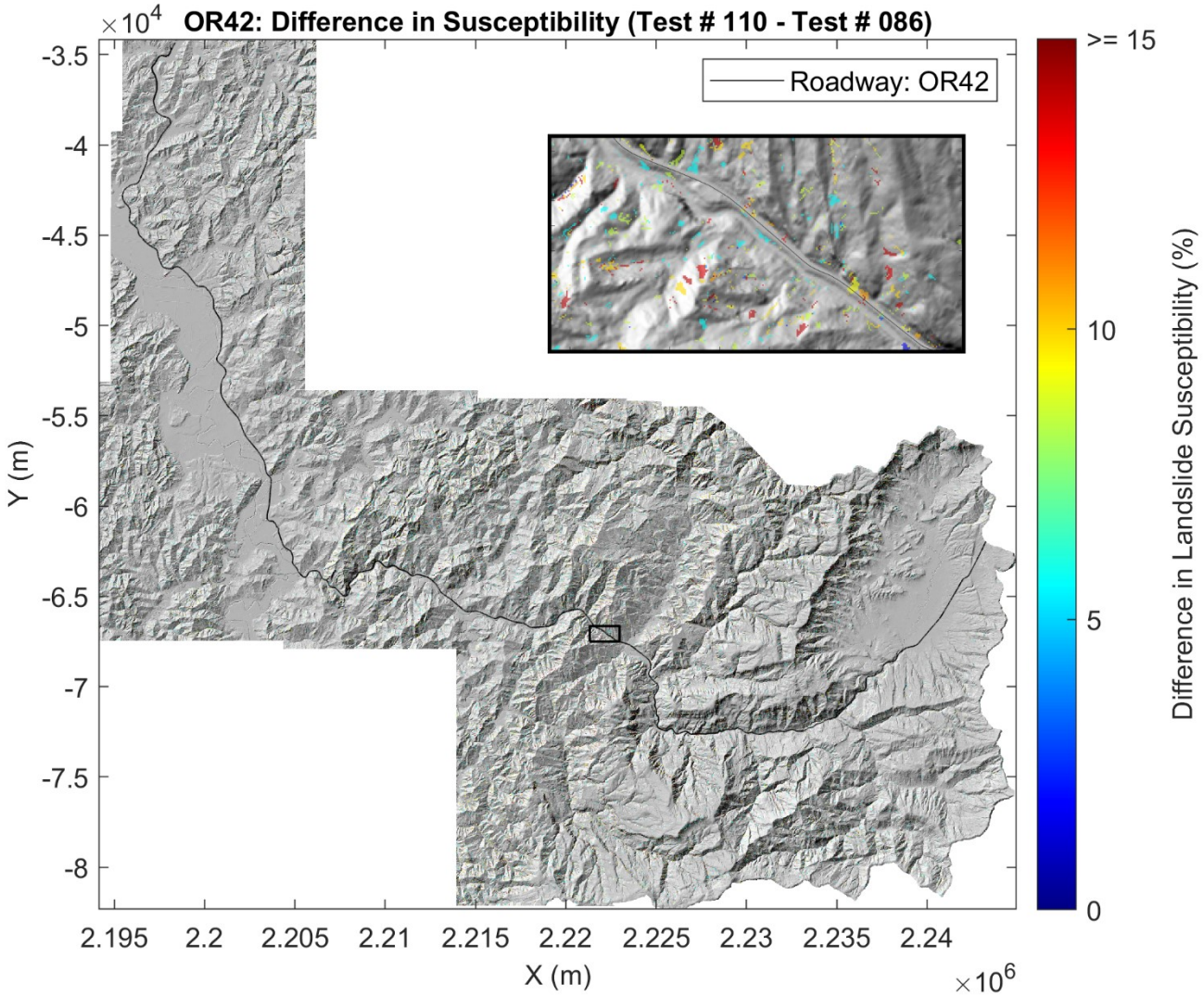

Figure 4.156: Increase in susceptibility for corridor OR42 when a future climate 10-year rainfall event is applied (RCP 8.5; 2040-2069), in comparison to a current climate 10-year rainfall event.

5.0 VALIDATION

The proposed susceptibility methodology is validated through two means: a spatial comparison of rainfall-induced landslides in Oregon during the winter of 1996-1997 and a comparison of published area-volume empirical relationships for shallow landslides.

5.1 COMPARISON OF SUSCEPTIBILITY TO RAINFALL-INDUCED LANDSLIDES IN OREGON DURING THE 1996-1997 WINTER

The winter of 1996-1997 saw widespread landslide activity within the Oregon Coast Range, USA due to heavy and prolonged rainfall events throughout the state (Chleborad et al., 1998). The proposed methodology aims to compute rainfall-induced landslide susceptibility by modeling changes in pore water pressure and slope failures that occur as a result. The methodology presented in Section 3.8 is validated here by comparing rainfall induced susceptibility to SLIDO inventoried landslide points. SLIDO landslide points are first filtered to only use those inventoried in 1996 and 1997. It is assumed that many of these are associated with the rainfall events witnessed in 1996-1997. Landslide points containing any of the following attributes (in the SLIDO landslide inventory shapefile; Burns and Madin, 2009) are used in this analysis:

"YEAR" = 1996

"YEAR" = 1997

"DATE_RANGE" = '02/1996-01/1997'

"DATE_RANGE" = '11-12/1996'

"DATE_RANGE" = '12/1996-01-1997 and other'

"DATE_RANGE" = '12/1996-01/1997'

"DATE_RANGE" = '1996-1997'

The resulting landslide points are then buffered using a 40-foot (12.2-m) radius to account for potential spatial misalignments in landslide points or landslide susceptibility. Buffered points are then superimposed in top of susceptibility for two scenarios: OR06 in winter subjected to a 100-year rainfall event (test #: 041) and US20 in winter subjected to a 100-year rainfall event (test #: 066). Susceptibility is extracted to the buffered points as a means of comparing susceptibility outputs to points of known landslide activity in the SLIDO inventory. Points with extracted susceptibility for OR06 and US20 are shown in Figures 5.1 and 5.2, respectively. Note that in Figure 5.1, only points in the western region of the DEM are sampled, as they best represent natural landsliding behavior, as opposed to fill failures. Visual inspection of Figures 5.1 and 5.2 suggests that many of the sampled landslide points correspond with regions of high

susceptibility. Further, histograms showing the distribution of sampled susceptibility points show that there is agreement between observed rainfall-induced landslides and areas of high susceptibility for these scenarios (Figures 5.3 and 5.4).

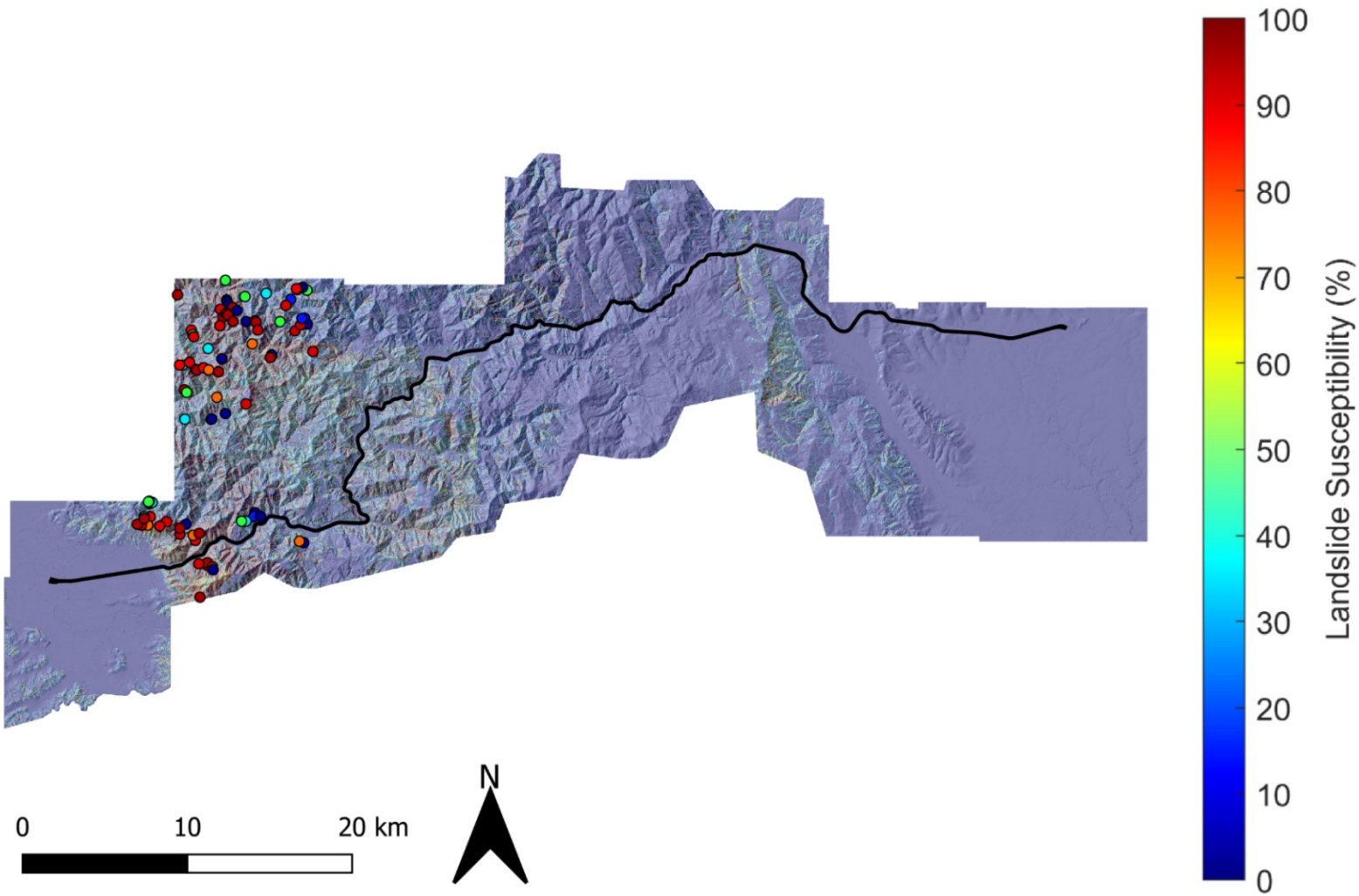

Figure 5.1: Susceptibility extracted to SLIDO inventoried landslide points from 1996-1997 for OR06: winter, 100-year rainfall event (test #: 041).

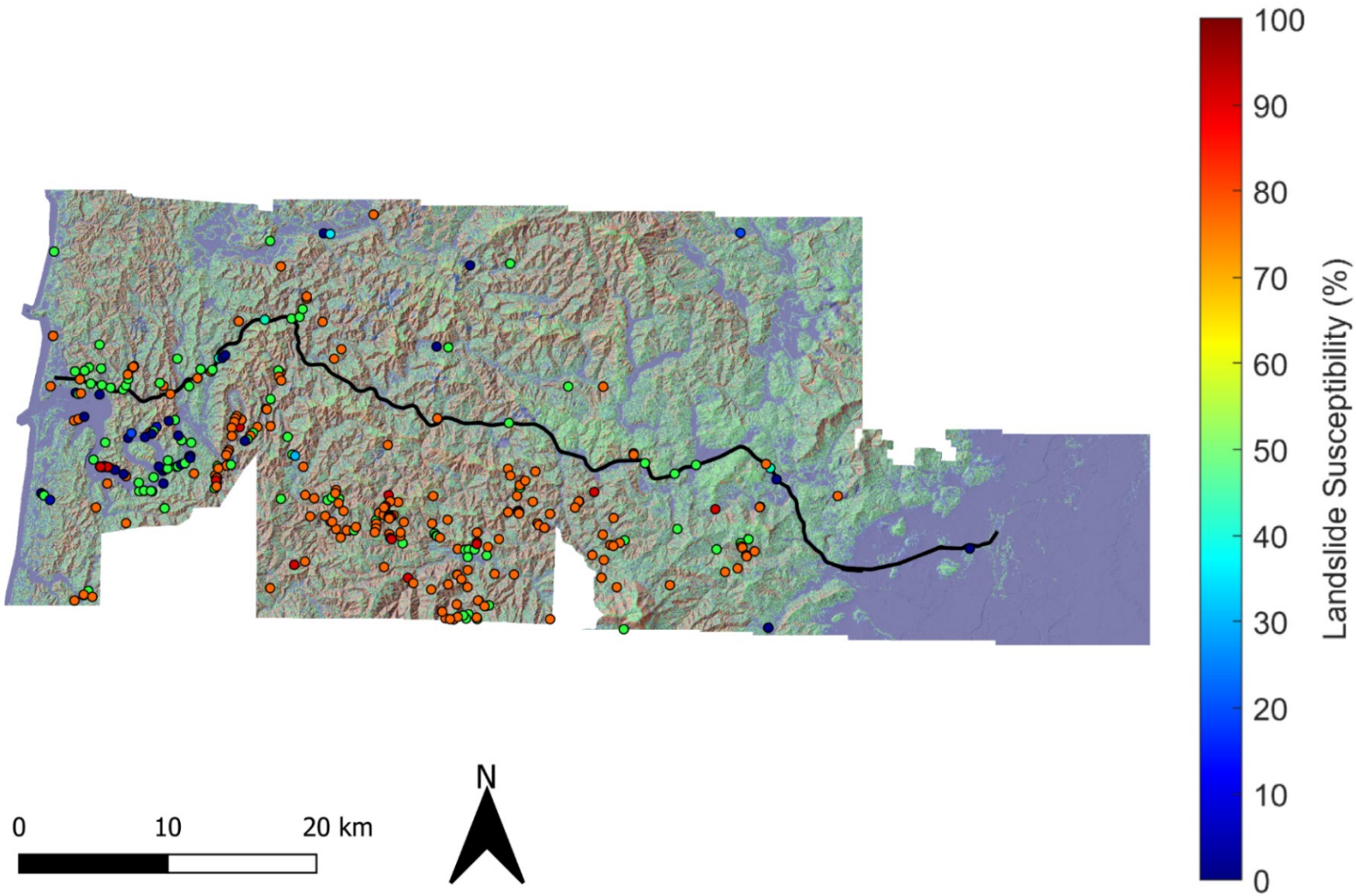

Figure 5.2: Susceptibility extracted to SLIDO inventoried landslide points from 1996-1997 for US20: winter, 100-year rainfall event (test #: 066).

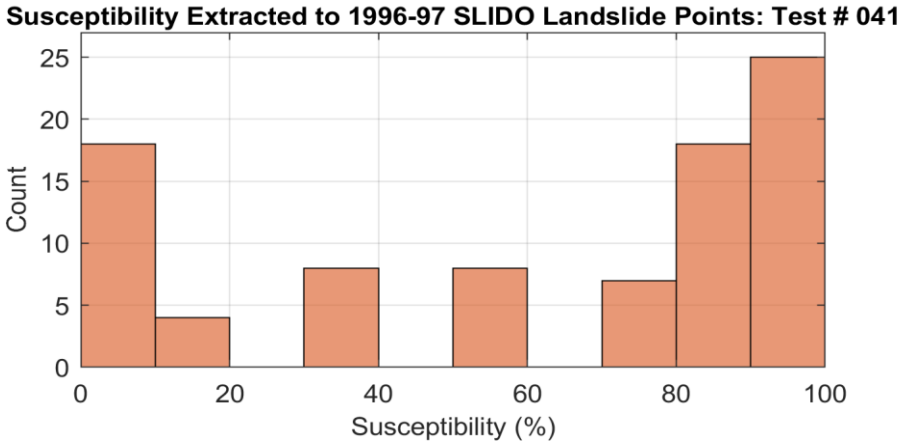

Figure 5.3: Counts of susceptibility values extracted to SLIDO inventoried points from 1996-1997 for OR06: winter, 100-year rainfall event (test #: 041).

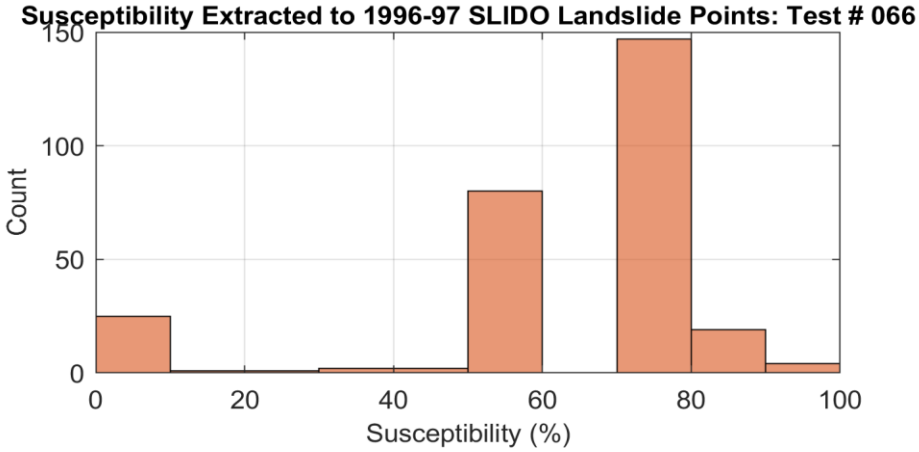

Figure 5.4: Counts of susceptibility values extracted to SLIDO inventoried points from 1996-1997 for US20: winter, 100-year rainfall event (test #: 066).

5.2 AREA-VOLUME RELATIONSHIPS

Regional landsliding behavior is commonly characterized using empirical relationships between landslide planform area and landslide volume (Guzzetti et al., 2009). As a 3D analysis, the methodology herein provides volume for each computed landslide polygon, allowing for the generation of empirical area-volume relationships. Area-volume relationships for each corridor, under varying physical inputs (seismicity and rainfall) are generated and compared to an empirical relationship from the literature for landslides in the Queen Charlotte Islands, British Columbia (Martin et al., 2002). In this study, susceptibility maps subjected to a susceptibility threshold of 50% and re-clustered into discrete landslide polygons (see Section 3.10.1) are fitted to the following power law function:

$$V_L = \varepsilon * A_L^{\alpha} \quad \textbf{(5-1)}$$

Where:

V_L is landslide volume,

A_L is landslide area, and

ε and α are fitting parameters.

Note that area and volume data are log-transformed and fit using a robust linear regression to reduce the influence of outliers in the dataset (Guzzetti et al., 2009).

Figures 5.5-5.8 show area-volume relationships for each corridor, sorted into the following categories: 1) rainfall-driven; 2) seismically-driven; and 3) multi-hazard driven. All relationships show close agreement with the published relationship produced by Martin et al. (2002). Further, values of α range from 0.76-1.00, indicating that most landslides produced in this study are shallow failures. This is likely partially due to the hillslope evolution model used to compute soil depths (Section 3.5.1), as for this study, all soil depth is assumed to start at 1-m in depth and is adjusted using a numerical model (Roering, 2008). Overall, most of the area-volume fits demonstrate similar behavior, even with significant disturbance. However, increasing disturbance (e.g. precipitation, seismicity) causes larger failures in both area and volume, which is reflected in the plots below. At a glance, it would seem that lower magnitudes of disturbance result in deeper landslides, but this is not entirely true, as greater disturbance destabilizes more cells, including those with shallower soil depths.

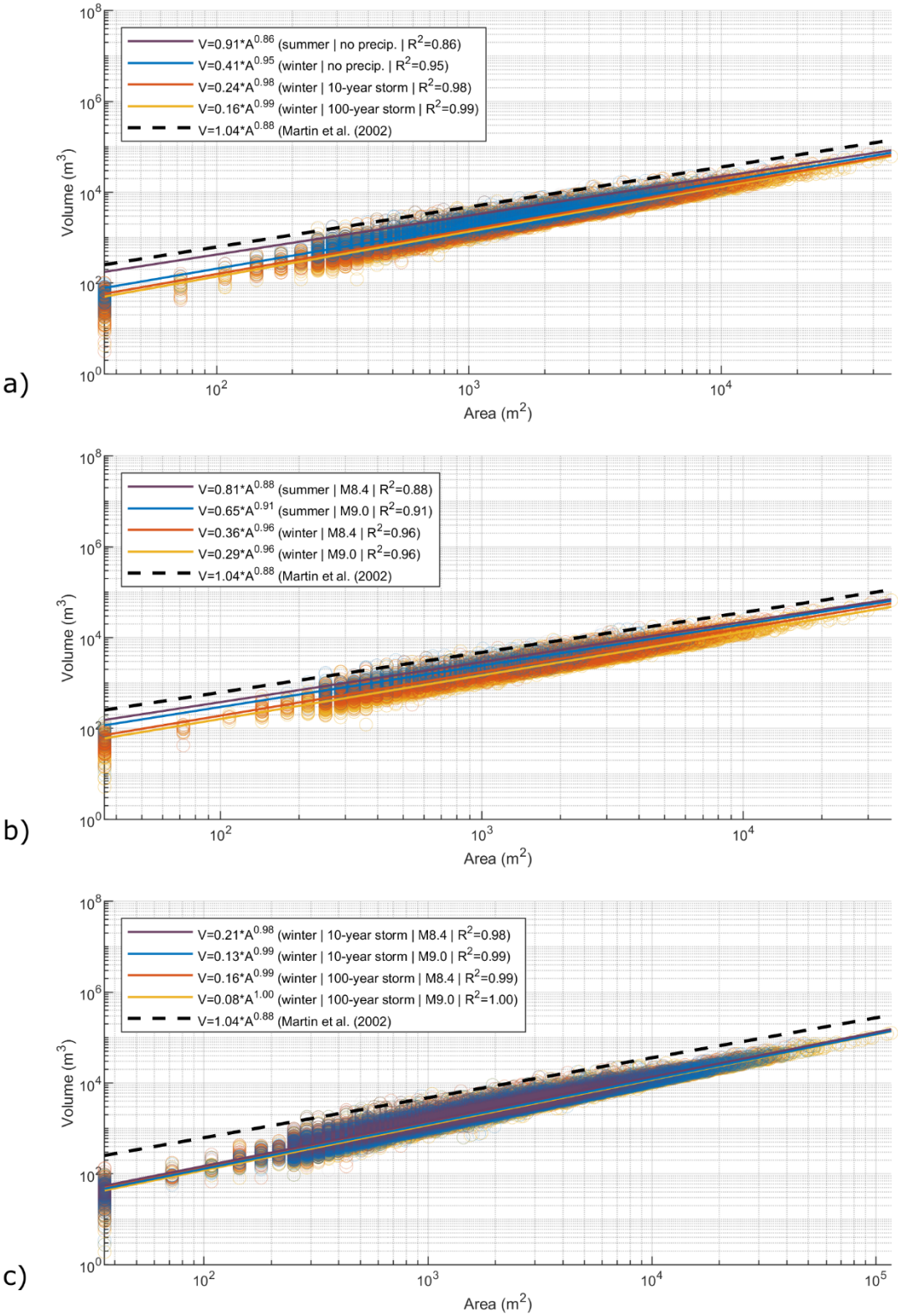

Figure 5.5: Empirical relationships between landslide area and volume for US30: a) rainfall-driven landslides; b) seismically-driven landslides; c) multi-hazard driven landslides.

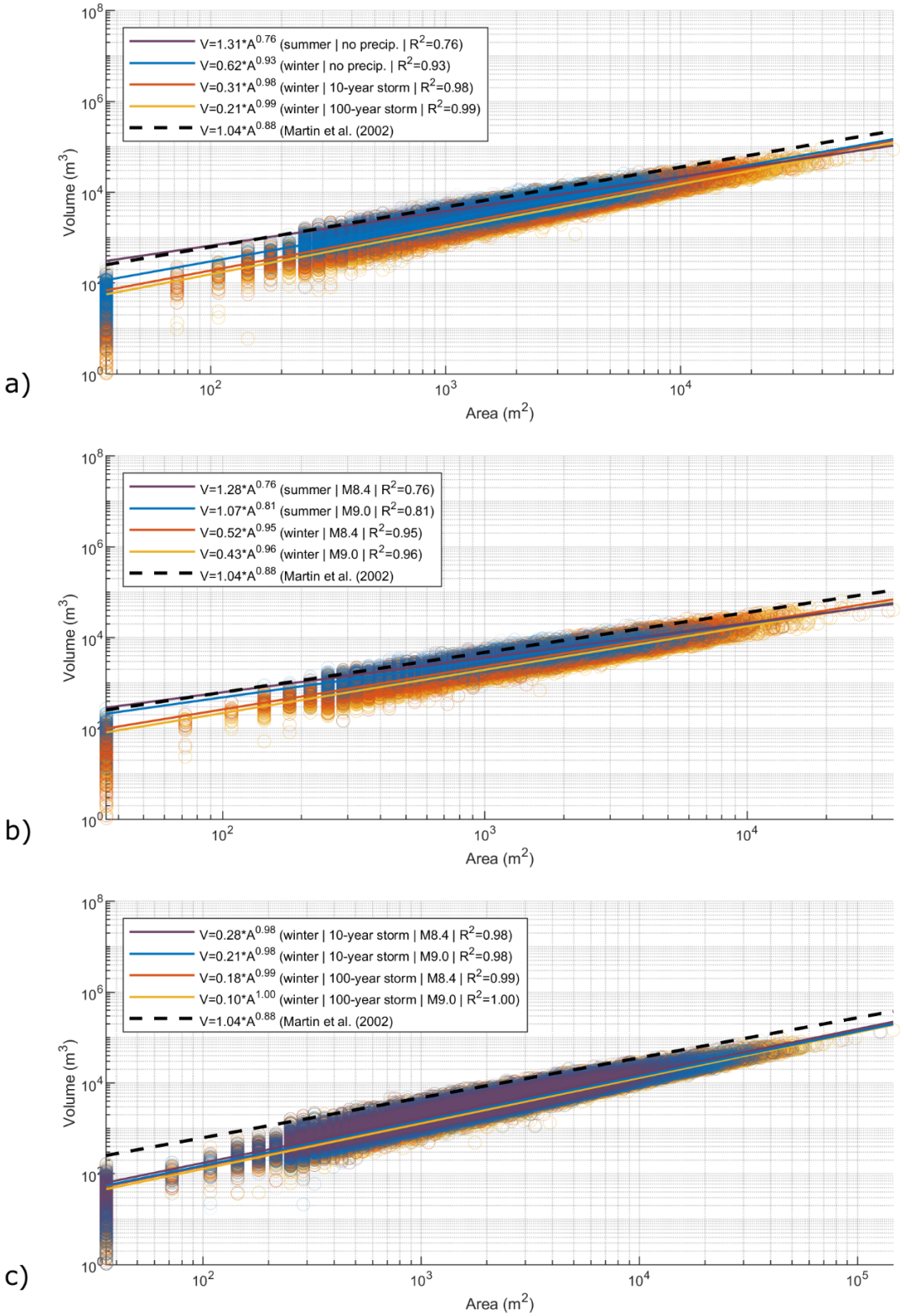

Figure 5.6: Empirical relationships between landslide area and volume for OR06: a) rainfall-driven landslides; b) seismically-driven landslides; c) multi-hazard driven landslides.

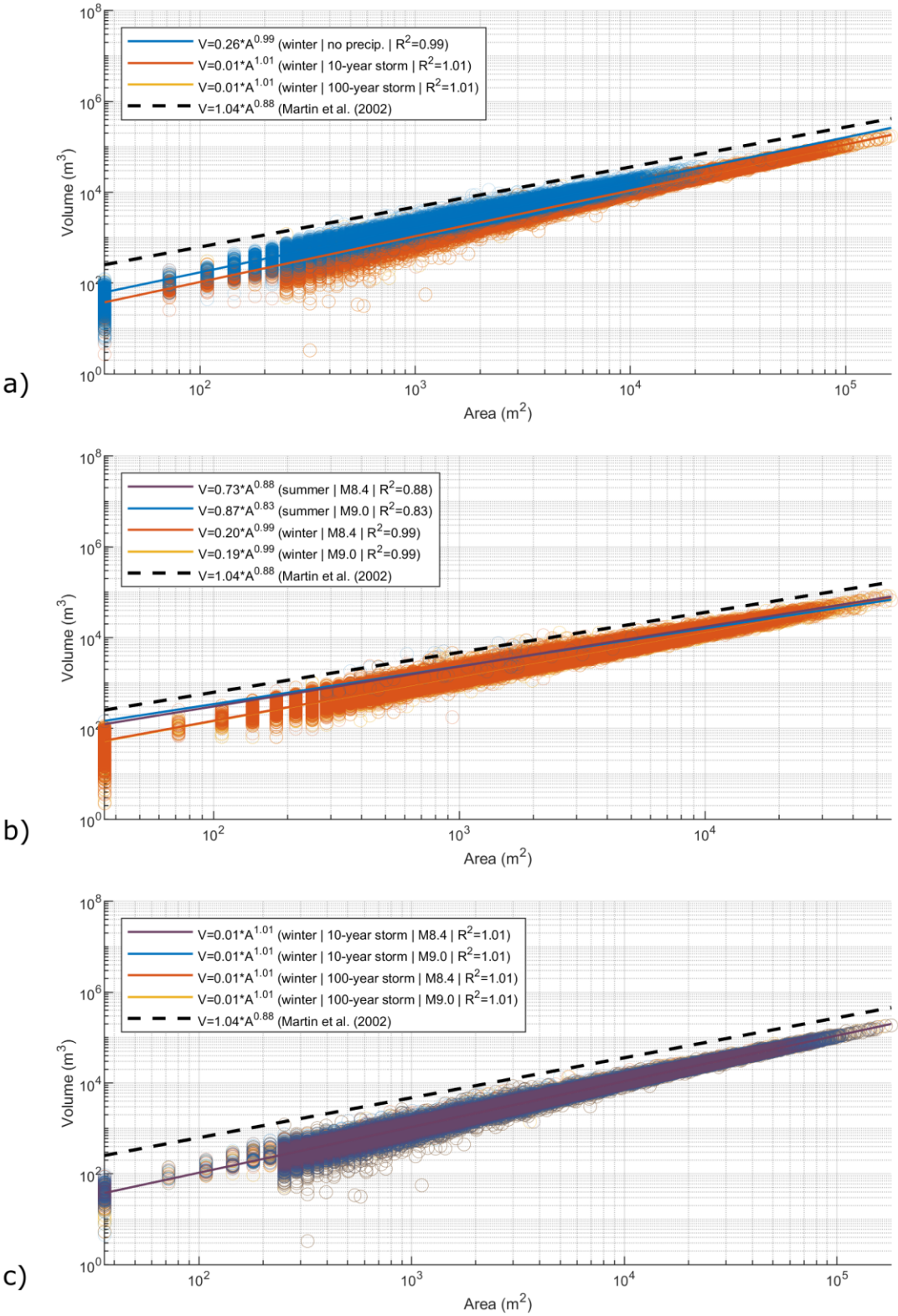

Figure 5.7: Empirical relationships between landslide area and volume for US20: a) rainfall-driven landslides; b) seismically-driven landslides; c) multi-hazard driven landslides.

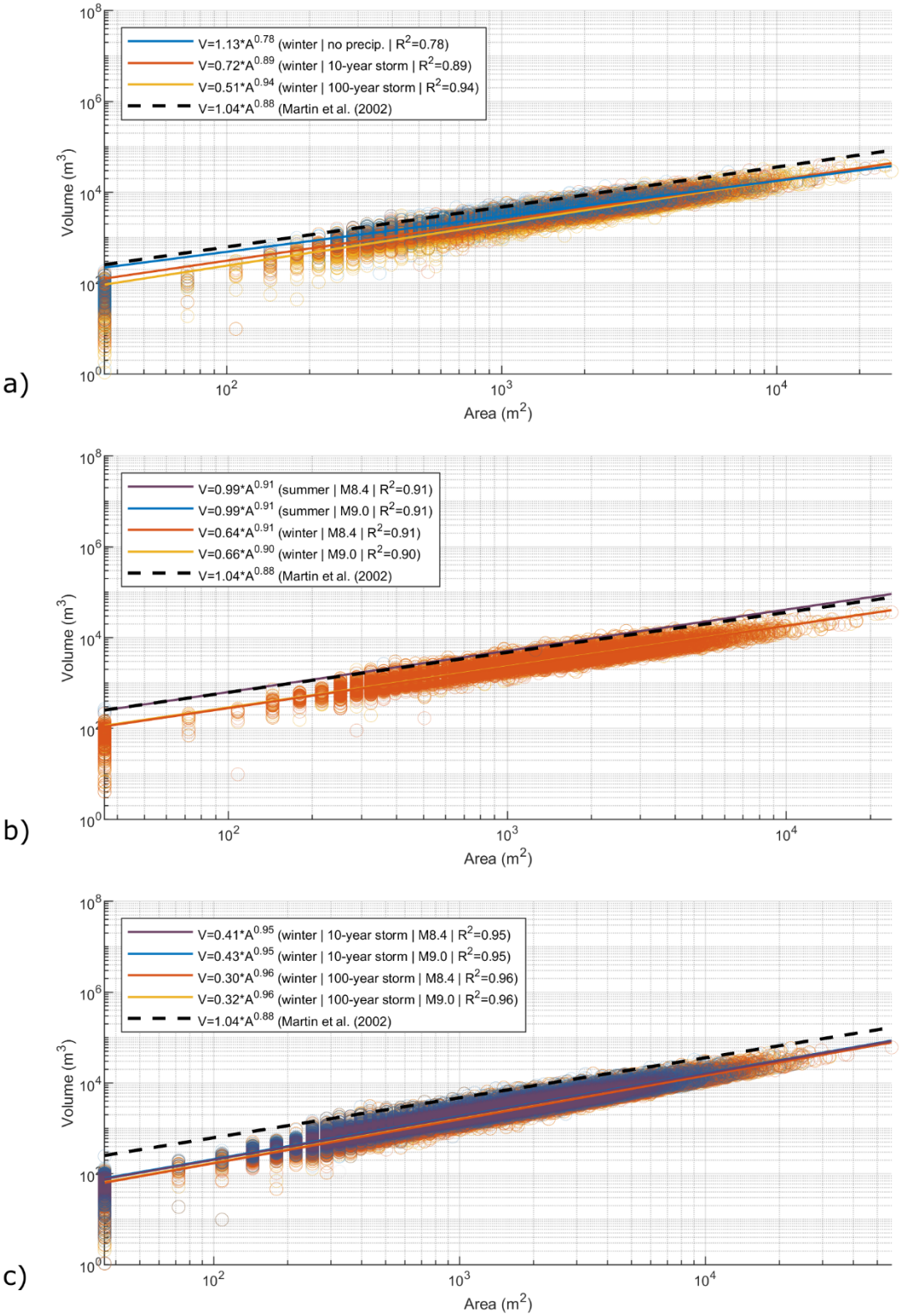

Figure 5.8: Empirical relationships between landslide area and volume for OR42: a) rainfall-driven landslides; b) seismically-driven landslides; c) multi-hazard driven landslides.

6.0 CONCLUSIONS AND RECOMMENDATIONS

6.1 CONCLUSIONS

This report presents an enhanced methodology for evaluating susceptibility through creation of novel 3D slope stability and 3D forensics analyses. Also presented is a new relationship between landslide age and roughness for the Pacific Northwest, enabling advances in forensic analyses of inventoried landslides. Further, a recent surge in displacement at the Hooskanaden Landslide and inferred hydrological and landslide characteristics from the Highway 20 PME realignment are discussed. The key points in Chapters 1-5 are as follows:

- Landslides are hazards that cause significant damage to infrastructure and communities in Oregon. Resilience in the wake of landslides may be augmented through enhanced analysis of landslide susceptibility, hazard, and risk accounting for present and future physical drivers, such as extreme rainfall and seismicity. A framework to account for these three metrics based on region-specific conditions is presented in this report and provided in digital appendices.

- A new age-roughness relationship for the Pacific Northwest reveals that numerous SLIDO inventoried landslides within corridors US30, OR06, and US20 may have been initiated during the most recent (~ 1700 A.D.) Cascadia Subduction Zone earthquake (Figures 4.21-423), as well as in a region north of OR42 (Figure 4.24). These CSZ-induced landslides are especially prevalent in corridor OR06 (Figure 4.22) and in the SLIDO inventory north of OR42 (Figure 4.24).

- Existing landslide inventories may be leveraged to produce distributions of geotechnical parameters, namely shear strengths, useful in predicting future landslide behavior or other geotechnical works. A framework for this process is presented herein.

- Applying seismic intensity measures (PGA in this study) or typical wintertime groundwater conditions specific to climate enable forensic back-analyses that provide a refined means of developing shear strength distributions, which inform enhanced susceptibility analyses.

- A new relationship between age and landslide deposit roughness may be used to date landslide activity, allowing for estimation of physical drivers tied to individual landslides. This relationship enables more informed forensic assessment of inventoried landslides and glimpse into the potential impacts of a subduction zone earthquake in the PNW.

- Susceptibility maps are developed using the Region Grow 3D method, which are then used to develop risk maps and data showing: 1) time of repair along ODOT right-of-way, 2) estimated costs of repair; 3) estimated costs of commodity loss and traffic

rerouting. These maps serve as an index for the potential impact of landslides along a series of lifeline corridors in Oregon and may be expanded further within Oregon or other states.

- The Region Grow 3D method develops discrete landslide shapes informing susceptibility analyses. This is of value, as it provides quantitative inputs for runout, potential volumes of landslide debris, and context towards the scale of impact of landslides. Susceptibility is shown to be reasonable for two corridors through comparison to inventoried, rainfall-induced landslides. Further, landslide polygons derived from susceptibility analyses are used to develop an empirical relationship between area and volume. This relationship shows agreement with a relationship from literature.

- Susceptibility outputs using the proposed methodology are validated by comparing susceptibility maps to inventoried rainfall-driven landslide failures and by comparing developed empirical relationships between landslide area and volume to those in peer-reviewed literature.

- The impacts of an earthquake event are notably amplified if occurring during wintertime conditions, where wet soils are under weaker conditions. These conditions are notably worse during or following a major storm event. However, the likelihood of these events coinciding may be exceedingly small. It is likely that the most deleterious outcome would be the occurrence of a subduction zone earthquake during typical wet wintertime conditions. Coseismic landslide impacts during summertime conditions are significant, but more muted than if conditions occurred during wet, wintertime conditions.

- Hazard maps are developed to show the likelihood of slope failures given specific physical drivers. While simple, these hazard maps reflect the likelihood of the occurrence of various destabilizing events, or combinations thereof.

- Corridors react differently to physical inputs based on antecedent moisture, distribution of earthquake-induced ground acceleration, rainfall distribution, and hydrological parameters. For instance, US20 is especially sensitive to rainfall inputs, showing drastic spikes in susceptibility when compared to drier conditions. Another example is the distribution of susceptibility for OR06 when seismicity is applied, which exhibits noticeably higher values of susceptibility nearer to the Cascadia Subduction Zone, or in the western region.

- Susceptibility is shown to be sensitive to increased precipitation during future rainfall events, driven by climate change. All corridors exhibit increases in incipient failure of cells and susceptibility, subsequently increasing highway closure times and total repair costs.

- Multihazard hazard scenarios, in which rainfall events and earthquakes occur simultaneously, are shown to exhibit severe values of susceptibility and risk metrics.

However, the relatively low probability of these driving events occurring at the same time results in relatively low values of hazard for these severe scenarios.

- Risk maps and profiles showing closure times and repair costs may be used to identify "hot spots" for each corridor and various physical drivers, providing a useful tool for resilience planning. Each corridor exhibits stretches of ROW – typically located in narrow valleys – that are particularly prone to landslide impacts. The methodology for closure times may be used to provide a coarse metric for potential impacts and is provided in the digital appendix. While repair costs are likely an unconservative estimate (i.e. representative of labor and material costs associated with the removal and placement of material), they may be modified to encapsulate any combined set of construction estimates (e.g. concrete, quarrying, retaining structures, pavement, barriers, etc.).

- As expected, increasing magnitudes of disturbance result in increasing closure times and commensurate costs and commodity impacts. These provide a glimpse towards the potential impact of a subduction zone earthquake and suggest that planners may (1) place stockpiles of material or equipment near corridor hotspots to expedite recovery, (2) choose to implement mitigation techniques in areas that are unstable but of manageable size, and (3) make decisions regarding the scope of repairs in context of prioritizing reopening and/or safety.

6.2 RECOMMENDATIONS FOR FUTURE WORK

The activities described herein describe a step forward in characterizing landslide susceptibility, hazard, and risk, especially for considering region-specific climatic, seismic, hydrologic and geologic conditions. As with any product, however, there is always room to improve and expand scope, accuracy, and implementation. Some key future directions and potential areas for improvement include:

- The presented framework and associated outputs (digital maps, shapefiles, corridor closure time plots) serve as valuable planning tools. While the presented framework captures these important, yet complex, components, it still reflects a superficial characterization of site conditions. In order to improve estimates of susceptibility, region- or site-specific monitoring would be of benefit for refinement and calibration of outputs.

- The presented analyses are valuable as they reflect typical and projected climatic conditions; however, they are static "snapshots" of potential scenarios. Future efforts could expand the proposed platform towards a living tool that uses remotely monitored (e.g. satellite or other platform) datasets, such as precipitation forecasts and soil moisture. Through this, a landslide "now-cast" or "forecast" could be developed to provide both planners and drivers with information valuable to safety.

- The approach described herein could provide a physical basis towards empirical rainfall-thresholds (i.e. intensity-duration relationships associated landslide occurrence). A process-based framework combined observed uncertainties from field

monitoring would help ODOT make decisions regarding impending climatic or seismic disturbance. Of importance is such a relationship following a seismic event, where landslide susceptibility remains heightened for months to years.

- This approach would benefit from improved characterization of subsurface data, such as those from boring logs, geologic or geophysical characterization. While the described approach uses region-specific conditions and material properties, determined through inversions, they still only represent a first-order estimate of site conditions. Of particular relevance would be expanded subsurface information relating to fractures and discontinuities deep in bedrock. Better information regarding these planes of weakness would enable more direct and comprehensive assessment of very deep failures stemming from precipitation or seismic activity.

- Future work could expand the approach presented herein to describe the progressive or delayed failure of newly-initiated or existing, active landslides that are not catastrophic in post-failure behavior. This could be considered through inversions of soil shear strength and consideration of viscous effects associated with progressive landslide movements. Such an approach could easily be adapted into the presented framework to provide estimates expected landslide activity (e.g. magnitude and/or frequency of surface movements). This data could inform planning activities surrounding the small, but nearly-continual maintenance of hundreds of active landslides around the state.

7.0 REFERENCES

Alberti, S., Senogles, A., Kingen, K., Booth, A., Castro, P., DeKoekkoek, J., . . . Leshchinsky, B. (2020). The Hooskanaden Landslide: Historic and recent surge behavior of an active earthflow on the Oregon Coast. *Landslides*, *17*(11), 2589–2602. https://doi.org/10.1007/s10346-020-01466-8

Alonso, E. E., Gens, A., & Lloret, A. (1993). The landslide of Cortes de Pallas, Spain. *Géotechnique*, *43*(4), 507–521. https://doi.org/10.1680/geot.1993.43.4.507

Anbalagan, R. (1992). Landslide hazard evaluation and zonation mapping in mountainous terrain. *Engineering Geology*, *32*(4), 269–277. https://doi.org/10.1016/0013-7952(92)90053-2

Arellano, D., & Stark, T. (2000). Importance of three-dimensional slope stability analyses in practice. In *Slope Stability 2000 (GSP 101)* (pp. 18–32). Reston, VA; American Society of Civil Engineers (ASCE).

Aruperes, L., Ganug, N. and A. Maryono. (June 22, 2016). Extreme weather persists, blocking access to victims. *Jakarta Post.* Retreived from: https://www.thejakartapost.com/news/2016/06/22/extreme-weather-persists-blocking-access-victims.html

Atwater, B., Tuttle, M., Schweig, E., Rubin, C., Yamaguchi, D., & Hemphill-Haley, E. (2003). Earthquake recurrence inferred from paleoseismology. *Developments in Quaternary Science*, *1*, 331–350. https://doi.org/10.1016/S1571-0866(03)01015-7

Avouac, J. P. (1993). Analysis of scarp profiles: Evaluation of errors in morphologic dating. *Journal of Geophysical Research: Solid Earth*, *98*(B4), 6745–6754. https://doi.org/10.1029/92jb01962

Ayalew, L., & Yamagishi, H. (2005). The application of GIS-based logistic regression for landslide susceptibility mapping in the Kakuda-Yahiko Mountains, Central Japan. *Geomorphology*, *65*(1–2), 15–31. https://doi.org/10.1016/j.geomorph.2004.06.010

Baum, R., Savage, W., & Godt, J. (2008). *TRIGRS-A Fortran program for transient rainfall infiltration and grid-based regional slope-stability analysis* (2008–1159). Reston, VA: U.S. Geological Survey. https://doi.org/10.3133/ofr20081159

Beguería, S. (2006). Changes in land cover and shallow landslide activity: A case study in the Spanish Pyrenees. *Geomorphology*, *74*(1–4), 196–206. https://doi.org/10.1016/j.geomorph.2005.07.018

Belardinelli, M. E., Antonioli, A., Bizzarri, A., & Vogfjord, K. S. (2005). *The early events after the June 17 2000 mainshock in South Iceland: constraints for instantaneous dynamic*

triggering with rate-and state-dependent friction. Munich, Germany; European Geosciences Union. Retrieved from https://www.earth-prints.org/bitstream/2122/487/1/EGU_2005_Poster.pdf

Bellugi, D., Milledge, D. G., Dietrich, W. E., McKean, J. A., Perron, J. T., Sudderth, E. B., & Kazian, B. (2015). A spectral clustering search algorithm for predicting shallow landslide size and location. *Journal of Geophysical Research: Earth Surface*, *120*(2), 300–324. https://doi.org/10.1002/2014jf003137

Berti, M., Corsini, A., & Daehne, A. (2013). Comparative analysis of surface roughness algorithms for the identification of active landslides. *Geomorphology*, *182*, 1–18. https://doi.org/10.1016/j.geomorph.2012.10.022

Bilderback, E. L., Pettinga, J. R., Litchfield, N. J., Quigley, M., Marden, M., Roering, J. J., & Palmer, A. S. (2014). Hillslope response to climate-modulated river incision in the Waipaoa catchment, East Coast North Island, New Zealand. *Geological Society of America Bulletin*, *127*(1–2), 131–148. https://doi.org/10.1130/b31015.1

Bonzanigo, L., Eberhardt, E., & Loew, S. (2007). Long-term investigation of a deep-seated creeping landslide in crystalline rock. Part I: Geological and hydromechanical factors controlling the Campo Vallemaggia landslide. *Canadian Geotechnical Journal*, *44*(10), 1157–1180. https://doi.org/10.1139/t07-043

Booth, A. M., Dehls, J., Eiken, T., Fischer, L., Hermanns, R. L., & Oppikofer, T. (2014). Integrating diverse geologic and geodetic observations to determine failure mechanisms and deformation rates across a large bedrock landslide complex: The Osmundneset landslide, Sogn og Fjordane, Norway. *Landslides*, *12*(4), 745–756. https://doi.org/10.1007/s10346-014-0504-y

Booth, A. M., LaHusen, S. R., Duvall, A. R., & Montgomery, D. R. (2017). Holocene history of deep-seated landsliding in the North Fork Stillaguamish River valley from surface roughness analysis, radiocarbon dating, and numerical landscape evolution modeling. *Journal of Geophysical Research: Earth Surface*, *122*(2), 456–472. https://doi.org/10.1002/2016jf003934

Booth, A. M., Lamb, M. P., Avouac, J. P., & Delacourt, C. (2013). Landslide velocity, thickness, and rheology from remote sensing: La Clapière landslide, France. *Geophysical Research Letters*, *40*(16), 4299–4304. https://doi.org/10.1002/grl.50828

Booth, A. M., Roering, J. J., & Perron, J. T. (2009). Automated landslide mapping using spectral analysis and high-resolution topographic data: Puget Sound lowlands, Washington, and Portland Hills, Oregon. *Geomorphology*, *109*(3–4), 132–147. https://doi.org/10.1016/j.geomorph.2009.02.027

Borgatti, L., & Soldati, M. (2010). Landslides as a geomorphological proxy for climate change: A record from the Dolomites (northern Italy). *Geomorphology*, *120*(1–2), 56–64. https://doi.org/10.1016/j.geomorph.2009.09.015

Borghuis, A. M., Chang, K., & Lee, H. Y. (2007). Comparison between automated and manual mapping of typhoon-triggered landslides from SPOT-5 imagery. *International Journal of Remote Sensing*, *28*(8), 1843–1856. https://doi.org/10.1080/01431160600935638

Bovis, M. J., & Jones, P. (1992). Holocene history of earthflow mass movements in south-central British Columbia: The influence of hydroclimatic changes. *Canadian Journal of Earth Sciences*, *29*(8), 1746–1755. https://doi.org/10.1139/e92-137

Bray, J. D., & Rathje, E. M. (1998). Earthquake-Induced displacements of solid-waste landfills. *Journal of Geotechnical and Geoenvironmental Engineering*, *124*(3), 242–253. https://doi.org/10.1061/(asce)1090-0241(1998)124:3(242)

Bunn, M., Leshchinsky, B., Olsen, M., & Booth, A. (2019). A simplified, object-based framework for efficient landslide inventorying using LIDAR digital elevation model derivatives. *Remote Sensing*, *11*(3), 303. https://doi.org/10.3390/rs11030303

Bunn, M., Leshchinsky, B., & Olsen, M. J. (2020a). Estimates of three-dimensional rupture surface geometry of deep-seated landslides using landslide inventories and high-resolution topographic data. *Geomorphology*, *367*, 107332. https://doi.org/10.1016/j.geomorph.2020.107332

Bunn, M., Leshchinsky, B., & Olsen, M. J. (2020b). Geologic trends in shear strength properties inferred through three-dimensional back analysis of landslide inventories. *Journal of Geophysical Research: Earth Surface*, *125*(9). https://doi.org/10.1029/2019jf005461

Burns, S. (2014). The Oso Landslide, Washington, March 22, 2014 shows the need for susceptibility maps and insurance. In *GSA 2014 Annual Meeting & Exposition*. Vancouver, BC, Canada; GSA.

Burns, W. J., & Madin, I. (2009). *Protocol for inventory mapping of landslide deposits from light detection and ranging (LiDAR) imagery* (Special Report 42). Portland, OR: Oregon Department of Geology and Mineral Industries.

Burns, W. J., Coe, J. A., Kaya, B. S., & Ma, L. (2010). Analysis of elevation changes detected from multi-temporal LiDAR surveys in forested landslide terrain in western Oregon. *Environmental and Engineering Geoscience*, *16*(4), 315–341. https://doi.org/10.2113/gseegeosci.16.4.315

Burns, W., & Watzig, R. (2014). *SLIDO 3.0* [Statewide landslide information database for Oregon].

Burns, W., Mickelson, K., & Madin, I. (2016). *Landslide susceptibility overview map of Oregon*. map, Salem, OR; Oregon Department of Geology and Mineral Industries.

Cai, F., & Ugai, K. (2004). Numerical analysis of rainfall effects on slope stability. *International Journal of Geomechanics*, *4*(2), 69–78. https://doi.org/10.1061/(asce)1532-3641(2004)4:2(69)

Caine, N. (1980). The rainfall intensity: Duration control of shallow landslides and debris flows. *Geografiska Annaler. Series A, Physical Geography*, *62*(1/2), 23. https://doi.org/10.2307/520449

Cao, W., Tong, X. H., Liu, S. C., & Wang, D. (2016). Landslides extraction from diverse remote sensing data sources using semantic reasoning scheme. *ISPRS - International Archives of the Photogrammetry, Remote Sensing and Spatial Information Sciences*, *XLI-B8*, 25–31. https://doi.org/10.5194/isprsarchives-xli-b8-25-2016

Carey, J. M., Massey, C. I., Lyndsell, B., & Petley, D. N. (2019). Displacement mechanisms of slow-moving landslides in response to changes in porewater pressure and dynamic stress. *Earth Surface Dynamics*, *7*(3), 707–722. https://doi.org/10.5194/esurf-7-707-2019

Carrara, A., Cardinali, M., Detti, R., Guzzetti, F., Pasqui, V., & Reichenbach, P. (1991). GIS techniques and statistical models in evaluating landslide hazard. *Earth Surface Processes and Landforms*, *16*(5), 427–445. https://doi.org/10.1002/esp.3290160505

Cevasco, A., Pepe, G., & Brandolini, P. (2014). The influences of geological and land use settings on shallow landslides triggered by an intense rainfall event in a coastal terraced environment. *Bulletin of Engineering Geology and the Environment*, *73*(3), 859–875. https://doi.org/10.1007/s10064-013-0544-x

Chigira, M., & Yagi, H. (2006). Geological and geomorphological characteristics of landslides triggered by the 2004 Mid Niigta prefecture earthquake in Japan. *Engineering Geology*, *82*(4), 202–221. https://doi.org/10.1016/j.enggeo.2005.10.006

Chleborad, A., Schuster, R., & Baum, R. (1998). *Landslides triggered by the winter 1996–97 storms in the Puget Lowland, Washington* (Open-File Report 98–239). Washington, D.C.: U.S. Geological Survey. Retrieved from https://pubs.usgs.gov/of/1998/0239/report.pdf

Coe, J., Ellis, W., Godt, J., Savage, W., Savage, J., Michael, J., . . . Debray, S. (2003). Seasonal movement of the Slumgullion landslide determined from global positioning system surveys and field instrumentation, July 1998–March 2002. *Engineering Geology*, *68*(1–2), 67–101. https://doi.org/10.1016/s0013-7952(02)00199-0

Collins, B. D., & Jibson, R. W. (2015). *Assessment of existing and potential landslide hazards resulting from the April 25, 2015 Gorkha, Nepal earthquake sequence* (Open-File Report 2015-1142). Washington, D.C.: U.S. Geological Survey. https://doi.org/10.3133/ofr20151142

Conner, J. C., & Olsen, M. J. (2014). Automated quantification of distributed landslide movement using circular tree trunks extracted from terrestrial laser scan data. *Computers & Geosciences*, *67*, 31–39. https://doi.org/10.1016/j.cageo.2014.02.007

Crank, J. (1975). *The mathematics of diffusion* (2nd Edition). Clarendon Press-Oxford. Retrieved from http://www-eng.lbl.gov/~shuman/NEXT/MATERIALS&COMPONENTS/Xe_damage/Crank-The-Mathematics-of-Diffusion.pdf

Crozier, M. (2010). Deciphering the effect of climate change on landslide activity: A review. *Geomorphology*, *124*(3–4), 260–267. https://doi.org/10.1016/j.geomorph.2010.04.009

Cruden, D. M. (1976). Major rock slides in the Rockies. *Canadian Geotechnical Journal*, *13*(1), 8–20. https://doi.org/10.1139/t76-002

Cruden, D. M. (1991). A simple definition of a landslide. *Bulletin of the International Association of Engineering Geology*, *43*(1), 27–29. https://doi.org/10.1007/bf02590167

Cruden, D. M., & Varnes, D. J. (1996). Landslide types and processes. In *Landslides, Investigation and Mitigation* (Special Report 247 ed., pp. 36–75). Washington, D.C.: Transportation Research Board.

Dai, F., & Lee, C. (2002). Landslide characteristics and slope instability modeling using GIS, Lantau Island, Hong Kong. *Geomorphology*, *42*(3–4), 213–228. https://doi.org/10.1016/s0169-555x(01)00087-3

Dai, F., Lee, C., & Ngai, Y. (2002). Landslide risk assessment and management: An overview. *Engineering Geology*, *64*(1), 65–87. https://doi.org/10.1016/s0013-7952(01)00093-x

Dai, F., Xu, C., Yao, X., Xu, L., Tu, X., & Gong, Q. (2011). Spatial distribution of landslides triggered by the 2008 Ms 8.0 Wenchuan earthquake, China. *Journal of Asian Earth Sciences*, *40*(4), 883–895. https://doi.org/10.1016/j.jseaes.2010.04.010

Dalton, M., Dello, K., Hawkins, L., Mote, P., & Rupp, D. (2017) *The third Oregon climate assessment report*. Corvillas, OR: Oregon Climate Change Research Institute, College of Earth, Ocean and Atmospheric Sciences, Oregon State University. Retrieved from https://pnwcirc.org/sites/pnwcirc.org/files/ocar3_finalweb.pdf

DeBell, D. S. (1990). Black cottonwood. In *Silvics of North America: Volume 2, Conifers (Agriculture Handbook 654)* (First Edition, Vol. 2, pp. 570–576). Washington, D.C.: United States Department of Agriculture. Retrieved from https://www.srs.fs.usda.gov/pubs/misc/ag_654_vol2.pdf

Dietrich, W. E., McKean, J., Bellugi, D., & Perron, T. (2007). The prediction of shallow landslide location and size using a multidimensional landslide analysis in a digital terrain model. Proceedings of *The Fourth International Conference on Debris-Flow Hazards Mitigation: Mechanics, Prediction, and Assessment (DFHM-4);* Chengdu, China, September 10-13, 2007. The Netherlands, Amsterdam: IOS Press.

Dietrich, W. E., Reiss, R., Hsu, M. L., & Montgomery, D. R. (1995). A process-based model for colluvial soil depth and shallow landsliding using digital elevation data. *Hydrological Processes*, *9*(3–4), 383–400. https://doi.org/10.1002/hyp.3360090311

Dietrich, W. E., Wilson, C. J., Montgomery, D. R., McKean, J., & Bauer, R. (1992). Erosion thresholds and land surface morphology. *Geology*, *20*(8), 675-679. https://doi.org/10.1130/0091-7613(1992)020<0675:ETALSM>2.3.CO;2

Dufresne, A., Davies, T., & McSaveney, M. (2010). Influence of runout-path material on emplacement of the round top rock avalanche, New Zealand. *Earth Surface Processes and Landforms*, *35*(2), 190–201. https://doi.org/10.1002/esp.1900

Duncan, J. M. (1996). State of the art: Limit equilibrium and finite-element analysis of slopes. *Journal of Geotechnical Engineering*, *122*(7), 577–596. https://doi.org/10.1061/(asce)0733-9410(1996)122:7(577)

Duncan, J., & Wright, S. (1980). The accuracy of equilibrium methods of slope stability analysis. *Engineering Geology*, *16*(1–2), 5–17. https://doi.org/10.1016/0013-7952(80)90003-4

Eberhardt, E., Thuro, K., & Luginbuehl, M. (2005). Slope instability mechanisms in dipping interbedded conglomerates and weathered marls—the 1999 Rufi landslide, Switzerland. *Engineering Geology*, *77*(1–2), 35–56. https://doi.org/10.1016/j.enggeo.2004.08.004

Federal Highway Administration (FHWA). (2016). *Highway statistics 2016*. Washington, D.C.: Federal Highway Administration. Retrieved from https://www.fhwa.dot.gov/policyinformation/statistics/2016/

Fredlund, D. G., & Krahn, J. (1977). Comparison of slope stability methods of analysis. *Canadian Geotechnical Journal*, *14*(3), 429–439. https://doi.org/10.1139/t77-045

Garris, R. (2019). *Modeling surface roughness as an indicator of age to better understand landslide susceptibility and the spatial inventory of prehistoric landslides: Green River Valley, Washington* (Master Thesis). Portland, OR: Portland State University. Retrieved from https://pdxscholar.library.pdx.edu/cgi/viewcontent.cgi?article=6247&context=open_access_etds

Gill, J. C., & Malamud, B. D. (2017). Anthropogenic processes, natural hazards, and interactions in a multi-hazard framework. *Earth-Science Reviews*, *166*, 246–269. https://doi.org/10.1016/j.earscirev.2017.01.002

Glade, T. (2003). Landslide occurrence as a response to land use change: A review of evidence from New Zealand. *CATENA*, *51*(3–4), 297–314. https://doi.org/10.1016/s0341-8162(02)00170-4

Glenn, N. F., Streutker, D. R., Chadwick, D. J., Thackray, G. D., & Dorsch, S. J. (2006). Analysis of LiDAR-derived topographic information for characterizing and differentiating landslide morphology and activity. *Geomorphology*, *73*(1–2), 131–148. https://doi.org/10.1016/j.geomorph.2005.07.006

Goetz, J. N., Bell, R., & Brenning, A. (2014). Could surface roughness be a poor proxy for landslide age? Results from the Swabian Alb, Germany. *Earth Surface Processes and Landforms*, *39*(12), 1697–1704. https://doi.org/10.1002/esp.3630

Gokceoglu, C., Sonmez, H., Nefeslioglu, H. A., Duman, T. Y., & Can, T. (2005). The 17 March 2005 Kuzulu landslide (Sivas, Turkey) and landslide-susceptibility map of its near

vicinity. *Engineering Geology*, *81*(1), 65–83. https://doi.org/10.1016/j.enggeo.2005.07.011

Goldfinger, C., Nelson, C. H., Morey, A. E., Johnson, J. E., Patton, J. R., Karabanov, E., ... & Enkin, R. J. (2012). *Turbidite event history: Methods and implications for Holocene paleoseismicity of the Cascadia subduction zone* (Report No. 1661-F). Reston, VA: US Geological Survey. https://doi.org/10.3133/pp1661F

Guzzetti, F., Ardizzone, F., Cardinali, M., Rossi, M., & Valigi, D. (2009). Landslide volumes and landslide mobilization rates in Umbria, central Italy. *Earth and Planetary Science Letters*, *279*(3–4), 222–229. https://doi.org/10.1016/j.epsl.2009.01.005

Guzzetti, F., Mondini, A. C., Cardinali, M., Fiorucci, F., Santangelo, M., & Chang, K. T. (2012). Landslide inventory maps: New tools for an old problem. *Earth-Science Reviews*, *112*(1–2), 42–66. https://doi.org/10.1016/j.earscirev.2012.02.001

Hammond, C. M., Meier, D., & Beckstrand, D. (2009). Paleo-landslides in the Tyee Formation and highway construction, central Oregon Coast Range. In *Volcanoes to Vineyards* (Vol. 15, pp. 481–494). Boulder, CO: Geological Society of America. https://doi.org/10.1130/2009.fld015(23)

Hanks, T. C. (2000). The age of scarplike landforms from diffusion-equation analysis. In *Quaternary Geochronology: Methods and Applications* (Vol. 4, pp. 313–338). Washington, D.C.: American Geophysical Union. https://doi.org/10.1029/RF004p0313

Hanks, T. C., Bucknam, R. C., Lajoie, K. R., & Wallace, R. E. (1984). Modification of wave-cut and faulting-controlled landforms. *Journal of Geophysical Research: Solid Earth*, *89*(B7), 5771–5790. https://doi.org/10.1029/jb089ib07p05771

Harp, E. L., & Jibson, R. W. (1996). Landslides triggered by the 1994 Northridge, California, earthquake. *Bulletin of the Seismological Society of America*, *86*(1 suppl. B), S319–S332.

Haugerud, R. A., Harding, D. J., Johnson, S. Y., Harless, J. L., Weaver, C. S., & Sherrod, B. L. (2003). High-Resolution lidar topography of the Puget Lowland, Washington —A bonanza for earth science. *GSA Today*, *13*(6), 4. https://doi.org/10.1130/1052-5173(2003)13<0004:hltotp>2.0.co;2

Hermanns, R. L., & Strecker, M. R. (1999). Structural and lithological controls on large quaternary rock avalanches (sturzstroms) in arid northwestern Argentina. *Geological Society of America Bulletin*, *111*(6), 934–948. https://doi.org/10.1130/0016-7606(1999)111<0934:salcol>2.3.co;2

Hervas, J., & Bobrowsky, P. (2009). Mapping: Inventories, susceptibility, hazard and risk. In *Landslides - Disaster Risk Reduction* (pp. 321–349). Berlin, Germany: Springer. https://doi.org/10.1007/978-3-540-69970-5_19

Hess, D. M., Leshchinsky, B. A., Bunn, M., Benjamin Mason, H., & Olsen, M. J. (2017). A simplified three-dimensional shallow landslide susceptibility framework considering

topography and seismicity. *Landslides*, *14*(5), 1677–1697. https://doi.org/10.1007/s10346-017-0810-2

Hilley, G. E. (2008). *The landslide handbook: A guide to understanding landslides* (Circular 1325 ed.). Reston, VA: US Geological Survey.

Hilley, G., Chamberlain, C., Moon, S., Porder, S., & Willett, S. (2010). Competition between erosion and reaction kinetics in controlling silicate-weathering rates. *Earth and Planetary Science Letters*, *293*(1–2), 191–199. https://doi.org/10.1016/j.epsl.2010.01.008

Hoffmann, H. (2021). Soil_classification(sand, clay, T,varargin) (Version 1.1.0.0) [Soil Classification (USDA) according to texture]. Natick, MA: MATLAB Central File Exchange. Retrieved from https://www.mathworks.com

Hopkinson, C., Chasmer, L., Young-Pow, C., & Treitz, P. (2004). Assessing forest metrics with a ground-based scanning lidar. *Canadian Journal of Forest Research*, *34*(3), 573–583. https://doi.org/10.1139/x03-225

Hungr, O. (1987). An extension of Bishop's simplified method of slope stability analysis to three dimensions. *Géotechnique*, *37*(1), 113–117. https://doi.org/10.1680/geot.1987.37.1.113

Iida, T. (2004). Theoretical research on the relationship between return period of rainfall and shallow landslides. *Hydrological Processes*, *18*(4), 739–756. https://doi.org/10.1002/hyp.1264

Iverson, R. M. (2000). Landslide triggering by rain infiltration. *Water Resources Research*, *36*(7), 1897–1910. https://doi.org/10.1029/2000wr900090

Jaboyedoff, M., Oppikofer, T., Abellán, A., Derron, M. H., Loye, A., Metzger, R., & Pedrazzini, A. (2012). Use of LIDAR in landslide investigations: A review. *Natural Hazards*, *61*(1), 5–28. https://doi.org/10.1007/s11069-010-9634-2

Jaboyedoff, M., Oppikofer, T., Derron, M. H., Blikra, L. H., Böhme, M., & Saintot, A. (2011). Complex landslide behaviour and structural control: A three-dimensional conceptual model of Åknes rockslide, Norway. *Geological Society, London, Special Publications*, *351*(1), 147–161. https://doi.org/10.1144/sp351.8

Jacoby, G. C., Williams, P. L., & Buckley, B. M. (1992). Tree ring correlation between prehistoric landslides and abrupt tectonic events in Seattle, Washington. *Science*, *258*(5088), 1621–1623. https://doi.org/10.1126/science.258.5088.1621

Jakob, M. (2000). The impacts of logging on landslide activity at Clayoquot Sound, British Columbia. *CATENA*, *38*(4), 279–300. https://doi.org/10.1016/s0341-8162(99)00078-8

James, T. S., Clague, J. J., Wang, K., & Hutchinson, I. (2000). Postglacial rebound at the northern Cascadia subduction zone. *Quaternary Science Reviews*, *19*(14–15), 1527–1541. https://doi.org/10.1016/s0277-3791(00)00076-7

Janbu, N. (1973). *Slope stability computations*. New York, NY: Wiley (John) and Sons, Incorporated.

Jebur, M. N., Pradhan, B., & Tehrany, M. S. (2014). Optimization of landslide conditioning factors using very high-resolution airborne laser scanning (LiDAR) data at catchment scale. *Remote Sensing of Environment*, *152*, 150–165. https://doi.org/10.1016/j.rse.2014.05.013

Jebur, M. N., Pradhan, B., & Tehrany, M. S. (2015). Using ALOS PALSAR derived high-resolution DInSAR to detect slow-moving landslides in tropical forest: Cameron Highlands, Malaysia. *Geomatics, Natural Hazards and Risk*, *6*(8), 741–759. https://doi.org/10.1080/19475705.2013.860407

Jibson, R. W. (2011). Methods for assessing the stability of slopes during earthquakes—A retrospective. *Engineering Geology*, *122*(1–2), 43–50. https://doi.org/10.1016/j.enggeo.2010.09.017

Kargel, J. S., Leonard, G. J., Shugar, D. H., Haritashya, U. K., Bevington, A., Fielding, E. J., ... & Anderson, E. (2016). Geomorphic and geologic controls of geohazards induced by Nepal's 2015 Gorkha earthquake. *Science, 351*(6269), aac8353. https://doi.org/ 10.1126/science.aac8353

Keaton, J. R., & DeGraff, J. V. (1996). Surface observation and geologic mapping. In *Landslides: Investigation and Mitigation (National Research Council (U.s.) Transportation Research Board Special Report)* (First ed., pp. 178–230). Washington, D.C.: Transportation Research Board.

Keefer, D. K. (1984). Landslides caused by earthquakes. *Geological Society of America Bulletin*, *95*(4), 406–421. https://doi.org/10.1130/0016-7606(1984)95<406:lcbe>2.0.co;2

Khazai, B., & Sitar, N. (2000). Assessment of seismic slope stability using GIS modeling. *Annals of GIS*, *6*(2), 121–128. https://doi.org/10.1080/10824000009480540

Khazai, B., & Sitar, N. (2004). Evaluation of factors controlling earthquake-induced landslides caused by Chi-Chi earthquake and comparison with the Northridge and Loma Prieta events. *Engineering Geology*, *71*(1–2), 79–95. https://doi.org/10.1016/s0013-7952(03)00127-3

Korup, O., & Clague, J. J. (2009). Natural hazards, extreme events, and mountain topography. *Quaternary Science Reviews*, *28*(11–12), 977–990. https://doi.org/10.1016/j.quascirev.2009.02.021

Kumar, P., & Foufoula-Georgiou, E. (1997). Wavelet analysis for geophysical applications. *Reviews of Geophysics*, *35*(4), 385–412. https://doi.org/10.1029/97rg00427

LaHusen, S. R., Duvall, A. R., Booth, A. M., & Montgomery, D. R. (2016). Surface roughness dating of long-runout landslides near Oso, Washington (USA), reveals persistent

postglacial hillslope instability. *Geology*, *44*(2), 111–114. https://doi.org/10.1130/g37267.1

LaHusen, S. R., Duvall, A. R., Booth, A. M., Grant, A., Mishkin, B. A., Montgomery, D. R., . . . Wartman, J. (2020). Rainfall triggers more deep-seated landslides than Cascadia earthquakes in the Oregon Coast Range, USA. *Science Advances*, *6*(38), eaba6790. https://doi.org/10.1126/sciadv.aba6790

Larsen, M. C. (2008). Rainfall-triggered landslides, anthropogenic hazards, and mitigation strategies. *Advances in Geosciences*, *14*, 147–153. https://doi.org/10.5194/adgeo-14-147-2008

Lashermes, B., Foufoula-Georgiou, E., & Dietrich, W. E. (2007). Channel network extraction from high resolution topography using wavelets. *Geophysical Research Letters*, *34*(23). https://doi.org/10.1029/2007gl031140

Lee, S., Choi, J., & Min, K. (2002). Landslide susceptibility analysis and verification using the Bayesian probability model. *Environmental Geology*, *43*(1–2), 120–131. https://doi.org/10.1007/s00254-002-0616-x

Lee, S., & Sambath, T. (2006). Landslide susceptibility mapping in the Damrei Romel area, Cambodia using frequency ratio and logistic regression models. *Environmental Geology*, *50*(6), 847–855. https://doi.org/10.1007/s00254-006-0256-7

Lee, S., Choi, J., & Min, K. (2002). Landslide susceptibility analysis and verification using the Bayesian probability model. *Environmental Geology*, *43*(1–2), 120–131. https://doi.org/10.1007/s00254-002-0616-x

Leshchinsky, B. A., Olsen, M. J., & Bunn, M. D. (2018). *Enhancing landslide inventorying, lidar hazard assessment and asset management* (Report No. FHWA-OR-RD-18-18). Salem, OR: Oregon. Dept. of Transportation Research Section. Retrieved from https://www.oregon.gov/ODOT/Programs/ResearchDocuments/SPR%20786%20Inventorying,%20Lidar%20Hazard%20Assessment%20and%20Asset%20Management.pdf

Leshchinsky, B. A., Olsen, M. J., & Tanyu, B. F. (2015). Contour connection method for automated identification and classification of landslide deposits. *Computers & Geosciences*, *74*, 27–38. https://doi.org/10.1016/j.cageo.2014.10.007

Li, X., Cheng, X., Chen, W., Chen, G., & Liu, S. (2015). Identification of forested landslides using LiDar data, object-based image analysis, and machine learning algorithms. *Remote Sensing*, *7*(8), 9705–9726. https://doi.org/10.3390/rs70809705

Lu, N., & Godt, J. (2008). Infinite slope stability under steady unsaturated seepage conditions. *Water Resources Research*, *44*(11). https://doi.org/10.1029/2008wr006976

Lu, N., & Likos, W. J. (2004). *Unsaturated soil mechanics* (1st ed.). Hoboken, NJ: Wiley.

Luzi, L., Pergalani, F., & Terlien, M. (2000). Slope vulnerability to earthquakes at subregional scale, using probabilistic techniques and geographic information systems. *Engineering Geology*, *58*(3–4), 313–336. https://doi.org/10.1016/s0013-7952(00)00041-7

Madin, I.P., and Burns, W.J., (2013). *Ground motion, ground deformation, tsunami inundation, coseismic subsidence, and damage potential maps for the 2012 Oregon resilience plan for Cascadia subduction zone earthquakes* (Open File Report 0-13-06). Portland, OR: Oregon Department of Geology and Mineral Industries.

Madin, I. P., & Niewendorp, C. A. (2009). *Preliminary geologic map of the Dixie Mountain 7.5′ quadrangle, Washington, Multnomah, and Columbia Counties, Oregon* (Open-File Report O-08–07). Portland, OR: Oregon Department of Geology and Mineral Industries.

Mahalingam, R., & Olsen, M. J. (2016). Evaluation of the influence of source and spatial resolution of DEMs on derivative products used in landslide mapping. *Geomatics, Natural Hazards and Risk*, *7*(6), 1835–1855. https://doi.org/10.1080/19475705.2015.1115431

Mahalingam, R., Olsen, M. J., & O'Banion, M. S. (2016). Evaluation of landslide susceptibility mapping techniques using lidar-derived conditioning factors (Oregon case study). *Geomatics, Natural Hazards and Risk*, *7*(6), 1884–1907. https://doi.org/10.1080/19475705.2016.1172520

Malamud, B. D., Turcotte, D. L., Guzzetti, F., & Reichenbach, P. (2004). Landslide inventories and their statistical properties. *Earth Surface Processes and Landforms*, *29*(6), 687–711. https://doi.org/10.1002/esp.1064

Marano, K. D., Wald, D. J., & Allen, T. I. (2010). Global earthquake casualties due to secondary effects: A quantitative analysis for improving rapid loss analyses. *Natural Hazards*, *52*(2), 319–328. https://doi.org/10.1007/s11069-009-9372-5

Martin, Y., Rood, K., Schwab, J. W., & Church, M. (2002). Sediment transfer by shallow landsliding in the Queen Charlotte Islands, British Columbia. *Canadian Journal of Earth Sciences*, *39*(2), 189–205. https://doi.org/10.1139/e01-068

McCalpin, J. (1984). Preliminary age classification of landslides for inventory mapping. In *Proceedings of the Twenty-first Annual Engineering Geology and Soils Engineering Symposium: held at the University Inn, Moscow, Idaho, April 5 & 6, 1984* (pp. 99–111).

McKean, J., & Roering, J. (2004). Objective landslide detection and surface morphology mapping using high-resolution airborne laser altimetry. *Geomorphology*, *57*(3–4), 331–351. https://doi.org/10.1016/s0169-555x(03)00164-8

Meng, X., Currit, N., & Zhao, K. (2010). Ground filtering algorithms for airborne LiDAR data: A review of critical issues. *Remote Sensing*, *2*(3), 833–860. https://doi.org/10.3390/rs2030833

Meusburger, K., & Alewell, C. (2008). Impacts of anthropogenic and environmental factors on the occurrence of shallow landslides in an alpine catchment (Urseren Valley, Switzerland). *Natural Hazards and Earth System Sciences*, *8*(3), 509–520. https://doi.org/10.5194/nhess-8-509-2008

Milledge, D. G., Bellugi, D., McKean, J. A., Densmore, A. L., & Dietrich, W. E. (2014). A multidimensional stability model for predicting shallow landslide size and shape across landscapes. *Journal of Geophysical Research: Earth Surface*, *119*(11), 2481–2504. https://doi.org/10.1002/2014jf003135

Milledge, D. G., Griffiths, D. V., Lane, S. N., & Warburton, J. (2012). Limits on the validity of infinite length assumptions for modelling shallow landslides. *Earth Surface Processes and Landforms*, *37*(11), 1158–1166. https://doi.org/10.1002/esp.3235

Miller, D. J., & Sias, J. (1998). Deciphering large landslides: Linking hydrological, groundwater and slope stability models through GIS. *Hydrological Processes*, *12*(6), 923–941. https://doi.org/10.1002/(sici)1099-1085(199805)12:6<923::aid-hyp663>3.0.co;2-3

Montgomery, D. R., & Dietrich, W. E. (1994). A physically based model for the topographic control on shallow landsliding. *Water Resources Research*, *30*(4), 1153–1171. https://doi.org/10.1029/93wr02979

Mora, O.E., Toth, C.K., Grejner-Brzezinska, D.A., & Lenzano, M.G., (2014). A probabilistic approach to landslide susceptibility mapping using multi-temporal airborne lidar data. In *American Society for Photogrammetry and Remote Sensing Annual Conference: (ASPRS 2014): Louisville, Kentucky, USA, 23-28 March 2014*. Bethesda, MD.

Mudd, S. M., & Furbish, D. J. (2007). Responses of soil-mantled hillslopes to transient channel incision rates. *Journal of Geophysical Research*, *112*(F3). https://doi.org/10.1029/2006jf000516

National Academies of Sciences, Engineering, and Medicine. (2016). *Attribution of extreme weather events in the context of climate change*. Washington, DC: The National Academies Press. https://doi.org/10.17226/21852.

Nelson, A. R., Kelsey, H. M., & Witter, R. C. (2006). Great earthquakes of variable magnitude at the Cascadia subduction zone. *Quaternary Research*, *65*(3), 354–365. https://doi.org/10.1016/j.yqres.2006.02.009

Newmark, N. M. (1965). Effects of earthquakes on dams and embankments. *Géotechnique*, *15*(2), 139–160. https://doi.org/10.1680/geot.1965.15.2.139

Niebergall, S., Loew, A., & Mauser, W. (2007). Object-oriented analysis of very high resolution QuickBird data for mega city research in Delhi/India. In *2007 Urban Remote Sensing Joint Event Paris, France, 11 - 13 April 2007* (pp. 1–8). Piscataway, NJ; IEEE. doi: 10.1109/URS.2007.371836.

Niethammer, U., James, M., Rothmund, S., Travelletti, J., & Joswig, M. (2012). UAV-based remote sensing of the Super-Sauze landslide: Evaluation and results. *Engineering Geology*, *128*, 2–11. https://doi.org/10.1016/j.enggeo.2011.03.012

Norris, N. I., & Wyllie, D. C. (1996). Rock slope stability analysis. In *Landslides: Investigation and Mitigation* (First ed., pp. 391–425). Washington, D.C.: Transportation Research Board.

Ohlmacher, G. C., & Davis, J. C. (2003). Using multiple logistic regression and GIS technology to predict landslide hazard in northeast Kansas, USA. *Engineering Geology*, *69*(3–4), 331–343. https://doi.org/10.1016/s0013-7952(03)00069-3

Olsen, M. J. (2013). In Situ change analysis and monitoring through terrestrial laser scanning. *Journal of Computing in Civil Engineering*, *29*(2), 04014040. https://doi.org/10.1061/(asce)cp.1943-5487.0000328

Olsen, M.J., Allan, J.C., & Priest, G.R., (2012). *Movement and erosion quantification of the Johnson Creek, Oregon landslide through 3D laser scanning*. ASCE GeoCongress, Oakland, CA: ASCE GeoCongress. https://doi.org/10.1061/9780784412121.312

Olsen, M, Ashford, S.A., Mahlingam, R., Sharifi-Mood, M., O'Banion, M., & Gillins, D. (2015). *Impacts of Potential Seismic Landslides on Lifeline Corridors* (Rerpot No FHWA-OR-RD-15-06) Salem, OR: Oregon Department of Transportation. Retrieved from https://www.oregon.gov/ODOT/Programs/ResearchDocuments/SPR740SeismicLandslides.pdf

Oregon Department of Transportation. (2014). *Hydraulics Design Manual*. Salem, OR: Oregon Department of Transportation Highway Division.

Oregon Seismic Safety Policy AdivsoryCommission (OSSPAC). (2013). *The Oregon resilience plan, reducing risk and improving recovery for the next Cascadia earthquake and tsunami*. Salem, Oregon

Ouimet, W. B. (2010). Landslides associated with the May 12, 2008 Wenchuan earthquake: Implications for the erosion and tectonic evolution of the Longmen Shan. *Tectonophysics*, *491*(1–4), 244–252. https://doi.org/10.1016/j.tecto.2009.09.012

Pánek, T. (2015). Recent progress in landslide dating. *Progress in Physical Geography: Earth and Environment*, *39*(2), 168–198. https://doi.org/10.1177/0309133314550671

Passalacqua, P., Do Trung, T., Foufoula-Georgiou, E., Sapiro, G., & Dietrich, W. E. (2010). A geometric framework for channel network extraction from lidar: Nonlinear diffusion and geodesic paths. *Journal of Geophysical Research*, *115*(F1). https://doi.org/10.1029/2009jf001254

Passalacqua, P., Hillier, J., & Tarolli, P. (2014). Innovative analysis and use of high-resolution DTMs for quantitative interrogation of earth-surface processes. *Earth Surface Processes and Landforms*, *39*(10), 1400–1403. https://doi.org/10.1002/esp.3616

Passalacqua, P., Tarolli, P., & Foufoula-Georgiou, E. (2010). Testing space-scale methodologies for automatic geomorphic feature extraction from lidar in a complex mountainous landscape. *Water Resources Research*, *46*(11). https://doi.org/10.1029/2009wr008812

Pawłuszek, K., & Borkowski, A. (2016). Landslides identification using airborne laser scanning data derived topographic terrain attributes and support vector machine classification. *ISPRS - International Archives of the Photogrammetry, Remote Sensing and Spatial Information Sciences*, *XLI-B8*, 145–149. https://doi.org/10.5194/isprsarchives-xli-b8-145-2016

Pelletier, J. D. (2013). A robust, two-parameter method for the extraction of drainage networks from high-resolution digital elevation models (DEMs): Evaluation using synthetic and real-world DEMs. *Water Resources Research*, *49*(1), 75–89. https://doi.org/10.1029/2012wr012452

Perkins, J. P., Reid, M. E., & Schmidt, K. M. (2017). Control of landslide volume and hazard by glacial stratigraphic architecture, northwest Washington state, USA. *Geology*, *45*(12), 1139–1142. https://doi.org/10.1130/g39691.1

Perron, J. T., Kirchner, J. W., & Dietrich, W. E. (2008). Spectral signatures of characteristic spatial scales and nonfractal structure in landscapes. *Journal of Geophysical Research*, *113*(F4). https://doi.org/10.1029/2007jf000866

Petley, D. (2012). Global patterns of loss of life from landslides. *Geology*, *40*(10), 927–930. https://doi.org/10.1130/g33217.1

Pradhan, B., & Lee, S. (2010). Delineation of landslide hazard areas on Penang Island, Malaysia, by using frequency ratio, logistic regression, and artificial neural network models. *Environmental Earth Sciences*, *60*(5), 1037–1054. https://doi.org/10.1007/s12665-009-0245-8

Pradhan, B., Lee, S., & Buchroithner, M. F. (2009). Use of geospatial data and fuzzy algebraic operators to landslide-hazard mapping. *Applied Geomatics*, *1*(1–2), 3–15. https://doi.org/10.1007/s12518-009-0001-5

Ragno, E., AghaKouchak, A., Love, C. A., Cheng, L., Vahedifard, F., & Lima, C. H. R. (2018). Quantifying Changes in Future Intensity-Duration-Frequency Curves Using Multimodel Ensemble Simulations. *Water Resources Research*, *54*(3), 1751–1764. https://doi.org/10.1002/2017wr021975

Rahardjo, H., Li, X. W., Toll, D. G., & Leong, E. C. (2001). The effect of antecedent rainfall on slope stability. *Geotechnical and Geological Engineering 19,* 371–399. https://doi.org/10.1023/A:1013129725263

Ramsey, C. B. (2009). Bayesian analysis of radiocarbon dates. *Radiocarbon*, *51*(1), 337–360. https://doi.org/10.1017/s0033822200033865

Rankine, W. J. M. (1857). II. On the stability of loose earth. *Philosophical Transactions of the Royal Society of London*, *147*, 9–27. https://doi.org/10.1098/rstl.1857.0003

Reichle, R. H., De Lannoy, G., Koster, R. D., Crow, W. T., Kimball, J. S., & Liu, Q. (2018). *SMAP L4 global 3-hourly 9 km EASE-grid surface and root zone soil moisture geophysical data, version 4*. Boulder, Colorado: NASA National Snow and Ice Data Center Distributed Active Archive Center. https://doi.org/10.5067/KPJNN2GI1DQR.

Riahi, K., Rao, S., Krey, V., Cho, C., Chirkov, V., Fischer, G., . . . Rafaj, P. (2011). RCP 8.5—A scenario of comparatively high greenhouse gas emissions. *Climatic Change*, *109*(1–2), 33–57. https://doi.org/10.1007/s10584-011-0149-y

Roering, J. J. (2008). How well can hillslope evolution models "explain" topography? Simulating soil transport and production with high-resolution topographic data. *Geological Society of America Bulletin*, *120*(9–10), 1248–1262. https://doi.org/10.1130/b26283.1

Roering, J. J., Kirchner, J. W., & Dietrich, W. E. (1999). Evidence for nonlinear, diffusive sediment transport on hillslopes and implications for landscape morphology. *Water Resources Research*, *35*(3), 853–870. https://doi.org/10.1029/1998wr900090

Roering, J. J., Kirchner, J. W., & Dietrich, W. E. (2005). Characterizing structural and lithologic controls on deep-seated landsliding: Implications for topographic relief and landscape evolution in the Oregon Coast Range, USA. *Geological Society of America Bulletin*, *117*(5), 654. https://doi.org/10.1130/b25567.1

Roering, J. J., Perron, J. T., & Kirchner, J. W. (2007). Functional relationships between denudation and hillslope form and relief. *Earth and Planetary Science Letters*, *264*(1–2), 245–258. https://doi.org/10.1016/j.epsl.2007.09.035

Rosenbloom, N. A., & Anderson, R. S. (1994). Hillslope and channel evolution in a marine terraced landscape, Santa Cruz, California. *Journal of Geophysical Research: Solid Earth*, *99*(B7), 14013–14029. https://doi.org/10.1029/94jb00048

Rupp, D. E., Abatzoglou, J. T., & Mote, P. W. (2017). Projections of 21st century climate of the Columbia River Basin. *Climate Dynamics*, *49*(5–6), 1783–1799. https://doi.org/10.1007/s00382-016-3418-7

Santamarina, J. C., & Cho, G. C. (2004). Soil behaviour: The role of particle shape. In *Advances in geotechnical engineering: the Skempton conference* (pp. 604–617). London; Thomas Telford.

Saygili, G., & Rathje, E. M. (2008). Empirical predictive models for earthquake-induced sliding displacements of slopes. *Journal of Geotechnical and Geoenvironmental Engineering*, *134*(6), 790–803. https://doi.org/10.1061/(asce)1090-0241(2008)134:6(790)

Schaap, M. G., Leij, F. J., & van Genuchten, M. T. (2001). Rosetta : A computer program for estimating soil hydraulic parameters with hierarchical pedotransfer functions. *Journal of Hydrology*, *251*(3–4), 163–176. https://doi.org/10.1016/s0022-1694(01)00466-8

Schmidt, K. M., & Montgomery, D. R. (1995). Limits to relief. *Science*, *270*(5236), 617–620. https://doi.org/10.1126/science.270.5236.617

Schulz, W.H. (2004). *Landslides mapped using LIDAR imagery* (Open File Report 2004-1396) Washington, D.C.: United States Geological Survey. Retrieved from https://pubs.usgs.gov/of/2004/1396/OF2004-1396_508.pdf

Schulz, W. H. (2007). Landslide susceptibility revealed by LIDAR imagery and historical records, Seattle, Washington. *Engineering Geology*, *89*(1–2), 67–87. https://doi.org/10.1016/j.enggeo.2006.09.019

Schulz, W. H., Galloway, S. L., & Higgins, J. D. (2012). Evidence for earthquake triggering of large landslides in coastal Oregon, USA. *Geomorphology*, *141–142*, 88–98. https://doi.org/10.1016/j.geomorph.2011.12.026

Schuster, R., & Highland, L. (2001). *Socioeconomic and environmental impacts of landslides in the western hemisphere* (Open File Report 2001-276) Washington, D.C.: United States Geological Survey. https://doi.org/10.3133/ofr01276

Schuster, R. L., Logan, R. L., & Pringle, P. T. (1992). Prehistoric rock avalanches in the Olympic Mountains, Washington. *Science*, *258*(5088), 1620–1621. https://doi.org/10.1126/science.258.5088.1620

Schwanghart, W., & Scherler, D. (2014). Short communication: TopoToolbox 2 – MATLAB-based software for topographic analysis and modeling in earth surface sciences. *Earth Surface Dynamics*, *2*(1), 1–7. https://doi.org/10.5194/esurf-2-1-2014

Sharifi-Mood, M., Olsen, M. J., Gillins, D. T., & Mahalingam, R. (2017). Performance-based, seismically-induced landslide hazard mapping of Western Oregon. *Soil Dynamics and Earthquake Engineering*, *103*, 38–54. https://doi.org/10.1016/j.soildyn.2017.09.012

Sithole, G., & Vosselman, G. (2004). Experimental comparison of filter algorithms for bare-Earth extraction from airborne laser scanning point clouds. *ISPRS Journal of Photogrammetry and Remote Sensing*, *59*(1–2), 85–101. https://doi.org/10.1016/j.isprsjprs.2004.05.004

Snyder, G.I., (2012). *The 3D elevation program: Summary of program direction* (Report No. 2012-3089). Washington, D.C.: US Department of the Interior, US Geological Survey. https://doi.org/10.3133/fs20123089

Soldati, M., Corsini, A., & Pasuto, A. (2004). Landslides and climate change in the Italian Dolomites since the late glacial. *CATENA*, *55*(2), 141–161. https://doi.org/10.1016/s0341-8162(03)00113-9

Spitzer, K. U. T. (2016, April 17). “Buried alive”: Japan rushes to aid earthquake victims as storm approaches. *Usatoday*. Retrieved from https://eu.usatoday.com

Stott, P. (2016). How climate change affects extreme weather events. *Science*, *352*(6293), 1517–1518. https://doi.org/10.1126/science.aaf7271

Sugarbaker, L.J., Constance, E.W., Heidemann, H.K., Jason, A.L., Lukas, V., Saghy, D.L., & Stoker, J.M. (2014). *The 3D elevation program initiative – A call for action* (Circular 1399). Washington, D.C. United States Geological Survey. https://dx.doi.org/10.3133/cir1399.

Terzaghi, K. (1950). Mechanism of landslides. In *Application of Geology to Engineering Practice* (p. 41). Washington , D.C.: Geological Society of America. https://doi.org/10.1130/Berkey.1950.83

Trauth, M. H., Bookhagen, B., Marwan, N., & Strecker, M. R. (2003). Multiple landslide clusters record quaternary climate changes in the northwestern Argentine Andes. *Palaeogeography, Palaeoclimatology, Palaeoecology*, *194*(1–3), 109–121. https://doi.org/10.1016/s0031-0182(03)00273-6

Trimble, D. E. (1963). *Geology of Portland, Oregon, and adjacent areas* (Bulletin No. 1119). Washington, D.C.: US Government Printing Office. https://doi.org/10.3133/b1119

Tsai, T. L., & Yang, J. C. (2006). Modeling of rainfall-triggered shallow landslide. *Environmental Geology*, *50*(4), 525–534. https://doi.org/10.1007/s00254-006-0229-x

United Stated Department of Agriculture, Natural Resources Conservation Service Soils. (n.d.). *Soil texture calculator*. Software, Washington, D.C.: United Stated Department of Agriculture, Natural Resources Conservation Service Soils. Retrieved from https://www.nrcs.usda.gov

van Genuchten, M. T. (1980). A closed-form equation for predicting the hydraulic conductivity of unsaturated soils. *Soil Science Society of America Journal*, *44*(5), 892–898. https://doi.org/10.2136/sssaj1980.03615995004400050002x

van Westen, C. J., Castellanos, E., & Kuriakose, S. L. (2008). Spatial data for landslide susceptibility, hazard, and vulnerability assessment: An overview. *Engineering Geology*, *102*(3–4), 112–131. https://doi.org/10.1016/j.enggeo.2008.03.010

van Westen, C. J., & Terlien, M. J. T. (1996). An approach towards deterministic landslide hazard analysis in GIS: A case study from Manizales (Colombia). *Earth Surface Processes and Landforms*, *21*(9), 853–868. https://doi.org/10.1002/(sici)1096-9837(199609)21:9<853::aid-esp676>3.0.co;2-c

van Westen, C., van Asch, T., & Soeters, R. (2006). Landslide hazard and risk zonation—why is it still so difficult? *Bulletin of Engineering Geology and the Environment*, *65*(2), 167–184. https://doi.org/10.1007/s10064-005-0023-0

Wang, G., Joyce, J., Phillips, D., Shrestha, R., & Carter, W. (2013). Delineating and defining the boundaries of an active landslide in the rainforest of Puerto Rico using a combination of airborne and terrestrial LIDAR data. *Landslides*, *10*(4), 503–513. https://doi.org/10.1007/s10346-013-0400-x

Wang, J. J., Liang, Y., Zhang, H. P., Wu, Y., & Lin, X. (2014). A loess landslide induced by excavation and rainfall. *Landslides*, *11*(1), 141–152. https://doi.org/10.1007/s10346-013-0418-0

Warner, M. D., Mass, C. F., & Salathé, E. P. (2012). Wintertime extreme precipitation events along the Pacific Northwest Coast: Climatology and synoptic evolution. *Monthly Weather Review*, *140*(7), 2021–2043. https://doi.org/10.1175/mwr-d-11-00197.1

Wartman, J., Dunham, L., Tiwari, B., & Pradel, D. (2013). Landslides in Eastern Honshu induced by the 2011 Tohoku earthquake. *Bulletin of the Seismological Society of America*, *103*(2B), 1503–1521. https://doi.org/10.1785/0120120128

Wills, C. J., & McCrink, T. P. (2002). Comparing Landslide Inventories: The Map Depends on the Method. *Environmental and Engineering Geoscience*, *8*(4), 279–293. https://doi.org/10.2113/8.4.279

Wu, W., & Sidle, R. C. (1995). A distributed slope stability model for steep forested basins. *Water Resources Research*, *31*(8), 2097–2110. https://doi.org/10.1029/95wr01136

Xu, C., Xu, X., & Yu, G. (2013). Landslides triggered by slipping-fault-generated earthquake on a plateau: An example of the 14 April 2010, Ms 7.1, Yushu, China earthquake. *Landslides*, *10*(4), 421–431. https://doi.org/10.1007/s10346-012-0340-x

Yin, Y., Wang, F., & Sun, P. (2009). Landslide hazards triggered by the 2008 Wenchuan earthquake, Sichuan, China. *Landslides*, *6*(2), 139–152. https://doi.org/10.1007/s10346-009-0148-5

Zhou, G., Esaki, T., Mitani, Y., Xie, M., & Mori, J. (2003). Spatial probabilistic modeling of slope failure using an integrated GIS Monte Carlo simulation approach. *Engineering Geology*, *68*(3–4), 373–386. https://doi.org/10.1016/s0013-7952(02)00241-7